AN EVANESCENT-WAVE BASED PARTICLE IMAGE VELOCIMETRY TECHNIQUE

A Thesis
Presented to
The Academic Faculty

by

Haifeng Li

In Partial Fulfillment
of the Requirements for the Degree
Doctor of Philosophy in the
George W. Woodruff School of Mechanical Engineering

Georgia Institute of Technology
December 2008

AN EVANESCENT-WAVE BASED PARTICLE IMAGE VELOCIMETRY TECHNIQUE

Approved by:

Professor Minami Yoda,
Committee Chair
George W. Woodruff School of
Mechanical Engineering
Georgia Institute of Technology

Professor Cyrus Aidun
George W. Woodruff School of
Mechanical Engineering
Georgia Institute of Technology

Professor Andrei Fedorov
George W. Woodruff School of
Mechanical Engineering
Georgia Institute of Technology

Professor Cheng Zhu
Wallace H. Coulter Department of
Biomedical Engineering
Georgia Institute of Technology

Professor Victor Breedveld
School of Chemical and Biomolecular
Engineering
Georgia Institute of Technology

Date Approved: November 7 2008

ACKNOWLEDGEMENTS

The research involved in this thesis would not have been possible without the help and support of many people. Foremost, I would like to express my sincere gratitude to my advisor Professor Minami Yoda for her constant encouragement, trust and invaluable suggestions over all of these years. I am grateful to my reading committee members: Professor Cyrus Aidun, Professor Victor Breedveld, Professor Andrei Fedorov and Professor Cheng Zhu for their effort in reviewing this work and their advices and clarifying remarks.

I would also like to extend my appreciation to Dr. Jean Pierre Alarie and Professor J. Michael Ramsey at the University of North Carolina for helping me fabricating the microchannels used in this thesis work; to Ms. Gwenaelle Philibert and Professor Susan V. Olesik at the Ohio State University and Dr. Yonghao Xiu and Professor C. P. Wong at the Georgia Institute of Technology for their help in surface modification and characterization; to Dr. Christel Hohenegger and Professor Peter J. Mucha at the University of North Carolina for their many insightful discussions on Brownian dynamic simulations; to Dr. Subhra Datta and Professor A. Terrence Conlisk for their help in the electroosmotic flow experiments; to Mr. Zhengchun Peng and Professor Peter Hesketh for helping me with the photo mask and PDMS fabrications; to Mr. Jack Wei Chen for his helpful suggestions on using micropipettes in the calibration experiments.

The discussions and cooperations with all of my laboratory colleagues have also contributed substantially to this work. I would like to specially thank Dr. Reza Sadr for helping me get started with the experimental work and for always being

there and providing great advices. Thanks also to my other colleagues, Keith Suda-Cederquist for constructing the hydrostatic flow-driving system; Domenico Lippolis for his help on the diffusion measurements; Myeongsub Kim for sharing his setup with me, Charlotte Kotas and Tim Koehler for their many helpful suggestions on the experimental setup.

Finally, my deepest gratitude goes to my family and my wife for their continuous and unconditional support and persistent confidence in me. Without the love, none of this would have been possible.

TABLE OF CONTENTS

LIST OF TABLES

LIST OF FIGURES

Nomenclature

Abbreviations

AOM Acousto-optical modulator

CW Continuous-wave

DOF Depth of field

EDL Electric double layer

EOF Electroosmotic flow

FCS Fluorescence correlation spectroscopy

FRAP Fluorescence recovery after photobleaching

HPIV Holographic particle image velocimetry

LDM Laser-Doppler microscope

LDV Laser-Doppler velocimetry

LJ Lennard-Jones

μPIV Micro-particle image velocimetry

MD Molecular dynamics

MnPIV Multilayer nano-particle image velocimetry

MTV Molecular tagging velocimetry

NA Numerical aperture of microscope objective

nPIV Nano-particle image velocimetry

CNT Carbon nanotubes

PIV Particle image velocimetry

PTV Particle tracking velocimetry

SAM Self-assembled monolayer

SFA Surface force apparatus

SPIV Stereoscopic particle image velocimetry

TIR Total internal reflection

TIRF Total internal reflection fluorescence

TIRM Total internal reflection microscopy

Greek Letters

α Contact angle [°]

α_p Polarizability

$\beta_{\parallel}$, $\beta_{\perp}$ Correction factors for hindered Brownian diffusion in the directions parallel and perpendicular to the wall, respectively

ΔP Pressure difference that drives the Poiseuille flows [Pa]

Δt Time interval within one PIV image pair [ms]

Δx Particle displacement measured in PIV

δt Time step used in Brownian dynamic simulations [μs]

ξ Dimensionless distance measured from particle center and wall (Equation 19)

ϵ	Cut-off threshold (normally set as 0.01) below which particle images are too dim to contribute to the cross-correlation (Equation 2)	
ϵ_f	Lennard-Jones energy of fluid	
ϵ_{wf}	Lennard-Jones wall-fluid interaction energy	
$\epsilon_{\Delta x}$	Average error in the measured particle displacement in PIV	
$\sigma_{\Delta x}$	Standard deviation of the error in the measured particle displacement in PIV	
ϕ	Particle-wall interaction potential energy	
ϕ_p	The volume fraction of the original particle suspension	
κ	Invert Debye length	[nm^{-1}]
λ	Wavelength	[nm]
μ	Dynamic viscosity	[Pa·s]
ω	Angular frequency of the fluorescence emission	
θ_B	Bragg angle	
θ_b	Angle between the side wall and bottom of the microchannel	
θ_c	Critical angle in total internal reflection	
θ_i	Angle of incidence	
θ_t	Angle of refraction	
ρ_f	Fluid density	
ρ_p	Particle density	
σ_d	Size parameter in a simulated particle image (Section 3.1.1)	

τ Normalized time interval by a Brownian diffusion time scale (Equation 17)

τ_B Relaxation time of the Brownian fluctuations [s]

Ψ_m, Ψ_s Mean and standard deviation of the random background noise in the synthetic image modeled as a Gaussian distribution

ζ Zeta potential [mV]

Symbols

a Particle radius [nm]

b Slip length [nm, μm]

C Molar concentration of a solution [mM]

c Particle number density [m^{-3}]

C_f Final molar salt concentration of a working fluid [mM]

C_i Molar salt concentration of a "stock" solution [mM]

D_∞ Unconfined Brownian diffusion coefficient [m^2/s]

$D_\parallel$ In-plane component of the near-wall hindered Brownian diffusion coefficient tensor [m^2/s]

d_c Diameter of capillary [μm]

d_{diff} Diffraction limited particle image diameter

d_{pi} Diameter of the particle image

d_s Distance between two adjacent TIR spots

d_t Thickness of the microchannel piece

$\overline{\mathbf{E}}_{\text{ins}}$	Refracted wave that is transmitted into the particle due to the elastic scattering of the incident wave by the particle	
e	Eccentricity of a particle image	
e_{c}	Magnitude of charge on an electron	[C]
F	Fraction of "mismatched" particles in MnPIV for a given time interval	[%]
$f_{\#}$	Microscope objective f-number	
G	Shear rate	[s^{-1}]
G_{M}	Multiplication gain of the CCD camera	
H	Channel depth	[mm]
h	Distance between the particle's lower edge and the wall	[nm]
I_{pi}^{M}	Intensity of a synthetic particle image determined from particle tracking defined as mean grayscale value of the image (Section 3.2)	
I_0	Intensity of evanescent wave at the refractive index interface	
I_{c}	Maximum grayscale value of a simulated particle image	
$I_{\text{d,off}}$	Intensity of the diffracted light by an AOM with the acoustic wave off	
$I_{\text{d,on}}$	Intensity of the diffracted light by an AOM with the acoustic wave on	
I_{in}	Intensity of the light entering an AOM	
I_{pi}	Intensity distribution within a synthetic particle image	
I_{p}	Particle image intensity defined as the peak grayscale value of the image	
I_{p}^0	Image intensity defined as the peak grayscale value of the image for a particle at the wall	

k Boltzmann's constant $= 1.38 \times 10^{-23}$ $\mathrm{m^2 kgs^{-2} K^{-1}}$

L Channel length [mm]

μ_p magnetic permeability of the particle

M Microscope objective magnification

m Mass of the particle

M_eff Effective magnification of the imaging system

m_s Mass of salt [mg]

n_1 Refractive index of the incident medium

n_2 Refractive index of the refraction medium

n_3 Refractive index of the particle

N_A Avogadro's number 6.02×10^{23}

n_o Refractive index of the immersion medium between the microscope objective lens and object

P Power of the light incident on the CCD [mW]

$P(z)$ Probability density function for a z-position to be sampled by the matched particles for given set of dimensional parameters Δt, Z and a or dimensionless parameters W and τ

$p(z)$ Probability of finding a particle at a given z-position for obtaining particle potential (Appendix F)

P_n Normalized power of the light incident on the CCD

R Reflection coefficient

T	Absolute temperature	[K]
t_0	Beginning of the time interval	
t_{d1},t_{d2}	Time delay between the rising edge of the master trigger signal and the rising edges of the first and second laser pulses, respectively	[ms]
t_{exp}	Effective exposure time for image recording using frame straddling	[ms]
$\bar{u}_p$	Mean particle velocity of a range of z	[m/s]
u'	Particle velocity	
u_c	Velocity at the geometric center of the region of interest	[m/s]
u_w	Fluid slip velocity at the wall	
V	Grayscale value of a pixel	
V_d	Grayscale value of a CCD pixel corresponding to the dark noise of the camera	
v_f	Volume of the final solution	[mL]
v_i	Volume of the "stock" solution	[mL]
V_n	Normalized grayscale value of a CCD pixel	
v_p	Volume of the original particle suspension needed to seed the working fluid	[μL]
v_s	Desired volume of the seeded solution	[mL]
W	Dimensionless thickness of the experimental volume in MnPIV (Equation 19)	
W_c	Width of the cross-correlation function	[pixels]
$\langle \bar{z} \rangle$	Mean z-position sampled by the matched particle	
Z	Thickness of the volume of interest over which velocity is measured in MnPIV	[nm]

z	Distance between particle center and the wall	[nm]
z_{L},z_{U}	Lower and Upper limits of a layer considered in MnPIV	
z_{p}	Intensity-based e^{-1} penetration depth of evanescent wave	[nm]
z_{corr}	Depth of correlation used in μPIV	[μm]

SUMMARY

Quantifying transport, specifically the velocity field inside microfluidic devices, especially in the interfacial or near-wall region, is important since surface (*vs.* bulk) effects become significant at micro- to nanometer scales. Recently, experimental studies and molecular dynamics simulations have suggested that "no-slip" boundary condition may break down in microscale flows even for Newtonian liquids. Due to the limited near-wall spatial resolution of current tracer-based velocimetry techniques, the amount of slip is usually inferred from the velocity components tangential to the wall measured far from the wall. This doctoral thesis presents a new technique for measuring the two tangential velocity components at different distances from and within about 500 nm of the wall and describes using this technique to study liquid slippage over solid walls of varying wettability.

The technique, "multilayer nPIV" (MnPIV), uses evanescent waves, which have an intensity that decays exponentially with distance normal to the wall z, to illuminate colloidal fluorescent tracer particles. Since the length scale of the decay is typically $O(100)$ nm, only the tracers within about 500 nm of the wall are illuminated. The nonuniform nature of the illumination also makes it possible to "bin" the particles, based on their image intensities, into different layers spanning different distances from the wall, and therefore to obtain the tangential velocity components at multiple z-positions for $z < 500$ nm.

The feasibility of this technique was first demonstrated using synthetic images of plane Couette flow that incorporate hindered Brownian diffusion, evanescent-wave illumination and imaging noise. The errors in MnPIV data due to the non-uniform

illumination and the asymmetric Brownian diffusion of the tracers in the near-wall region were quantified with Brownian dynamics simulations. Calibration experiments were then carried out to verify that the particle image intensities decay exponentially with z with a decay length scale comparable to that of the evanescent-wave illumination.

Multilayer nPIV, was then used to determine the z-positions of the particles and therefore the particle distribution as a function of z in experimental studies of incompressible, steady and fully-developed Poiseuille flows of aqueous solutions through slightly trapezoidal microchannels. After dividing the tracers into three distinct layers, the temporally and spatially averaged velocity of each layer, determined by particle tracking, was placed at the average z-position sampled by the particles in that layer, based on the measured particle distribution. The velocity gradients obtained with MnPIV were within 6% on average of predictions based on the analytical solution for two-dimensional Poiseuille flow.

Finally, MnPIV was used to determine slip lengths of aqueous ammonium bicarbonate and ammonium acetate solutions through microchannels with naturally hydrophilic (*i.e.*, bare) and hydrophobically-coated fused silica surfaces. The measured slip lengths are within the experimental uncertainty in both the hydrophilic and hydrophobic channels. The MnPIV results therefore suggest that if the slip lengths are nonzero for both of these surfaces, they are less than the uncertainty in these results, or 27 nm and 31 nm for the hydrophilic and hydrophobic channels, respectively..

CHAPTER I

INTRODUCTION

1.1 Motivation

Microfluidics, which involves the delivery, processing and manipulation of small volumes of fluid (10^{-9} to 10^{-18} L) through conduits with overall dimensions ranging from tens to hundreds of micrometers, has great potential for applications in areas from chemistry and biology to optics and transport processes. Over the past two decades, a wide variety of microfluidic devices have been designed, fabricated and commercialized. Perhaps the best known of these devices are "Labs-on-a-chip" (LOC) that scale down an entire analytical biochemistry laboratory, integrating multiple steps (*e.g.*, injection, reaction, separation, and detection) down to a few square inches. LOC devices have been used to analyze clinical, environmental and food samples [38], for example, to detect nerve agents in blood [177], pathogens in food or water [133], and explosive compounds [152]. Despite their different functions, LOC devices share a number of advantages, such as shorter reaction and analysis time, reduced sample consumption and therefore reduced cost and chemical waste, and, given their compactness, the capability to conduct analyses at the sample point of origin. Microfluidic devices are also used to create microsructure heat exchangers that manifold numerous microchannels [17], and optofluidic chips with tunable optical properties [151].

Rapid development of these microfluidic devices, most of which involve liquid-phase flows, has motivated new research on such flows with overall dimensions ranging from micrometers down to nanometers. As a result of the reduction in length scales, surface (*vs.* bulk) effects become significant; consequently, an understanding of how surface properties (*e.g.*, roughness, charge, wettability) can affect the flow conditions

is of both fundamental and engineering interests.

One such example is the possibility that liquids may "slip" over solid nonwetting walls. In macroscale fluid mechanics, the standard boundary condition on the flow velocity at a solid wall is the "no-slip" condition, where the velocity component tangential to the wall is continuous across the fluid-solid interface. Although this boundary condition, originally proposed by Prandtl, is supported by more than a century of macroscopic experimental data, recent molecular dynamics (MD) simulations and experimental studies have suggested that fluid slip could occur over a non-wetting (*i.e.*, hydrophobic for the case of water) wall. This slippage is usually described by the partial-slip boundary condition, or Navier's condition, for the velocity component tangential to the wall (Figure 1 and Equation 1) given in terms of the slip length b, which can be interpreted as the distance "inside" the wall at which the linearly-extrapolated fluid velocity becomes zero.

$$u_{\mathrm{w}} = b\frac{\partial u}{\partial z}\bigg|_{z=0} \tag{1}$$

Here, z is the coordinate normal to the solid wall ($z = 0$ at the wall surface) and u_{w} is the slip velocity of the fluid relative to the wall, or the fluid velocity component tangential to the and at the wall. For the no-slip condition, $b = 0$.

Typical magnitudes of the slip length reported in the literature range from a few nanometers to several micrometers. Clearly, such small nonzero b, if correct, would have few practical consequences in macroscopic flows. In microfluidic devices with their large surface-to-volume ratio, however, slip at the liquid-solid interface may be a promising way to reduce the very high flow resistance associated with flow through channels of small hydraulic diameters (*e.g.*, for pressure driven flow inside a capillary of diameter d_{c}, the flow resistance scales with d_{c}^{-4}). A non-zero slip length would reduce the pressure difference required to achieve a given flowrate in Poiseuille flow through the capillary by a factor of $1 + 8b/d_{\mathrm{c}}$ for a $d_{\mathrm{c}} = 1$ μm capillary, a 100 nm

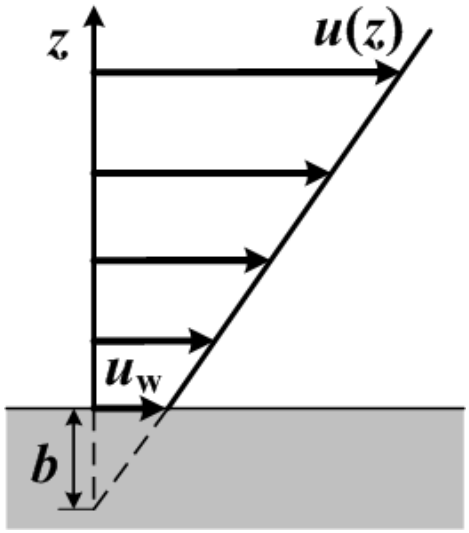

Figure 1: Illustration of slip and slip length.

slip length would almost halve the required pressure gradient. Majumder et al. [113] reported slip lengths of $O(10\ \mu m)$ inside carbon nanotubes (CNT) with an inner diameter of 7 nm and obtained flow rates up to five orders of magnitude larger than those predicted assuming no slip.

The possibility of "engineered" surfaces with different slip lengths is of great interest in microfluidic applications. To design such surfaces and to accurately model microscale flows with appropriate boundary conditions also require a fundamental understanding of the mechanism underlying slip and accurate models to predict the magnitude of slip length.

Despite the numerous experimental studies reporting nonzero slip lengths, there is currently no consensus on the mechanism behind this phenomenon. One major difficulty with measuring slip lengths or studying any micro- or nano-scale flows is that the measurements must have a near-wall spatial resolution of 1 μm or less while minimally disturbing the flow. To date, a wide range of diagnostic techniques, mainly tracer-based velocimetry techniques, including particle-image velocimetry (PIV), laser-Doppler

velocimetry (LDV), fluorescence correlation spectroscopy (FCS), and molecular tagging velocimetry (MTV), have been used for experimental microfluidic studies. Comprehensive reviews on such techniques are given by Breuer [20] and Sinton [168]. In the next sections, an overview of these techniques is provided, focusing on their near-wall velocimetry capabilities and spatial resolution.

1.2 Tracer-Based Near-Wall Velocimetry Techniques

1.2.1 Fluorescence Correlation Spectroscopy (FCS)

One technique used to measure liquid flows inside microchannels is fluorescence correlation spectroscopy (FCS). Standard single-focus FCS normally uses fluorescent molecules as tracers and a diffraction-limited laser focus with a Gaussian intensity profile as the illumination source. As the molecules move across the volume defined by the focus, the fluctuations in fluorescence intensity over time are recorded, and the "flow time" can be determined from these fluctuations with appropriate calibration. The velocity is then obtained by dividing the diameter of the focus by the flow time. Using such a system, Gosch et al. [58] measured flow velocities up to 50 mm/s inside a 50 μm square microchannel using a laser focus with a e^{-2} waist diameter of 0.4 μm. Although velocity profiles across the channel height and width were obtained in 1 μm steps by moving the focal spot, their near-wall measurements were limited by the inability of the technique to distinguish displacements due to convection, *vs.* diffusion, and by difficulties in controlling the size of the focus close to the wall. Lumma et al. [110] overcame these disadvantages by using a FCS system with two distinct laser foci 6 μm apart. In this system, the focal spots record two fluorescence-time signals that can be cross-correlated to calculate the "flow time," or the time it takes for the tracers to move across both of the two spots. Using this technique, the authors obtained a velocity profile across a 100 μm channel with both 40 nm diameter fluorescent latex particles and fluorescent molecules (Alexa 568, Invitrogen) by scanning

both foci across the channel. The spatial resolution in the direction normal to the wall was estimated from the height of the focal spot to be 1.6 μm.

1.2.2 Molecular Tagging Velocimetry (MTV)

Molecular tracers are also used in "molecular tagging velocimetry" (MTV) to measure fluid velocities. The technique relies on molecules that can be turned into long lifetime tracers, once excited or "tagged," that follow the flow field. In MTV applications, the molecules located in regions of interest are first illuminated by a pulsed laser (usually at UV wavelengths) so that they either become phosphorescently "tagged," or are uncaged. For the uncaged line (in the latter case), they have to be excited by a second laser at visible wavelengths and the fluorescent emission is recorded. In either case, the displacement of the tagged lines over a known time interval gives the flow velocity. In a one-dimensional flow, a single tagged line normal to the primary flow direction and the optical axis of the imaging system is sufficient for the measurement; in a tow-dimensional flow, however, a grid of intersecting laser beams in a plane normal to the optical axis of the imaging system is needed to obtain the two velocity components in a "slice" of the fluid. Based on the distortion of the tagged lines over time, the velocities of the "tagged" regions can be determined. Koochesfahani and Nocera [93] gave a comprehensive review of MTV in macroscale flows.

In microscopic settings, both the tagging and excitation lights are oriented along the optical axis of the imaging system due to the very limited optical access and so the camera images the fluorescence integrated across the entire depth of the channel. Paul et al. [136] created a 20 μm thick and 500 μm wide laser sheet normal to the flow direction to tag the molecules and visualized pressure- and electrokinetically-driven steady flows within capillaries having inner diameters up to 365 μm. A similar setup was also been used by Maynes and Webb [116] to study Poiseuille flows inside 705 μm diameter capillary, by Thompson et al. [180] who measured entrance lengths in

laminar Poiseuille flows (Re $<$ 400) through capillaries with an inner diameter of 182 μm using a tagging beam with a waist size of about 30 μm, and by Sinton et al [169] who studied the influence of axial temperature gradient on electroosmotic flows inside microchannels. All of these applications are examples of "single-line" MTV, measuring just one velocity component. More recently, Roetmann et al. [154] proposed a 2D micro-MTV approach that introduces a structured mask in the optical path to create a dye pattern (Figure 2a) *vs.* a single line. The two in-plane velocity components were obtained from the evolution of the pattern (Figure 2). As shown in the Figure, the pattern recorded at a later time is blurred compared with the initial image, especially along the flow direction, due to Taylor dispersion and molecular diffusion, which limit accuracy of the measurements. The spatial resolution of the technique in near-wall region is also limited by the dimension of the dots which have a diameter of about 160 μm.

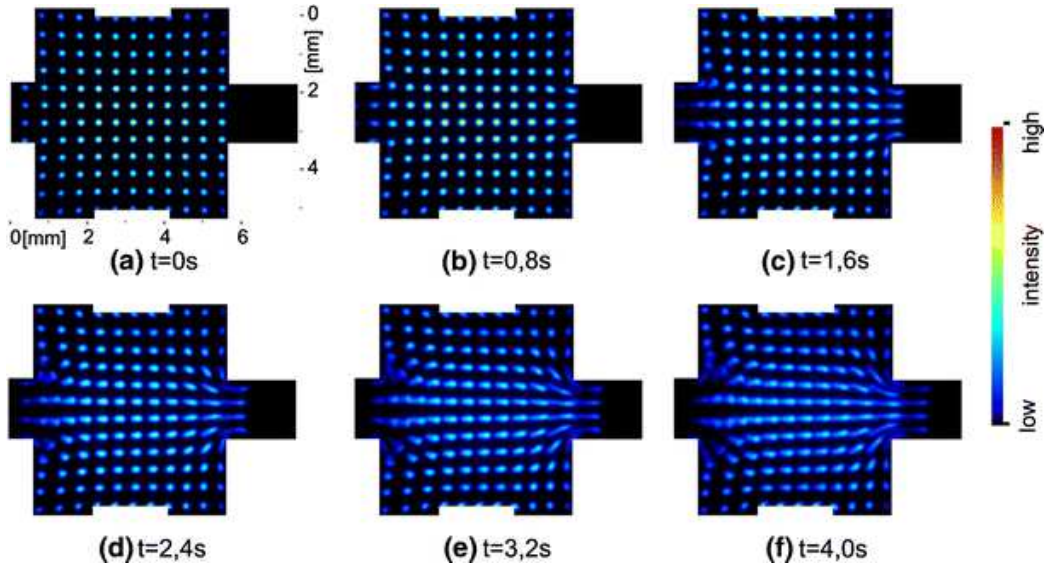

Figure 2: Two dimensional MTV image series of a laminar flow inside a mixing chamber (5 mm × 5 mm) by Roetmann et al. [154]. Here, a regular dot pattern was used to mark the flow and the dots have a diameter of about 160 μm.

1.2.3 Laser-Doppler Velocimetry (LDV)

Alternatively, velocity measurements can be accomplished using techniques based on optical Doppler effect, for example, laser Doppler velocimetry (LDV). In the widely used "differential Doppler system," two coherent laser beams intersect at their waists in an ellipsoidal-shaped region and the wavefronts of the beams generate alternating bright and dark interference fringes. When a tracer particle in the fluid moves through this set of fringes, the frequency of the light scattered by the moving particle is related to its velocity component normal to the fringes and the fringe spacing based on the optical Doppler effect. The spatial resolution of the LDV technique is determined by the probe volume or the intersection volume of the two beams, which is typically $O(1$ mm) long and has a cross section diameter of $O(0.1$ mm)[2]. Applications of the technique in macroscopic settings are reviewed by Penner and Jerskey [137], Tropea [188] and Durst et al. [48].

Several groups have extended LDV to microfluidic studies by improving the spatial resolution of LDV. One effective way of reducing the size of the probe volume is to sharply focus the laser beams. Tieu et al. [184] reduced the LDV measurement volume down to 5 μm$\times$10 μm (diameter by length) using short-focal-length lenses and a solid state laser. Their measured Poiseuille flow profile in a 175 μm capillary was in good agreement with the analytical solution, but the authors were unable to obtain data within 18 μm of the wall. A much earlier LDV configuration, the "laser Doppler microscope" (LDM) of Mishina et al. [123] integrated a compact differential LDV system into a microscope, using the microscope objective to focus the laser beams. The LDM system had a probe volume with a diameter of about 10 μm and gave velocity data as close as 100 μm from the wall. Later, Einav [49] used LDM to measure velocity profiles of blood flows in arterioles with diameters of 38-l35 μm, obtaining near-wall measurements as close as 7-10 μm from the wall. Although these different approaches for focusing the laser beams does improve the spatial resolution

of LDV, focusing the beams also introduces the following disadvantages: (i) highly focused beams with Gaussian intensity profiles leads to non-uniform fringe-spacing across the measurement volume due to chromatic dispersion of the focusing lens [100]; (ii) as the probe volume shrinks, the number of fringes is also reduced, which causes significant uncertainty in determining the Doppler frequency and limits the accuracy of the resultant velocity measurement.

Czarske et al. [43] proposed to overcome these disadvantages with a setup that obtains the velocity profile inside the measurement volume, which superposes two rather long ($\sim$5 mm in length and 300 μm in diameter) probe volumes with convex and concave wavefront shapes at different wavelengths λ_1 and λ_2, respectively, as shown in Figure 3. Note that the fringe spacing of the convex wavefront increases, while that of the concave wavefront decreases, with increasing y, resulting in a ratio of fringe spacings that varies monotonically with y. This enables the authors to simultaneously measure both the y-position and the velocity of a tracer inside the measurement volume. The technique was validated by measurements in laminar boundary layers and Poiseuille flow through round pipes [42]. Although an average spatial resolution of 2.5 μm was achieved inside the measurement volume, the technique was unable to obtain velocities within 40 μm of the wall due to the light scattering at the liquid-solid interface.

1.2.4 Micro-Particle Image Velocimetry (μPIV)

Perhaps the most popular tracer particle-based velocimetry technique, particle image velocimetry (PIV), has been widely used for non-intrusively measuring two and three fluid velocity components within a two-dimensional plane of the flow. In its most common implementations, tracer particles suspended in the fluid are illuminated by a laser light sheet and successive images of the illuminated particles are recorded on photographic film or by a digital camera. The particle displacements are then

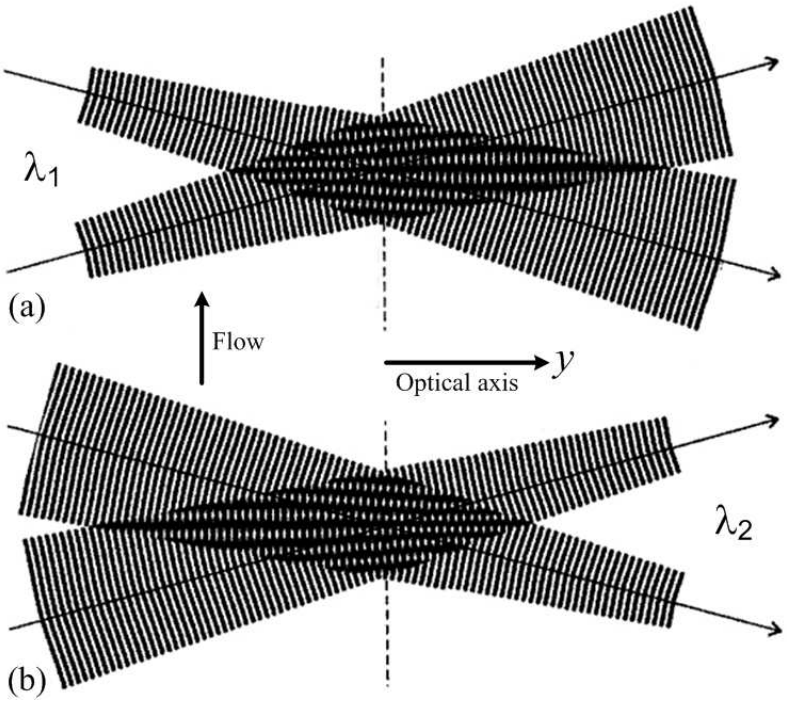

Figure 3: Schematic of the LDV velocity profile sensor proposed by Czarske et al. [42]. Two (superposed) interference fringe systems are generated by means of two laser wavelengths, with convex (λ_1) and concave (λ_2) wavefronts respectively. Note that due to the chromatic dispersion of the focusing lens and difference in wavefront shape, the spacing of the fringe system at wavelength λ_1 increases while the one at λ_2 decreases with y.

determined using cross-correlations between two sequential images separated by a known time interval. The two in-plane fluid velocity components are then these displacements divided by the time interval, assuming the tracer particles faithfully follow the motion of the fluid [153].

PIV has been extended to microscopic applications, where it is usually known as micro-scale PIV (μPIV) [160]. Because of the difficulty in creating laser light sheets with a thickness of a few micrometers, μPIV, unlike conventional PIV, uses volume illumination and relies on the depth of the field (DOF) of the imaging optics to record a "slice" of a flowing fluid seeded with colloidal (typically 100 - 500 nm in diameter) neutrally buoyant fluorescent tracer particles (Figure 4).

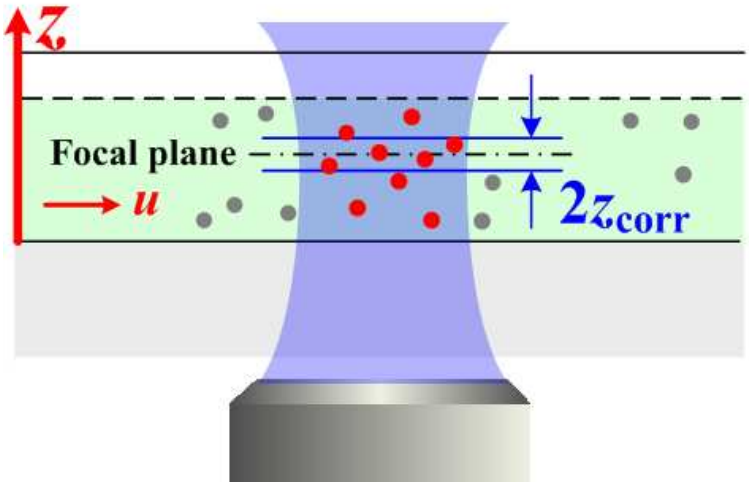

Figure 4: Schematic of a typical μPIV setup.

Micro-PIV has been used to measure near-wall velocities in two different configurations. As shown in Figure 5, Tretheway and Meinhart [186, 187] studied Poiseuille flow in a central slice of a micro-channel (30 μm deep and 300 μm wide) and included a side wall in the region imaged. The flow velocities were then obtained by cross correlating elongated interrogation regions with a length of 14.7 μm along the flow (x) direction and a width of 0.9 μm along the cross-stream (y) direction. The near-wall spatial resolution is therefore determined by the y-dimension of the interrogation window.

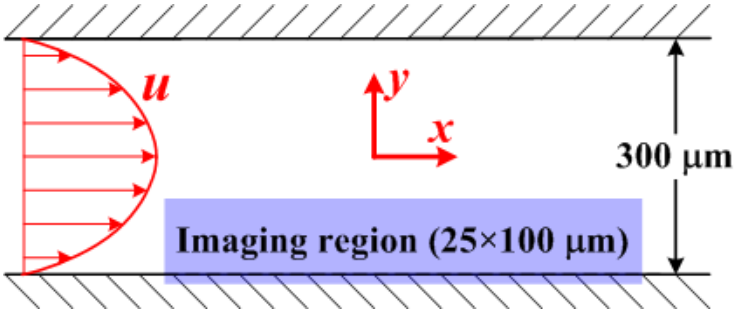

Figure 5: Imaging setup used by Tretheway and Meinhart [186]. Diagram not to scale.

Another way of obtaining near-wall velocities in μPIV is to image the particles

in a plane parallel and close to either the top or bottom walls of the microchannel (Figure 4). The near-wall spatial resolution of this approach is determined by the accuracy in positioning the focal plane and the thickness of the imaged volume along the wall-normal (z) direction. This thickness can be quantified by the "depth of correlation," z_{corr} in Equation 2 [128]. By definition, only the images of the particles located within $\pm z_{\text{corr}}$ of the focal plane will contribute significantly to the cross correlation used to determine the tracer displacement in PIV.

$$z_{\text{corr}} = \left\{ \left(\frac{1-\sqrt{\epsilon}}{\sqrt{\epsilon}} \right) \left[4f_{\#}^2 a^2 + \frac{5.95(M+1)^2 \lambda^2 f_{\#}^4}{M^2} \right] \right\}^{1/2} \tag{2}$$

Here, ϵ is a cutoff threshold (normally set as 1%) below which the particle images are too dim to contribute to the cross-correlation, a is the particle radius, M, NA, and $f_{\#} = 1/(2\text{NA})$ are the magnification, numerical aperture and f-number of the microscope objective and λ is the wavelength of the illumination. Bourdon et al. [15], who experimentally verified this model, reported excellent agreement between their experimental results and Equation 2 for dry microscope objectives with NA up to 0.4. Bourdon et al. [14] later showed that the model works for "wet" (oil- and water-immersion) objectives of higher NA if the expression for $f_{\#}$ in Equation 2 is replaced by the more rigorous definition $f_{\#} = 0.5\sqrt{(n_{\text{o}}/\text{NA})^2 - 1}$ (n_{o} is the refractive index of the immersion medium of the objective lens) derived by Meinhart and Wereley [118] for infinity-corrected microscope objective lenses. Apparently, z_{corr} depends strongly upon both the $f_{\#}$ or numerical aperture (NA) of the objective and the particle size and is usually of $O(1\ \mu\text{m})$. Table 1 shows the calculated depths of correlation for various microscope objective lenses and particle sizes.

Using the approach described above, Joseph and Tabeling [83] imaged particles in a plane parallel to the wall and obtained velocities within 0.5 μm of the bottom wall of the channel using a high-NA (1.3) objective and manually removing out-of-focus particle images in post-processing. Another way to reduce the depth of field and

Table 1: Depth of correlation $2z_{\text{corr}}$ calculated using Equation 2.

M	NA	a [nm]	$2z_{\text{corr}}$ [μm]
10	0.22	250	41.3
40	0.55	150	4.7
40	0.55	250	5.0
63	0.7	50	2.0
63	0.7	150	2.2
63	0.7	250	2.5

minimizing the background noise due to out-of-focus particle images is to include a spinning Nipkow disk-based confocal scanner with a conventional μPIV system. The pinhole at the beam focus spatially filters out the light from the particles beyond the focal plane, resulting in images of a slice of the flow with an effective thickness of $O(1\ \mu\text{m})$. A confocal scanning laser microscopy (CSLM) system with a 40×, 0.75NA microscope objective was used by Park et al. [135] to measure velocity profiles along the optical axis in the Poiseuille flow of water inside capillaries with nominal diameter of 100 μm. The depth of field of their images, based on the optical characteristics of their objective, was 1.3 μm. Lima et al. [104], who studied pressure-driven flows of water and Hanks solution (HS) containing 10% (by volume) human blood cells through a microchannel achieved a depth of field of about 5 μm with a 20×, NA 0.75 objective, while Kinoshita et al. [89] reported a depth of field of 1.3 μm with a 63×, NA 1.4 objective in their velocity measurements inside oil droplets suspended in the pressure-driven flow of water. To date, most confocal μPIV studies have, however, focused on bulk, rather than near-wall, flow in microchannels.

1.2.5 Nano-Particle Image Velocimetry (nPIV)

To further improve the near-wall spatial resolution of PIV, another technique, nano-particle image velocimetry (nPIV) was developed by Zettner and Yoda [205], who

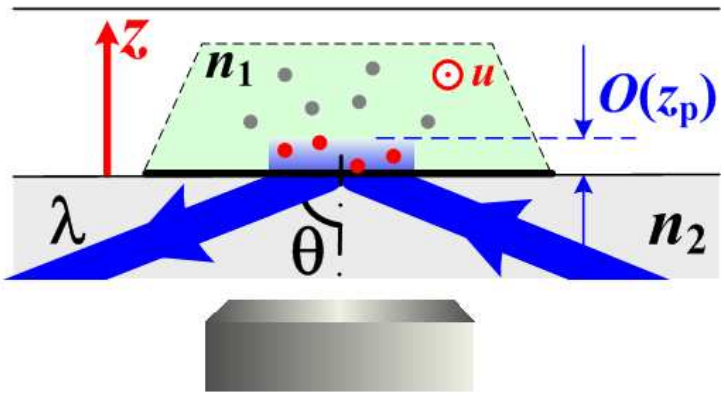

Figure 6: Experimental setup for nano-PIV.

obtained velocity data within 380 nm of the wall in a rotating Couette flow. Nano-PIV utilizes evanescent-wave illumination, unlike the volume illumination in μPIV. As shown in Figure 6, when a beam of light undergoes total internal reflection (TIR) at a planar interface between two materials with refractive indices n_1 and n_2 (where $n_1 > n_2$), an "evanescent wave" is generated in the lower refractive-index, or less optically dense, medium. While the wave travels parallel to the interface, its intensity decays exponentially along z, or the distance normal to the interface:

$$I(z) = I_0 \exp\left\{ -\frac{z}{z_\mathrm{p}} \right\} \tag{3}$$

Here, I_0 is the intensity of evanescent wave at the interface ($z = 0$) and z_p is the intensity-based penetration depth, or the distance into the less dense medium from the interface where the wave intensity is reduced by a factor of $1/e$. This decay in illumination intensity in conjunction with the detection limit of the camera restricts the region illuminated by the evanescent wave to a few z_p or the first few hundred nanometers next to the wall. Nano-PIV can therefore be used to measure the two velocity components tangential to the wall within this illuminated region.

The different illumination scheme used by nPIV gives it a few advantages over μPIV for near-wall velocimetry. First, nPIV images have a much lower background

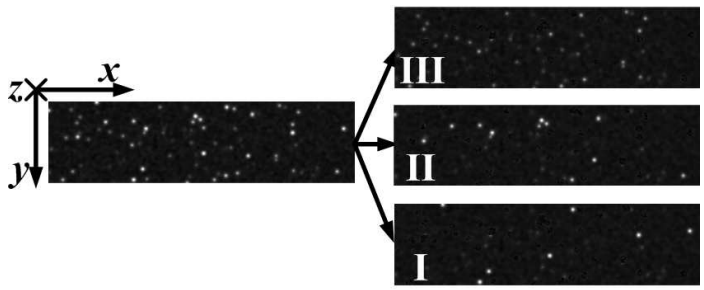

(a)

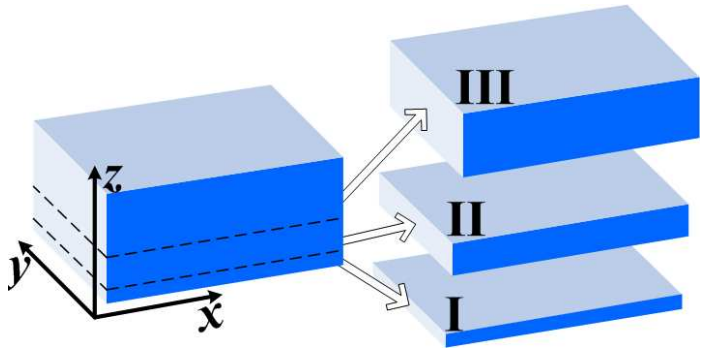

(b)

Figure 7: Schematic of multi-layer nano-particle image velocimetry.

noise compared with μPIV data since all the illuminated particles in nPIV are within the depth of field of the objective and therefore in focus. Moreover, nPIV's out-of-plane resolution is primarily determined by illumination and is less than that of typical μPIV near-wall measurements. Finally, a unique advantage of nPIV in near-wall measurements is that the evanescent-wave illumination in nPIV is bounded—and created—by the refractive-index interface, *i.e.*, the wall itself. This eliminates many of the difficulties in determining the actual location of the wall in μPIV measurements.

1.3 Objectives

The primary objective of this thesis is to develop and apply an extension of the nPIV technique, "multi-layer nPIV" (MnPIV). This new technique, which uses the same experimental setup as "standard" nPIV, exploits the non-uniform nature of the evanescent-wave illumination and divides the tracers in a typical nPIV image into multiple bins, or sub-layers (Figure 7), based upon the particle image intensity

which can, with appropriate calibration, be correlated to the tracer's z-location (*i.e.*, the distance between the particle center and the wall). By processing these sub-images with cross-correlation or particle-tracking based methods, MnPIV determines a velocity profile, or velocities at different distances from the wall, within a few hundred nanometers of the wall. As will be discussed in this thesis, multi-layer nPIV has been used to:

- determine velocity gradients (and hence wall shear stress) in microscale Poiseuille flows,
- obtain near-wall distribution of colloidal particles, and
- study fluid slippage over surfaces of varying wettability.

A secondary objective of this thesis is to quantify how factors such as Brownian diffusion and non-uniform illumination affect the accuracy of evanescent wave-based PIV techniques. Brownian motion is obviously significant for these sub-micron-sized colloidal tracers. In the near-wall region, the Brownian diffusion becomes anisotropic due to the additional hydrodynamic drag imposed by the presence of the wall and asymmetric because of the "no-flux" condition at the wall. Moreover, given the extremely small z-dimension of the illuminated region, the diffusion can easily lead to particles randomly moving into and out of this region, causing very high levels of particle mismatch between two consecutive PIV images. Also, the non-uniform illumination used in nPIV implies that particles closer to the wall have brighter (higher intensity) images than those farther away from the wall. Since images with different intensities will have different contributions to the cross-correlation function, the velocity measured with nPIV may be biased towards that sampled by the higher-intensity images. Quantifying the effects of Brownian diffusion and non-uniform illumination provides a fundamental understanding of the accuracy and reliability of the technique and valuable guidance for future nPIV measurements.

1.4 Outline

The thesis is organized as follows. The literature review of Chapter 2 spans several topics: three-dimensional PIV techniques, the theory and applications of evanescent wave illumination, near-surface hindered Brownian diffusion, and previous experimental and numerical studies of liquid slip over wetting and non-wetting solid walls. Chapter 3 describes initial tests of MnPIV using synthetic images of plane Couette flows incorporating non-uniform illumination, hindered Brownian diffusion and imaging noises. Chapter 4 discusses the effects of hindered diffusion and non-uniform illumination on accuracy of the technique. Chapter 5 details the experimental setup for creating and imaging incompressible, steady and creeping Poiseuille flows that is used to validate the technique. The image processing procedure and results are presented in Chapter 6. In Chapter 7, the MnPIV technique is used to study liquid slippage over bare (hydrophilic) and modified (hydrophobic) fused silica surfaces. Finally, the major conclusions and contributions of the thesis are presented in Chapter 8.

CHAPTER II

LITERATURE REVIEW

The primary objective of this thesis is to develop and apply "multi-layer nPIV" (MnPIV), a technique based on nonuniform evanescent-wave illumination, to, among other applications, obtain near-wall distribution of colloidal particles and study liquid slippage over surfaces of varying wettability. This Chapter reviews previous work in areas relevant to this objective. First, extensions of traditional PIV, which obtains two velocity components over a single 2D slice of the flow, to three-dimensional techniques-both 2D-3C (two-dimensional-three-component) and 3D-3C (three-dimensional-three-component) techniques, which obtain all three velocity components over a single 2D plane and a 3D volume, respectively, of the flow, will be discussed. Second, evanescent waves and their properties are defined, and their applications in tracer-based velocimetry techniques are briefly reviewed. Third, the theory of Brownian diffusion hindered by the additional hydrodynamic drag due to the presence of a wall, which is used to create synthetic images of MnPIV, is detailed. Note that the theory is also used in this thesis to determine how hindered Brownian diffusion of the tracer particles affect the accuracy of near-wall velocimetry techniques including MnPIV. Finally, the somewhat controversial topic of liquid slippage over surfaces with varying wettability is reviewed.

2.1 Three Dimensional Particle Image Velocimetry Techniques

Although particle-image velocimetry (PIV) is only about twenty years old [1], it has rapidly become one of the most popular methods for measuring velocity fields in both liquid and gas flows. Although "traditional" PIV obtains only two of the

three velocity components, several groups have extended it to measurements of all three components. This section summarizes some of these 2D-3C and 3D-3C PIV techniques.

2.1.1 Single-Camera Based 2D-3C PIV Techniques

Like the approach proposed here, a number of PIV studies have used variations in tracer image properties to determine the tracer position along the direction normal to the image plane and therefore the "out-of-plane" velocity component. Note that most of these techniques use one single camera.

In macroscopic PIV, a light sheet is usually used to illuminate the tracer particles over a single plane of the flow. To measure the third velocity component, Dinkelacker et al. [45] created a light sheet with an intensity profile that varied exponentially in the direction normal to the sheet and obtained the positions and velocities of particles located inside the light sheet from the particle image intensities. Similarly, Cenedese and Paglialunga [23] used two parallel light sheets of different colors to determine the out-of-plane velocity component from chromatic variations in tracer images. An even more complex system has been proposed by Herpfer and Jeng [64], who combined a 1.18 mm thick laser sheet from a continuous-wave (CW) laser with a standard double-pulsed PIV illumination system. While the double-pulsed laser sheet with short pulse duration freezes the tracer particle motion and records a pair of images of each tracer at the beginning and end of the time delay, the CW laser sheet provides tracer pathlines by illuminating the tracers between the two pulses. Note that the length of the particle trajectory is determined by the thickness of the CW laser sheet. Using standard PIV methods, the in-plane velocity components (and hence the in-plane speed) are first determined from the particle images resulting from the pulsed illumination, and the ratio of the length of the pathline and this speed gives the residence time of the tracer inside the CW laser sheet. The out-of-plane velocity is

then obtained by dividing the thickness of the CW laser sheet by the residence time. More recently, Jehle and Jarhne [78] measured 3D velocity fields close to a water-air free surface. The authors, who illuminated the free surface from above using LEDs and created a non-uniform illumination by adding absorbing molecules to the water, were able to obtain the distance between the tracer particles (30 μm radius hollow glass spheres) suspended in water and the free surface based on variations in tracer image intensity.

Aside from using specially-designed illumination schemes, the tracer position normal to the laser sheet can also be calculated from the tracer scattering pattern [124, 170], or particle image size [174]. Ikeda et al. [74] developed "multi-intensity-layer PIV" to study spray dynamics of droplets of various sizes, dividing one PIV image into eight layers based on image intensity since the intensity of light elastically scattered by a particle varies with its size.

"Defocused PIV," originally proposed by Willert and Gharib [196], measures the particle position along the optical axis by adding a mask with three off-axis apertures in the camera lens to record particle image "triplets," whose sizes and center locations are directly related to the out-of-plane and in-plane particle positions within the illumination volume, respectively. The technique was used to obtain all three velocity components for particles located in a volume with a dimension of 50 mm along the optical axis near a vortex ring. Several variations of this technique have been reported. Tien et al. [183] added different color filters over each of the three apertures to overcome the difficulty in identifying overlapping triplets in the images recorded using the original technique. Lin et al. [106] replaced the three-aperture mask with an annular aperture, giving ring-shaped images for particles away from the object plane which can be detected using a circular Hough transform algorithm, and reported a measurement uncertainty of 23 μm in the out-of-plane particle positions over a range of 10 mm. The "defocused PIV" concept has also been implemented by TSI Incorporated

into their commercial V3V system which has in-plane and out-of-plane uncertainties in the particle position of 20 μm and 80 μm, respectively.

In microscale flows, Ovryn [131] used particle image patterns formed by a high numerical aperture (NA) microscope to obtain particle positions along the third dimension for 3D particle tracking velocimetry (PTV) studies of Poiseuille flow through a microchannel. A similar approach has also been used by Speidel et al. [171], who determined the particle location along the optical axis by measuring radius of the outermost ring of off-focus images of 216 nm fluorescent particles. "Defocused PIV" has also been extended to microscale applications by Yoon and Kim [203] (among others), who attached a three-pinhole mask on the back of a 20× microscope objective to obtain a time-averaged 3D velocity field of the flow over a backward-facing step in a 50 μm deep microchannel. The differences between the multi-optical-element microscope objective and the single-lens imaging setup in traditional "defocused PIV" necessitated new calibrations to correlate the size and shape of the recorded particle image pattern to its 3D position. A similar setup was also used by Pereira et al. [138], who imaged the evaporation-induced circulation flow inside a water droplet and reported an uncertainty of less than 100 nm in the measured particle position along the optical axis based on calibrations using stationary fluorescent particles attached to a substrate. Similar calibrations were also done by Lin et al. [106] who attached an annular aperture on the back of a 20× objective in an epifluorescent microscope and recorded ring-shaped images for particles located over a volume with a dimension along the optical axis of 4.5 μm. They reported an uncertainty in the measured particle position of 180 nm.

2.1.2 Stereoscopic and Holographic PIV

In contrast to the single-camera 2D-3C techniques that measures all three velocity components over a 2D plane, stereoscopic PIV (SPIV) uses two cameras to record

simultaneous but distinct off-axis views of the same 2D plane. The two views are then combined based on a separate calibration to reconstruct the three velocity components over the planar region. Stereoscopic systems can be broadly classified into two categories: 1) translational configurations where the planes imaged by the two cameras coincide with that illuminated by the laser light sheet; and 2) angular configurations where the image planes of the two cameras are at a nonzero angle with respect to the laser light sheet. Prasad [143], who gave a comprehensive review of various SPIV applications, discussed these two configurations and the accuracies of the in-plane and out-of-plane velocity data. The technique has been used to study a variety of flows, including flows in various jet configurations [69, 121, 202] and axial compressors [108], flows near a sedimenting sphere [179] and flow separation at the tips of turbine blades [65]. SPIV has also been applied to measure droplet size and 3D velocities in fuel spray [204], to study flame structures [178, 172] and to visualize flows inside artificial heart valves [84].

The stereoscopic PIV principle has also been implemented in microscale flow studies. Klank et al. [90] used the translational configuration to acquire two successive images of the particles located inside the focal plane with a regular single-camera μPIV system. The field of view was shifted 320 μm laterally in the second imaging using a translational microscope stage. The overlapping part of the imaging planes is therefore viewed from two slightly different angles, allowing the authors to reconstruct the 3D flow field and obtain all three velocity components over a 16 μm thick plane of a pressure-driven flow inside a cell sorter. Although the results are in qualitative agreement with CFD simulations of the same geometry, the accuracy of the out-of-plane measurement was limited by the very small difference between the two view angles. More recently, Bown et al. [16] used two cameras to obtain simultaneous views of a flow of glycerol over a backward-facing step through a stereo-microscope that allowed views at two different angles along separate optical paths. The calibration

required to reconstruct the 3D velocity field was conducted in air, then corrected for the presence of glycerol with its higher refractive index. The velocities were obtained using particle-tracking over a plane 40 μm thick with a resolution 10 μm normal to the plane. Lindken et al. [107] used a similar setup to measure velocity profiles of Poiseuille flows of water inside a T-shaped micromixer, obtaining out-of-plane velocity data with a spatial resolution of 15 μm. The accuracy of the measurements is estimated by showing that the measured velocity profiles of a Poiseuille flow inside a rectangular channel agrees within 10% of the analytical solution. The authors point out that although the angle between their two view directions is 27.5 °, which is quite large for stereoscopic μPIV, it is still the major parameter limiting the accuracy of the out-of-plane velocity component. More recently, Hagsäter et al. [60] proposed using a mirror system containing three reflective prisms with dimensions of $O(1\text{ mm})$ between the front lens of the microscope objective and the flow to generate the two views required for SPIV; both views are then imaged onto a single camera. They reported initial experimental results of their optical system for flows over a forward facing step inside a microchannel.

Holographic PIV (HPIV) technique is, unlike SPIV, a truly 3D-3C technique, measuring all three velocity components over a volume of the fluid. The technique uses holography to store the amplitude and phase of the light wave scattered by the tracer particles in the measurement volume at two instants by recording the interference patterns between the scattered wave and a second, usually off-axis, reference wave onto a holographic film or a plate. The developed hologram is then illuminated with the reference beam (or its conjugate); the resultant diffraction of this beam by the interference pattern recorded in the hologram reproduces the wave scattered by the tracer particles in the measurement volume. An interrogation camera with a shallow depth of field can then be used to scan and obtain 2D "slices" of this volume to extract velocities.

HPIV is significantly more complicated than "standard" 2D-2C PIV in terms of optical setup and alignment. It is also more difficult to implement because HPIV, unlike digital PIV, requires coherent illumination and imaging, developing either holographic film or plate, and extensive image processing and reconstruction. The advantages and limitations of the technique were discussed in the early review by Royer [155]. Hinsch [66], in his review, summarized more recent developments in holographic recording and post processing. Finally, Meng et al. [120] discussed "digital HPIV," where a CCD camera (*vs.* holograph film or plates) is used to record the holograms.

The HPIV technique has also been applied to study microscale flows. Earlier studies by Cuche et al. [41] and Dubois et al. [47] have demonstrated that holographic microscopes can be used to obtain holograms of microscopic stationary objects in the absence of flows. Yang and Chuang [200], who incorporated holographic recording into their μPIV system, recorded successive image pairs on a photopolymer plate and obtained 3D-3C velocity data in the flow behind a backward-facing step inside a 500 μm deep channel using a cross-correlation algorithm. Satake et al. [162] used micro digital holographic particle tracking velocimetry (micro-DHPTV) to measure the 3D velocity field inside a 92 μm diameter capillary. Holograms were recorded at rate of 1 kHz onto a CCD camera and about 104 vectors were obtained over measurement volume of 410 μm × 70 μm × 70 μm from the numerically reconstructed flow field. Kim and Lee [88] used a similar technique to obtain 3D velocity data inside curved microcapillary with diameters of 100 μm or 300 μm and radii of curvatures of 100 μm, 600 μm and 1200 μm; the particle trajectories derived from these velocity vectors were used to visualize the secondary flows in the capillary.

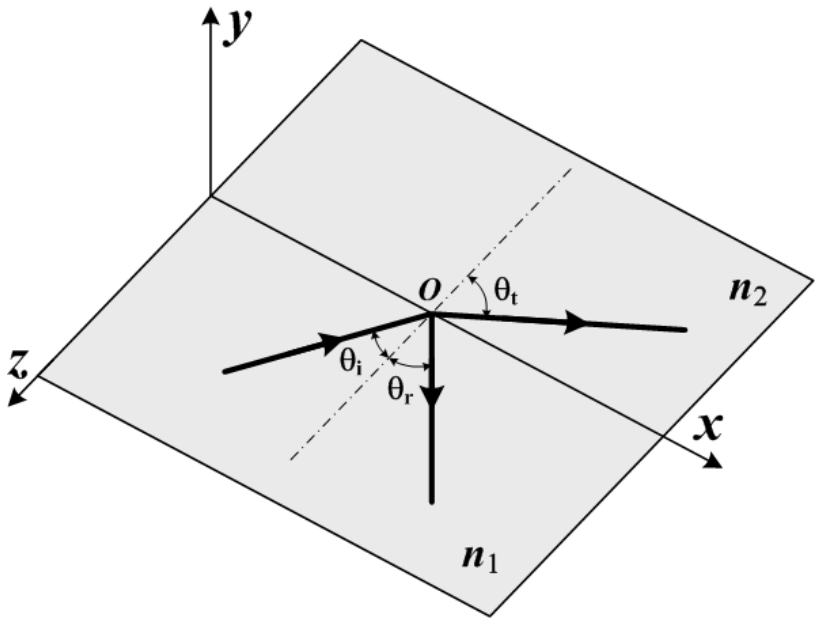

Figure 8: Sketch showing light incident upon and reflected and refracted off an interface (x-y plane) separated by two media with different refractive indices ($n_1 > n_2$).

2.2 Evanescent Waves and Their Application in Tracer-based Velocimetry Techniques

Both the MnPIV technique and its predecessor, nPIV, rely on evanescent-wave illumination, a powerful tool to limit the region of illumination to the first few hundred nanometers next to an interface. This section first introduces evanescent waves and their properties, then reviews evanescent-wave velocimetry techniques.

2.2.1 Total Internal Reflection

Consider a beam of light (Figure 8) incident at an angle of incidence θ_i onto a planar interface (the x-y plane) separating two isotropic media with different refractive indices n_1 and n_2. At the refractive-index interface, the beam is partially reflected and partially transmitted. The direction of propagation of the transmitted waves, or the angle of refraction θ_t is given by Snell's Law:

$$n_1 \sin\theta_i = n_2 \sin\theta_t \tag{4}$$

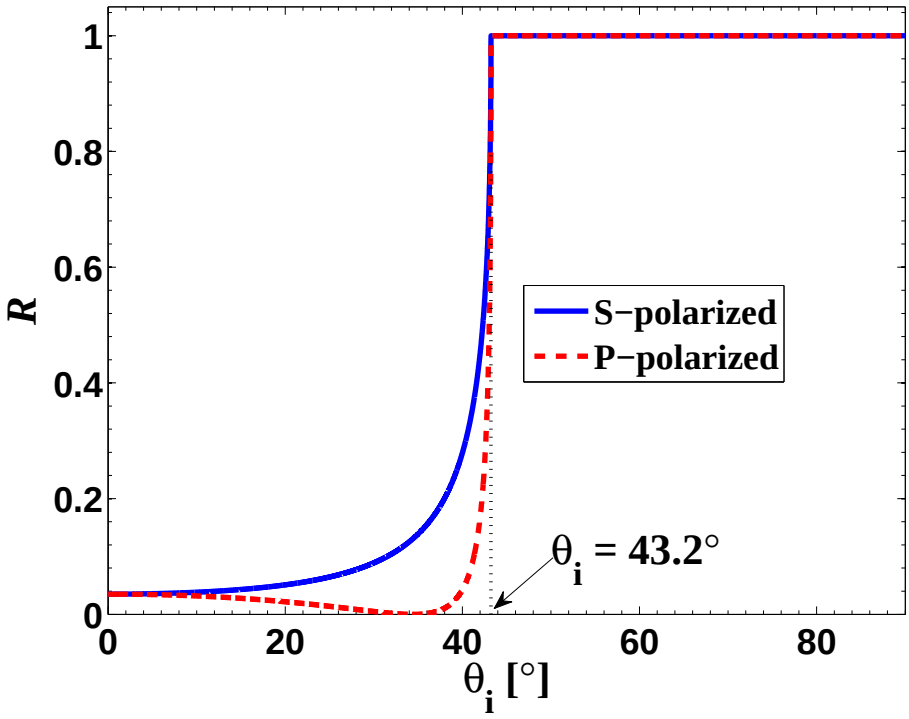

Figure 9: Reflection coefficient R calculated using Fresnel Equations as a function of the angle of incidence θ_i for light of both s- (solid blue line) and p-polarizations (dashed red line). Here, the light is incident upon a fused silica ($n_1 = 1.46$)-air ($n_2 = 1$) interface.

The fraction of power that is reflected (*i.e.*, reflection coefficient R), is given by the Fresnel Equations.

As discussed in Section 1.2.5, when the beam is incident upon the refractive-index interface from the optically denser (*i.e.*, higher refractive index) side so that $n_1 > n_2$ (*e.g.*, from glass to air), the beam will be wholly reflected back into the incident medium if θ_i exceeds the critical angle $\theta_c = \sin^{-1}(n_2/n_1)$. Figure 9 showed that the reflection coefficient R quickly reaches unity, corresponding to total internal reflection (TIR), as the angle of incidence θ_i approaches $\theta_c = 43.2^\circ$ at the fused silica-air interface where $n_1 = 1.46$ and $n_2 = 1.00$ irrespective of the polarization of the light. It is this phenomenon of TIR that enables light to be transmitted within thin optical fibers and bends the light in compact prism-based binocular designs.

2.2.2 Evanescent Wave

The term TIR suggests that the incident light should be totally reflected at the interface. However, the electromagnetic field actually penetrates a small distance into the less optically dense medium and propagates parallel to the interface. The physical explanation for this phenomenon is that when applying Maxwell's equations to the interface between two dielectrics, the tangential components of both the electric and magnetic fields must be continuous across the interface; this boundary condition can only be satisfied if the electromagnetic field crosses the interface, creating the so-called "evanescent wave". Note that the energy carried by the wave re-enters the optically denser medium after propagating along the interface for a short distance (the Goos Hänchen shift, which is usually a fraction of the wavelength).

The evanescent wave has a "diminishing" intensity that decays exponentially along z or the normal distance from the refractive-index interface where the wave is created (Equation 3). The intensity-based penetration depth z_p can be calculated based on the refractive indices of the two media n_1 and n_2, the angle of incidence θ_i and the wavelength of illumination λ:

$$z_\mathrm{p} = \frac{\lambda}{4\pi\sqrt{n_1^2 \sin^2 \theta_\mathrm{i} - n_2^2}} \tag{5}$$

Note that z_p is independent of the polarization of the light and usually of an order of magnitude comparable to or less than λ, except when $\theta_\mathrm{i} \to \theta_\mathrm{c}$, as shown in Figure 10. The exponential decay of the evanescent-wave intensity to less than 2% of its maximum value within $4z_\mathrm{p}$, or a few λ, of the refractive-index interface makes the waves ideally suited for probing interfacial phenomena, as described in the next section.

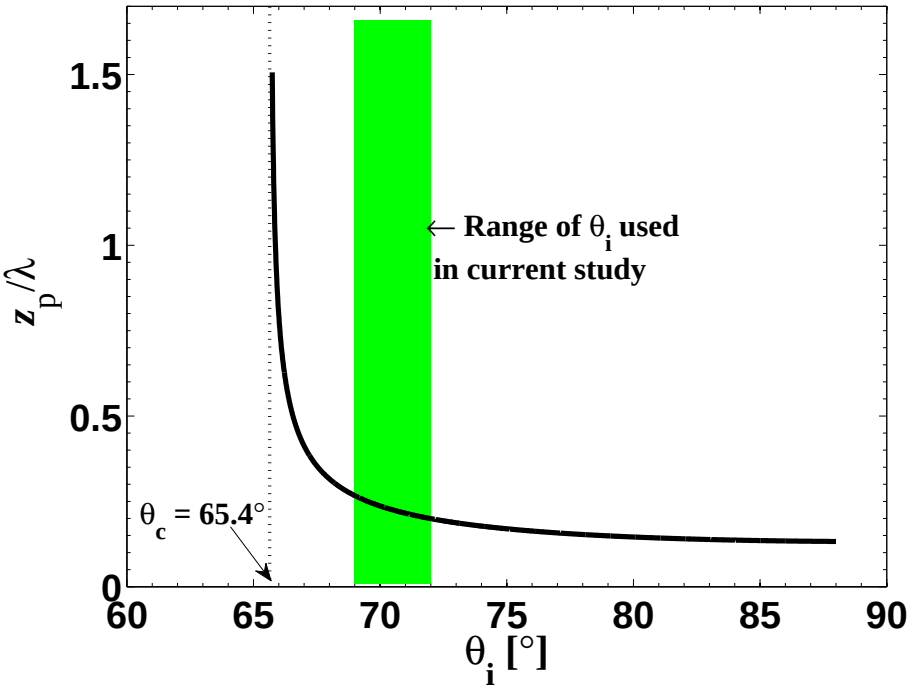

Figure 10: Normalized evanescent wave penetration depth z_p/λ calculated using Equation 5 for TIR at fused silica ($n_1 = 1.46$)-water($n_2 = 1.33$) interface. Here λ is the illumination wavelength.

2.2.3 Evanescent Wave-Illumination in Tracer-Based Velocimetry Techniques

Evanescent waves have been used in tracer-based near-wall velocimetry techniques over the last five years. Zettner and Yoda [205] first demonstrated the utility of evanescent-wave illumination to obtain velocity data within 380 nm of the wall in a rotating Couette flow. Later, Sadr et al. [159] successfully measured electroosmotic flow (EOF) velocities in microchannels for monovalent aqueous electrolyte solutions and reported measurements of the velocity deficit inside the electric double layer (EDL) for the EOF of very dilute electrolyte solutions [158]. Li et al. [103] used a similar experimental setup to show that even trace amounts (a few percent of the total cation molar concentration) of divalent cations can dramatically reduce flow rates for EOF of monovalent electrolyte solutions through microchannels with negatively charged walls; their results were found to be in good agreement with

numerical simulations [44].

The exponential decay in evanescent wave intensity implies that the particle-wall separation distance can be directly obtained from the particle image intensity. Kihm et al. [87] developed a particle-tracking based technique "ratiometric total internal reflection microscopy" utilizing the variation in image intensity of a particle illuminated by evanescent waves with its normal distance from the wall to measure the displacements of fluorescent colloidal particles in three dimensions due to hindered Brownian diffusion near a solid wall. The technique was also used to correlate the minimum particle-wall distance of suspended polystyrene particles subject to EDL interactions with the surface of a glass wall to the ionic strength of the suspending fluid and the size of the particles [114]. More recently, Kanda et al. [86] used "total internal reflection fluorescence microscopy" (TIRFM) to measure near-wall concentration profiles of 100 nm particles in distilled water and 1 mM phosphate buffer solution and reported non-uniform particle distribution with concentrations lower than the bulk value in the region immediately adjacent to the wall. Similar techniques have also been used to study liquid slippage over surfaces with different wettability [79, 72, 71, 95], as reviewed in Section 2.4.1.1.

Although the majority of evanescent-wave based velocimetry studies have used fluorescent colloidal polystyrene particles with diameters as small as 100 nm as tracers, Pouya et al. [142] reported a statistical particle tracking method for obtaining velocity data using quantum-dot tracers with a effective hydrodynamic diameter of about 10 nm illuminated by evanescent waves. Guasto and Breuer [59] have also reported preliminary results on using quantum-dot tracers illuminated by evanescent waves to simultaneously measure the velocity and temperature within 200 nm of a solid wall.

Evanescent-wave illumination has also been applied to techniques beyond PIV or PTV. Thompson et al. [181] discussed the theoretical basis for using evanescent-wave illumination in FCS and fluorescence recovery after photobleaching (FRAP).

Pit et al. [140] studied slip in hexadecane on surfaces with different wettability by measuring the fluid velocity within 80 nm of the wall using TIR-FRAP. In addition to applications that use traveling evanescent wave, Yamada [199] proposed a technique "Evanescent wave Doppler velocimetry" that creates "standing" wave from interfering two counter-propagating evanescent waves. Fluid velocity can then be determined from the blinking frequency of the light scattered by the tracers as they move across the interference fringes, similar to the conventional LDV.

2.3 Hindered Brownian Diffusion: Theory and Modeling

The vast majority of evanescent-wave velocimetry techniques described in the previous section measure the displacements of sub-micron particles as they are convected by the flow, assuming that the displacements of these tracers over a known time interval are identical to the fluid velocity. When a small (typically of diameter less than 1 μm) particle is suspended in a fluid, it undergoes random Brownian motion due to collisions with the fluid molecules that are constantly in thermal motion as well as the coherent motion due to flow. For a single particle surrounded by an infinite medium, the statistics of the diffusion are isotropic and the displacement over a small time interval (*i.e.*, $\delta t \to 0$) can be represented by a Gaussian distribution with zero mean and a variance proportional to $D_\infty(\delta t)$. Here, D_∞, the unconfined diffusion coefficient, can be calculated for a spherical particle from the Stokes-Einstein relationship [50]:

$$D_\infty = \frac{kT}{6\pi\mu a} \tag{6}$$

where k is the Boltzmann's constant and T and μ are the temperature and viscosity of the fluid, respectively.

If the particle comes within a few radii of a rigid planar surface, its Brownian motion is reduced because of the hydrodynamic drag in the presence of the wall and the motion becomes anisotropic with respect to the directions parallel and perpendicular to the wall. The diffusion coefficient is then described by a tensor:

$$\overline{\overline{\mathbf{D}}}(z) = D_\infty \begin{bmatrix} \beta_\parallel(z) & 0 & 0 \\ 0 & \beta_\parallel(z) & 0 \\ 0 & 0 & \beta_\perp(z) \end{bmatrix} \tag{7}$$

where $\beta_\parallel$ and $\beta_\perp$ are correction factors for hindered Brownian diffusion parallel and perpendicular to the wall, respectively. Faxén [52] evaluated $\beta_\parallel$ by using method of reflections to solve the Laplace equation for the motion of a rigid sphere parallel to a planar surface and reported:

$$\beta_\parallel(z) = 1 - \frac{9}{16}\left(1+\frac{h}{a}\right)^{-1} + \frac{1}{8}\left(1+\frac{h}{a}\right)^{-3} - \frac{45}{256}\left(1+\frac{h}{a}\right)^{-4} - \frac{1}{16}\left(1+\frac{h}{a}\right)^{-5} \tag{8}$$

Later, Goldman et al. [56] showed that for $h/a > 0.04$, Faxén's solution is in reasonable agreement with the exact solution given by O'Neill [130]; for $h/a < 0.04$, however, Faxén's approximation underestimates the hydrodynamic force and O'Neill's solution [130] should be used instead. Brenner [19] solved the Stokes equation for creeping flow to calculate $\beta_\perp$ in a form of summation of infinite series. Bevan and Prieve [9] later showed that Brenner's results can be approximated using a simpler expression:

$$\beta_\perp = \frac{6h^2 + 2ah}{6h^2 + 9ah + 2a^2} \tag{9}$$

Figure 11, which compares the solutions of Brenner [19] (black lower curve), Faxén [52] (blue upper curve), and O'Neill [130] (points), shows that both $\beta_\parallel$ and tend to vanish as the sphere approaches the wall and slowly reach unity as the particle moves away from the wall. Note that $\beta_\perp$ is still less than $\beta_\parallel$ even 5 particle radii away from the wall.

These analyses have been experimentally validated by several groups. Lin et al. [105] used digital video microscopy to measured the 3D hindered Brownian diffusion coefficient of a sphere (1 μm in diameter), whose position and diffusion range were

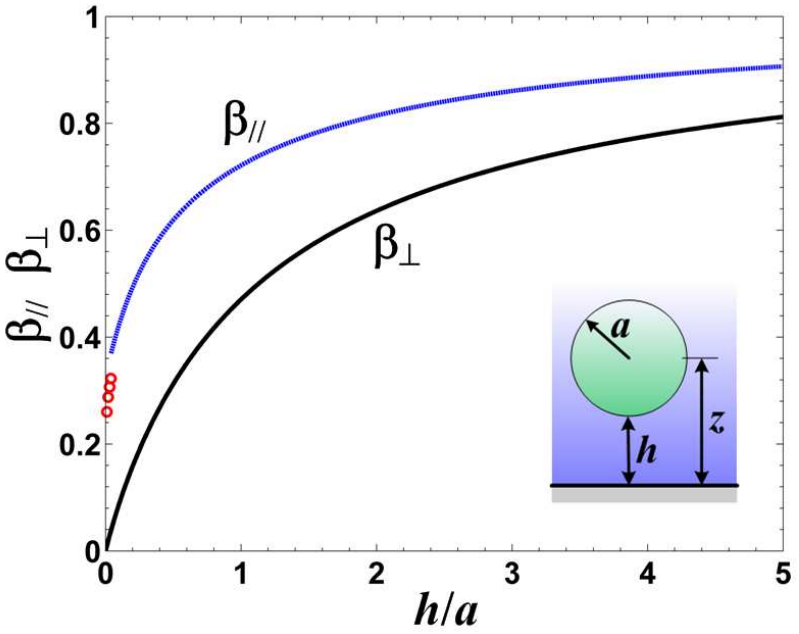

Figure 11: Correction factors for calculating hindered Brownian diffusion coefficient as functions of h/a. Here, the data points ($\circ$) represent the solution of $\beta_{\parallel}$ given by O'Neill [130] for $h/a \leq 0.04$.

controlled by optical tweezers. They concluded that both $\beta_{\parallel}$ and $\beta_{\perp}$ for $3.7 < h/a < 60$ are in good agreement with theory. Pagac et al. [132] and Oetama and Walz [127] both used TIRM to verify that the mobility normal to the wall for colloidal spheres ($a \sim O(1\ \mu\text{m})$) suspended in aqueous solutions within 500 nm of a planar surface is in good agreement with that predicted by Brenner [19]. Similar experiments on sub-micron particles by Banerjee and Kihm [6] demonstrated that the components of the diffusion tensor parallel to the wall agree well with the theory, but the diffusion normal to the wall deviates from the calculations. They attributed this discrepancy to interactions other than hydrodynamic effects that are neglected in the models. Later, the authors from the same group further showed [30] using TIRF that varying ionic strength of the fluid does not affect the particle's near-wall Brownian diffusion parallel to the wall while the diffusion perpendicular to the wall increases significantly with ionic strength at a given separation distance. Huang and Breuer [70] used the three dimensional total internal reflection velocimetry (3D-TIRV) technique with 1.5

μm radius particles to demonstrate that both the in-plane and out-of-plane diffusion coefficients are in good agreement with the theory of Goldman [56] and Brenner [19] for $h/a < 0.15$.

The stochastic nature of the Brownian motion suggests that it can only be described in a statistical manner. In general, the time evolution of dynamics of colloidal particles due to Brownian diffusion is modeled by the Langevin equation, while the statistics of these properties are solved directly from the Fokker-Planck equations.

The Langevin equations are based on Newton's equation of motion, where the forces acting on a Brownian particle due to its interactions with the surrounding fluid molecules are divided into two parts: a drag force proportional to the velocity of the particle and a randomly fluctuating force $\overline{\mathbf{A}}(t)$. This random force is assumed to be independent of the particle velocity and fluctuates rapidly compared to changes in velocity. If the particle is also subject to an external force $\overline{\mathbf{F}}$, Newton's second law reads:

$$m\frac{d\overline{\mathbf{u}}}{dt} = \overline{\mathbf{F}} - \beta\overline{\mathbf{u}} + \overline{\mathbf{A}}(t) \tag{10}$$

where m, β, and $\overline{\mathbf{u}}$ are the particle mass, friction coefficient, and velocity, respectively.

When the statistics of the location, *vs.* the actual particle location itself, are of interest, the Brownian diffusion can also be described by the Fokker-Planck equations. Unlike the Langevin equations, the Fokker-Planck equations directly solve the conditional probability density functions of the particle properties at a later time t based upon known initial conditions at a time t_0. The classic review by Chandrasekhar [24] discuses the application of the Fokker-Planck equations to a statistical description of Brownian diffusion.

Since Langevin equations deal with the dynamics (*i.e.*, acceleration, velocity and displacement) of Brownian particles, the evolution of these variables over time can be

determined by numerically integrating the Langevin equations. Ermak and McCammon [51] developed an algorithm for simulating diffusive behavior of a system of N interacting Brownian particles and included the effects of hydrodynamic interactions by introducing an inter-particle friction tensor, which is a function of space. Later, Clark et al. [33] used a similar approach to study the dynamics of a single particle located in the immediate proximity of a solid wall. The displacement $\triangle\overline{\mathbf{x}}$ of a particle subject only to hindered Brownian diffusion over a time interval from t_0 to $t_0 + \delta t$ is given by:

$$\triangle\overline{\mathbf{X}} = (\nabla \cdot \overline{\overline{\mathbf{D}}})\delta t + \overline{\mathbf{R}} \tag{11}$$

The first term on the RHS of the equation is the displacement caused by the variation in $\overline{\overline{\mathbf{D}}}$ with z. The second term $\overline{\mathbf{R}}$ is the stochastic displacement due to the Brownian motion and is normally distributed about a mean of zero with a variance equal to the square of the expected root-mean-square (rms) Brownian displacement due to $\overline{\overline{\mathbf{D}}}$ over δt. Here, δt must be greater than the relaxation time of the Brownian fluctuations $\tau_B = m/(6\pi\mu a)$ (for a particle suspended in water $a = 100$ nm, $\tau_B \sim 10^{-9}$ s). Moreover, since the diffusion coefficient tensor $\overline{\overline{\mathbf{D}}}$ varies with z, both $\overline{\overline{\mathbf{D}}}$ and $\nabla \cdot \overline{\overline{\mathbf{D}}}$ are evaluated at the beginning of the interval t_0 and assumed to remain constant over δt. The time step δt must also be small enough to ensure that the diffusion coefficient tensor does not change significantly over δt. Equation 11 can be used to simulate the time evolution of particle locations due to hindered Brownian diffusion and this simulation over a large number of particles for a given time interval and initial conditions leads to the histogram of the particle displacements, which approximates the corresponding conditional probability density function.

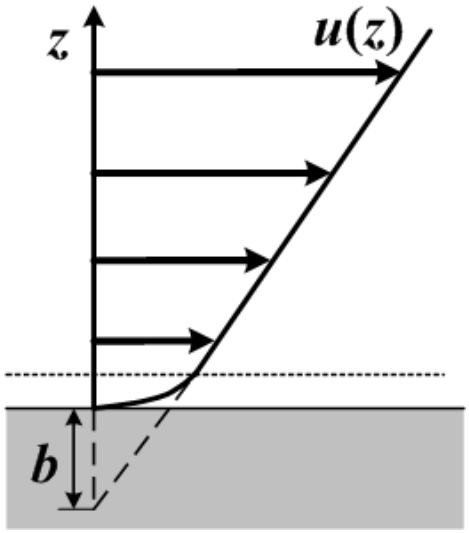

Figure 12: Illustration of apparent slip and slip length.

2.4 Liquid Slippage at the Submicron Scale

The "no-slip" boundary condition that the fluid molecules immediately adjacent to a solid surface have the same tangential velocity as the surface has been the fundamental boundary condition at a liquid-solid interface for nearly a century. Though the validity of the "no-slip" boundary condition has been theoretically demonstrated by Koplik et al. [94] using molecular dynamics (MD) simulations and has also been supported by various macroscopic experimental measurements [57], experimental and numerical investigations have reported results that indicate the no-slip boundary condition does not hold within 1 μm (or less) for Newtonian liquids flowing over surfaces with varying wettability. As shown in Section 1.1, the slip length b, based on Navier's partial slip boundary condition, is usually used to quantify the magnitude of slip, which can appear in different forms: "true" slip on the molecular level (Figure 1) and "apparent slip" depicted in Figure 12. The latter is more commonly used in slip studies because experiments are usually unable to distinguish true tangential flow at an interface from a tangential velocity profile that seems to extrapolate to a non-zero value at a wall but might abruptly decrease to zero over very small range of z.

To our knowledge, all investigations reporting nonzero b have obtained values of b less than or at the order of 1 μm. Regardless of the exact value of b, the breakdown of the no-slip condition, if true, has little if any practical consequences in macroscale flows. For example, the flow rate for laminar Poiseuille flow through a capillary of diameter d_c would increase by a factor of $1 + 8b/d_c$ for a nonzero b, suggesting that the enhancement in flow rate due to the breakdown of the no-slip condition would be negligible for $d_c > O(10\ \mu m)$.

Numerous studies on liquid slip over solid surfaces have been conducted using a variety of methods. Lauga et al. [97] provided a comprehensive review of many experimental and numerical investigations of liquid slippage over solid surfaces, and discuss the dependence of slip on various physical parameters. The more recent review of Neto et al. [126] focuses on experimental studies of slip for Newtonian liquids. Bocquet and Barrat [11] provide instead an overview of the theoretical studies of slip with a focus on slip mechanisms at different length scales (smooth, patterned and porous surfaces) and discussed the potential benefits of a nonzero slip length on "interface driven" (*e.g.* electro-osmotic) flows. Finally, Maccarini [112] summarizes the available theoretical and experimental data on interactions of water with non-ionic surfaces and suggested that the slippage of water over hydrophobic surfaces may be related to changes in the molecular structure of the layer of water in direct contact with the hydrophobic wall, as indicated by observations of a deficiency in the water density at the interface obtained from experimental measurements using neutron and x-ray reflectometry.

This section first summarizes the most recent experimental studies on liquid slippage, focusing on the studies utilizing tracer-based velocimetry techniques. The section then discusses the major factors that have been shown both experimentally and analytically to affect slip.

2.4.1 Experimental Measurements of Slip Length

2.4.1.1 Tracer-Based Velocimetry Techniques

From its definition in Figure 1, the slip length is directly related to the velocities and is usually obtained from a linear extrapolation of the near-wall profile of the tangential velocity component, which has been measured using a variety of tracer-based velocimetry techniques. These methods are usually considered as "direct" approaches.

As indicated in Section 1.2.4, μPIV has been used to measure velocity profiles in a horizontal plane near a side wall of the microchannel (Figure 5). Tretheway and Meinhart [186], who extrapolated velocity profiles obtained using μPIV in Poiseuille flow of water through a glass microchannel with walls that were rendered hydrophobic using a self-assembled monolayer of Octadecyltrichlorosilane (OTS), reported slip lengths of almost 1 μm, and attributed such large slip lengths to apparent slip due to the presence of a gas layer. Joseph and Tabeling [83] used μPIV with fluorescent particles up to 200 nm in diameter to "scan" the fluid velocity profile across the channel depth for Poiseuille flows through a rectangular microchannel with hydrophobic walls. By extrapolating the measured velocity profile to the solid wall, whose location is also experimentally determined, they reported that their slip lengths were within the measurement uncertainty (±100 nm) and independent of shear rate.

Liquid slippage has also been studied using evanescent-wave based velocimetry techniques. Jin et al. [79] used evanescent wave illumination of submicrometer tracer particles and PTV-based approaches to obtain velocities of water flowing through both hydrophilic and hydrophobically-modified glass channels. Although the authors were unable to directly measure the magnitude of the slip length due to uncertainties in the characteristics of their illumination, they showed that the statistical difference between the velocities measured over hydrophilic and hydrophobic surfaces was minimal. Using a similar system, Huang et al. [72] obtained the slip length by comparing

the measured mean velocity over a portion of the region illuminated by the evanescent wave to the theoretical predictions. A statistical model was proposed to account for the uncertainty in tracer image intensity due to the polydispersity in tracer size. The authors reported a shear rate-dependent slip length of water over hydrophobic surfaces, reaching a maximum of 96 nm at their highest shear rate $G = 1800\ \mathrm{s}^{-1}$. Later, they extended this work to measure slippage of low concentration ($0.1 - 1$ mM) aqueous sodium chloride solutions over hydrophobic surfaces [71]. Based on their results that varying the ionic strength of the working fluid had minimal effects on the measured slip length, the authors concluded that the observed slip velocities reflected true boundary slip, *vs.* electrostatic and electrokinetic effects. More recently, Lasne et al. [95] measured near-wall velocities of a oscillatory squeeze flow between two flat glass slides based on statistics of the velocities (derived from the length of the recorded streaks) *vs.* the image intensity of fluorescent tracer particles (20 or 40 nm in diameter) and molecules ($\sim$1 nm in diameter) illuminated by evanescent wave and reported slip length $b = 45 \pm 15$ nm for water flowing over glass with hydrophobic coating.

As briefly mentioned in Section 2.2.3, the average near-surface velocity can also be obtained using the TIR-FRAP velocimetry technique based on photobleaching of fluorophores using evanescent-wave illumination [122]. Pit et al. [139] used this technique, which was originally designed for measuring near-wall velocity of sheared polymer melts, to study slip of a rotating Couette flow of hexadecane over a wetting sapphire surface. They showed that the recovery of fluorescence after photobleaching occurs more rapidly than the baseline case of pure hexadecane when surfactant was added to the solvent, making the sapphire surface less wettable, and hypothesized that this was because the non-bleached fluorophores move into the measurement site more easily under slip at the solid-liquid interface in the case with surfactant. Unfortunately, no numerical values of b were reported in this study. Pit et al. [140]

later extended their earlier work to measuring slip lengths of 400 nm for hexadecane on sapphire surfaces with hydrophobic OTS coatings, observing that even a slightly incomplete OTS coating layer reduced the measured slip to 100 nm. Schmatko et al. [164] used a similar setup to measure slip lengths in two organic solvents: hexadecane and squalane, that have identical surface tensions (and therefore identical contact angles) but different molecular conformations (hexadecane is a long-chain molecule, while squalane is more "ball-shaped") over three surfaces with varying wettability. Although the measured slip length increases with contact angle for either of the liquids, the slip lengths for the two liquids differ for a given surface. The authors attributed this variation in b to the possibility that the long-chain (*vs.* spherical-shaped) molecules are more easily aligned at the interface and facilitate wall slip. The same group also studied the effects of roughness on slip, creating surfaces of varying roughness but similar surface chemistry by forming a monolayer of polymetric nano-particles on a hydrophobized sapphire disk. By controlling the surface coverage fraction and particle size, the authors were able to study separately the effect of the wavelength and height (amplitude) of the surface roughness on slip, and showed that the slip is suppressed by increasing surface roughness and the height (*vs.* wavelength) of the surface roughness has a greater effect on b.

Liquid slippage has also been studied using FCS, briefly reviewed in Section 1.2.1. Lumma et al. [110], who used double-focus FCS to obtain velocity profiles in the Poiseuille flow of water and aqueous sodium chloride solution at salt molar concentrations up to 1 mM seeded with particle and molecular tracers over glass and mica surfaces, reported "apparent slip lengths" of about $0.2 - 1$ μm that decreased as the ionic strength of the working fluid increased. The authors also hypothesized that their relatively large measured slip length on wetting surfaces could be "artificial" and possibly due to the hydrodynamic and electrostatic interactions between the tracers and wall. Joly et al. [81] also used FCS, to measure the in-plane Brownian diffusion

coefficient $D_{\|}$ of 218 nm silica particles in a confined geometry in the absence of flow as a function of the particle-wall separation distance. Since the diffusion is affected by the slip at the liquid-wall interface, they were able to infer slip lengths from their measured change in $D_{\|}(z)$ over hydrophilic and hydrophobically-coated surfaces, obtaining zero slip on the hydrophilic surface and shear rate-independent slip lengths of 18 ± 5 nm on the hydrophobic surface.

2.4.1.2 Other Techniques

Slip at the nano-scale has also been studied by measuring flow quantities other than velocity, including flowrate and force. Choi et al. [29], measured flowrates for the Poiseuille flow of water at various gradients through hydrophobized silicon microchannels and used their data to estimate the slip velocity at the wall. They found shear rate-dependent slip length that reaches a maximum value of 30 nm at a shear rate of 10^5 s^{-1}. Cheng and Giordano [25] measured slip in the Poiseuille flow of various fluids through glass channels of depth ranging between 40 nm and 2.7 μm and reported that their measured flow rates for water agreed well with predictions based on no-slip condition for all the channels studied. For other non-wetting or partially-wetting liquids, however, the measured flow rates deviated from the predictions for channels with depths below 100 nm; in these cases, the slip lengths were estimated to range from 9 nm to 30 nm for different fluids.

Slip lengths can also be determined from force measurements, by measuring, for example, the surface force between solids immersed in liquids using the surface force apparatus (SFA) [76]. The viscous force due to the drainage of a fluid film sandwiched between a sphere and a plate or two crossed cylinders is typically measured using SFA or atomic force microscopy (AFM). The slip length can then be obtained by comparing this measured force with that predicted by theory under "no-slip" assumption. Bonaccurso et al. [12] used AFM to study the slip of sucrose solutions over perfectly

wetting silicon surfaces of varying surface roughness. Although they were unable to uniquely determine the slip lengths on the sphere and plate, the authors did show that slip exists in even a completely wetting system, and that b increases with the surface roughness. Henry et al. [63] also used an AFM to study the effects of surface wettability and surface charge on slip lengths in water and cationic surfactant solutions (cetyltrimethylammonium bromide (CTAB) at molar concentrations $C \leq 10$ mM) flowing over mica surfaces. As C increases, the wettability of the mica surface first increases, then decreases while the surface becomes more positively charged as the polymer molecules absorb onto the mica surface. For pure water over a hydrophilic surface, the reported slip length depends on the shear rate, and varies between 80 and 140 nm. For the polymer solutions, however, this dependence of b on G diminishes as C increases. The studies also suggest that b increases with the surface charge density, although the authors could not exclude the effects of changes in roughness and compliance of the surface due to the presence of the absorbed polymer molecules. The slippage of various non-polar and polar liquids over alkysilane-coated glass surface was studied by Cho et al. [28], using an AFM. They showed that although the slip length increases with contact angle α for non-polar liquids ($\alpha = [10\,^\circ : 40\,^\circ]$), the polarity of the liquid determines b for polar liquids with larger α of $60\,^\circ - 100\,^\circ$. By measuring the viscous force, Honig and Ducker [68] showed that the "no-slip" boundary condition was valid for a completely wetting system for G up to 2.5×10^5 s^{-1}. Unlike earlier AFM studies, the authors used an independent method to measure the sphere-plate separation distance based on the variation in the intensity of light scattered by the particle when illuminated by evanescent-waves. Cottin-Bizonne et al. [36] measured, using a dynamic SFA, slip lengths of water and n-dodecane over surfaces with varying wettability and showed although the "no-lip" condition holds for completely wetting systems, there is slippage for partially wetting systems, with a b that is independent

of shear rate (at least for $G = 10 - 5000\ \mathrm{s}^{-1}$) and that increases with hydrophobicity, reaching a maximum of 20 nm at a contact angle of 105°. Finally, Maali et al. [111] avoided the variability in other surface properties (*e.g.*, roughness, charge and compliance of the surface) introduced when the surface is coated to change the wettability by measuring slippage of water flowing over a naturally partially wetting graphite surface, and reported $b = 8$ nm.

2.4.2 What Affects Slip?

The previous section demonstrates that a wide variety of studies have observed that various physical parameters, or combinations of these parameters, can greatly affect the slip at the solid-liquid interface. Although there is little agreement on which of the many proposed theoretical mechanisms underlie slip and a number of the studies report contradictory results, this section attempts to summarize the most commonly accepted conclusions on what affects slip lengths.

2.4.2.1 Surface Wettability

Numerous studies suggest that liquid slip at a solid surface is related to a reduction in the solid-liquid interactions that liquid molecules can overcome these interactions and "slide" over the solid surface. Such interactions are most commonly described by the wettability of the solid surface, quantified by the contact angle α. For a three-phase system (liquid, vapor and solid) at equilibrium the relationship between α and the liquid-vapor, solid-vapor and solid-liquid interfacial tensions (γ_{lv}, γ_{sv}, and γ_{sl}, respectively) for a perfectly flat solid surface can be described by Young's Equation, $\gamma_{\mathrm{sv}} = \gamma_{\mathrm{sl}} + \gamma_{\mathrm{lv}} \cos\alpha$. The fluid is said to be partially wetting the surface for $\alpha \leq 90°$ and nonwetting for $90° < \alpha < 180°$.

Early theoretical work by Tolstoi [185], later extended by Black [10], appears to be the first attempt to relate slip to the surface energies (and therefore α) by considering the change in mobility of the liquid molecules close to a solid surface. The results

showed that for a partially wetting system, the liquid molecules have larger mobilities near the interface, leading to a slip length that increases with α. Similar phenomena has also been observed in molecular dynamic (MD) simulations. For example, Barrat and Bocquet [7], who modeled slip in a fluid-solid system where the solvent and solid interact via Lennard-Jones (LJ) potentials, showed that b increases as the interaction potential between the liquid and wall molecules decreases.

As discussed in the previous section, extensive experimental studies have shown that slip occurs only on partially or non-wetting surfaces [186, 68, 192, 40, 95, 36]. Experimental evidence of b increasing with α has also been obtained using different techniques [36, 28, 164, 140]. Nevertheless, a smaller number of investigations report occurrence of slip in completely wetting systems [12, 13, 63, 164, 175]. Sun et al. [175], for example, reported $b = 10 - 14$ nm by measuring the hydrodynamic drainage force of 1-propanol on a completely wetting mica surface using AFM. Similar experiments done by Henry et al. [63] reported values of b as great as 140 nm for water flowing over hydrophilic mica surface and observed no correlation between b and surface wettability for partially wetting surfaces. Cho et al.[28] found that b depends on surface wettability only for non-polar liquids, and that b was independent of wettability for both non-polar ring-shaped (*e.g.*, Benzene) or polar liquids. These contradictory results suggest that wettability of the solid surface may affect slip but that wettability is unlikely to be the primary or sole determinant of slip.

2.4.2.2 Gaseous Nanobubbles

The presence of sub-microscopic bubbles on the hydrophobic surfaces has long been proposed to explain the "long-range attractive forces" between hydrophobic surfaces [31, 3]. The formation of a stable thin gas layer at the wall has been theoretically studied [109, 191] and experimentally visualized (using *e.g.*, tapping-mode AFM) [189]. It has also been shown that the appearance of these bubbles is promoted

by dissolved gases in the aqueous phase. Tapping-mode AFM (TMAFM) studies of water supersaturated with carbon dioxide have detected formation of bubbles (as large as 800 nm in diameter and 200 nm in height) on methylated (hydrophobic) silica surfaces [201]. Surface roughness also affects bubbles formation; Yang et al. [201], among other studies, compared two methylated silica surfaces with rms roughness of 0.1 and 2.7 nm, and observed larger and more sparsely distributed nanobubbles for the rougher surface using TMAFM.

Recently, gas layer formation, whether due to surface hydrophobicity or roughness, has been proposed as the explanation for apparent slip at the liquid-solid interface [22, 32, 46], especially for drag reduction using superhydrophobic surfaces in micro-channels. For example, Celata et al. [22] estimated slip by comparing their measured friction coefficients at various Reynolds numbers with predictions assuming the no-slip condition. They reported that the agreement for degassed water cases is within experimental uncertainties even for silicon-coated hydrophobic capillaries. Neutron reflectometry measurements were used by Doshi [46] to study water density distribution next to a solid wall. The authors reported that removing dissolved gas from the water reduces the width of water layer with a reduced density at the interface; this reduction in interfacial density has been proposed as a cause of slip. Using a different approach, Churaev et al. [32] inferred formation of gas bubbles on the wall from variations in the measured wall zeta-potential ζ of a hydrophobic (methylated) quartz capillary. They observed that the magnitude of ζ decreased with the formation of bubbles on the solid surface, generated from the nitrogen gas-saturated solution. When pressure is increased, forcing the bubbles back into solution, ζ recovers to the initial value.

The effect of nanobubbles at the solid surface on slip has also been analytically studied, usually by approximating the nanobubbles as either a continuous gas layer

or a regular grid of gas bubbles. Tretheway and Meinhart [187] used a 2D continuum fluid dynamic analysis to show that their measured slip lengths ~ 0.92 μm [186] were consistent with that calculated assuming the presence of a 18 nm thick air gap between the bulk fluid and the wall. The problem was further studied using the 3D lattice Boltzmann method by Zhu et al. [206]. Although their single-phase simulation agreed well with the experimental results, the model cannot be used to predict the actual value of the slip because the parameters related to the boundary conditions in the model are empirical and must hence be manually adjusted. Lauga and Brenner [96] calculated the forces acting on an oscillatory sphere above a thin liquid film as in typical SFA or AFM force measurements using a model which assumed that the surface of the sphere is covered by gas bubbles and included the hydrodynamic force and the elastic force due to pressure fluctuation inside the bubbles. Their results indicated that the force, from which the slip length is estimated, decreases rapidly as the fraction of surface covered by the bubbles increases. Lauga and Stone [98] simulated flow inside circular pipes whose walls are patterned with alternating regions of no-slip and perfect slip boundary conditions by solving the Stokes equations assuming that the gas bubbles acted like a zero shear stress boundary, and showed that the slip length greatly depends on the fraction of pipe wall covered by the "perfect-slip" surface.

Although most of the studies of gas bubbles at the solid surface showed that they enhance liquid slippage, a few studies have found that gas bubbles may actually suppress slip under certain conditions. Steinberger et al. [173], who used SFA to study slippage over an engineered "superhydrophobic" surface with a lattice of cylindrical holes (1.3 μm in diameter and 3.5 μm in height), reported that their system had slip lengths that increased at high pressure or when the fluids completely filled the holes compared with the case when the pressure is low enough to allow formation of a liquid-air interface inside the holes. Their 3D finite-element method study of

this superhydrophobic suface concluded that b depends strongly on the curvature of the liquid-air interface. Hyvaluoma and Harting [73], who modeled Couette flow over structured surface with gas bubbles attached using a two-phase lattice Boltzmann method, observed similar phenomena, reporting that changing either the shape of the air-liquid interface or the distribution of the bubbles affects b for a given bubble area fraction, and that the flow resistance increases if the bubbles protrude into the channel.

2.4.2.3 Surface Roughness

The majority of the studies investigating how surface roughness affects slip have been theoretical (*vs.* experimental) because of the practical difficulties in creating surfaces that have different well-defined roughness distributions with otherwise identical surface properties. A number of these theoretical analyses predict that the presence of roughness either reduces [149, 150] or enhances [163] slip. Priezjev [149] and Priezjev and Troian [150] used MD simulations to study constant-force driven flows between two atomistic walls and reported that both the random and periodic surface roughness even at values below the molecular diameter can strongly reduce b and the rate at which b increases with G. Sbragaglia et al. [163] showed, based on their lattice Boltzmann simulations, that there is a pressure-dependent critical roughness, above which the flowrate (and therefore slip) increases with the roughness.

Some other groups, however, have shown that the relation between surface roughness and b depends on the scale of the roughness [34, 54]. Galea and Attard [54] showed, in their MD simulations of a Lennard-Jones fluid in plane Couette flow at constant pressure that although the no-slip condition holds at intermediate roughness values where the wall and fluid atoms are of comparable size and density, there was slip for both very rough and very smooth walls. This non-monotonic relationship between roughness and slip has also been verified by MD studies of plane Couette flows

between a smooth and a rough patterned surfaces [34]. The results demonstrated that increasing roughness of a initially smooth hydrophobic surface reduces the slip length while increasing the roughness enhances slip at the "super-hydrophobic" state, or when gas bubbles are trapped between the asperities of the surface.

The smaller number experimental studies probing the relationship between b and surface roughness also report conflicting results. Zhu and Granick [208] used SFA to compare three mica surfaces coated with a monolayer of OTS with rms surface roughness values of $0.2-6$ nm, and reported that b decreased with increasing surface roughness irrespective of surface chemistry; no slip was observed for the roughest surface over the entire range of G studied. Similar phenomena has also been observed by Schmatko et al. [165] using TIR-FRAP. On the other hand, Bonaccurso et al. [12] reported that slip over hydrophilic silica surfaces increased with surface roughness for AFM studies of native oxide layers on silicon with rms roughness ranging from 0.7 to 12.2 nm. Joseph et al. [82] estimated b based on near-wall velocity data for flows over surfaces roughened by CNTs. They studied both a regular "mat" of vertically aligned CNTs, which they hypothesized could trap air bubbles, and a "mat" of tangled CNTs of random orientation, which they hypothesized could not trap such bubbles, and showed that the measured slip length was proportional to the surface roughness in the former. The slip length over the tangled CNTs is smaller than for the case of the aligned CNTs under otherwise identical conditions, and b was only a weak function of the surface roughness in the latter case.

Finally, a number of papers suggest that the conflicting results on the relationship between b and surface roughness may be due to difficulties in defining the true "wall" position of a roughened surface. Vinogradova and Yakubov [192] used an AFM to measure hydrodynamic force acting on a rough sphere with an rms roughness $10-11$ nm due to an aqueous film squeezed between the sphere and a smooth plate. The authors reported that the measured force matched well with that predicted based on

no-slip boundary conditions at a surface located at an intermediate position between peaks and valleys of the sphere surface roughness. Joly et al. [81], who studied slip at zero shear rate by measuring the Brownian diffusion of tracers close to a solid surface as a function of tracer-surface separation distance, reported that the measured diffusion-distance function for a rough hydrophobic surface is equivalent to that predicted on a smooth "non-slip" surface located 40 nm below the roughness peaks on the hydrophobic surface.

2.4.2.4 Shear Rate

In general, slip is expected to be a (possibly discontinuous) function of shear rate. In the pioneering MD simulation by Thompson and Troian [182], the authors modeled a planar Couette flow (*i.e.*, boundary driven shear flow) of a simple fluid past an atomically smooth rigid wall with weak wall-fluid interactions ($\epsilon_{\mathrm{wf}}/\epsilon_{\mathrm{f}} \leq 0.6$; ϵ_{wf} and ϵ_{f} are LJ wall-fluid interaction energy and energy of the fluid phase, respectively) and suggested that at low G, b is shear rate-independent. As G increases and exceeds a system-dependent critical shear rate G_{c}, however, b increases nonlinearly with G as follows:

$$\frac{b}{b_0} = \left(1 - \frac{1}{G_{\mathrm{c}}}\frac{\partial u}{\partial z}\bigg|_{\mathrm{wall}}\right)^{-1/2} \tag{12}$$

where b_0 is the slip length at low G. Note that G_{c} was found to be $O(10^{11}\ \mathrm{s}^{-1})$ for water, a value which may not be practically achievable in a macroscopic setup. This non-linear relationship has also been verified by other groups [148, 193]. A number of the experimental studies, especially those performed using the SFA and AFM, have also reported that slip is "shear rate-dependent" [207, 37, 63, 125].

The observation that b increases with G implies that $b \to \infty$ as $G \to \infty$, which is practically impossible. Several recent studies have reported results suggesting that b is bounded at higher G. Priezjev [147] showed using MD simulations that in reality,

even a slight increase in the surface roughness of a rigid wall reduces the slip length and its dependence on shear rate. Martini et al. [115] pointed out that for a flexible wall, b approaches a constant value at the limit of high G because of the frictional dissipation caused by the momentum transfer from the fluid to wall atoms, which was considered in their MD simulations by attaching the wall atoms to their lattice sites by linear springs.

Several experimental measurements also suggest that there is a limiting value of b at high G. Willmott and Tallon [197] inferred slip length by measuring the damping force acting on a fused silica rod with hydrophobic coating oscillated in water by a torsional ultrasonic oscillator and obtained $b \approx 50$ nm for $G = [500\ \mathrm{s}^{-1} : 3500\ \mathrm{s}^{-1}]$. Cottin-Bizonne et al. [35] observed, with dynamic SFA, $b = 20$ nm for water over an OTS-silanized Pyrex plate that was independent of G for values up to 5000 s^{-1}. The authors [36] then extended this work to a variety of liquid-solid combinations, and reported roughly constant slip length for $10 \leq G \leq 5000\ \mathrm{s}^{-1}$; they also pointed out that errors in the measured particle-plate separation distance, especially in the limit of small separations, and misapplication of the analytical solution of viscous drainage force acting on the sphere derived under the assumption that b is independent of G could lead to reports by other investigators of "shear-dependent" b in AFM or DSFA studies of slip. Lauga and Brenner [96] modeled slip studies based on dynamic drainage measurements by simulating the forces acting on an oscillating sphere and showed that if the sphere surface is covered by gas bubbles, the resultant "shear-dependence" of the measured values of b may instead be due to the compression and dilatation of these bubbles, *vs.* the actual slip.

CHAPTER III

EVALUATING MNPIV USING SYNTHETIC IMAGES

In order to better understand the impact of various factors (*e.g.* background noise, Brownian diffusion and non-uniform illumination) on accuracy of MnPIV, the technique was first tested using pairs of synthetic images of a constant-shear flow that incorporated camera noise, digitization errors, hindered Brownian diffusion and illumination with an exponential intensity profile. Section 3.1 describes how the synthetic images were generated and Section 3.2 discusses the image processing procedure, followed by the results and discussions in Section 3.3.

3.1 Generation of Synthetic MnPIV Images

PIV images essentially consist of a number of particles randomly distributed over a "noisy" background. An in-house MATLAB code was used to produce synthetic MnPIV image pairs with a know displacement to simulate actual experimental data. To generate such images, a number of parameters (*e.g.*, those related to the particle image size and intensity, background noise and illumination) must be adjusted so that synthetic images closely match the experimental data. This section details how these parameters were determined.

3.1.1 Creating a Single Particle Image

In MnPIV experiments, particles with diameters typically less than 300 nm are used as tracers. Since the tracers themselves are smaller than the illumination wavelength $\lambda = 488$ nm, it is difficult to image particles relying on elastic scattering. In most cases, fluorescently-labeled polystyrene particles are chosen and the red-shifted fluoresce from inelastic scattering of the light by the particles is imaged and recorded instead.

When determining the size of particle images, one has to consider the regime of "diffraction limited imaging," which sets the lower limit of the particle image size that can be obtained for a given optical configuration independent of actual particle size. Olsen and Adrian [128] proposed an expression for the diameter of the particle image:

$$d_{\mathrm{pi}} = \left[d_{\mathrm{diff}}^2 + 4M^2a^2 + \frac{M^2 z_{\mathrm{f}}^2 d_{\mathrm{a}}^2}{(s_{\mathrm{o}} + z_{\mathrm{f}})^2} \right]^{\frac{1}{2}} \tag{13}$$

by combining diffraction effects with the geometric magnification of the particle image and spreading of the geometric image as the particle moves away from the focal plane (the first, second, and third terms, respectively on the right hand side (RHS) of Equation 13). In this equation, z_{f} is the distance between the particle center and the focal plane, d_{a} is the lens aperture diameter and s_{o} is the object distance. Meinhart and Wereley [118] derived the diffraction-limited spot size d_{diff} for infinity-corrected optics:

$$d_{\mathrm{diff}} = 2.44M\lambda f_{\#} = 1.22M\lambda \left[\left(\frac{n_{\mathrm{o}}}{NA} \right)^2 - 1 \right]^{\frac{1}{2}} \tag{14}$$

The model in Equations 13 and 14 was used to estimate the particle image size in the code for generating the synthetic data. For the parameters used in current study ($M_{\mathrm{eff}} = 31.5\times$, $a = 50$ nm, $\lambda = 488$ nm, $NA = 0.7$), it showed that the diffraction term in Equation 13 is more than two orders of magnitude greater than the other two terms. For a CCD camera, with a pixel size of 7.4 μm and a system magnification of 31.5× a particle image spans about 5 pixels in the final digital image. Although the particle image size is set constant in the synthetic data since all particle images in MnPIV data are considered to be in "perfect" focus (Section 1.2.5) under our assumptions of fixed optical magnification and monodisperse particles, dimmer particle images or images of those particle farther away from the wall appear smaller due to the possibility that some pixels on the edges of these dimmer images may have

grayscale values below the background noise.

In the synthetic images, the intensity distribution in each individual particle image was simulated as a 2D Gaussian function [195]:

$$I_{\mathrm{pi}}(x,y) = I_{\mathrm{c}}(z_{\mathrm{i}})\exp\left\{ -\frac{(x-x_{\mathrm{i}})^2 + (y-y_{\mathrm{i}})^2}{\sigma_{\mathrm{d}}^2} \right\} \tag{15}$$

The equation is evaluated at the integer pixel locations $[x,\ y]$ in the digital image while the true position of particle center $[x_{\mathrm{i}},\ y_{\mathrm{i}},\ z_{\mathrm{i}}]$ can be non-integer. The peak grayscale value of the particle image, I_{c}, is assumed to decay exponentially with the distance between the particle center and the wall: $I_{\mathrm{c}} \propto \exp(z_{\mathrm{i}}/z_{\mathrm{p}})$, to simulate the effects of evanescent-wave illumination. The parameter that characterizes the size of the particle image, σ_{d}, is determined so that the image intensity I_{pi} decreases to the background noise level $\Psi_{\mathrm{m}} + \Psi_{\mathrm{s}}$ (Ψ_{m} and Ψ_{s} are the mean and standard deviation of the random background noise modeled as a Gaussian distribution, as discussed in the next section) at the edge of the image where $\sqrt{(x-x_{\mathrm{i}})^2 + (y-y_{\mathrm{i}})^2} = d_{\mathrm{pi}}/2$.

3.1.2 Generating an Image Pair

A synthetic image starts as a matrix of normally-distributed random numbers that simulate the image background noise, following the approach proposed by Westerweel [195], who observed that the background noise of PIV image can usually be described by a Gaussian distribution. The parameters for this model (essentially the mean Ψ_{m} and standard deviation Ψ_{s} of the background noise) were obtained by fitting the noise portion of the gray-scale value histogram of the experimental images to a Gaussian function.

To create the first image of each pair, about 600 particles are uniformly and randomly distributed in a 120 μm × 25 μm × 0.8 μm ($x \times y \times z$) volume. Note that the x- and y-dimensions corresponds to 720 and 150 pixels in the image, respectively, and the z-dimension is much larger than z_{p} which is assumed to be 160 nm. The

simulated particle images were "placed" in the matrix of background noise using these parameters and Equation 15. Given the exponential decay in image intensity and the simulated "camera detection threshold," only particles at z-locations within about $2z_\mathrm{p}$ of the wall have a peak grayscale value above the background noise and are hence "visible" in the synthetic images.

These particles are then convected by a plane Couette flow and hindered Brownian diffusion over the time interval Δt to generate the second image of the pair. The plane Couette flow velocity profile was assumed to have only one nonzero velocity component, u, along the x-direction, where $u(z) = Gz$ with the shear rate $G = 3000\ \mathrm{s}^{-1}$. Any particle displacement along the y and z directions is thus due only to Brownian diffusion. The particle motion due to Brownian diffusion was simulated using the method discussed in Section 2.3. As mentioned previously, a time step δt that is much smaller than the time interval within each image pair $\Delta t = O(1\ \mathrm{ms})$ is required for this simulation. For each time step, the displacements along y and z of each particle are first calculated to determine its y- and z-positions. The particle x-location, which is also affected by the flow, is then given by:

$$x(t_0 + \delta t) = x(t_0) + G\left[\frac{z(t_0) + z(t_0 + \delta t)}{2}\right] \cdot \delta t + \phi\sqrt{2D_{\|}(t_0) \cdot \delta t} \qquad (16)$$

where $x(t_0)$ is the initial x-location of the particle and ϕ is a random number normally distributed about a mean of zero with a variance of unity. Tests with $1\ \mu\mathrm{s} \leq \delta t \leq 25\ \mu\mathrm{s}$ are conducted and gave virtually identical results. All simulations shown in this chapter are therefore carried out at $\delta t = 5\ \mu\mathrm{s}$. Using Equation 16, the particle positions at the end of the time interval $(t_0 + \Delta t)$ are obtained and particle images with these updated locations are placed in a new matrix of background noises to form the second image of the pair. Finally, the two images were cropped to the final image size (640×100 pixels) to minimize the number of particles that are convected out of the image region by the flow. Figure 13 compares a synthetic image with an actual

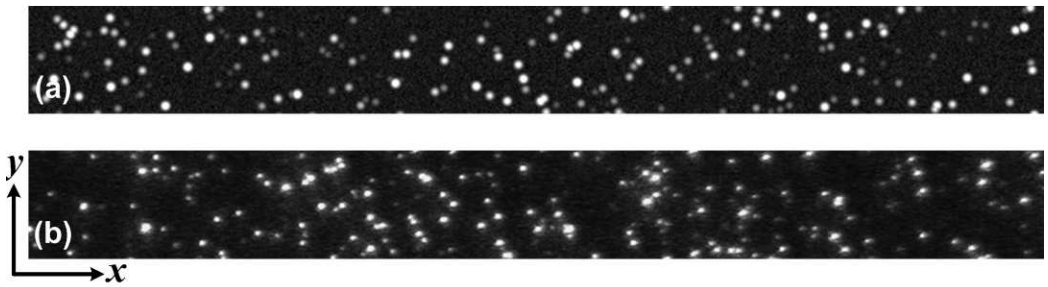

Figure 13: Comparison between typical synthetic (a) and experimental (b) MnPIV images. Note that the flow is in x direction.

experimental one.

3.2 Image Processing

The synthetic images were first used to determine how the particle image intensity varies with its z-position in order to obtain criteria for dividing a single MnPIV image into sub-images. At each given z-location, a sequence of 100 synthetic images, each of which contains about 30 individual particle images, were generated. To detect the particles, we first determine the background noise grayscale level. Since less than 0.3% of the pixels are particle images at these low seeding densities, the mean gray value over each dataset of 100 images was calculated as an initial estimate of the background noise and used as the threshold to binarize the raw images. A standard MATLAB algorithm was then used to perform connected-component labeling, where two pixels with grayscale values above the threshold are defined as "connected" if the second pixel occupies one of the eight neighboring pixels of the first. These connected regions, which should correspond for the most part to particle images, were eliminated and the mean and standard deviation of the grayscale values of the remaining pixels were calculated over the original images. Next, the background noise level was taken to be twice the standard deviation above this mean, and used as the new threshold for re-binarizing the raw images. Particle images were then identified as connected

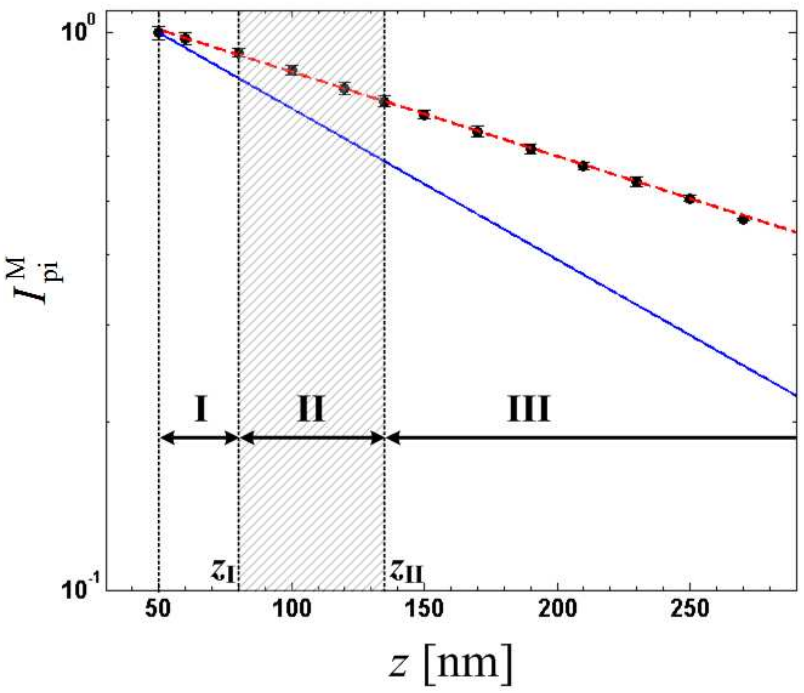

Figure 14: The normalized mean (filled circles) grayscale values $I_{\rm pi}^{\rm M}$ versus distance z from the wall in the synthetic data. The solid line represents the intensity decay corresponding to the evanescent-wave illumination, or $\exp\{-z/z_{\rm p}\}$. The error bars denote a standard deviation

.

regions, and the pixel location of each particle image was defined as its grayscale-weighted centroid. Here, we define the particle image intensity as the mean grayscale value over all pixels that are located within the particle image with grayscale values above the background noise level. Finally, the mean particle image intensity $I_{\rm pi}^{\rm M}$ averaged over about 3000 particle images for each z location was calculated. Note that $I_{\rm pi}^{\rm M}$ was normalized by its maximum or the image intensity of particles at the wall.

Figure 14 shows how $I_{\rm pi}^{\rm M}$ varies with z; the error bars denote one standard deviation. As expected, $I_{\rm pi}^{\rm M}$ decreases monotonically with increasing z. Using this curve, we tentatively divided the particles into three layers (I, II and III):

I. $[a = 50\ {\rm nm} < z \leq z_{\rm I} = 80\ {\rm nm}]$ Particles with normalized mean grayscale values $I_{\rm pi}^{\rm M} \geq I_{\rm b1} = I_{\rm pi}^{\rm M}(z_{\rm I}) - \sigma_{\rm pi}^{\rm M}(z_{\rm I})$, where $\sigma_{\rm pi}^{\rm M}(z_{\rm I})$ is the standard deviation in $I_{\rm pi}^{\rm M}$ at

$z = z_{\mathrm{I}}$;

II. $[z_{\mathrm{I}} < z \leq z_{\mathrm{II}} = 135$ nm] Particles with $I_{\mathrm{b1}} > I_{\mathrm{pi}}^{\mathrm{M}} \geq I_{\mathrm{b2}} = I_{\mathrm{pi}}^{\mathrm{M}}(z_{\mathrm{II}}) - \sigma_{\mathrm{pi}}^{\mathrm{M}}(z_{\mathrm{II}})$;

III. $[z_{\mathrm{II}} < z \leq z_{\mathrm{III}} = 350$ nm] Visible particles with normalized mean grayscale values $I_{\mathrm{pi}}^{\mathrm{M}} < I_{\mathrm{b2}}$. Note that the upper boundary was determined by comparing the particles' peak grayscale values to the background noise level of the images.

An ensemble of 2000 image pairs was created; each of these images was then divided into three layers as follows. All particle images were first detected and their normalized grayscale values $I_{\mathrm{pi}}^{\mathrm{M}}$ were calculated. For each sub-layer, only the particle images that satisfied the criteria above were preserved; all other particle images were replaced by random grayscale values similar to the background noise. Figure 15 shows one typical original image Figure 15a and the three sub images Figure 15b-15d with increasing distances from the wall and decreasing particle image intensities, corresponding to the layers I, II and III shown in Figure 14, respectively.

Once divided, the 2000 image pairs in each layer were processed using the FFT-based cross-correlation and Gaussian surface fit peak-finding algorithm described by Sadr et al. [157]. Relatively large interrogation windows ($400(x) \times 90(y)$ pixels) were used because of Brownian-diffusion-induced particle mismatch [157]. Both correlation averaging [119] and window shift [194] were also applied to further increase the signal-to-noise ratio (SNR) of the correlation function. Since the flow considered here is steady and one-dimensional, the results were both spatially and ensemble averaged over the 2000 independent image pairs to obtain the mean velocity u.

A few studies have shown that particle polydispersity and variations in fluorescent dye concentration between particles can cause significant uncertainties in the particle image intensity even for particles located at the same z-location [101, 72]. The sensitivity of the obtained velocity results to variations in the grayscale boundaries I_{b1} and I_{b2} used to divide the images into layers was also evaluated. Sub-images were

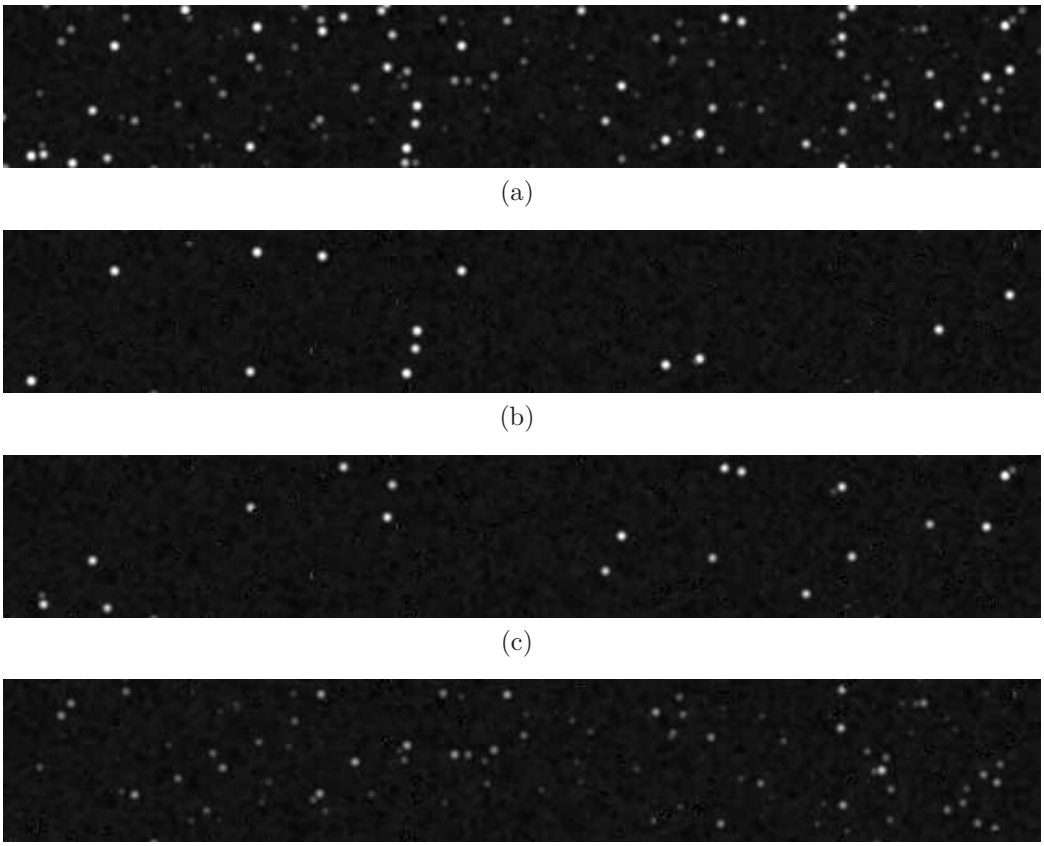

(a)

(b)

(c)

(d)

Figure 15: Images used in MnPIV test. (a): an original or "undivided" synthetic image; (b)-(d): sub-images corresponding to the sub-layers I, II and III in Figure 14.

generated using boundaries corresponding to 5% variation in the values of I_{b1} and I_{b2} and processed as described above.

3.3 Results and Discussion

3.3.1 Results

Figure 16 shows the average velocity u (data points) obtained by processing the sub-images corresponding to layers I, II and III (bounded by the dashed lines) for $\Delta t = 1$ ms and $a = 50$ nm as a function of distance normal to the wall z. Here, the three MnPIV velocity datapoints are plotted at the z-location corresponding to the geometric center of each layer, under the assumption that the particles are uniformly illuminated and uniformly sample all the z-locations within each layer and

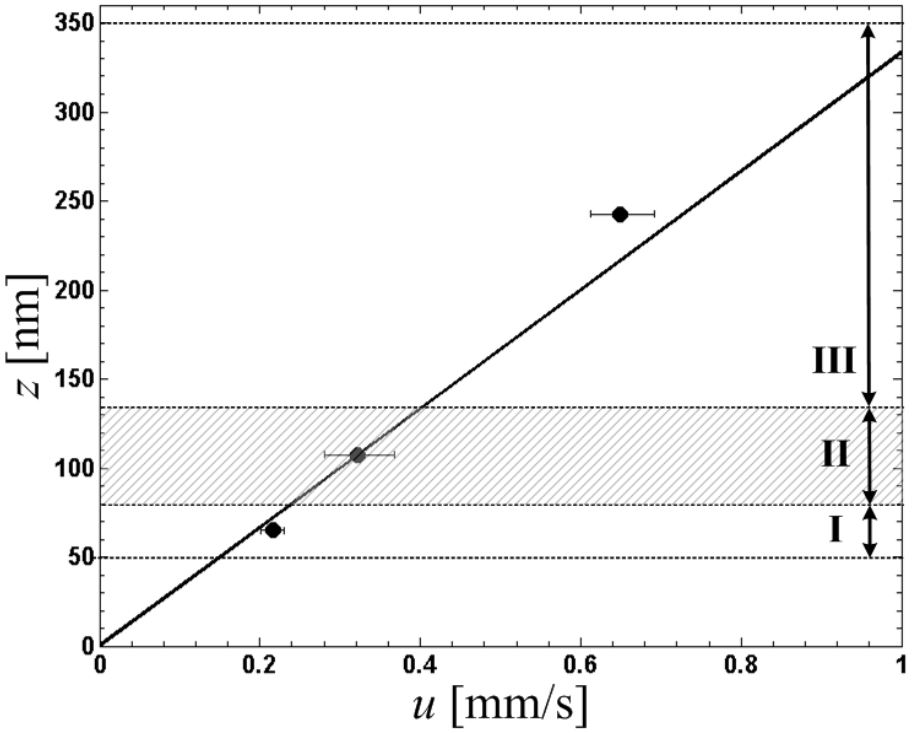

Figure 16: Average velocity u (data points) obtained by applying MnPIV to synthetic image of plane Couette flow for $\Delta t = 1$ ms, $a = 50$ nm and $G = 3000$ s^{-1}. The datapoints are placed at the geometric center of each layer and the errorbars correspond to variations in the "measured" velocities for 5% deviation in I_{b1} and I_{b2}. The solid line represents the linear Couette flow velocity profile $u(z) = Gz$.

are compared with the linear plane Couette velocity profile (solid line).

To study the effects of the time interval within one image pair Δt on the accuracy of the method, several other cases were simulated at the same shear rate G, but for different values of Δt. Figure 17 plots the average velocity u in layers I, II and III normalized by u_{M}, the expected velocity at the geometric center of each of the three layers, as a function of the normalized time interval τ:

$$\tau = \frac{\Delta t}{a^2/D_\infty} \tag{17}$$

One advantage of working with synthetic images is that the location of each particle is known *a priori*; the velocity can therefore also be calculated by averaging these exact locations, an approach similar to the particle tracking. The "tracked" velocity values of the three layers were in all cases within 6% of the velocities calculated from

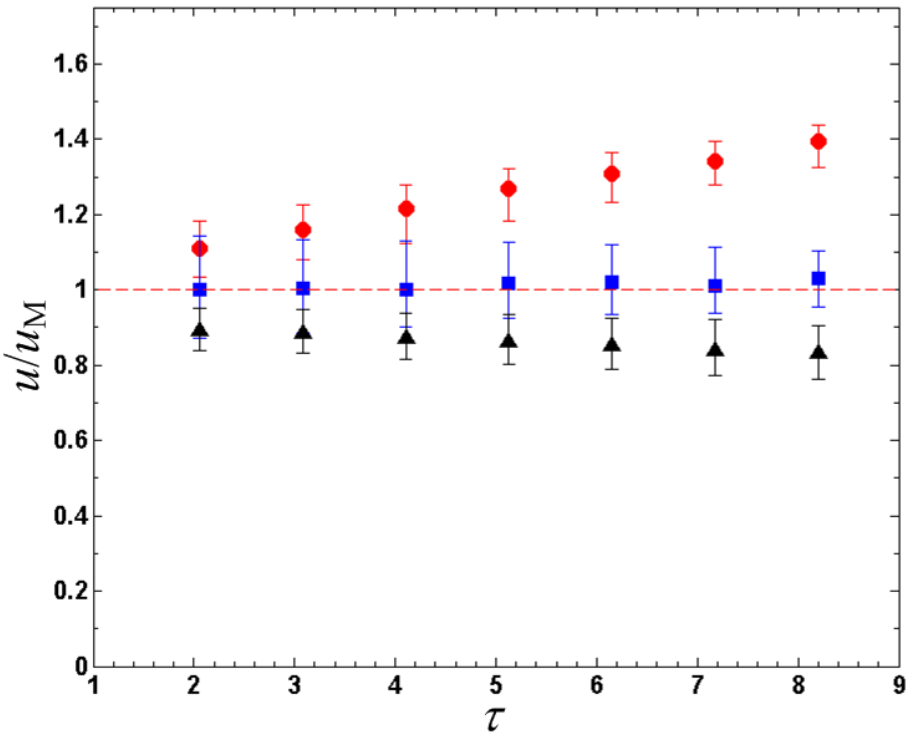

Figure 17: Normalized velocities u/u_{M} for layer I (filled circles), II (filled squares), and III (filled triangles) as a function of dimensionless time τ (Equation 17). Here, u_{M} represents the expected velocities at the geometric center of the three layers. The error bars again correspond to velocities obtained for a 5% deviation in I_{b1} and I_{b2}.

the cross-correlation in Figure 17; the error in the multilayer nPIV results from these synthetic images is therefore estimated to be about 6%. As expected, the largest errors are in layer I, the thinnest layer and the one nearest the wall, where only about 20% percentage particle images are "matched" within an image pair over this 30 nm thick layer.

3.3.2 Biases in the Measured Velocity Data

In the absence of Brownian diffusion, the nPIV result in each layer should be essentially u_{M} for this linearly varying flow velocity profile assuming that the tracers uniformly sample the flow field. And indeed, u does match u_{M} in layers II and the measured velocities are roughly constant over the time interval studied. However, u is more than 20% higher than u_{M} in layer I, and the discrepancy increases with τ, becoming about 40% by $\tau = 8$; simulation results also show that u actually exceeds the maximum velocity in layer I, or Gz_{I}, for τ larger than 5. This overestimation is primarily due to the asymmetric nature of hindered Brownian diffusion in a region adjacent to a solid wall. Because the "no-flux" boundary condition at the wall and the increase in the diffusion coefficients with wall-normal distance, particles subject to this type of diffusion have much greater probability of moving away from, *vs.* towards the wall, and hence have a much higher likelihood of sampling velocities greater than Gz_{I}, even if they are "matched," or present in layer I at the times of the two exposures. This bias is particularly pronounced for layers that are "thin," *i.e.*, have a z-extent of $O(a)$, and immediately next to the wall.A model describing this bias and a correlation that compensates for this bias in certain cases based on Brownian dynamic simulations will be discussed in more detail (Section 4.2).

Finally, the velocities u in layer III are roughly constant across the range of τ studied, but consistently less than u_{M}. Since the hindered Brownian diffusion effects described above should have minimal impact in this layer, and the behavior due these

effects would result in an overestimation, we instead attribute this underestimation to the exponential decay in the intensity of evanescent-wave illumination. Particles closer to the wall have larger and brighter images and hence a greater contribution to the cross-correlation. These brighter particles with their smaller velocities therefore bias the results towards values near the lower boundary of the layer (*i.e.*, slightly greater than z_{II}), resulting in an "underestimation" of velocities in layer III. This effect is discussed further in Section 4.1.

3.4 Summary

The feasibility and accuracy of MnPIV, a technique for obtaining the two velocity components parallel to and at different distances from the wall within the region illuminated by the evanescent wave, were tested using synthetic images of plane Couette flow incorporating hindered Brownian diffusion, non-uniform illumination and image noise. More specifically, synthetically generated images of particles at known z-locations were first used to establish criteria for dividing the MnPIV images into three sub-layers, with thicknesses of 30, 55, and 215 nm, respectively. These sub-layer images were then processed using standard cross-correlation based techniques to obtain velocity data at three different z-locations within 400 nm of the wall. The obtained MnPIV results are within 6% of the values averaged over the "true" particle locations recorded when creating the images. The tests successfully demonstrated that MnPIV can obtain near-wall velocities at multiple z-locations, and therefore wall shear stresses, using a single set of images obtained with one camera. Note that the closest near-wall velocity measurement is done within the first 80 nm next to the wall, representing a further improvement in spatial resolution compared with the "original" nPIV experiments.

The tests in this chapter also showed that both the hindered Brownian diffusion and the non-uniform illumination cause biases in the measured velocities. Careful

characterizations of these effects will help find ways for correcting the biases and some initial efforts will be discussed in the next Chapter.

CHAPTER IV

A FURTHER LOOK INTO THE BIASES IN MNPIV

As discussed in the previous chapter, the non-uniform nature of evanescent-wave illumination and the asymmetry of the Brownian diffusion in the near-wall region can both affect the accuracy of MnPIV. In this chapter, the effects of non-uniform illumination on MnPIV velocities obtained from synthetic images (similar to those used in the previous Chapter) with correlation-based methods are characterized in Section 4.1. The effects of the asymmetric diffusion based on Brownian dynamic simulations are then detailed in Section 4.2.

4.1 The Effect of Non-uniform Illumination on the Accuracy of MnPIV

When cross-correlation methods are used to obtain velocities in a non-uniform flow with the MnPIV technique, the non-uniform evanescent-wave illumination can bias the resultant velocity towards the values sampled by the tracers with brighter images, as shown in Figure 17. This section quantifies this effect using synthetic images generated with known displacements and tracer properties.

To isolate the non-uniform illumination effects from those due to Brownian diffusion or background noise, synthetic images of planar Couette flows ($G = 2500$ s^{-1}) were created with evanescent-wave illuminations (specifically, an illumination with an exponential intensity profile $I(z) = I_0 \exp(-z/z_\mathrm{p})$ where z_p varied from 150 nm to 1000 nm) in the absence of Brownian diffusion and background noise. Each image contained about 200 particles ($a = 50$ nm) whose centers were uniformly and randomly distributed over a region within 300 nm of the wall. Figure 18 depicts the variation in particle image intensities with z for $z_\mathrm{p} = 150$ nm, 300 nm, 500 nm and 1000 nm;

the maximum drop in image intensity over the first 300 nm next to wall is about 80% at the smallest z_p, 150 nm. Figure 19 compares typical tracer images for (a) uniform illumination and (b) exponentially decaying evanescent-wave illumination with $z_p = 150$ μnm.

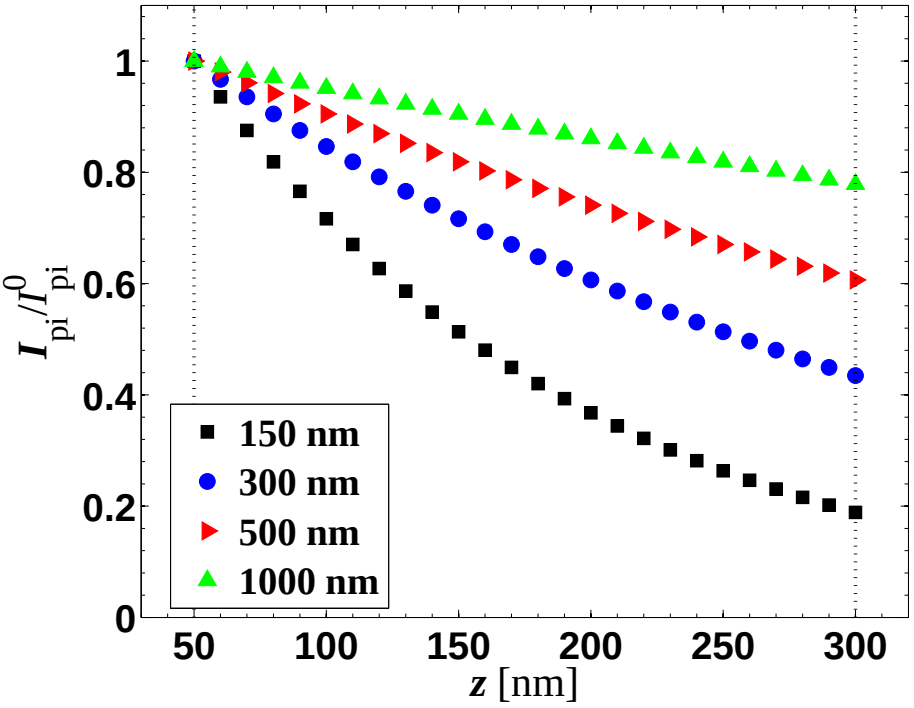

Figure 18: Image intensity variation for particles illuminated by evanescent waves for different penetration depths z_p.

For each case, a total of 1000 individual image pairs, or 2000 images, each with dimensions of 100×640 pixels or physical dimensions of 17×107 μm, were generated and processed with both cross-correlation (Section 3.2) and particle-tracking [5] based algorithms. In the former case, relatively large interrogation windows of 80×80 pixels and correlation averaging over every 100 images were used to increase the signal-to-noise ratio (SNR) of the correlation functions.

Figure 20 graphs the normalized "measured" velocities u_m/u_c from the cross-correlation (■) and particle tracking (●) approaches as a function of z_p, where u_c is

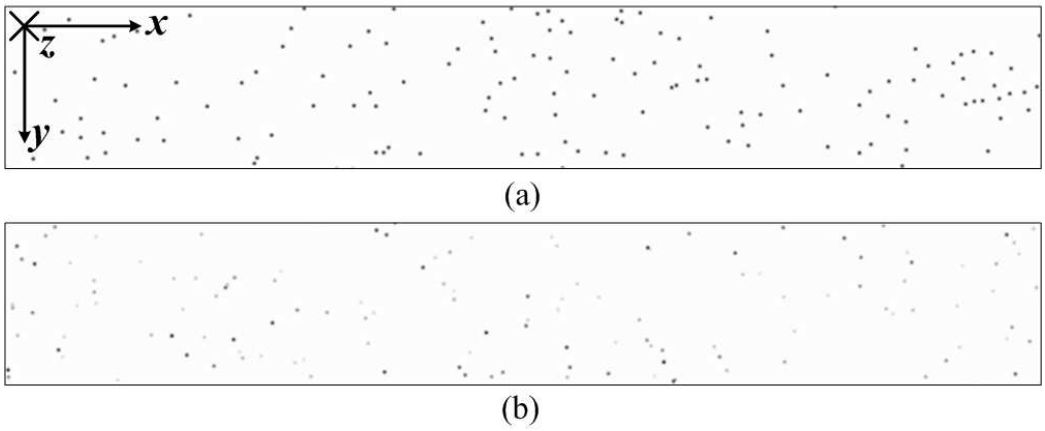

Figure 19: Synthetic images with (a) uniform image intensity; (b) exponentially decaying image intensity $I_{\mathrm{pi}} \propto (-z/z_{\mathrm{p}})$ where $z_{\mathrm{p}} = 150$ nm. The images are inverted to improve the visibility of the tracers.

the expected velocity at the geometric center of the region of interest (ROI) calculated from the known flow parameters. For the uniformly illuminated images (dotted line), the cross-correlation results are in good agreement with the expected velocities. For the images illuminated by evanescent waves, however, the cross correlation velocity results are significantly smaller than u_{c} and the discrepancy increases with decreasing z_{p}, corresponding to larger variations in particle image intensity (over the given z-dimension). The particle-tracking velocities obtained from the non-uniformly illuminated images are however, much closer to the expected values, with roughly constant discrepancy of less than 4%. Particle-tracking techniques were therefore used to obtain the tracer velocities in the subsequent chapters.

4.2 The Effect of Hindered Brownian Diffusion on the Accuracy of MnPIV

The Brownian diffusion of sub-micron-sized tracers is an important factor in microscale tracer-based velocimetry techniques. In this Section, the effects of Brownian diffusion—which becomes asymmetric and hindered near the wall—on the accuracy of MnPIV is modeled using synthetic images and Brownian dynamic simulations based

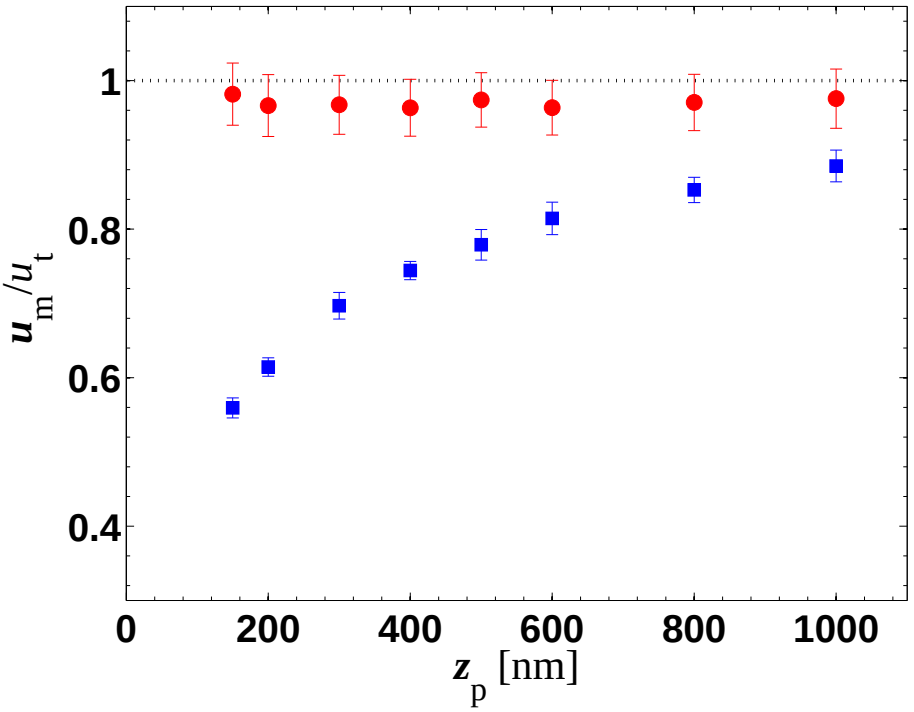

Figure 20: Comparison of velocities (normalized by the expected velocity u_c at the center of the layer, or $z_c = 175$ nm) obtained from cross-correlation (■) and particle tracking (●) methods from synthetic images with non-uniform image intensities. The dotted line represents the velocity obtained using cross-correlation based method for images with uniform intensity.

on the Langevin Equations.

4.2.1 Effects of "In-Plane" Brownian Diffusion

Olsen and Adrian [129], who derived an analytical description of cross-correlation based processing of PIV images that included the "in-plane" Brownian diffusion of the tracers, showed that the random walk due to the diffusion process reduced the SNR and increased the width of the correlation function, leading to uncertainty in the resultant velocity measurement. This error can be reduced in most cases by averaging correlation functions or alternatively, by averaging a large number of velocities obtained using relatively large interrogation windows to minimize the number of spurious vectors. This effect was illustrated by considering pairs of synthetic images of tracers convected by a uniform flow subject to in-plane Brownian diffusion at varying time intervals within the image pair Δt. For each value of Δt, 1000 image pairs were generated and processed using standard cross-correlation methods with no correlation averaging. The resultant displacements Δx were then compared with the expected value. Figure 21, which presents the mean $\epsilon_{\Delta x}$ and standard deviation $\sigma_{\Delta x}$ in this discrepancy as a function of Δt, shows that while the average discrepancy between the heavily averaged displacements and the expected values are negligible, $\sigma_{\Delta x}$ increases rapidly with Δt, presumably due to the associated increase in diffusion effects. These results suggest that averaging over a large number of samples is required to obtain an accurate displacement for large Δt, given the rather large values of $\sigma_{\Delta x}$.

4.2.2 "Mismatched" Particles Due to "Out-of-Plane" Diffusion

Since PIV measures velocities based on the displacements of tracers whose positions are recorded at the beginning and end of the time interval (*i.e.*, t_0 and $t_0 + \Delta t$), the tracers must be located within the imaged region (volume) at these two instants. In MnPIV, this region, which is bounded by the wall, has a z-dimension of $O(100$ nm) determined by the penetration depth of the evanescent-wave illumination and the

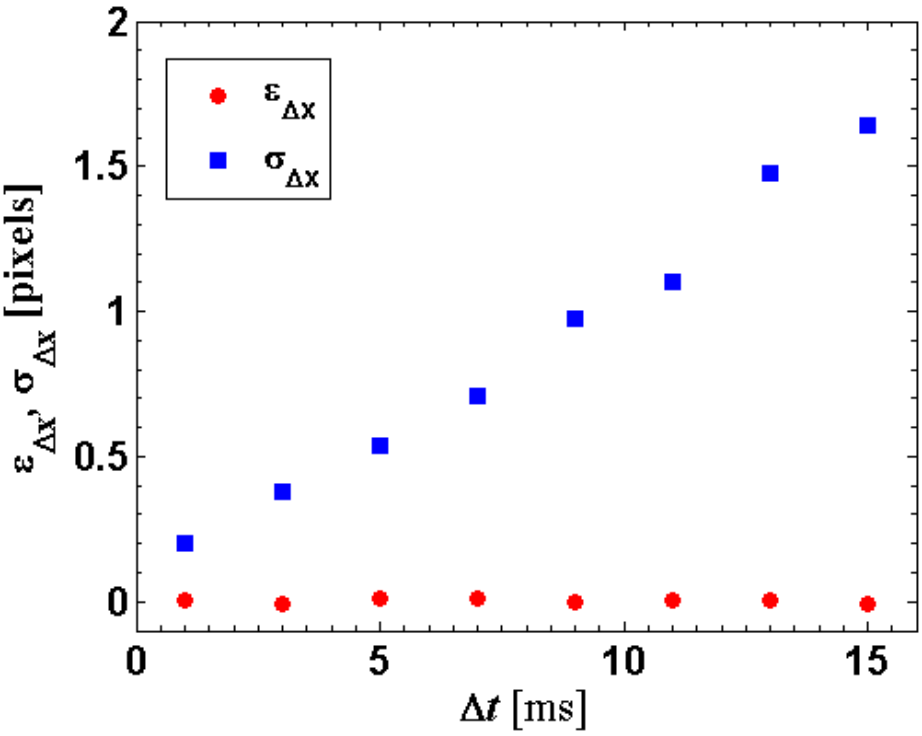

Figure 21: The mean $\epsilon_{\Delta x}$ (●) and standard deviation $\sigma_{\Delta x}$ (■) in the discrepancy between the displacements obtained using cross-correlation methods from synthetic images of uniformly displaced tracers subject to in-plane Brownian diffusion and actual values used to create the synthetic images.

camera detection limit. This z-dimension is comparable to the rms displacement of tracers over Δt normal to the wall due to Brownian diffusion: for example, the rms displacement $\sqrt{2D\Delta t} = 202$ nm for $\Delta t = 4$ ms for a 100 nm diameter particle in water at 300 K. Brownian diffusion normal to the wall or "out-of-plane" diffusion therefore is likely to move a significant fraction of the tracer particles randomly into or out of the imaging volume during this time interval Δt. Particles may therefore appear in only one of the two frames of an image pair, resulting in so-called "mismatched" particle images, which effectively increase the noise and uncertainty in velocities obtained using MnPIV.

To quantify the effect of "mismatched" particles, 5000 synthetic image pairs with time intervals Δt ranging between 1 ms and 14 ms were generated using the procedure described in Section 3.1. The particles, which are initially distributed randomly in a volume with a z-dimension of $5z_{\mathrm{p}}$, are convected by hindered Brownian diffusion and a uniform flow. A "mismatched" particle is defined to be a particle whose image is visible in only one of the two frames of an image pair, where "visible" implies that the particle is located inside the imaged volume. The z-dimension of this volume is estimated to be about $2z_{\mathrm{p}}$ based on the exponential decay in the illumination intensity and the simulated background noise level of the synthetic images. Figure 22 shows that the mismatched particles as a fraction of the total number of particles within an image pair F increases rapidly with Δt and that $F \propto (\Delta t)^N$ where $N = 0.4$.

The displacements obtained by processing the image pairs with a cross correlation-based method (no correlation averaging) were compared with the actual values used to generate the images. Figure 23 shows the average and standard deviation of the displacement error $\epsilon_{\Delta x}$ and $\sigma_{\Delta x}$ as functions of the fraction of mismatched particles F. The mean absolute difference is negligibly small ($\epsilon_{\Delta x} \sim 0.07$ pixels) for $F \leq 45\%$, then increases nearly exponentially with F for $F > 45\%$. The surprisingly small $\epsilon_{\Delta x}$ for $F < 45\%$ is due to the large interrogation windows used in the processing: even at

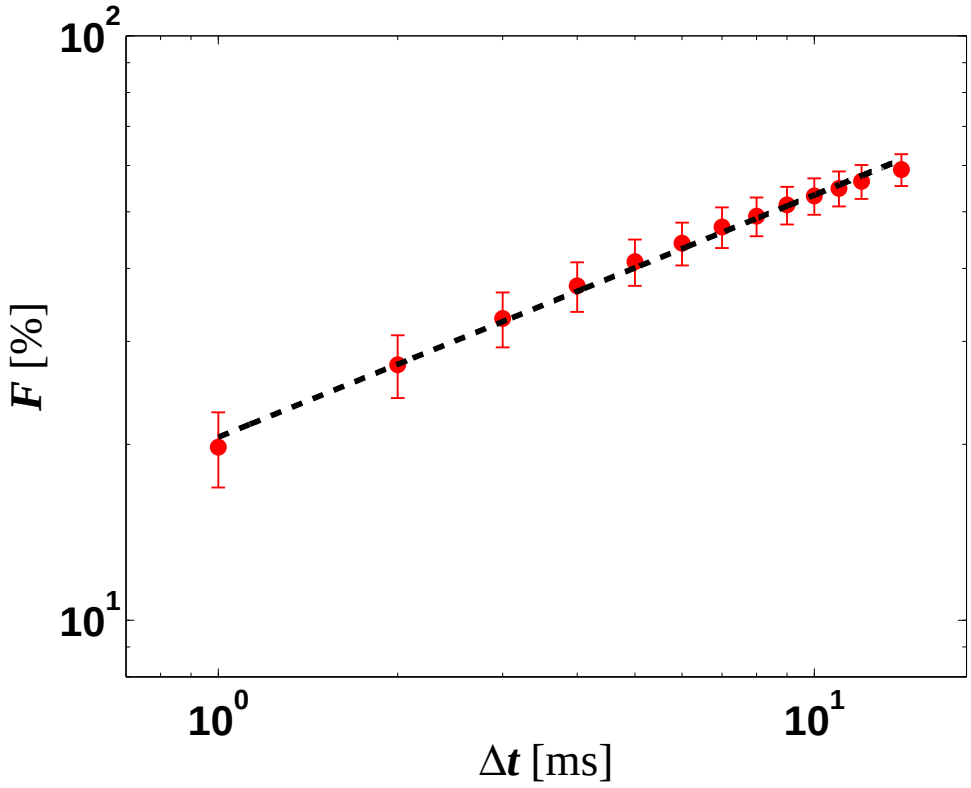

Figure 22: Fraction of mismatched particles as a function of the time interval within the image pair for particles subject to hindered Brownian diffusion.

$F = 45\%$, there are on average about 15 matched particle images in the interrogation windows within one image pair. The standard deviation of the displacement error $\sigma_{\Delta x}$, plotted in the same figure, is about an order of magnitude larger than $\epsilon_{\Delta x}$ for a given F and increase rapidly with F.

The increases in both $\epsilon_{\Delta x}$ and $\sigma_{\Delta x}$ are primarily due to the decrease in the SNR and the increase in the width of the cross-correlation function used to determine the tracer displacement. Figure 24 shows that the SNR of the correlation function (●) defined as the ratio of the peak of the correlation to the noise level, decreases monotonically with Δt. This decrease in the SNR of the correlation function may make it more difficult to accurately determine the location of the correlation peak, leading to errors in estimating particle displacements. Figure 24 also shows the width of the cross-correlation peak for tracers subject to 3D (■) and 2D (*i.e.*, in-plane) (▲)

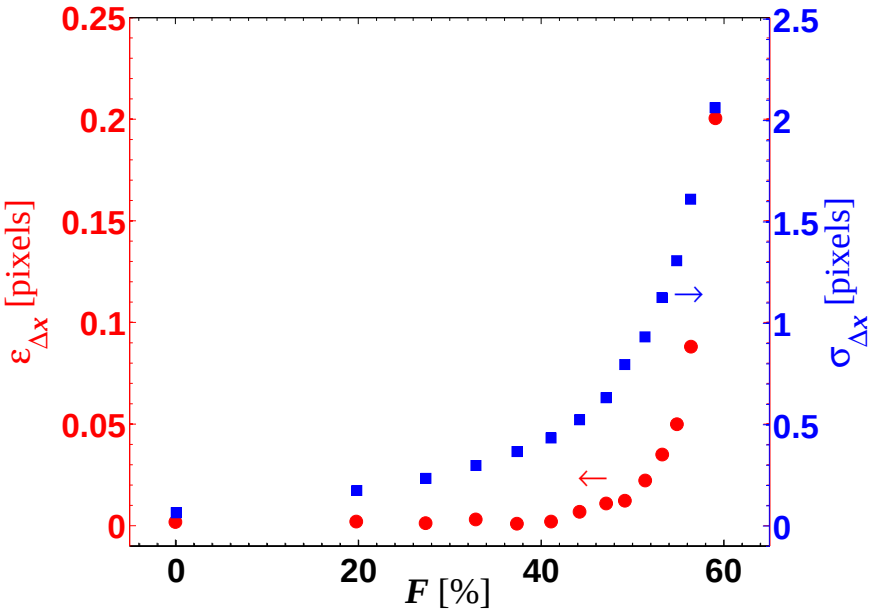

Figure 23: The mean $\epsilon_{\Delta x}$ (•) and standard deviation $\sigma_{\Delta x}$ (■)of the displacement error as functions of the fraction of mismatched particles F.

Brownian diffusions as functions of Δt. Note that the peak widths were determined by fitting the correlation functions with 2D Gaussian functions. The comparison shows that an increase in "mismatched" particles due to out-of-plane Brownian diffusion broadens the correlation peak compared with the "in-plane" cases and therefore further increases the uncertainties in the measured displacements.

Since this particle "mismatch" is essentially due to particles randomly moving out of and into the imaged region over the time interval Δt, the errors can be minimized by either increasing the thickness of the imaged region (thereby increasing the extent over which particles can diffuse in a given time) and/or reducing Δt (reducing the diffusion displacements). In MnPIV, however, the half-a-micrometer-thick imaged region is further divided into sublayers, which is equivalent to reducing the thickness of the imaged region.

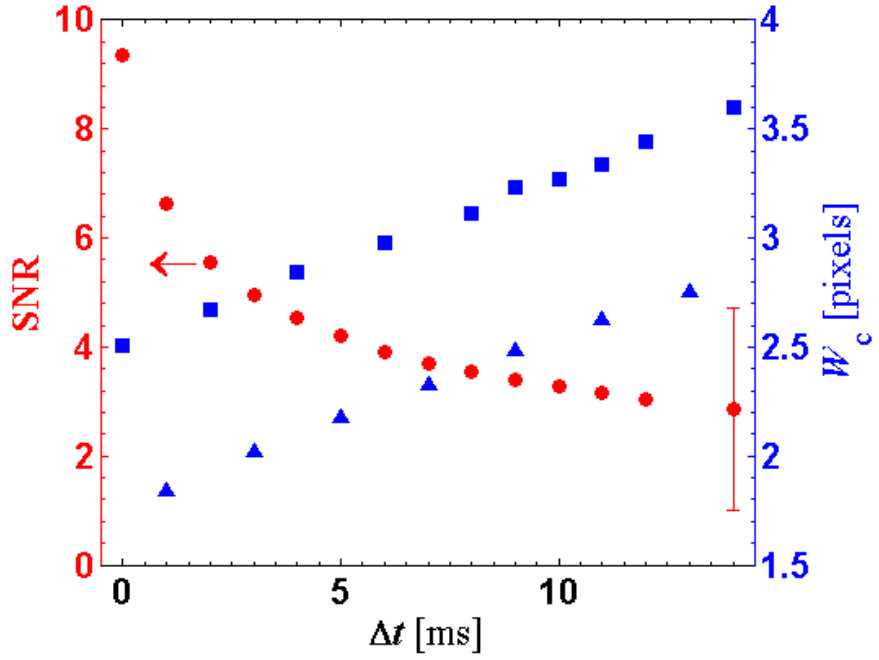

Figure 24: The average SNR (•) and width W_c of the correlation function (based on Gaussian function surface fitting) as functions of the time interval Δt. The widths of the cross-correlation peak for tracers subject to 3D (■) and 2D (*i.e.*, in-plane) (▲) Brownian diffusions are shown here.

4.2.3 Overestimation of Near-Wall Velocities

As discussed previously, MnPIV obtains near-wall tracer velocities over a ROI $a \leq z \leq Z$ as shown in Figure 25, by measuring an ensemble of tracer displacements over a short time interval Δt based on the two images of the tracers taken at the ends of the interval, or times t_0 and $t_0 + \Delta t$. Consider a spherical tracer of radius a in a constant-shear-rate flow where the velocity component parallel to the wall u varies linearly with distance normal to the wall $u = Gz$ (Figure 25), as is usually the case in the near-wall region for many microscale flows. If the particles are assumed to be uniformly distributed over the ROI and to be imaged and "matched" only if they are located inside the ROI at t_0 and $t_0 + \Delta t$, the velocity determined from the displacements of those matched particles $\bar{u} = \Delta x/\Delta t$ is a good approximation of the velocity sampled by these particles averaged over Δt. For the simple shear flow

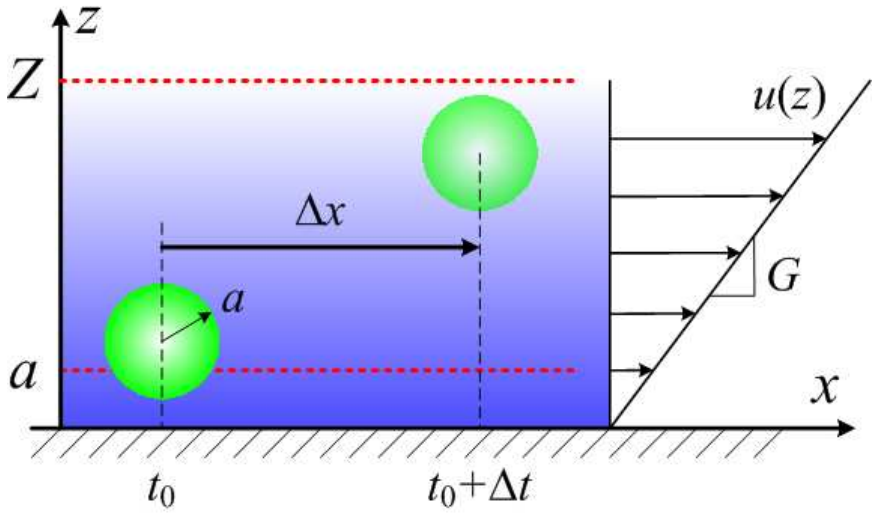

Figure 25: Schematic of a particle of radius a convected by a near-wall constant-shear flow $u(z) = Gz$. Two exposures required by MnPIV measurements are taken at time instants of t_0 and $t_0 + \Delta t$.

considered here, this velocity can also be expressed as $G\langle\bar{z}\rangle$, where $\langle\bar{z}\rangle$ is the average z-position sampled by the matched particles over Δt.

Ideally, if the matched particles remain uniformly distributed inside ROI over Δt and therefore uniformly sample the velocities in this range, $\langle\bar{z}\rangle$ should match the geometric center z_c of the ROI $\langle\bar{z}\rangle = z_c = (Z + a)/2$. In reality, however, the tracers sample the flow field inside the ROI nonuniformly because the "no-flux" boundary condition at the wall and the increase in the out-of-plane Brownian diffusion coefficient with z enable the tracers on average much likelier to move away from, *vs.* towards, the wall. The particles will therefore sample velocities in the flow region $z > z_c$ with a greater probability than those in the flow region $z < z_c$. Hence the Δx obtained from the matched particles represents an average displacement of tracer particles at a distance greater than z_c from the wall.

Figure 26 shows "snapshots" of the z-position of the center of a near-wall matched particle ($a = 50$ nm) subject to hindered Brownian diffusion over a time interval of 4 ms. Although the ROI is set to be between $a \leq z \leq Z$, the particle center is clearly

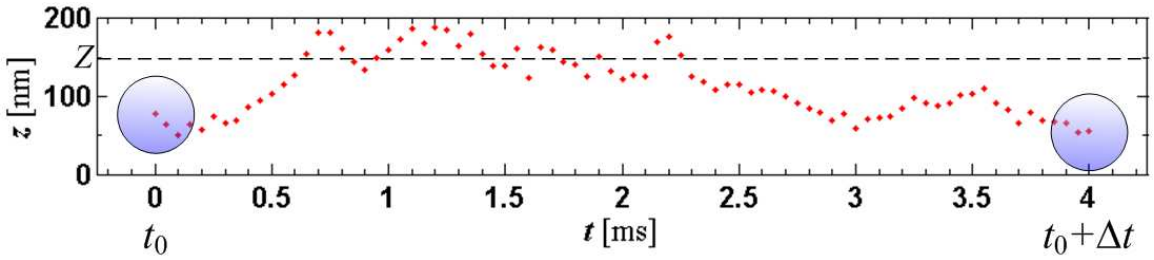

Figure 26: Snapshots spaced 50 μs apart (red dots) of the z-position of the center of a 50 nm radius matched particle subject to hindered Brownian diffusion for a single realization. The positions were obtained from Brownian dynamic simulation with a time step of 5 μs.

at z-positions beyond $z_c = 100$ nm more than half the time, even occasionally moving beyond the upper boundary of the region Z to sample velocities that exceed those inside the ROI.

This effect is especially evident if tracer particles of radius a are used to measure velocities within a ROI adjacent to wall with the $Z \sim O(a)$ for Δt values greater than the diffusion time scale a^2/D_∞, or the time for a tracer to diffuse over a rms displacement of a. As shown in Section 3.3.2, the velocity obtained from 100 nm tracers over a region 50 nm $\leq z \leq$ 80 nm is 40% larger than that at the geometric center of the region when $\tau = \Delta t/(a^2/D_\infty) = 8$.

4.2.3.1 Prediction of the Velocity Overestimation

The bias due to the non-uniform sampling of the near-wall velocity field by particles subject to asymmetric and hindered Brownian diffusion can be quantified by modeling the 1D diffusion of the particles normal to the wall. In current study, Brownian dynamic simulations based on Langevin equation (Section 2.3) was used to obtain an ensemble of instantaneous z-positions over Δt for a large number of matched particles. A histogram of these z-positions can then be used to determine the probability density function $P(z)$ of a z-position sampled by the matched particles over the Δt for a given ROI. The "true" mean z-position sampled by the matched particle over the time interval Δt is then:

$$\langle \bar{z} \rangle = \int_a^\infty z P(z) dz \tag{18}$$

$P(z)$ depends on five parameters, namely a (the tracer lengthscale), Z (the thickness of the ROI over which velocity is measured), z (the particle's center-wall distance), Δt (the temporal resolution), and D_∞ (the characteristic diffusion coefficient). Dimensional analysis reduces this set of five dimensional parameters to three independent dimensionless groups, namely the dimensionless time interval τ, the thickness of the ROI W and the particle position ξ:

$$\tau = \frac{\Delta t}{a^2/D_\infty}, \qquad W = Z/a, \qquad \xi = z/a \tag{19}$$

Note that the time interval is normalized by a Brownian diffusion time scale.

Simulations were carried out for an ensemble of 10^6 $a = 50$ nm particles subject to hindered Brownian diffusion in quiescent water at $T = 300$ K over time intervals Δt ranging from 0 ms to 6 ms. The initial z-positions of the particles at t_0 were generated to ensure that the tracers were uniformly distributed in the ROI: $1 \leq \xi \leq W$, where $W = 2$. In all cases, the Langevin equation was evaluated numerically over a sequence of constant time steps $\delta t = 1$ μs and the instantaneous particle z-positions were recorded at the end of each time step. The z-positions of the matched particles, which again were those located inside the ROI (*i.e.*,$1 \leq \xi \leq 2$) at $t_0 + \Delta t$, were used to calculate $P(z)$. Since the time step δt used in these simulations is finite, numerical errors can "push" particles through the wall even though $D_\perp = 0$ at the wall. It is therefore assumed that the particles interact with the wall when its center is at $\xi < 1$ via perfectly elastic collision. Simulations for namely inelastic collision with a coefficient of restitution of 0.5 showed that the resultant PDFs were within 1% of those obtained under the assumption of perfectly elastic collision.

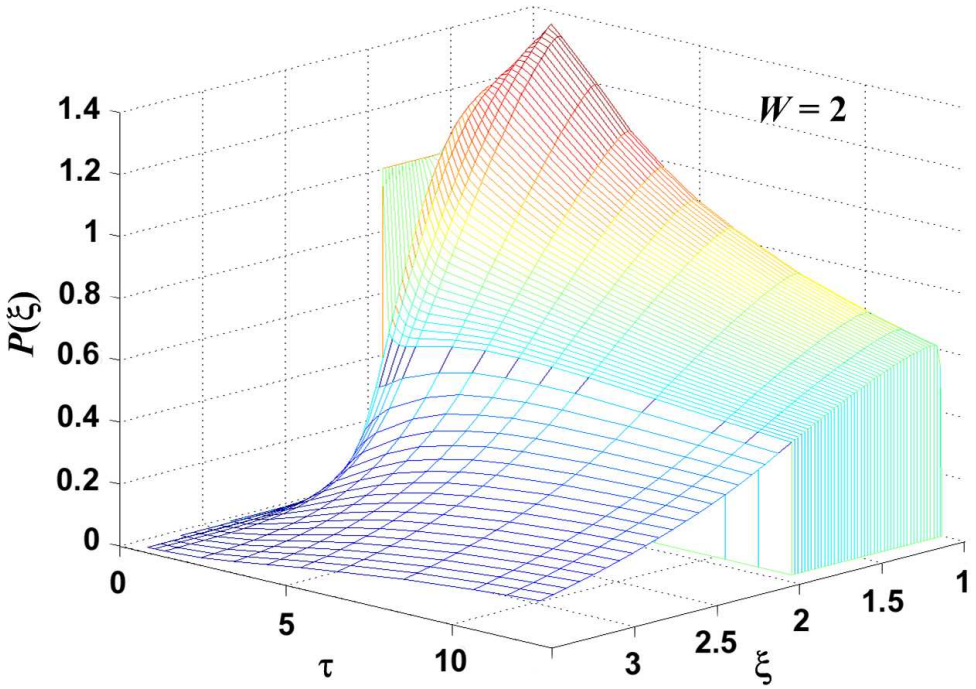

Figure 27: PDFs $P(\xi, \tau)$ obtained for $W = 2$.

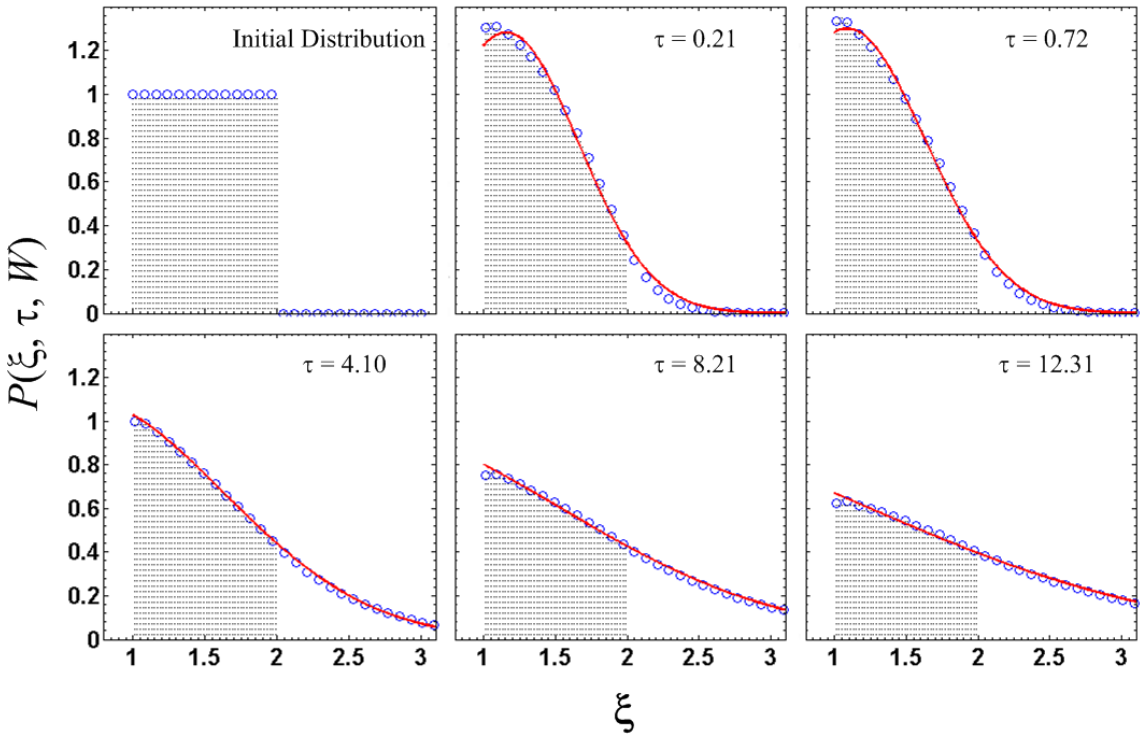

Figure 28: Two-dimensional slices of the PDF shown in the previous Figure at $\tau = 0.21, 0.72, 4.1, 8.21,$ and 12.31. The solid lines represent Gaussian curve fits to these data.

4.2.3.2 Results

Figure 27 shows the PDFs $P(\tau, \xi)$ for $W = 2$ obtained from more than 2×10^5 matched tracers for τ up to 12 (recall that for each case, the simulations are initialized with 10^6 particles uniformly distributed over $1 \leq \xi \leq W$). A few cross-sections of this PDF at $\tau = 0$, 0.2, 0.7, 4.1, 8.2 and 12.3 are plotted in Figure 28. As shown in the Figure, all the tracer particles at $\tau = 0$ are uniformly distributed within the ROI ($1 \leq \xi \leq 2$ denoted by the shaded region), giving a PDF consisting of a step function of unit height. As τ increases, the PDF flattens out, developing a "tail" at $\xi > 2$, as more of the matched particles diffuse out of the ROI. The velocity sampled by these matched particles will therefore correspond to a z-position beyond the geometric center of the ROI or $\xi = 1.5$. For a simple shear flow, the resultant overestimation in velocity can be quantified by the ratio of the mean z-position $\langle\bar{z}\rangle$ sampled by the particle over the time interval (calculated from $P(z)$ using Equation 18) and the geometric center of ROI z_c.

Figure 29, which depicts this ratio $\langle\bar{z}\rangle/z_c$ as a function of the normalized time interval τ, shows that $\langle\bar{z}\rangle > z_c$, corresponding to an overestimation in the velocity, for $\tau > 2$ and the ratio increases almost linearly with τ. Note that for the simulation parameters given here, the Brownian diffusion timescale $a^2/D_\infty \approx 490$ μs; suggesting that velocities will be overestimated for $\Delta t > 1$ ms. For $\tau < 2$, $\langle\bar{z}\rangle/z_c$ is slightly less than 1, corresponding to an "underestimation" in the measured velocity. This may be because the PDFs at these small τ become skewed towards the wall due to hindered Brownian diffusion: as a particle diffuses towards the wall, its mobility (for motion normal to the wall) decreases, implying that tracers closer to the wall move a smaller distance than those farther from the wall. The particles near the wall therefore remain in this region, sampling smaller velocities for a longer period of time.

The choice of dimensionless groups (Equation 19) was verified by generating PDFs for several different sets of experimental parameters (*e.g.*, a, Z, Δt) that gave the same

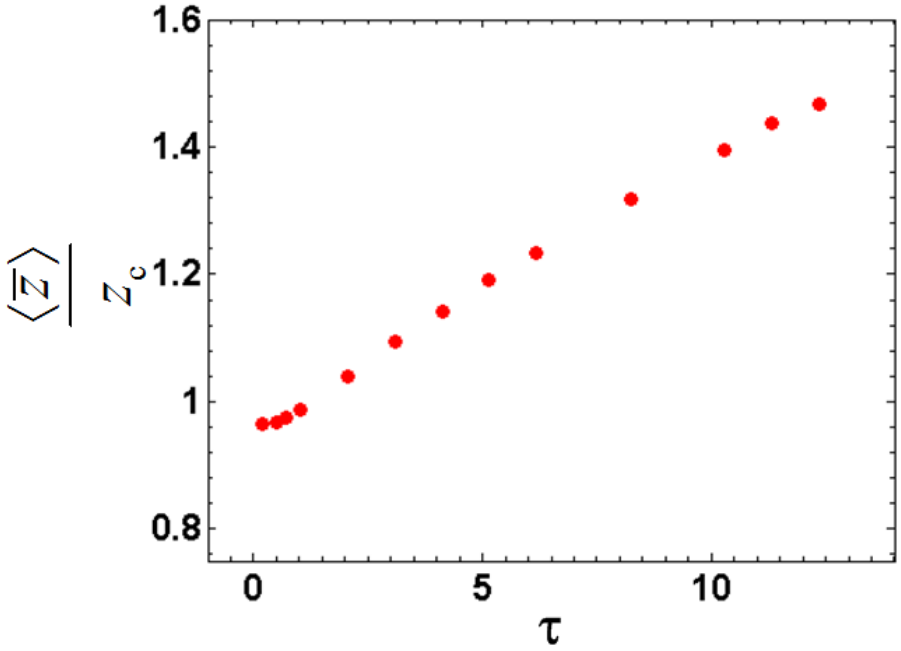

Figure 29: Bias error due to tracers sampling velocities beyond the region of interest in plane Couette flow for $W = 2$ using the PDFs shown in Figure 27.

values of the dimensionless groups W and τ. Figure 30 shows two examples for the experimental parameters listed in Table 2; the PDFs for cases I and II, which give the same (W, τ) are essentially identical; cases III and IV, which give the same (W, τ) (but (W, τ) different from that of cases I and II), also have essentially identical PDFs. These results suggest that the PDF is completely and uniquely specified by these dimensionless groups.

Table 2: Experimental parameters for the PDFs shown in Figure 30.

Case	a [nm]	Z [nm]	Δt [ms]	W	τ
I	100	200	4	2	1.03
II	50	100	0.5	2	1.03
III	100	300	0.5	3	0.13
IV	150	450	1.69	3	0.13

Clearly, the mean z-position sampled by particles subject to near-wall Brownian diffusion can be determined from the experimental parameters (Z, a, Δt, D_∞), or the

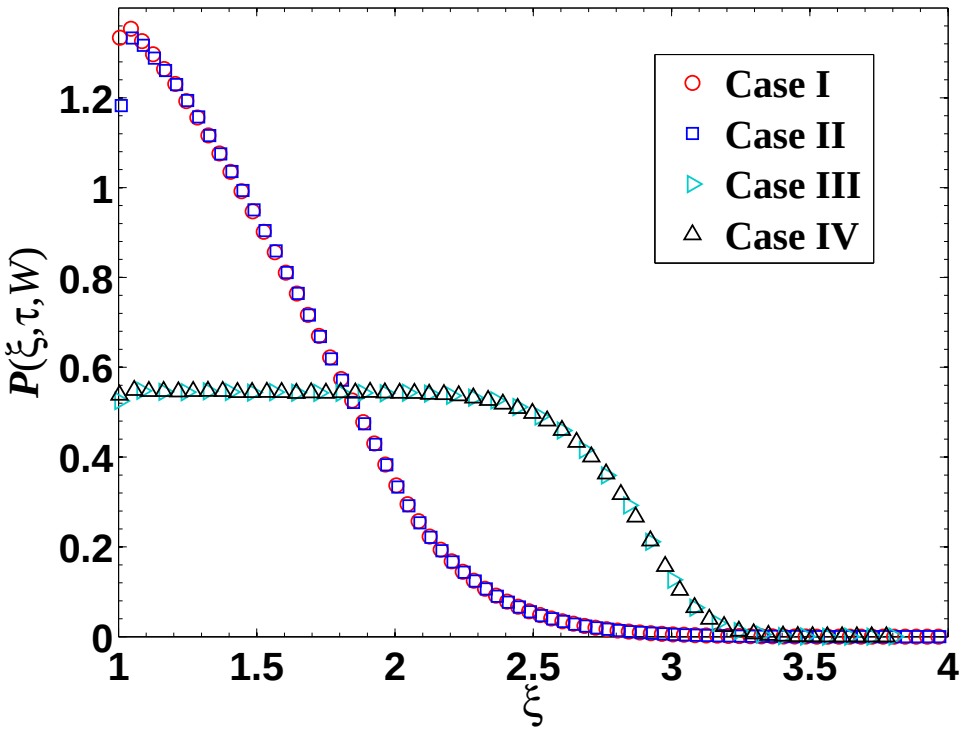

Figure 30: PDFs obtained from four sets of different dimensional experimental parameters (Table 2).

dimensionless groups (W, τ). Obtaining the PDFs with a Langevin-based approach, however, is highly computation incentive. Sadr et al. [156] therefore used a Fokker-Planck-based approach to obtain the PDFs. They defined a new dimensionless time interval:

$$\Omega = \frac{D_\infty \Delta t}{Z^2} \tag{20}$$

where Δt is normalized by the time required for the particle to diffuse across a rms distance corresponding to the thickness of the ROI (*vs.* the particle radius a). As shown in Figure 31, which plots $\langle \bar{z} \rangle / z_c$ as a function of Ω for various values of W, this new dimensionless time interval collapses the data over a wide range of experimental parameters relevant to the experimental studies discussed here (*i.e.*, $Z < 500$ nm; $\Delta t < 10$ ms; $a = 50$ nm). The results indicate that $\langle \bar{z} \rangle / z_c < 1$ for $\Omega < 0.2$ (*i.e.*, either large ROI Z and/or small Δt), corresponding to the skewed PDF observed in

Figure 28. The ratio $\langle\bar{z}\rangle/z_c > 1$ for $\Omega > 0.4$, corresponding to overestimations of the measured velocities; this overestimation then increases monotonically with Ω. The authors proposed a second dimensionless time $\Omega^* = D_\infty \Delta t/(Z + 0.8a)^2$ which further reduced the variation among different datasets for larger Δt. Figure 31b shows $\langle\bar{z}\rangle/z_c$ as function of Ω^* (points), and a curve-fit to these data (line):

$$\frac{\langle\bar{z}\rangle}{z_c} = f(\Omega^*) = 0.21 + 0.79\exp\{-1.72\sqrt{\Omega^*}\} + 0.86\sqrt{\Omega^*} \tag{21}$$

This empirical correlation can then be used to estimate the overestimation in velocity based on the experimental parameters Z, a and Δt with an accuracy of 7%.

Figure 31 shows that the velocity is overestimated by about 100% for $\Omega^* \approx 20$. Practically speaking, such high values of Ω^* in evanescent-wave based near-wall velocity measurements, are associated with smaller tracers (and hence larger D_∞) and/or larger values of Δt; the thickness of the ROI is usually nearly constant because it is determined by the exponential decay of the evanescent wave illumination. The smallest PIV tracers that have been used to date are the colloidal semiconductor crystals known as "quantum dots." Pouya et al. [141] used quantum dots with hydrodynamic diameters of ~ 16 nm to measure velocities within about 300 nm of the wall in Poiseuille flow through a 200 μm deep microchannel. Although the temperature was not reported, an estimation of Ω^* assuming $T = 300$ K gives Ω^* values ranging from 0.7 to 18 for Δt values between 2 ms and 52 ms, respectively. These values correspond to overestimations in the velocity, based on Equation 21, of $10 - 280\%$. The experimental results of Pouya et al. showed that the measured velocities increased significantly with Δt; the velocity obtained at $\Delta t = 52$ ms ($\Omega^* = 18$) nearly doubled that at $\Delta t = 2$ ms ($\Omega^* = 0.7$). The discrepancy between the experimentally observed overestimations and the values predicted by Equation 21 may be due to the additional particle-wall interactions that are not considered in the model.

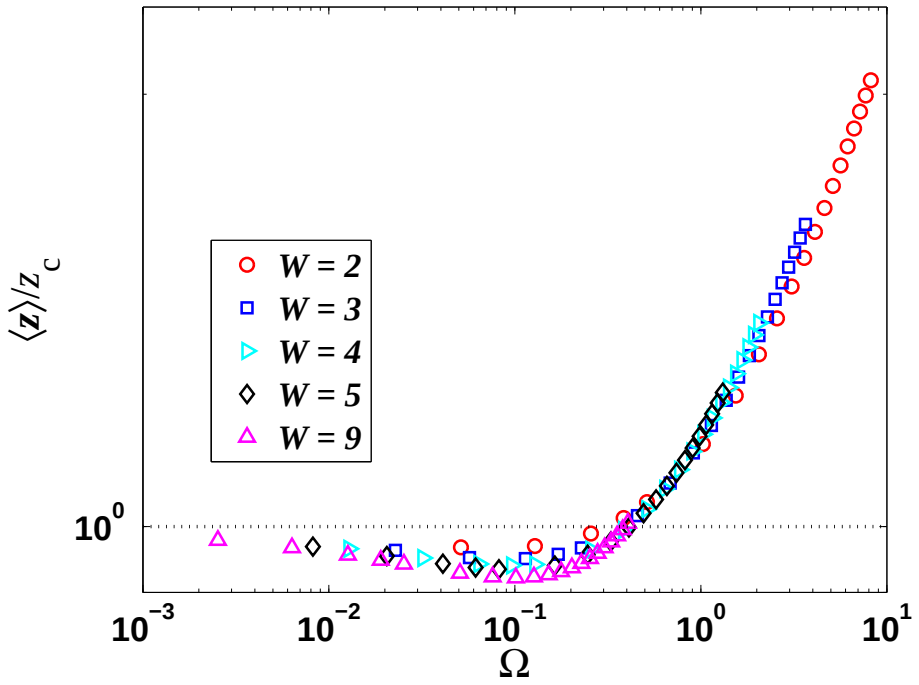

(a)

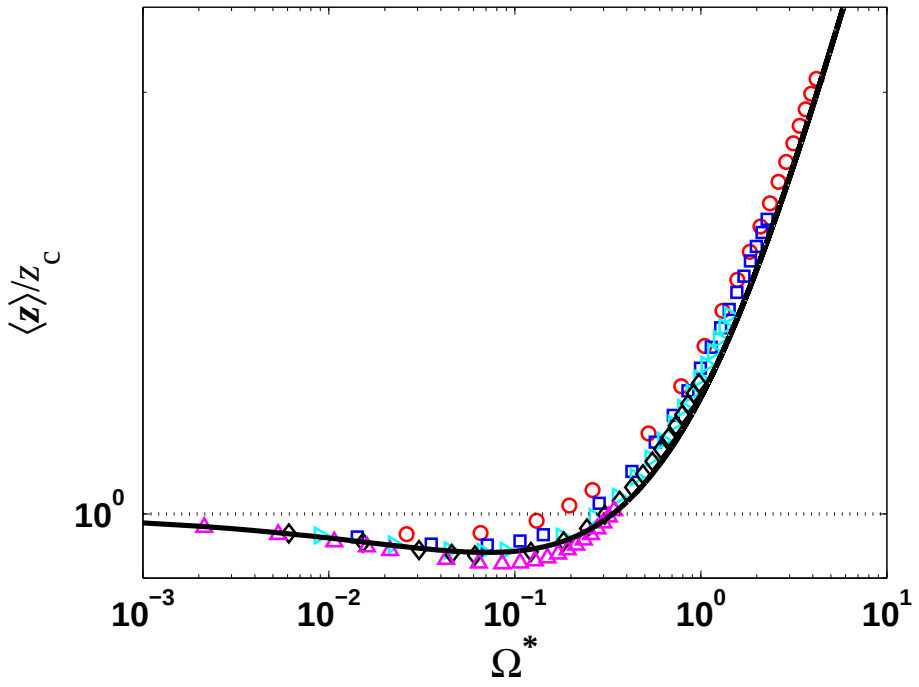

(b)

Figure 31: The overestimations obtained from the PDFs of various W as functions of dimensionless time (a). Ω and (b). Ω^*.

4.3 Summary

The results presented in this chapter show that both the non-uniform nature of evanescent-wave illumination and the asymmetric and hindered Brownian diffusion of the tracers can bias the measured velocities for near-wall tracer based velocimetry techniques. The non-uniform illumination leads in most cases to an underestimation of the velocity obtained with cross-correlation approaches; this underestimation increases as the particle image intensity within one frame varies in a greater range. Unfortunately, this underestimation can not be easily quantified since the correlation function depends on many system-specific parameters, such as the imaging noise, thickness of the illumination volume and the camera gain. Using particle-tracking methods in lieu of cross-correlation-based approaches to determine velocities appears, however, to greatly reduce this bias; the particle-tracking results shown in Figure 20 are within 4% of the expected value. Particle tracking methods are therefore used in the subsequent chapters to determine velocities.

Analyses of the effects of near-wall Brownian diffusion show that the effects of in-plane Brownian diffusion—mainly an increase in the standard deviation of the obtained displacements—can be minimized by averaging either the correlation function or alternatively the actual displacements. The standard deviation in the measured displacements is further increased by particle mismatch due to the particles randomly moving into and out of the "thin" region ($Z \sim O(100\text{ nm})$) illuminated by evanescent wave. Simulations using synthetic images show that increasing the size of the interrogation window or reducing the time interval within the image pair reduces the effects of particle mismatch.

Finally, out-of-plane Brownian diffusion near the wall, which increases the probability that the particle moves away from, *vs.* towards, the wall, can lead to overestimation of near-wall velocities. This overestimation is especially noticeable for tracers imaged over a near-wall ROI with a z-dimension comparable to the tracer diameter

and with time interval between the image pair greater than the time required for a tracer to diffuse an rms distance corresponding to its radius. The effect was quantified by determining the PDF of z-positions sampled by an ensemble of matched particles over a given time interval using Brownian dynamics simulations. The results were used to propose an empirical correlation that relates the overestimation in velocity for a linearly varying velocity profile to the experimental parameters. Although this model is in qualitative agreement with the observed overestimation in measured velocity, it considers only near-wall hindered Brownian diffusion and neglects all other particle-wall interactions (*e.g.* electrostatic forces) which are significant in these experiments, as shown later in the measurements of particle distribution (Chapter 6). It is not clear whether the standard Stokes-Einstein expression for the Brownian diffusion coefficient, which only considers thermal and hydrodynamic forces, or the corrections to the Stokes-Einstein expression that account for the additional hydrodynamic drag induced on the particle by the presence of the wall [19], are valid in this near-wall region. Choi et al. [30] did show that the mobility at a given wall-normal distance of near-wall colloidal particles suspended in an aqueous electrolyte solution increases as the ionic strength of the solution increases. Schumacher and van de Ven [166] have also reported that the unconfined Brownian diffusion coefficient of a particle suspended in a fluid is reduced by as much as 10% when the thickness of the electric double layer surrounding a charged particle (*i.e.*, the Debye length) is comparable to the particle radius.

Despite the limitations of the model, however, clearly reducing the diffusion (*e.g.*, by using bigger tracers or shorter Δt) or increasing the thickness of the ROI would help reduce the bias due to near-wall diffusion. Since the thickness of the illuminated region, which scales with z_{p}, can only be varied over a limited range in our experimental studies, this bias was minimized instead by reducing the time interval within one image pair Δt, which should also help minimize the particle mismatch. The lower

practical limit on this time interval was set by the minimum exposure time required to record particle images with intensities that were above the noise floor and had a high enough SNR to ensure accurate particle-tracking results.

CHAPTER V

EXPERIMENTAL SETUP AND PROCEDURE FOR VALIDATING MNPIV

The results in Chapter 3 have provided the "proof of concept" for MnPIV. In this and the following chapters, the multilayer nano-particle image velocimetry technique is validated for incompressible, steady, fully-developed and creeping Poiseuille flow of water and aqueous sodium tetraborate ($Na_2B_4O_7$) solutions. This chapter details the experimental setup, which consists of the system for creating the flow (Section 5.1) and the optical system to illuminate and image the flow (Section 5.2). The tests of the system was then discussed in Section 5.3. The experimental procedure is presented finally in Section 5.4.

5.1 Creating Poiseuille Flows

This Section describes the microchannels, the apparatus used to generate the pressure-gradient driving the Poiseuille flows, and the procedure for preparing the working fluids.

5.1.1 Microchannels

Steady Poiseuille flows were created inside microchannels (Figure 32) that were fabricated using standard photolithographic, wet chemical-etching and high-temperature bonding techniques [77]. The channel design as shown in Figure 33 was first transferred onto a 1 mm thick fused silica substrate (25 mm $\times$ 50 mm Esco Products Inc. Catalog No. R320110) via an e-beam photomask and UV light after the substrate was coated first by gold, followed by photoresist. The exposed portion of the gold

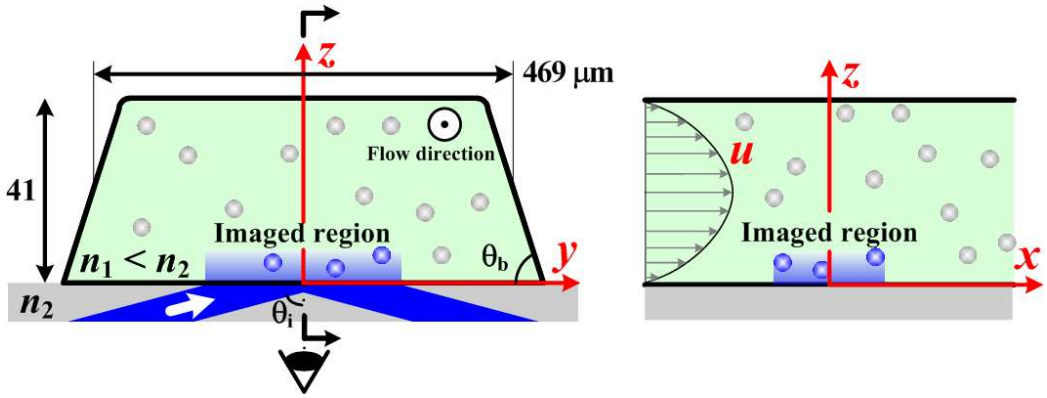

Figure 32: A cross-section of the microchannel showing fluorescent tracers illuminated by the evanescent wave generated at the interface between the fused silica wall and the water flowing through the channel under a constant pressure gradient. Dimensions are given in μm; the flow direction x is out of the page.

film was etched using KI/I_2 and the channel pattern was then etched into the substrate in a dilute stirred HF/NH_4F bath at 50 °C. Because the wet chemical etch in glass is isotropic, the resulting channel has a roughly trapezoidal cross-section of nominal dimensions 41 μm (z) × 469 μm (y) determined using a profilometer before sealing the channel. The y-dimension quoted here refers to width of the channel at the channel half-depth (Figure 32). Two 1 mm-diameter holes were then ultrasonically drilled through the etched substrate at both ends of the channel to create the channel inlet and exit. To form the closed channel networks, the etched substrate and another fused silica "lid" were cleaned, joined and then annealed at about 1100 °C for 5 h. Finally, two pieces of glass tubing (12 mm in length, 4 mm ID and 6 mm OD) were attached to form reservoirs on the etched substrate centered about the 1 mm dimameter holes using optical adhesive (Norland Products Inc. Norland optical adhesive 81).

To calculate the pressure gradient that drives Poiseuille flow, the length of the channel L was measured by imaging portions of the channel using the built-in Bertrand lens of the microscope with a system magnification of 0.51. A total of five image were required to cover the entire channel and these images were then "stitched" together

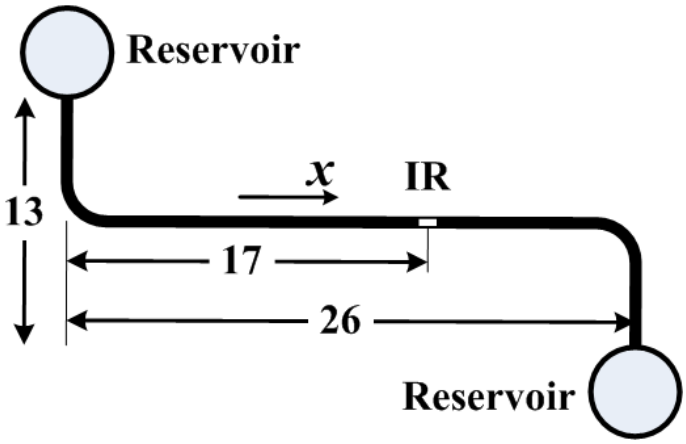

Figure 33: Sketch of the entire microchannel showing the imaged region (IR). Dimensions are given in mm; flow goes from the upper to the lower reservoir along x-direction.

to form a composite image the entire channel (Figure 34). The length L, estimated in pixels from this composite image, was then converted to physical dimensions using the overall system magnification, giving $L = 35.4 \pm 0.27$ mm. The calculation of the measurement uncertainty in L is in Appendix C.

Figure 34: A sample image that was used to measure channel length. The image combines 5 pictures taken with the microscope's built-in Bertrand lens with a magnification of about 0.51×. The measured channel length was 35.4 ± 0.27 mm.

Figure 33 also indicated that the imaged region is about 17 mm, or more than $200D_{\mathrm{h}}$ (the hydraulic diameter of the channel $D_{\mathrm{h}} = 75\ \mu m$), downstream of the bend nearest the inlet to ensure fully-developed flow.

5.1.2 System for Driving the Flow

The pressure gradient driving the Poiseuille flow was hydrostatically generated. The system, as shown in Figure 35, contains a 2L bottle 130 mm in diameter (component 1, Kimax 14607-2000) mounted on a platform that moves along a vertical rail, three pieces of Tygon tubing (component 2 with ID and OD 0.375" and 0.5", respectively, and components 4 and 7, both ID and OD 0.125" and 0.188", respectively), a reducing coupling connector, two T-connectors, and an elbow consisting of a bent piece of glass tubing. The driving pressure was varied by connecting the upstream reservoir of the channel to the bottle and adjusting the height of the bottle by moving the platform up and down along the rail. The downstream reservoir was connected to the elbow to form an exit along the horizontal, ensuring that the free surface at the exit would remain at the same altitude over time. All the elements upstream of the second T-connector (component 6 in Figure 35) were filled with distilled water; tubing element (7) downstream of this T-connector was filled with the working fluid containing fluorescent tracers and served as an extended reservoir. To minimize cross contamination between experiments, this tubing element was replaced by a new piece of tubing before each experiment and filled by a syringe connected to the T-connector (6); this T-connector was also used (after filling) to remove any air bubbles present in the system. The T-connector (5) was connected to a manometer and used to measure the pressure difference between the free surfaces inside the bottle and the elbow at the exit reservoir. The driving pressure gradient is then taken to be the ratio of this measured pressure difference and the channel length L determined as described in Section 5.1.1. Poiseuille flows driven by three different nominal pressure gradients $\Delta P/L = 0.3$, 0.4 and 0.8 Bar/m, corresponding to height differences between the free surfaces of water inside the container and exit reservoir of 0.1, 0.17 and 0.3 m, respectively, were used to validate the technique.

Since the pressure difference is calculated from the measured heights of the free

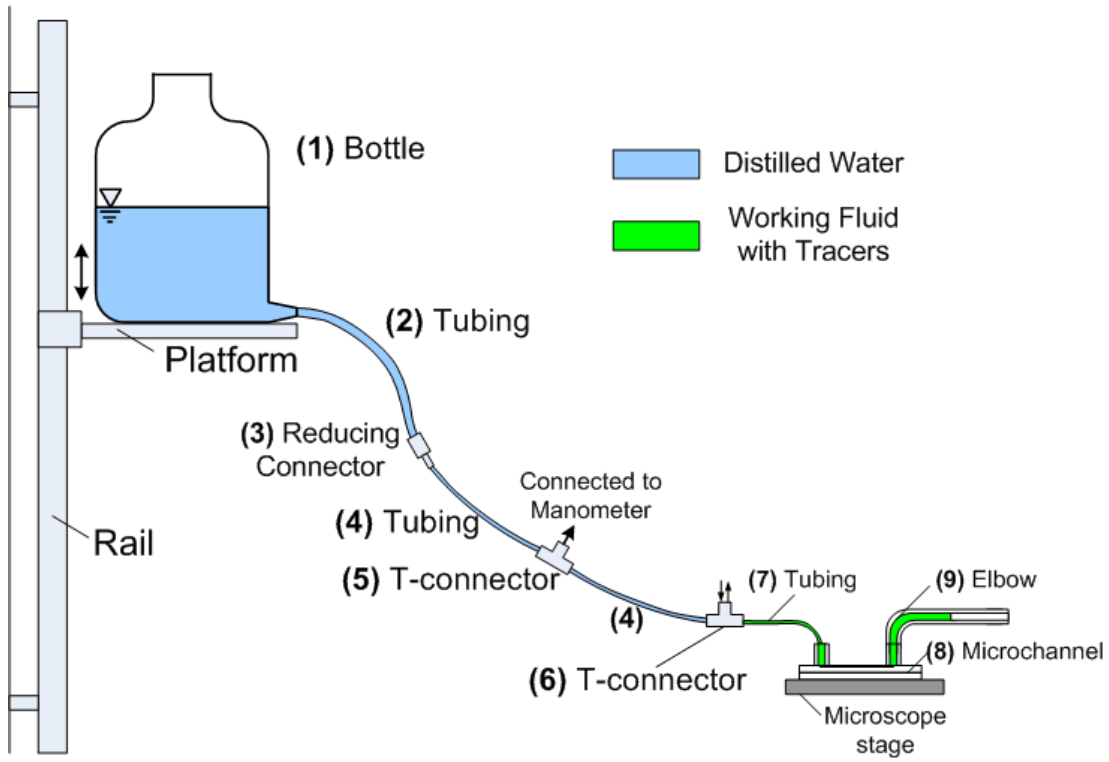

Figure 35: An illustration of the system that generates a pressure difference along the length of the channel to drive the flow.

surface inside the bottle, the major head loss along the flow path (tubing No. 2, 4 and 7 in Figure 35) and minor head losses due to the various components between the bottle and channel inlet should be quantified. The calculation that is detailed in Appendix E shows that the maximum of these head losses is at the order of 1 μm. The effect is therefore considered minimal compared with the height differences between the upstream and downstream free surfaces $O(0.1\text{ m})$.

5.1.3 Preparation of the Working Fluids

Experiments were performed with two different types of working fluids: Nanopure water and sodium tetraborate ($Na_2B_4O_7$) solutions at three different molar concentrations $C = 1$, 10, and 20 mM. The ACS Reagent Grade Nanopure water, with a quoted conductivity less than 0.056 μS/cm, or a resistivity exceeding 18 MΩ·cm, was purchased from Ricca Chemical Company (Catalog No. 9150-32). According to the

manufacturer, the water is first softened, then filtered through an activated carbon filter, processed by reverse osmosis, triply deionized using a mixed bed deionizing filter, irradiated by UV light, and finally filtered through a 0.2 micron membrane filter.

To prepare the sodium tetraborate solutions, the solution at a given concentration C_f is always diluted from an intermediate "stock" solution with a concentration $C_\mathrm{i} \approx 10C_\mathrm{f}$. For example, to make a $C = 1$ mM solution, a mass m_s of decahydrate salt of sodium tetraborate (ACS reagent grade, Acros Organics), was measured using a precision scale (Mettler Toledo type H4 with a resolution of 1 mg) and then dissolved in 25 mL Nanopure water in a disposable beaker, to give a solution with a known concentration C_i which was usually around 10 mM. To obtain a volume v_f of final solution at $C_\mathrm{f} = 1$ mM, a volume $v_\mathrm{i} = C_\mathrm{f}v_\mathrm{f}/C_\mathrm{i}$ of this intermediate solution was measured by and transferred with a 1 mL graduated Serological pipette (Fisher Scientific, 13-676-10G, 1 mL in 0.01 mL increment) to a graduated cylinder (Pyrex Mixing Cylinder 2982-25, 25 mL in 0.2 mL increment). Nanopure water was then added to the cylinder to reach the final volume v_f. The concentration uncertainty of the solution, as calculated in Appendix C, is less than 1.4%.

The solution was then filtered through a PVDF membrane with a pore size of 200 nm using a syringe filter (Whatman Puradisc). The pH values of the solutions were measured to be between 9 and 9.1 for the sodium tetraborate solutions and on average 5.5 for water using a pH meter (Oakton Instrument, pH 11).

For PIV measurements, the working fluid is seeded with fluorescent polystyrene spheres (Invitrogen FluoSpheres f-8888) of radius $a = 50$ nm (with a standard deviation in radius of 6% according to the manufacturer) at a volume fraction of 2×10^{-5} or particle number density $c = 4.4 \times 10^{16}$ m^{-3}. To prepared a seeded solution of v_s [mL], a volume $v_\mathrm{p}[mL]$:

$$v_{\mathrm{p}} = \frac{4\pi a^3 c v_{\mathrm{s}}}{3\phi_{\mathrm{p}}} \tag{22}$$

(assuming monodisperse particles and uniform particle size and distribution in the original suspension) of the original particle suspension with a volume fraction of $\phi_{\mathrm{p}} = 2\%$ was measured and transferred to a glass vial with a 10 μL micro-syringe (Hamilton Gastight 1701) graduated in 0.01 μL increments. An appropriate amount of the solution without particle was then added to the vial to bring the final volume up to v_{s}. To prepare $v_{\mathrm{s}} = 2$ mL of tracer solution at the volume fraction specified above required 2.1 μL of the original particle suspension.

5.2 Optical Setup

The optical setup consists of the illumination and imaging systems. This section discusses the major components of these systems and their characteristics.

5.2.1 Illumination System

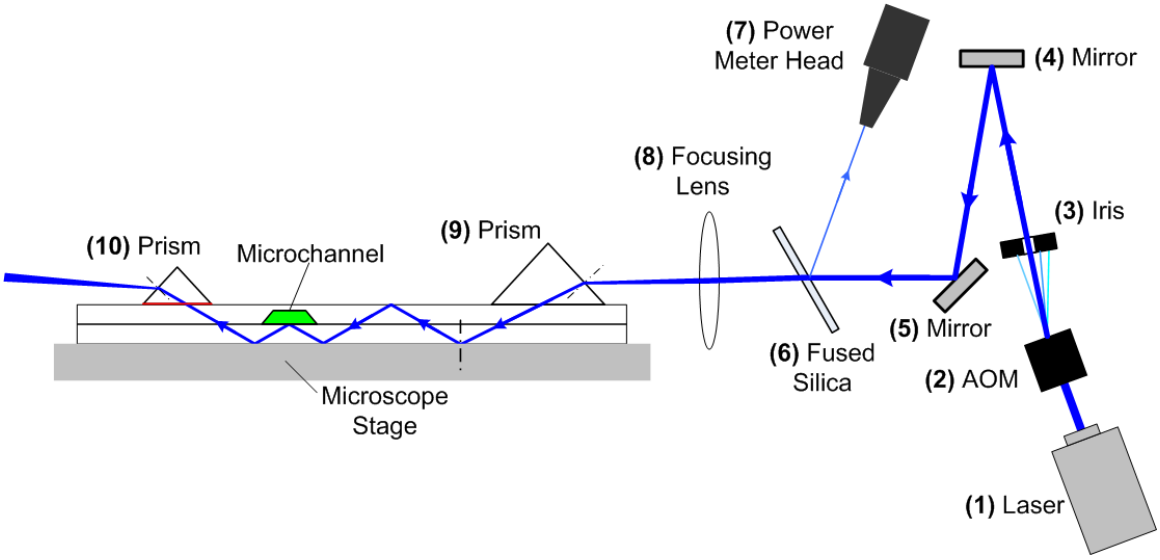

Figure 36: Schematic of the illumination system in the MnPIV setup.

Figure 36 shows a schematic of the illumination system; the major components are listed and specified in Table 3. A $\lambda = 488$ nm beam from a continuous-wave

Table 3: components of the illumination system.

Label	Item	Manufacturer	Model	Other
1	Argon-Ion Laser	Coherent Inc.	Innova 90	5W
2	AOM	IntraAction Corp.	AOM-40	
3	Iris Diaphragm	OptoSigma Corp.	089-0120	
4	Optical Mirror	Melles Griot	02 MPQ 007/001	
5	Optical Mirror	Melles Griot	02 MPQ 007/001	
6	Fused Silica Slide	Esco Product	Q325063	Optical Grade
7	Laser Power Meter	Coherent Inc.	Lasermate Q	
8	Focusing lens	Melles Griot	01 LDX 345	focal length 300 mm
9	Prism	OptoSigma Corp.	055-0190	Fused Silica
10	Prism	OptoSigma Corp.	055-0115	BK-7
-	Immersion oil	Cargille Laboratories	16242	$n = 1.5232$ at $\lambda = 486.1$ nm

(CW) argon-ion laser (Coherent Innova 90) at an output power of about 150 mW was reflected by two mirrors and focused down to a diameter of about 0.5 mm before striking the side of the right-angle prism at an angle of about 6° with respect to the horizontal. To monitor the laser power, a piece of fused silica was inserted to the optical path just before the focusing lens to reflect a portion ($\sim 8\%$) of the laser beam onto a laser power meter (Coherent Lasermate Q). As described subsequently in Section 5.2.2.2, an acousto-optic modulator (AOM) is used to shutter the CW laser to create pulsed illumination.

Upon reaching the air-glass interface of the prism, the laser beam is refracted towards the prism-channel interface, where the prism and channel surfaces are optically coupled by a few drops of immersion oil (Cargille Laboratories Inc. Catalog No. 16242, $n = 1.5232$ at wavelength of 486.1 nm). The beam crosses this interface with at an angle of incidence exceeding the critical angle $\theta_c = 65.6^\circ$ for a fused silica-water interface and propagates inside the two fused silica pieces comprising the channel (*i.e.*, the etched substrate and the lid) via TIRs at either the fused silica-air or fused silica-water interfaces, as shown in Figure 37a. Fused silica was used for all the channel

pieces because of its excellent transmission (about 92% for 400 nm $\leq \lambda \leq$ 600 nm) and extremely low autofluorescence (and hence minimal background image noise). Finally, a second prism is used to guide the laser beam out of the channel piece to minimize the reflections and scattering at the substrate edges.

When the beam is totally internally reflected at the fused silica-water interface (Figure 37a), an evanescent wave is generated which illuminates the particles above the unetched slide that seals the channel (Figure 32). The surface of this unetched slide is the smoothest of the four channel walls with a mean surface roughness of 3 nm according to the manufacturer. Figure 37b shows an imaged TIR spot; the colors denote the intensities normalized by their maximum value. To determine the penetration depth z_{p} of the wave using Equation 5, it is necessary to first determine the angle of incidence θ_{i}. This angle was calculated from the thickness of the sealed microchannel d_{t}, measured to be 1.84 ± 0.011 mm using a caliper (Starrett 120A with a resolution of 0.001 in), and the distance between two adjacent TIR spots d_{s} obtained by imaging the TIR spots with the built-in Bertrand lens of the microscope. To increase contrast of the image, the channel was filled with fluorescein solution and the bottom surface was also processed to become fluorescent after evaporation of fluorescein solution left on the surface. Figure 37c shows a sample image of three successive TIR spots;the dashed lines indicated positions of the side walls of the channel, imaged from underneath the channel. The centers of the imaged TIR spots (labeled in Figure 37c) were determined with a method similar to that discussed in Section 3.2 for locating the particle image center. Finally, the distance d_s, averaged over 10 independent samples, were determined to be 2.56 ± 0.046 mm, giving an angle of incidence of $70.2 \pm 0.3\,^{\circ}$, resulting in a penetration depth of 113 ± 3 nm (Appendix C). In this calculation, the refractive indices of all working fluids are taken to be that of water, giving $n_1 = 1.33$; the refractive index of fused silica $n_2 = 1.46$.

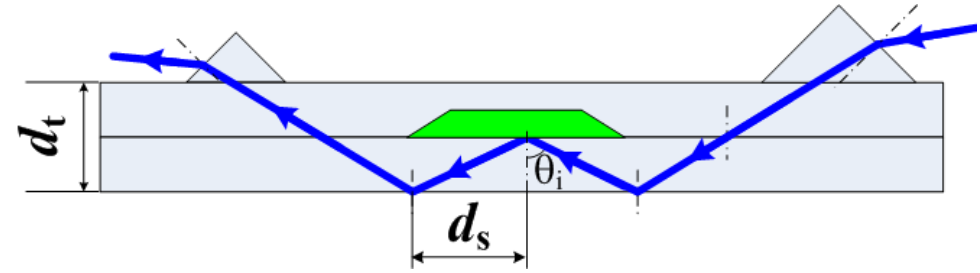

(a)

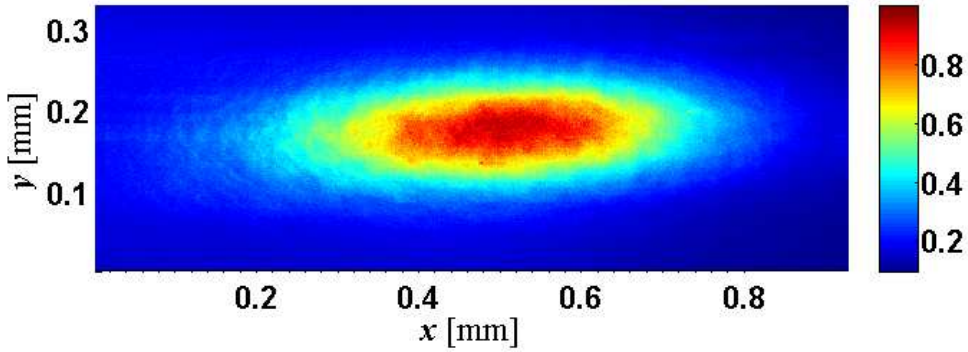

(b)

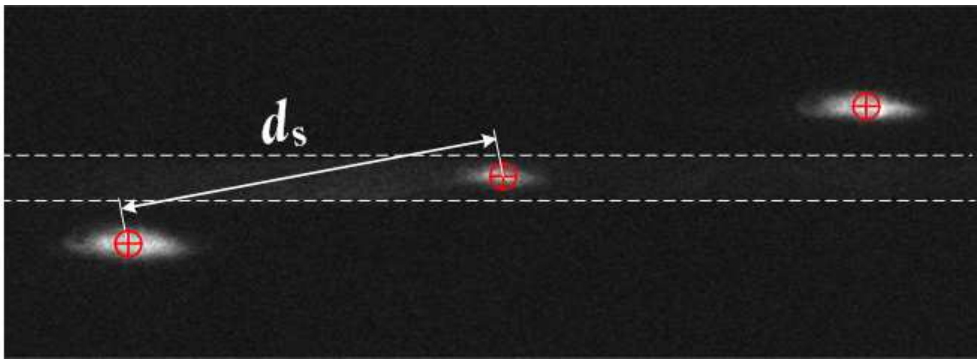

(c)

Figure 37: An expanded view of the illumination system. (a). Illustration of the TIRs of the laser beam inside the microchannel piece, showing the two quantities needed for calculating θ_i. (b). An image of a typical TIR spot; the color scale denotes the intensities within the spot as a fraction of the maximum value. (c). A sample image of the TIR spots for measuring the distance d_s.

5.2.2 Imaging System

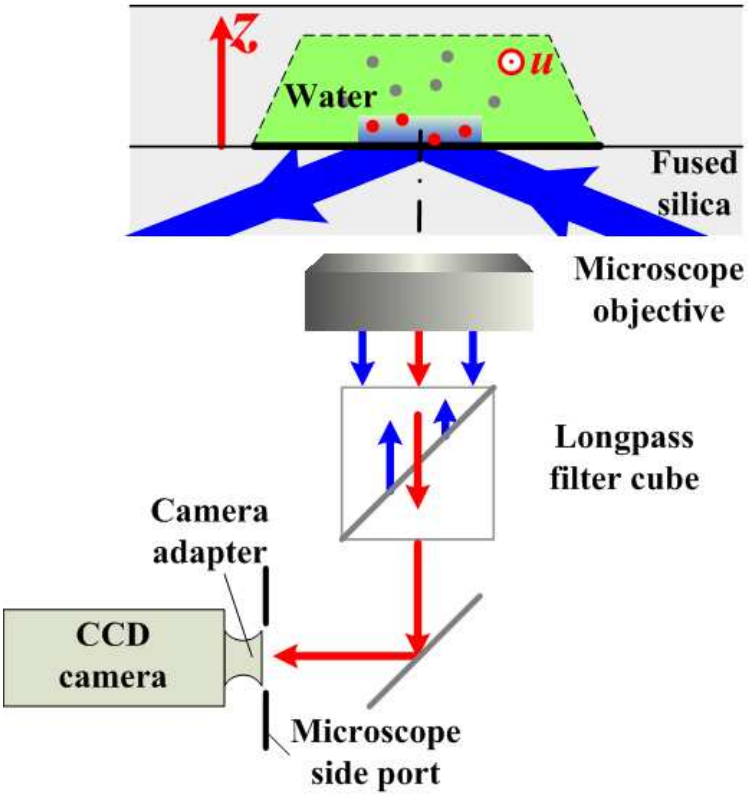

Figure 38: Schematic of the imaging system.

As shown in the schematic of the imaging system given in Figure 38, the fluorescence from the polystyrene tracers excited by the evanescent-wave illumination is imaged by an inverted epifluorescence microscope through a 63× magnification and 0.7 NA objective (Leica PL Fluotar L), then a longpass ($\lambda > 515$ nm) beamsplitter cube (Leica I3) and a 0.5× camera-microscope adaptor onto a CCD camera (Photometrics Cascade 650). As discussed in Section 3.1.1, fluorescent tracers are often used in microscale PIV experiments to increase the signal from the tracers because of the rather weak elastic scattering of these sub-micrometer-sized particles and to distinguish this signal by wavelength filtration from the illumination and elastically scattered light by the tracers and other scatterers (*e.g.*, solid surfaces). The excitation and emission spectra of the tracers labeled with fluorophore Bodipy FL (Invitrogen

f-8888, a = 50 nm) are given in Figure 39. The absorption and emission maxima of these tracers are at 505 nm and 515 nm, respectively. The longpass beamsplitter cube, which only passes the fluorescent emission at wavelengths above the cutoff value of 515 nm and reflects the $\lambda = 488$ nm illumination, ensures that only the fluorescence is imaged by the camera.

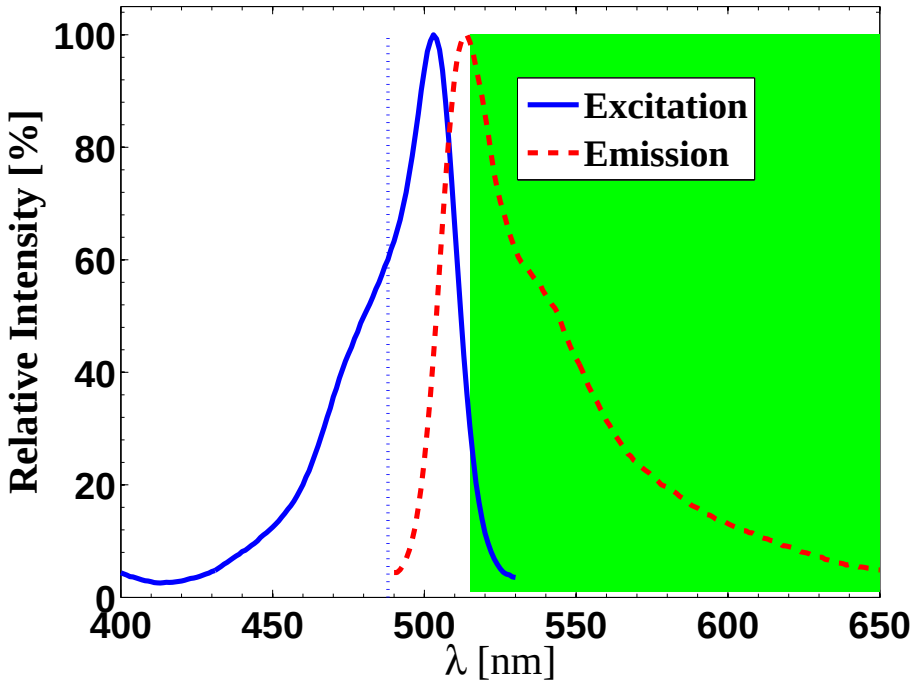

Figure 39: Absorption and emission spectra of the fluorescent particles used in current study. The dotted line denotes the illumination wavelength of 488 nm, while the shaded region represents the wavelength range imaged by the camera.

5.2.2.1 Effective Magnification of the System

The effective magnification of the imaging system should be 31.5, or the product of the magnifications of the camera adaptor, 0.5, and microscope objective, 63. To verify this value, a scale ruled with vertical lines spaced 20 μm apart was imaged by the CCD through the microscope objective and the camera adaptor, as shown in Figure 40a. The column-averaged grayscale values normalized by their maximum value of 255 (for 8-bit images) from the image of Figure 40a are plotted as a function of

the column coordinate x in Figure 40b. A discrete Fourier transform (DFT) of these normalized grayscale values shows a primary peak in spatial frequency at 0.01175 pixel^{-1}. Converting this spatial frequency to the known spatial frequency in physical space of 1/20 μm^{-1}, gives a ratio of 0.2351 μm/pixel or an effective magnification of 31.47 for a physical CCD pixel size of 7.4 μm, a value in excellent agreement with the expected value of 31.5.

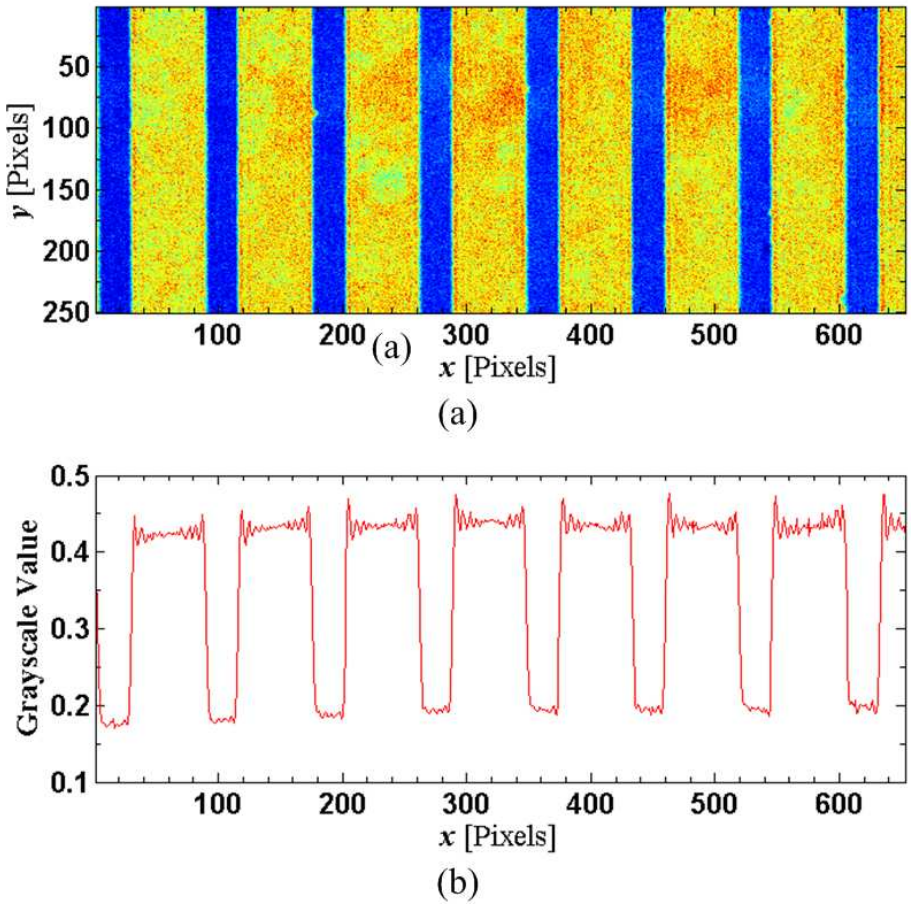

Figure 40: (a). A sample image of the vertically ruled lines spaced 20 μm apart used to measure the effective magnification of the imaging system. (b). Mean grayscale values averaged over the columns of the image.

5.2.2.2 Camera Working Mode

As discussed in Section 4.2, the asymmetric diffusion due to the no-flux boundary condition at the wall can greatly affect near-wall tracer-based velocimetry data. One

way to minimize this effect is to reduce the time interval within a PIV image pair, Δt. In current experiments, this interval is minimized by using the camera in its "overlap" mode, which enables readout of the first image during acquisition of the second image. A sample timing diagram for this mode is shown in Figure 41. When triggered, the CCD sensor is exposed for the specified exposure time (*e.g.*, 1 ms in our experiments) to record the first image. The second image exposure starts immediately after the first image is transferred into a temporary storage area inside the camera, and continues until the first frame is read out to the RAM on the computer.

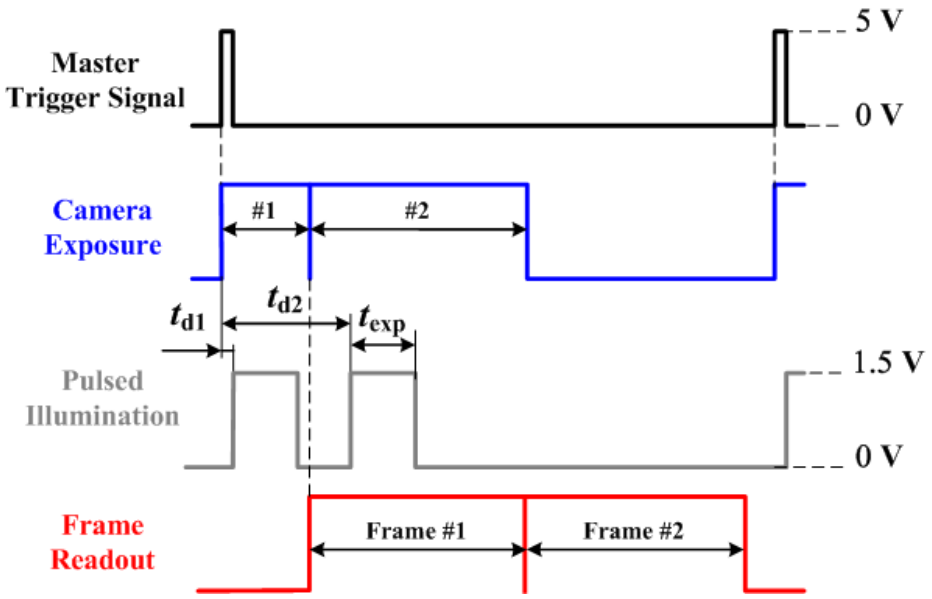

Figure 41: A timing diagram for the Cascade camera in overlap mode.

Since the readout time for the first frame determines the length of the second exposure, there can be a significant difference in the exposure times between the two images. The effective exposure times of the two images were therefore made identical by using two laser pulses of the same power and duration. The pulses were generated by shuttering the CW argon-ion laser with an acousto-optic modulator (AOM). An AOM diffracts light or shifts its frequency by creating a diffraction grating in a material such as flint glass using an acoustic wave in the material to introduce a strain field that changes the index of refraction of the glass in a periodic fashion. As

shown in Figure 42a, in the absence of the acoustic wave, the light beam is undisturbed while in the presence of the acoustic wave, ideally, a Bragg grating is created (if θ_i is equal to the Bragg angle θ_B), and portions of the incident laser beam are transmitted and diffracted at the Bragg angle θ_B above and below the horizontal. The ratio between the power of the diffracted beam and that of the incident one $I_{d,on}/I_{in}$ is primarily determined by the incident acoustic power, which can be controlled through the voltage signal that drives the piezoelectric transducer to create the incident sound wave. The diffracted beam can therefore be switched on and off to generate pulses of laser light by using a square-wave voltage signal. In current study, the AOM was installed on a rotational stage (Melles Griot 07-TRS-503 with a resolution of 15 arc sec) to adjust the angle of incidence of the laser beam θ_i. A square-wave voltage signal between 0 V and 1.5 V, as shown in Figure 41, was used to create the acoustic wave. Experimental measurements showed that at the optimized driving voltage 1.5 V, up to 85% of the incident laser power was coupled into the diffracted beam and the extinction ratio of this beam $I_{d,off}/I_{d,on}$ is well below 0.5%.

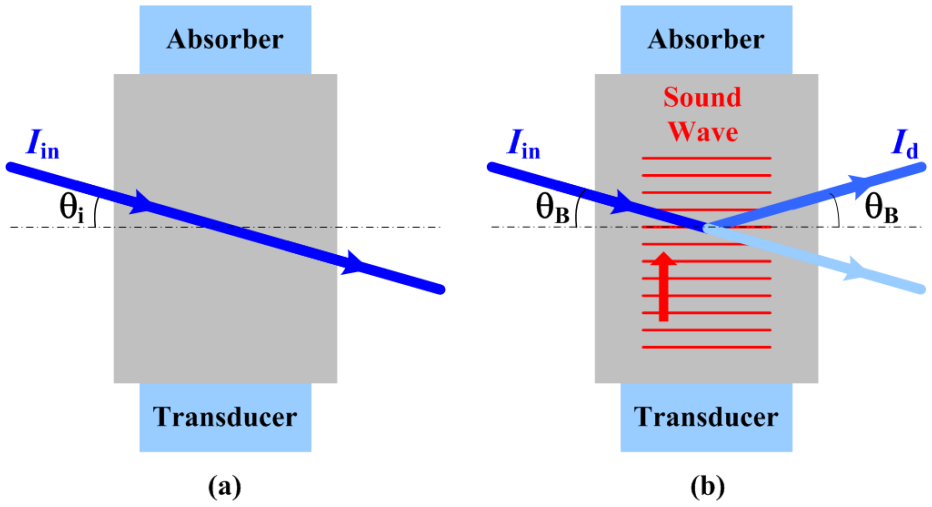

Figure 42: Schematic setup of an acousto-optic modulator. (a) No sound wave; (b) Light beam partially diffracted with a sound wave.

As shown in Figure 41, a master trigger signal at 50 Hz was used to synchronize the camera exposures with the pulsed illumination. Upon receiving a trigger pulse,

the AOM, driven by a square-wave going from 0 V and 1.5 V created by a function generator (Wavetek Datron 195), produces two pulses of nearly identical intensity with a width of 0.8 ms (*i.e.*, the effective exposure time t_{exp} for each image). The camera then records the two images separated by a time interval $t_{\mathrm{d2}} - t_{\mathrm{d1}} = 1.5$ ms using an in-house code written in the digital imaging software V++ (Digital Optics Ltd, version 4.0.7.240). Here, t_{d2} and t_{d1} are the time delays between the rising edge of the master trigger and the rising edges of the two pulses, respectively. Although the system is triggered at 50 Hz, the temporal spacing between successive image pairs increases over the course of a single experimental run from 20 ms to about 220 ms when recording a sequence of 300 image pairs because of limitations in the data transfer rate from the camera to RAM on the computer. In all cases, the total acquisition time was 33 ± 2 s for the 300 image pairs and two such sequences were recorded during each experimental run. Given that this is a steady flow, these variations in the temporal spacing between image pairs should not affect the actual results.

To verify that the time interval Δt is accurately determined by the difference between the delay time $t_{\mathrm{d2}} - t_{\mathrm{d1}}$ of the signal that drives the AOM (Figure 41), image pairs were recorded at different values of t_{d2} (t_{d1} is fixed at 0.1 ms) in the driving signal. Experimental image pairs were obtained for Poiseuille flows of 1 mM sodium tetraborate solutions driven at two different pressure gradients 0.44 and 0.25 Bar/m at 1.6 ms $\leq t_{\mathrm{d2}} \leq$ 7.1 ms, which ideally should give 1.5 ms $\leq \Delta t \leq$ 7 ms. For each case, 600 image pairs were recorded and processed using cross-correlation-based methods to obtain the temporally and spatially averaged displacements, which are plotted in Figure 43 as a function of $t_{\mathrm{d2}} - t_{\mathrm{d1}}$. As expected, the displacements increase linearly with $t_{\mathrm{d2}} - t_{\mathrm{d1}}$ and the linear curve-fits pass the origin, suggesting that the time interval Δt can be effectively controlled by varying the AOM driving function.

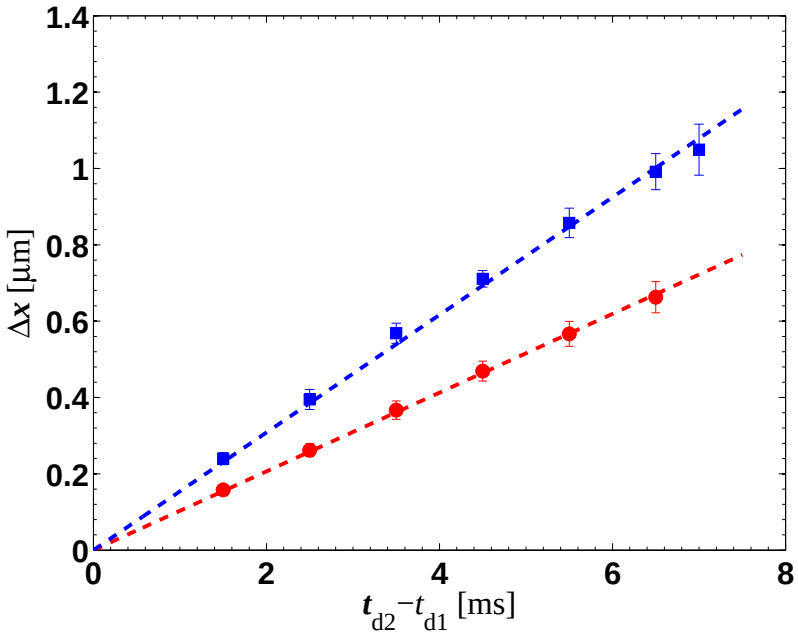

Figure 43: Near-wall displacements obtained from the undivided MnPIV images of Poiseuille flows of 1 mM sodium tetraborate solutions at two different pressure gradients $\Delta P/L = 0.44$ (■) and 0.25 Bar/m (●) as functions of $t_{d2} - t_{d1}$.

5.2.2.3 Camera Linearity Calibration

In MnPIV experiments, the particle image intensity is used to obtain the separation distance between the wall and particle that is illuminated by evanescent wave. Accurately quantifying the relationship between the light intensity incident upon a CCD camera pixel and the resultant grayscale value in the image recorded by the CCD is therefore required for the technique. This section details these calibration experiments.

Images were acquired of the Poiseuille flow of the aqueous solution of the fluorescent dye rhodamine B (RhB) at two different nominal molar concentrations of 20 μM and 50 μM through a rectangular microchannel with cross-section dimensions 24 μm × 50 μm. The relatively low concentrations of RhB ensured that the resultant fluorescence was directly proportional to the intensity of the illumination. The flow was illuminated by evanescent waves generated by the setup described in Section 5.2.1; the imaging system, including the microscope objective and camera settings, was also

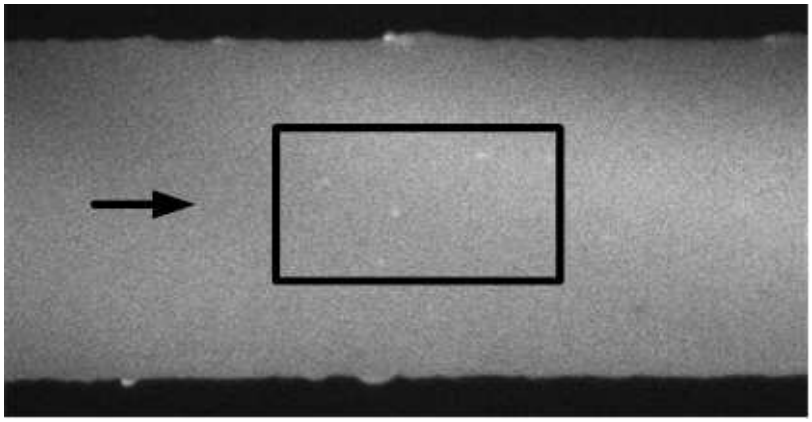

Figure 44: A typical camera calibration image of 20 μM RhB flowing through a rectangular microchannel illuminated by evanescent waves. The grayscale value V at a given laser power P was calculated by averaging the grayscale values for all the pixels inside the rectangular region in the center of the channel.

identical to that used in the experiments detailed in Section 5.2.1. Photobleaching effects [92] were minimized by imaging a flow where the fluorophore exposed to the illumination is continuously refreshed and by using RhB, which is relatively resistant to photobleaching.

The laser output power P, measured by a power meter (Coherent Lasermate Q), ranged from $P_{\min} = 0.01$ W to $P_{\max} = 1.5$ W; at this maximum value, the camera pixels became saturated. A sequence of 100 images was recorded at various intermediate values of P using the same exposure and framing rate as in the experiments of Section 6.1.2.1. This procedure was repeated several times for each value of P. Figure 44 shows a typical calibration image. The mean grayscale value V was calculated over the 100×200 pixel (row×col) region denoted by the rectangle in Figure 44.

The incident laser power and imaged fluorescence grayscale value were normalized (normalized parameters are denoted by the subscript n) as follows:

$$P_{\mathrm{n}} = \frac{P - P_{\min}}{P_{\max} - P_{\min}} \qquad V_{\mathrm{n}} = \frac{V - V_{\mathrm{d}}}{V_{\max} - V_{\mathrm{d}}} \tag{23}$$

The average grayscale value corresponding to the camera dark noise, V_{d}, is calculated from the (rectangular region in the center of) image obtained at $P_{\min}$; in these

calibrations, $V_{\mathrm{d}} \approx 12$ out of a maximum grayscale value of 255.

Figure 45a shows the normalized grayscale value V_{n} as a function of normalized power P_{n} for three different multiplication gains on the Photometrics Cascade 650 CCD camera $G_{\mathrm{M}} = 3070$, 3320 and 3400. Clearly, the response of the CCD at these high gains is highly nonlinear and the deviation from the linear relation $V_{\mathrm{n}} = P_{\mathrm{n}}$ (the dotted line shown in Figure 45a) increases as G_{M} decreases. The resultant functions from curve fitting to these calibration data were used to compensate for camera nonlinearity in the results shown in the rest of this work. Figure 45b and 45c, which compare data obtained using RhB solutions at two different concentrations at $G_{\mathrm{M}} = 3400$ and data obtained using different objective magnifications at $G_{\mathrm{M}} = 3070$, demonstrated that the fluorophore concentration and objective magnification have no effects on the camera response at a given multiplication gain G_{M}, suggesting that this nonlinearity is an inherent property of the camera.

5.3 Calibration of the Experimental System

5.3.1 Flow Simulation

The velocity profile of a Poiseuille flow of water through the microchannel discussed in Section 5.1.1 at a driving pressure gradient $dP/dx = 0.98$ Bar/m was calculated using three different methods: (i) Numerical simulation in FLUENT v6.2 through a trapezoidal channel cross-section with a base angle (between the channel side wall and bottom, as shown in Figure 32) $\theta_{\mathrm{b}} \approx 55^{\circ}$. The value for θ_{b} was estimated from a profilometry scan of an (open) etched channel; (ii) The analytical exact solution for Poiseuille flow in a rectangular duct [134]; and (iii) The classic analytic solution for 2D Poiseuille flow between infinite parallel plates. As shown in Figure 46, the three methods give velocity profiles across the vertical dimension of the channel, z, that are in excellent agreement. This result is hardly surprising since the channel cross-section has an aspect ratio exceeding 11 and the flow in the center of the channel can

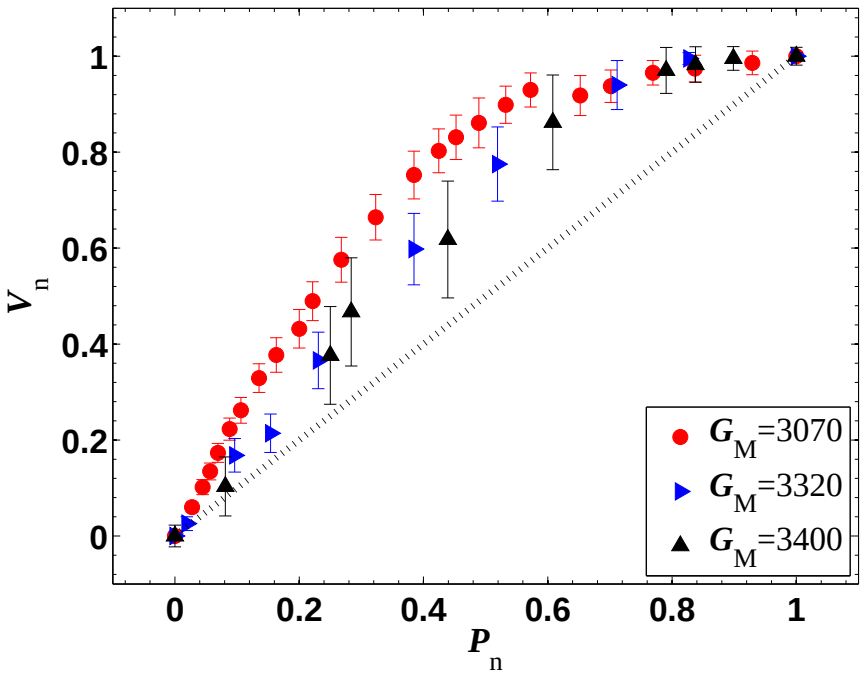

(a)

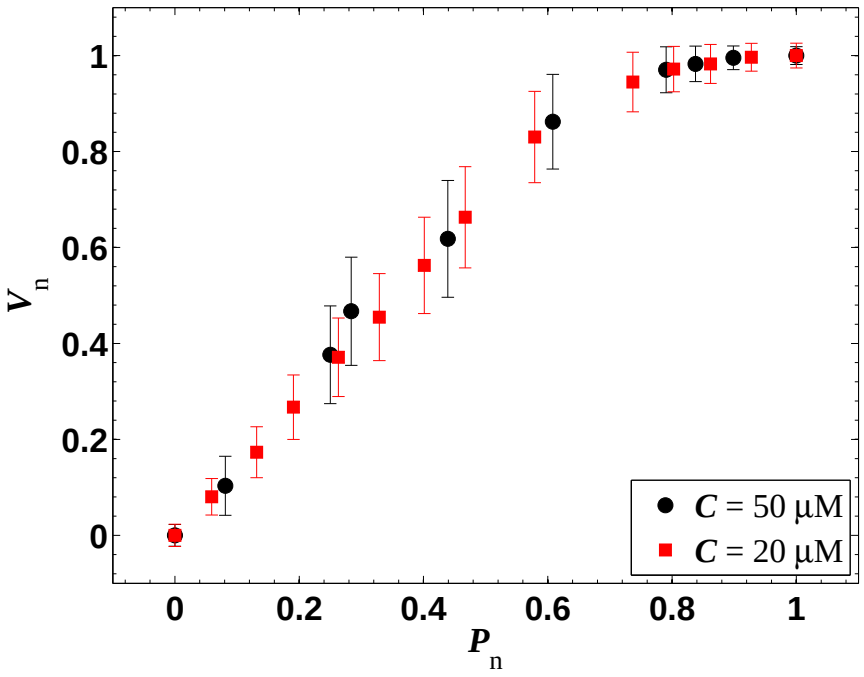

(b)

Figure 45: Camera calibration curve showing normalized laser output power P_{n} as a function of the normalized imaged fluorescence grayscale V_{n} for (a) different camera gains G_{M}; (b) dye solutions of different concentrations at $G_{\mathrm{M}} = 3400$; and (c) different magnifications (*i.e.*, objectives of different magnifications) M at $G_{\mathrm{M}} = 3070$. The errorbars represent the 95% confidence intervals.

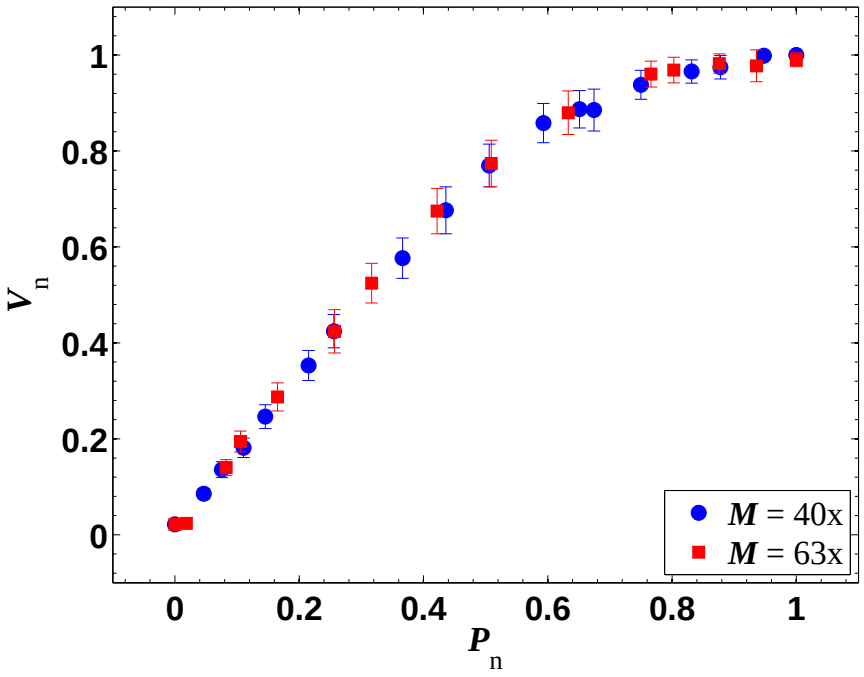

(c)

Figure 45: continued

be considered to be essentially 2D. Given the difficulties in accurately determining the channel cross-section geometry along the entire channel length for chemically wet-etched channels, the exact solution for two-dimensional Poiseuille flow was used to determine the velocity profile $u(z)$ across the channel of z-dimension $H = 41$ μ m:

$$u(z) = \frac{H^2}{2\mu}\frac{\Delta P}{L}\left[\frac{z}{H}\left(1 - \frac{z}{H}\right)\right] \tag{24}$$

Determining $u(z)$ from Equation 24 requires specifying the driving pressure gradient $\Delta P/L$ and the fluid viscosity μ. The pressure gradient was determined as described in Section 5.1.2. The fluid viscosity was taken to be that of water at the temperature of the exit reservoir measured with a K-type thermocouple probe. The temperature was then used to calculate the water viscosity based on a nonlinear least-squares curve-fit of the experimental water viscosity-temperature data [85]:

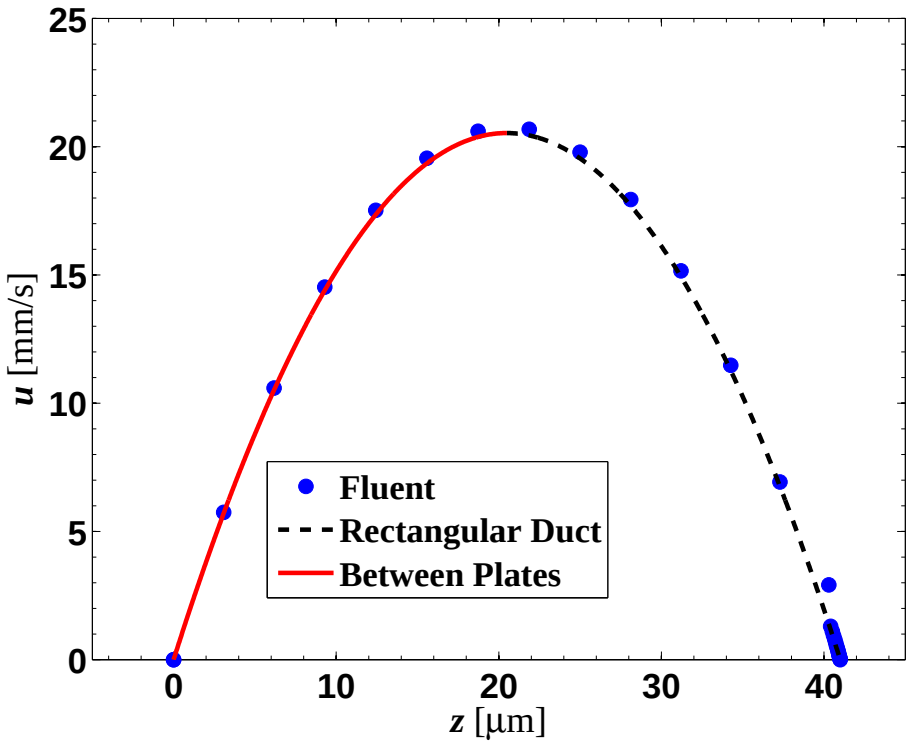

Figure 46: Poiseuille flow velocity profiles across the channel depth z obtained using three different techniques: numerical simulation with FLUENT (•) and analytical solutions of Poiseuille flow through a rectangular duct (dashed line) and between two infinite parallel plates (solid line). Water is driven through a microchannel that is 41 μm deep and 469 μm wide at a pressure gradient of 0.98 Bar/m.

$$\mu = \exp\left(-10.435 - \frac{507.881}{149.39 - T} \right) \tag{25}$$

where T is the absolute temperature in Kelvin. As shown in Table 4, in the range of temperature related to current study, the maximum deviation between the measured values and Equation 25 is less than 1%.

Table 4: Comparison between experimentally measured water viscosities at various temperatures and a curve fitting of the data as shown in Equation 25.

T_c [°C]	μ_m [10^{-4}Pa·s]	μ_f [10^{-4}Pa·s]	$(\mu_m - \mu_f)/\mu_m$ [%]
10	13.002	13.096	-0.72
20	10.054	10.056	-0.02
25	8.940	8.930	0.11
30	7.991	7.992	-0.01
35	7.223	7.202	0.29
40	6.557	6.532	0.38

5.3.2 Comparing Measured and Predicted Poiseuille Velocity Profiles

The system used to drive the flow was tested by comparing the measured Poiseuille velocity profile across the channel depth with the predictions described in Section 5.3.1. Since MnPIV can only measure the flow within about 500 nm of the wall, a μPIV setup is used to obtain tracer velocities at different z-locations across the channel depth.

As shown in Figure 47, light from a halogen lamp passed through a band-pass filter ($450 \leq \lambda \leq 490$ nm) and illuminated the fluorescent particles (Invitrogen, f-8813, $a = 250$ nm) seeded in water. The fluorescence emission was imaged through a 40× and 0.55 NA microscope objective and a long-pass filter ($\lambda \geq 515$ nm) onto the same CCD camera described in Section 5.2.2. For each driving pressure gradient, a sequence of 500 images with a constant frame rate of 156 Hz was taken at each of the 3 different z-locations ($z = 0.25$, 0.5 and $0.75H$, where H is the channel depth) and

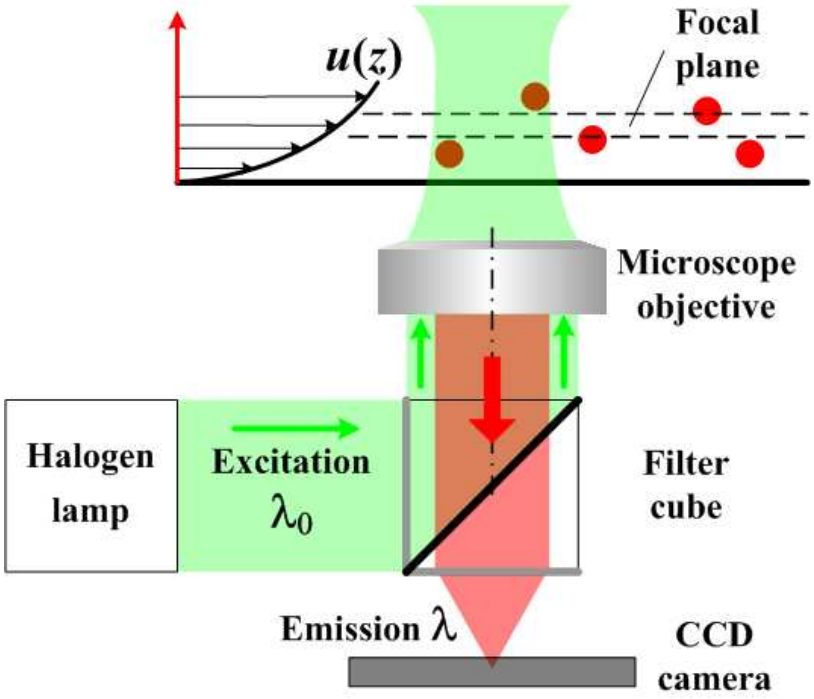

Figure 47: Measurement of the Poiseuille velocity profile along z using a μPIV system.

processed using cross-correlation based method to obtain velocities. Figure 48 shows a sample μPIV image taken at the center of the channel ($z = 0.5H$). Figure 49, which compares the measured velocities (data points) with the predictions (solid lines) at three different driving pressure gradients (1.9, 3.9 and 8.0 kPa/m), shows that the measured and predicted velocities are in reasonable agreement, with a maximum deviation of 6%. The vertical and horizontal error bars in the Figure represent the "depth of correlation" z_{corr} of 2.5 μm, as shown in Table 1 and the 95% confidence intervals for the measured velocities, respectively. Note that only Poiseuille flows of water driven by relatively low pressure gradients ($\leq$ 8 kPa/m) were considered to avoid particle streaks at these high magnifications and high velocities at the channel center over the exposure time of 1 ms (the minimum exposure time of the camera).

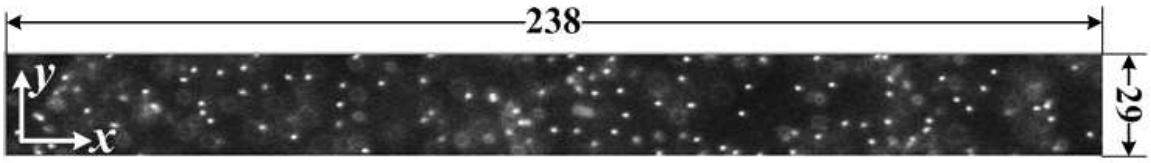

Figure 48: A μPIV image taken at center of the channel ($z = 0.5H$) for $\Delta P/L =$ 1.9 kPa/m. The dimensions are given in micrometers.

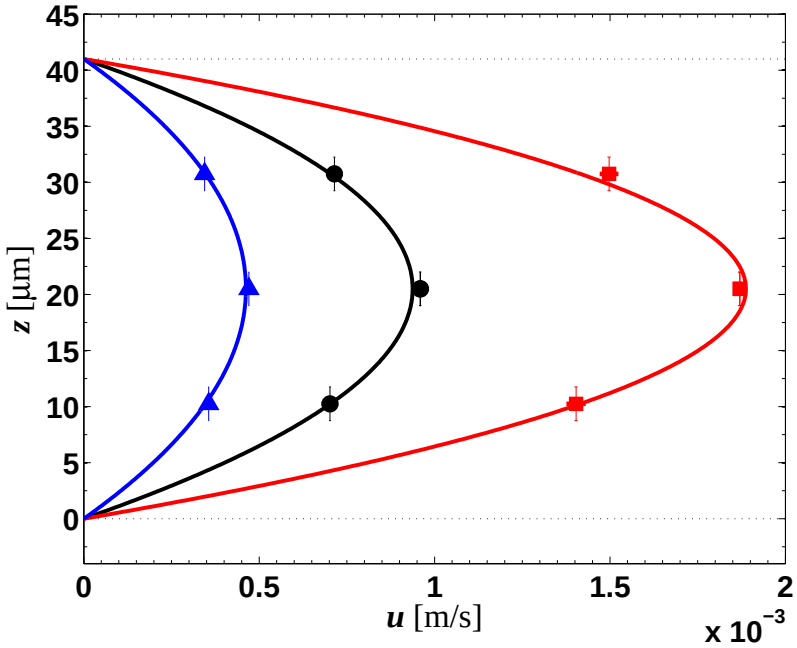

Figure 49: Comparison between experimentally measured Poiseuille velocities (data points) with predictions (solid lines) for three different pressure gradients 1.9 kPa/m (▲), 3.9 kPa/m (●) and 8.0 kPa/m (■). The vertical error bars correspond to the "depth of correlation" $z_{\text{corr}} = 2.5$ μm, as shown in Table 1 and the horizontal error bars represent the 95% confidence interval in the measured velocities. The dotted lines indicated the positions of the top and bottom walls of the microchannel.

5.3.3 Further Tests of the Flow Driving System

Two additional tests were carried out to verify the performance of the flow driving system. First, calibrations were performed to determine the variation in the driving pressure gradient and therefore velocity profile over time at the highest driving pressure gradient, namely 0.8 Bar/m, used in current study. The illumination and imaging systems discussed in Section 5.2 were used to acquire particle images over a course of 60 min. The results, as plotted in Figure 50, show that the measured mean

near-wall velocity varies by less than 3% over the entire period, which is more than double the time for a single MnPIV experimental run. The relatively large diameter (130 mm) of the adjustable-height bottle connected to the upstream reservoir and the constant-height exit at the elbow (*cf.* Figure 35) help to minimize the variation over time in the height difference between the bottle and downstream reservoir free surfaces, and hence $\Delta P/L$.

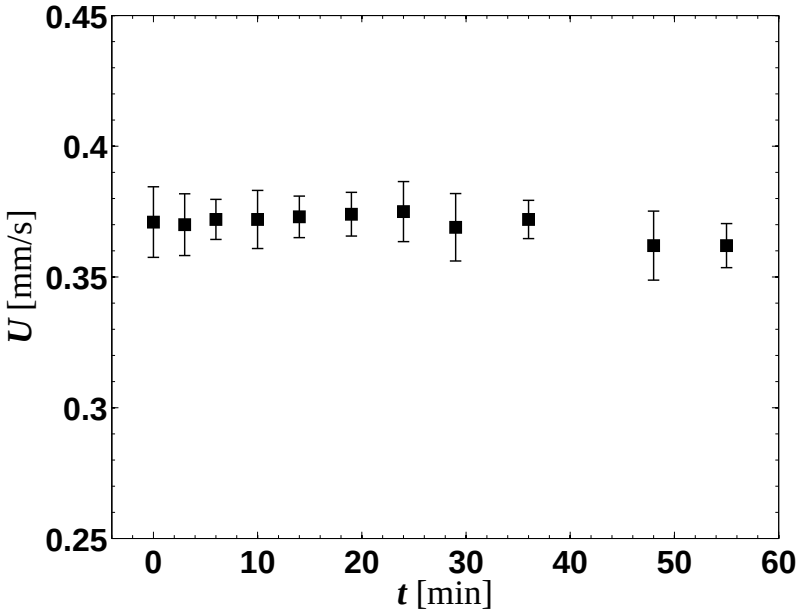

Figure 50: The measured mean near-wall velocity of tracers transported by a Poiseuille flow of water ($\Delta P/L = 0.8$ Bar/m). Each data point was averaged over 300 image pairs and the error bars represent 95% confidence intervals.

Moreover, Equation 24 shows that the velocity of a Poiseuille flow should vary linearly with the driving pressure gradient, which can be used to further test the flow driving system. Experimental images of Poiseuille flows of 1 mM sodium tetraborate solutions driven by pressure gradients ranging from 0.2 Bar/m to 1.2 Bar/m were obtained at $\Delta t = 1.5$ ms with an exposure $t_{\text{exp}} = 0.8$ ms. For each case, 600 image pairs were obtained and processed with correlation-based methods to obtain average velocities. Figure 51 shows these temporally and spatially averaged velocities as a function of $\Delta P/L$ for two sets of images recorded at different camera gains and laser

illumination intensities of the same flow. Although the velocities obtained from the images at lower camera gain and laser power (■) give average velocities lower than those obtained at higher camera gain and laser power (●), both sets of results verify that the velocity increases linearly with the driving pressure gradient.

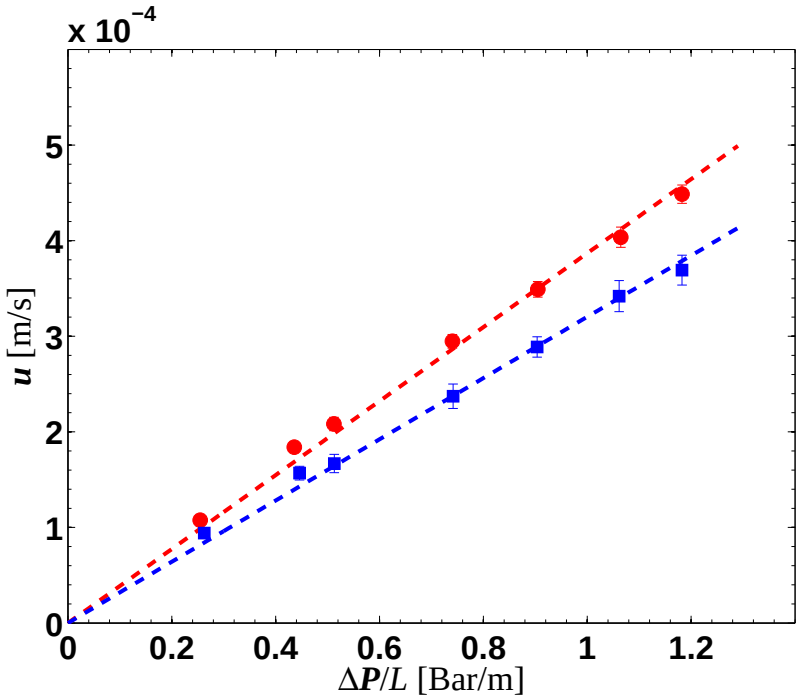

Figure 51: Near-wall velocities obtained from the undivided MnPIV images of Poiseuille flows of 1 mM sodium tetraborate solutions at two different imaging settings (lower (■) and higher (●) camera gain and laser illumination power) as functions of the driving pressure gradients $\Delta P/L$.

5.4 Experimental Procedure

The protocol for each experimental run of MnPIV was as follows:

1. Before each experiment, clean various components of the experimental system. The optical components, such as the two prisms and the outer surface of the channel piece are cleaned with methanol (certified ACS grade, Fisher Scientific A412P-4), then blown dry with compressed air. The devices required for preparing the working fluid (*e.g.*, the graduated cylinder and micro-syringe) are

rinsed by methanol, then water, then acetone (Fisher Scientific A929-4, ACS grade) and finally by Nanopure water.

2. To prepare the aqueous salt solution, 25 mL of the "stock" solution is first prepared and then diluted as described in Section 5.1.3 to the desired concentration. After filtration, about 2-3 mL of the diluted solution is transferred to a vial already containing the appropriate amount of (suspended) tracer particles. This seeded solution is then sonicated for about 20 min and degassed by placing the solution in a vacuum chamber for 5 min at -0.9 Bar. The pH of a sample of the remaining (unseeded) solution is measured.

3. While the seeded solution is being processed, the microchannel is rinsed first with a 1 mM sodium hydroxide solution, followed by water, then acetone, then water. Finally, the microchannel is rinsed by some of the unseeded working fluid, which is driven through the microchannel by applying vacuum to one of the reservoirs. The system driving the flow is then filled with distilled water and inspected for any air bubbles along the flow path. After tubing section (7) (*cf.* Figure 35), is replaced, the driving system is connected to the upstream reservoir of the microchannel while the downstream reservoir is linked to the elbow. A syringe is then used to fill tubing section (7) and the channel with the sonicated seeded solution. After the syringe is disconnected from the T-connector (component 6 in Figure 35), the tubing immediately upstream the T-connector is inspected for air bubbles, which are removed as required via the syringe port of the T-connector by applying an upstream hydrostatic pressure.

4. The microchannel is placed on the microscope stage with the imaged region (typically about 17 mm downstream the bend nearest the upstream reservoir) roughly aligned with the microscope objective. The two prisms are then coupled to the channel substrate surface using a small amount of immersion oil. The

laser beam is adjusted so that the evanescent wave "spot" generated by TIR is incident upon the center of the cross-section of the channel at the lid-liquid interface and is aligned with the center of the microscope objective. The position of the evanescent wave "spot" is adjusted by varying the angle of incidence of the laser beam on the prism by using the adjustment knobs on the rear of the mount for the mirror closest to the focusing lens (component 5 in Figure 36). Finally, the measurement head of the laser power meter (component 7 in Figure 36) is aligned with the reference beam reflected off the piece of fused silica (component 6 in Figure 36) to monitor the illumination power over the course of the experiment.

5. For each experiment, the flow is driven by the pressure gradient for several minutes before two sequences of 300 image pair are acquired as detailed in Section 5.2.2.2. Before and after each experimental run, the pressure different between the free surfaces in the bottle and the bent glass tubing is measured with the manometer and the temperature of the fluid at the channel exit is measured with the thermocouple.

CHAPTER VI

TEST MNPIV WITH EXPERIMENTAL IMAGES

This chapter describes the validation of the MnPIV technique using actual images of fluorescent 100 nm diameter polystyrene tracers convected by a flow. Section 6.1 details calibration experiments to determine how the image intensity of a particle illuminated by evanescent waves varies with its distance normal to and measured from the wall. The image processing procedure is presented in Section 6.2. Finally, the measured velocities and velocity gradients are compared in Section 6.3 with theoretical predictions of the velocity field for Poiseuille flows between two parallel plates based on the experimentally determined pressure drop per unit length $\Delta P/L$ and the fluid viscosity μ.

6.1 Image Intensity of Particles Illuminated by Evanescent Waves

The evaluation of MnPIV using synthetic images have shown that one major challenge in applying MnPIV to real images is accurately correlating the image intensity of a particle illuminated by evanescent waves with its distance from the wall. Yet this correlation is required to establish criteria for dividing particle images into different sublayers corresponding to different ranges of z. This section briefly summarizes theoretical studies on this topic, then describes experimental calibrations using two different methods for determining the relationship between particle image intensity and wall-normal distance.

6.1.1 Modeling the Fluorescence from a Colloidal Particle Illuminated by Evanescent Waves

There have been numerous analytical and numerical studies of the elastic and inelastic scattering by thin films and particles illuminated by evanescent waves. Gingell et al. [55], solved Maxwell's equations to model the fluorescence intensity from an aqueous fluorophore solution sandwiched between a glass plate and a cell membrane illuminated by evanescent wave created at the interface between the glass and the fluorophore solution. They showed that the distance between the glass and the cell membrane, therefore the thickness of the layer of fluorophore solution, can be related to the intensity of the fluorescence emitted by the solution. Heavens and Gingell [62] extended this model and used it to determine the thickness of thin MgF_2 films sandwiched between a dielectric surface (*e.g.*, glass) and a fluorescent medium. Lee et al. [99] modeled the angular distribution of the fluorescence from thick ($t_f \gg z_p$ films of fluorophore solutions excited by evanescent waves using Fresnel theory and experimentally validated their model predictions.

Extending these models from films to fluorescent monodisperse particles suspended in a fluid with a different refractive index is complicated, however, by the refractive-index mismatch at the particle-fluid interface. Chew et al. [26] (referred to hereafter as CMK76) performed the first (to our knowledge) analysis of the inelastic scattering of a single fluorophore molecule embedded inside a dielectric particle, excited by plane (non-evanescent) waves. In their study, the inelastic scattering was determined by first modeling the fluorescence inside the particle as an induced dipole with a moment proportional to the electromagnetic field inside the particle due to the elastic scattering of the plane wave by the particle. The fluorescent field outside the particle is then obtained by applying Maxwell's boundary conditions at the particle-fluid interface. The same group of authors later extended this work to model the elastic scattering of evanescent waves by dielectric particles [27] (referred to hereafter

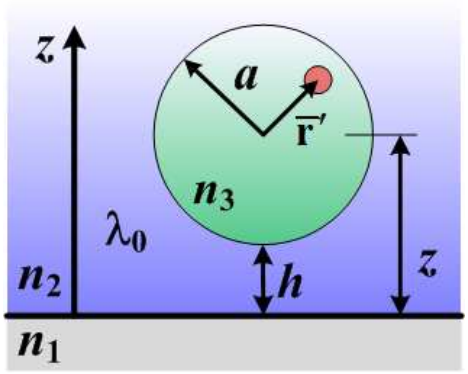

Figure 52: A fluorophore molecule inside a particle of radius a illuminated by evanescent waves.

as CWK79). Their results show although the intensity of the scattered wave is a complicated function of direction, the intensity in any given direction decays exponentially with the separation distance between the particle and wall. In both of these studies, the multiple reflections between the particle and plate where the evanescent wave is generated are neglected. Prieve and Walz [146] proposed a ray tracing model based on geometric optics principles to study scattering of evanescent wave by spherical particles that are large compared to the illumination wavelength. Their results predicted that the intensity of the elastically scattered light decays exponentially with the separation distance between the particle center and wall, and verified their model for 7-30 μm non-fluorescent particles illuminated by evanescent waves. Note that multiple reflection both inside the particle and between the particle and plate were considered in this model.

The fluorescence intensity emitted by a particle of radius a illuminated by evanescent waves was modeled by substituting the transmitted electromagnetic field inside the particle due to the elastic scattering of evanescent wave (derived in CWK79) into the formulation of the approach in CMK76. For simplicity, the model assumes that:

- there is only one fluorophore molecule inside the particle;
- the particle does not disturb the evanescent wave field; and

- re-scattering, or multiple scattering interactions between the particle, the fluid, and the interface, are negligible.

As defined in Figure 52, the fluorophore molecule is located at $\overline{\mathbf{r}}'$ (measured from the particle center), the particle is centered at a distance z from the interface, and the refractive indices of the solid (*i.e.*, the more optically dense medium), the fluid surrounding the particle (*i.e.*, the less optically dense medium) and the particle itself are denoted by n_1, n_2, and n_3, respectively, where $n_1 > n_2$. The particle and the surrounding fluid are illuminated by evanescent waves of wavelength λ_0 with an intensity that decays exponentially with distance normal to the interface.

The incident evanescent wave is assumed to be first elastically scattered by the particle. The resultant refracted light which is transmitted into the particle, then excites the fluorophore. The Stokes-shifted fluorescent emission by the fluorophore molecule is represented by a dipole, whose moment is defined as:

$$\overline{\mathbf{p}'} = \alpha_{\mathrm{p}} \overline{\mathbf{E}}_{\mathrm{ins}} \tag{26}$$

where, α_{p} is the polarizability, and $\overline{\mathbf{E}}_{\mathrm{ins}}$ is the refracted wave that is transmitted into the particle at the incident frequency due to the elastic scattering of the incident wave by the particle. This electric field for the case where the particle is illuminated by evanescent wave has been determined by CWK79 and was substituted into Equation 26 to obtain the fluorescence inside the particle due to evanescent-wave illumination. Although the incident waves in our case are evanescent (*vs.* the plane waves considered by CMK76), the electromagnetic fields of the resultant fluorescence inside and outside the particle can still be represented as an infinite series expansion in vector spherical harmonic functions, and hence have the same type of solutions (*cf.* Equations 1 and 2 in CMK76). The only difference between the result presented here and that of CMK76 is that the dipole moment $\overline{\mathbf{p}'}$ in our case has an extra term compared with that in CMK76 $\overline{\mathbf{p}}$:

$$\overline{\mathbf{p}'} = \overline{\mathbf{p}} \exp\left\{ -\frac{z}{2z_{\mathrm{p}}} \right\} \tag{27}$$

which was derived by comparing the $\overline{\mathbf{E}}_{\mathrm{ins}}$ (Equations 10, 11, and 12 in CWK79 for the elastic scattering of evanescent waves) to that of plane wave in CMK76 (Equations B7, B8, B15 and B16 in CMK76). Here, z_{p} is the $1/e$ intensity-based penetration depth of the evanescent-wave illumination.

The fluorescent emission transmitted outside the particle is then determined from this dipole moment by applying the boundary condition that the electromagnetic field is continuous across the particle-fluid interface. Due to the complexity of the result, analytical integration can only be done in a few special cases, for example, when the particles are much smaller than the illumination wavelength. In this case, the total power radiated by the lower half of the particle is derived in Equation 28 following the calculation in CMK76.

$$\begin{aligned}
\mathbb{P} &= \frac{3\omega^4 n_3^2 |\overline{\mathbf{p}'}|^2}{2c_{\mathrm{l}}^3(n_3^2 + 2\mu_{\mathrm{p}})} = \frac{3\omega^4 n_3^2 |\overline{\mathbf{p}}|^2}{2c_{\mathrm{l}}^3(n_3^2 + 2\mu_{\mathrm{p}})} \exp\left\{ -\frac{z}{z_p} \right\} \\
&= \underbrace{\frac{3\omega^4 n_3^2 |\overline{\mathbf{p}}|^2}{2c_{\mathrm{l}}^3(n_3^2 + 2\mu_{\mathrm{p}})} \exp\left\{ -\frac{a}{z_{\mathrm{p}}} \right\}}_{\mathbb{P}_0} \exp\left\{ -\frac{h}{z_p} \right\} \\
&= \mathbb{P}_0 \exp\left\{ -\frac{h}{z_p} \right\}
\end{aligned} \tag{28}$$

Here, ω is the (angular) frequency of the fluorescence, μ_{p} is the magnetic permeability of the particle and c_{l} is the speed of light in vacuum. The power therefore decays exponentially with h, or the distance measured from the lower particle edge to the interface. Note that because $a \ll \lambda$ and z_{p} is usually comparable in magnitude to λ, the term $\exp(-a/z_{\mathrm{p}}) \approx 1$.

6.1.2 Calibration Experiments

Several previous experimental studies [70, 117, 146] have shown the image intensity I_{p} of particles illuminated by evanescent waves of diameters a ranging from 100 nm to

15 μm decays exponentially with the distance between the particle and the refractive-index interface that creates the evanescent wave. The characteristic length scale of this decay is equal to z_p, the penetration depth of the evanescent-wave illumination, as shown in Equation 29.

$$I_p = I_p^0 \exp\left(-\frac{h}{z_p}\right) \tag{29}$$

where I_p^0 is the image intensity of a particle at the interface. The next sections describe calibration experiments using two different approaches to control the separation distance between the particle and the wall.

6.1.2.1 Method I: Using Magnesium Fluoride Films to Control Particle-Wall Separation

The approach described here was originally used by Prieve and Walz [146] to show that the intensity of the elastically scattered light by $7-30$ μm particles illuminated by evanescent waves decays exponentially with their particle-wall separation distance, with a length scale identical to the intensity-based penetration depth of the illumination. Essentially, the fluorescent particles, suspended in a liquid, were attached by electrostatic forces to a thin coating of magnesium fluoride (MgF_2) on a BK-7 glass substrate (Figure 53). The refractive index of the liquid was matched to that of the MgF_2 so that TIR (and generation of evanescent waves) occurs only at the glass-MgF_2 interface. The particle edge-refractive interface separation distance h is then varied by changing the thickness of the film.

In the calibrations performed for this thesis, five polished BK-7 glass slides (OPCO Laboratory Inc., Fitchburg, MA, USA) with a refractive index $n_{\text{BK-7}} = 1.5222$[1], were coated in the center with layers of MgF_2 ($n_{MgF_2} = 1.3861$) of thicknesses 50, 100, 150, 200 and 300 nm, as shown in Figure 54. These five coated slides plus a polished but

[1]All the refractive indices given in this chapter are for an illumination wavelength of 488 nm

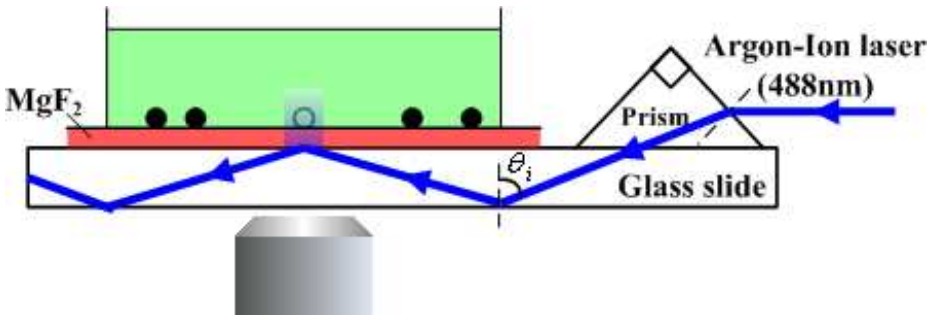

Figure 53: Experimental setup for particle image intensity calibrations.

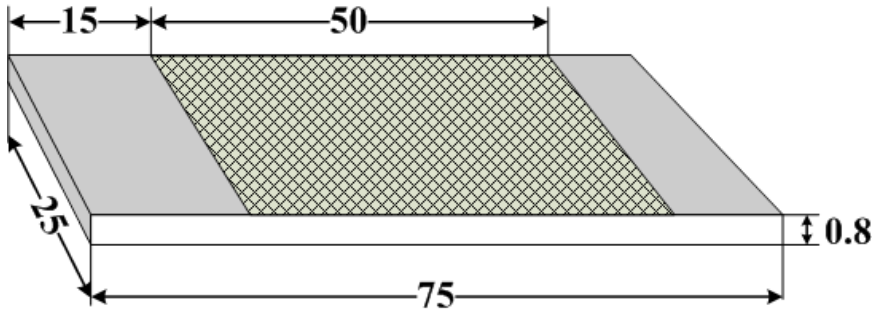

Figure 54: Schematic of the coated BK-7 slide. The patterned region is coated with MgF_2. All dimensions here are given in millimeters.

uncoated slide then give six different particle-glass separation distances h = 0, 50, 100, 150, 200 and 300 nm. A U-shaped polycarbonate enclosure was attached onto the slide to contain the working fluid, which consisted of a solution of about 10 mM $CaCl_2$ (ACS grade, EMD Chemicals) in reagent-grade 1-propanol with a refractive index n_{prop} = 1.3852 (Burdick & Jackson, Honeywell International). After being filtered with a 200 nm pore size syringe filter (Whatman PVDF), the working fluid is seeded with a = 250 nm polystyrene spheres (Invitrogen, f-8813) at a volume fraction of about 10^{-5}. These spheres have the same excitation and emission spectra as those described in Section 5.2.2. The divalent calcium cations in the solution suppress the electrical double layers at the (negatively charged) particle and glass surfaces so that the polystyrene particles become electrostatically attached to the MgF_2 surface. To minimize particle aggregation, the suspension was sonicated for about 10 min using a sonicator (VC600, Sonics & Materials, Inc. Danbury, CT, USA).

The glass slide was mounted on a microscope stage and the particle suspension was illuminated with evanescent waves using a setup similar to that described in the previous chapter. The angle of incidence θ_i determined using the approach discussed in Section 5.2.1 was estimated to be $70.1 \pm 0.3\,^\circ$, giving a penetration depth $z_p = 109 \pm 3$ nm. The fluorescence from the particles at wavelengths of 515 nm and above was imaged using the system detailed in Section 5.2.2. Particle images were recorded at an exposure of 1 ms using the CCD camera at framing rates of about 26Hz.

For each experiment, about 2 mL of the working fluid was placed in the well and the particles were allowed to sediment for about 5 min. A sequence of 100 492 (row) $\times$ 653 (col) pixel images was recorded; each image contained about 40 particle images. A new group of particles was then imaged by moving the microscope stage to another location within the well. During the experiment, the working fluid was replaced about every 5 min to minimize photobleaching [92] of the particles and changes in refractive index due to evaporation of the alcohol solution. This procedure was repeated about 30 times for each slide. The laser power, measured by a power meter (Coherent Lasermate Q) every time the working fluid was replaced, remained constant over the entire about 10 min experimental run time.

For each image sequence, the 100 images were first compensated for camera non-linearity using the procedure of Section 5.2.2.3, the mean image was then calculated from these rescaled images. The individual particles in this mean image were then located, and the characteristic image size was determined for each identified particle image as described in Appendix D.

The particle images were then filtered twice to remove non-stationary particles and aggregated particles, respectively. As discussed previously, each sequence of 100 images were recorded over an interval of about 4 s. If a particle is continuously in motion during this interval, it will not be evident in the mean image. If, on the other hand, a particle moves only during part of this interval, in the mean image, it

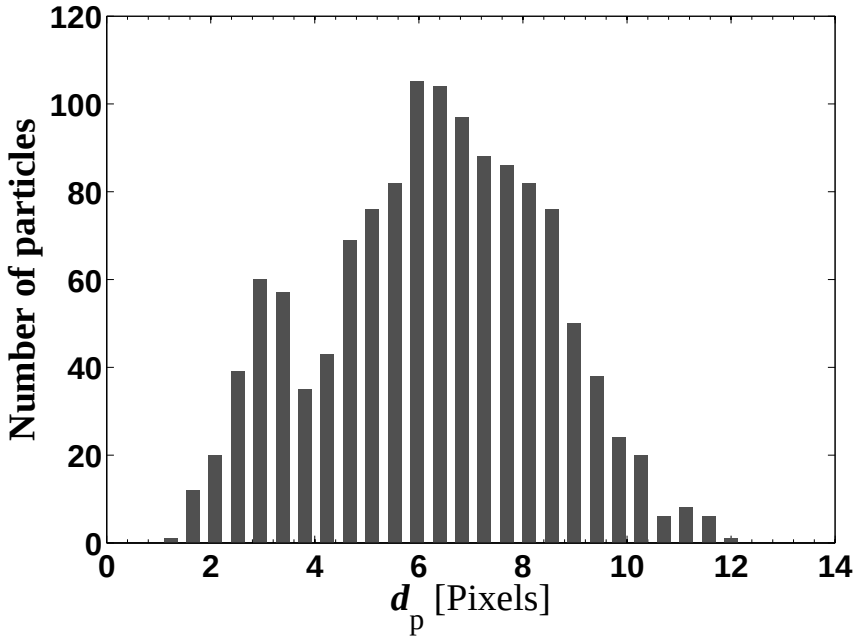

Figure 55: A typical histogram of particle sizes calculated over all the mean images for the uncoated slide.

appears significantly smaller (and less bright) than those of the stationary particles. Such particles were removed by filtering out particles in the mean images that had unusually small sizes below a specified threshold; this threshold was determined from a histogram of the particle diameters calculated over the mean images for all of the image sequences for each slide. An example of such a histogram for the uncoated slide (Figure 55) shows a secondary peak to the left of the primary peak (*i.e.*, at a smaller image size) that corresponds to the averaged images of particles that move during part of the interval. The threshold for the case in Figure 55 was taken to be 5.5 pixels. Typically about 20% of the particles in the mean images were removed by this filtering step.

For each remaining particle in the mean image, its location at each of the 100 individual images of the corresponding sequence was checked and the image intensity, size and eccentricity e of the particle that was located at the same location but in the individual images were determined. Since e is 0 for a circle and 1 for a line, the

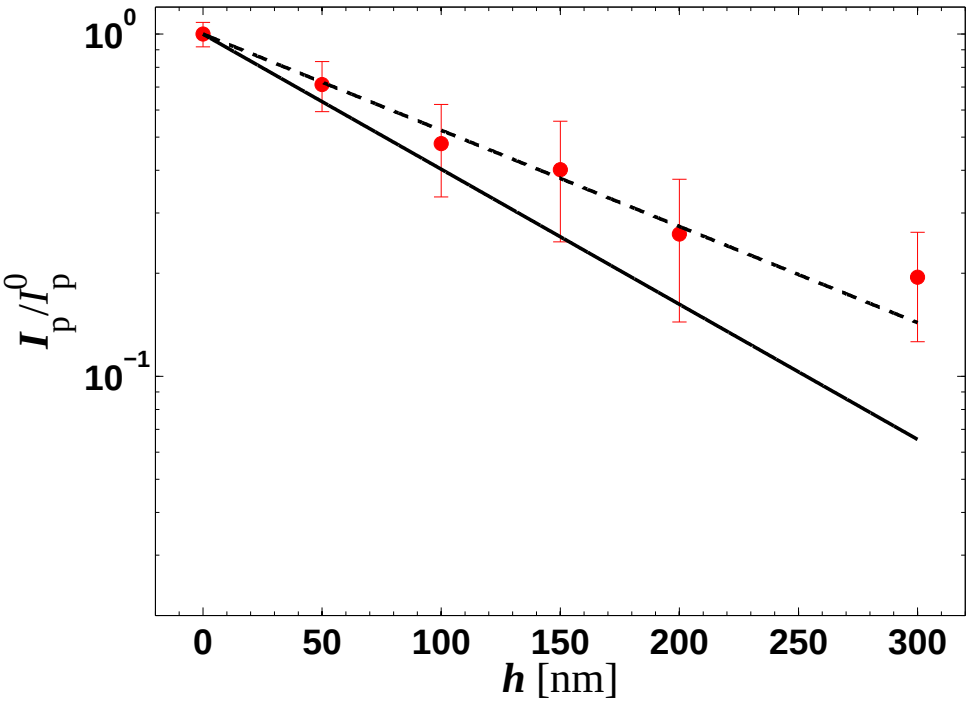

Figure 56: Semilog plot of normalized fluorescence intensity I_p/I_p^0 *vs.* separation distance h. The experimental data (•) are compared with the model of Section 6.1 (solid line) and an exponential curve-fit to the data (dashed line). The error bars denote one standard deviation.

images that are likely to be images of flocculated particles were removed by filtering out images with e above an empirical threshold of 0.1. Typically, about 10% of the particles were removed in this filtering step.

Figure 56 shows the image intensity I_p normalized by I_p^0, the image intensity for particles at $h = 0$, as a function of h for the six slides corresponding to $h = 0$, 50, 100, 150, 200 and 300 nm (points), as well as an exponential curve-fit to these data (dashed line). The solid line represents the model result $I \propto \exp\{-z/z_p\}$, for a nominal penetration depth $z_p = 109$ nm. The experimental data demonstrate that the fluorescence intensities do decay exponentially with h, in agreement with previous model predictions and experimental data [146, 161]. However, a curve-fit of the experimental data gives a $1/e$ length scale of about 155 nm, significantly larger than the predicted value of 109 nm.

The relatively high intensity fluctuations in Figure 56 (the error bars on the point represent one standard deviation) could be attributed to factors such as variations in the amount of fluorophore per particle, variations in the surface roughness, thickness and chemical composition of the MgF_2 coating layer, camera noise and photobleaching of the fluorophore molecules. The standard deviation in particle diameter or the polydispersity, of these 500 nm particles is only 3% according to the manufacturer, and thus likely to be negligible, since the particle images are diffraction-limited and span more than 5 pixels.

Variations in the amount of fluorophore in each particle can, however, result in significant variations in the recorded image intensity. In most cases, polystyrene (PS) particles are fluorescently-labeled by immersion in a saturated fluorophore solution; the porous PS spheres then "wick" dye inside the particle, where the fluorophore molecules are adsorbed onto the PS surfaces. Variations in particle porosity and dye adsorption can therefore lead to significant variation in the amount of fluorophore in and hence fluorescent signal from each particle. Unfortunately, such variations could not be easily quantified in these studies.

Since the evanescent wave propagates through both the the MgF_2 coating layer and the liquid, the uniformity of the evanescent-wave illumination can be affected by nonuniformities in the MgF_2 coating layer. The variation in the thickness of MgF_2 coating is reported by the manufacturer to be ± 1.5 nm, or 3% of the minimum coating thickness of 50 nm, suggesting that such variations will have a minimal effect on the evanescent-wave illumination. Similarly, the surface roughness of the MgF_2 layer, measured to be less than 3 nm by an AFM (Dimension 3100, Veeco Instruments Inc.) should have little effect on the illumination. Variations in the evanescent-wave intensity due to non-uniform chemical composition across the MgF_2 layer could, however, be a factor, since the purity of the MgF_2 coating was not characterized in these studies.

Camera noise is also a significant source of uncertainty in these studies. Since the particle image intensity was defined to be the peak grayscale value of the image, the difference in the response of individual pixels at a given uniform illumination can lead to uncertainties in the recorded grayscale values. Variations in the response of individual CCD pixels can be estimated from the camera calibration data at a gain $G_{\mathrm{M}} = 3400$ (triangles in Figure 45a). Since each of these data points is averaged over a uniformly illuminated window, the variation in the response of the pixels can be inferred from the standard deviation in the averaged grayscale value, which is nearly 6% at a typical normalized image intensity grayscale $V_{\mathrm{n}} = 0.85$.

The type of camera noise known as photon shot noise is due to statistical variations in the rate at which individual photons are incident upon the CCD sensor. Unfortunately, photon shot noise cannot be easily characterized since its properties depend strongly on both the type of CCD and the characteristics of the illumination [21]. CCD cameras used at low light levels, are usually electron multiplying CCD cameras that increase the signal by a gain factor using on-chip multiplication gain. This multiplication further increases the noise since both the signal and the noise are scaled up by the gain factor.

Finally, photobleaching effects [92] should be negligible, since the 100 images in each sequence were obtained within 4s, and independent calibrations show that the image intensity drops less than 4% over this time (Figure 57). The experimental data (points) were curve-fit to an exponential function (solid line), as shown in Figure 57.

6.1.2.2 Method II: Using a Microtranslation Stage to Control the Particle-Wall Separation Distance

Given the marked fluctuations in measured image intensity and the difficulties in characterizing the purity of the MgF_2 coating layer, independent calibrations were performed where the particle-wall distance was adjusted for a single particle using a micro-translation stage. Individual fluorescent $a = 250$ nm and 500 nm PS particles

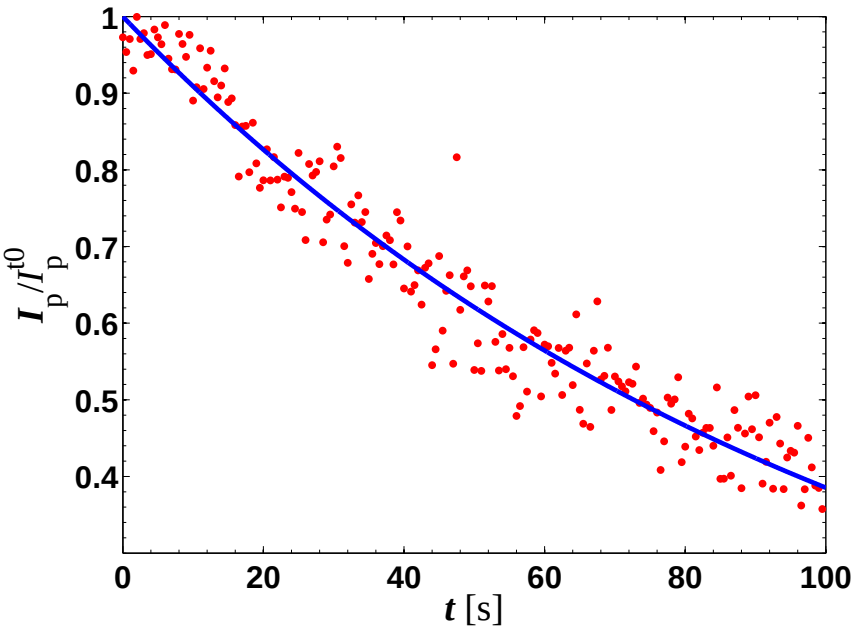

Figure 57: Decrease in normalized particle image intensity over time due to photobleaching. The solid line is a curve-fit of the data with an exponential function: $I_\mathrm{p}/I_\mathrm{p}^{t0} = \exp(-t/105)$.

(Invitrogen, f-8813 and f-8888, respectively) suspended in water were, after sonication for 30 min, attached to the tip of a glass micropipette (World Precision Instruments, Inc., Catalog No. TIP01TW1F) with a nominal inner diameter of 100 nm, supported by an electrode holder (World Precision Instruments, Inc., Catalog No. MPH6S). The particle-micropipette assembly was mounted on a microtranslation stage (Physik Instrumente, M-110) with a minimum incremental motion of 33 nm; the particle was traversed at a constant speed of 40 nm/s through the evanescent-wave illumination created by TIR at a fused silica-water interface. The fluorescence from the particle was imaged using a setup similar to that discussed in Section 5.2.2 at 10 Hz.

Figure 58 shows raw data from a typical experimental run of particle image intensities as a function of particle displacement. The data show that the particle image intensity increases as the particle, initially about 1 μm from the wall, moves

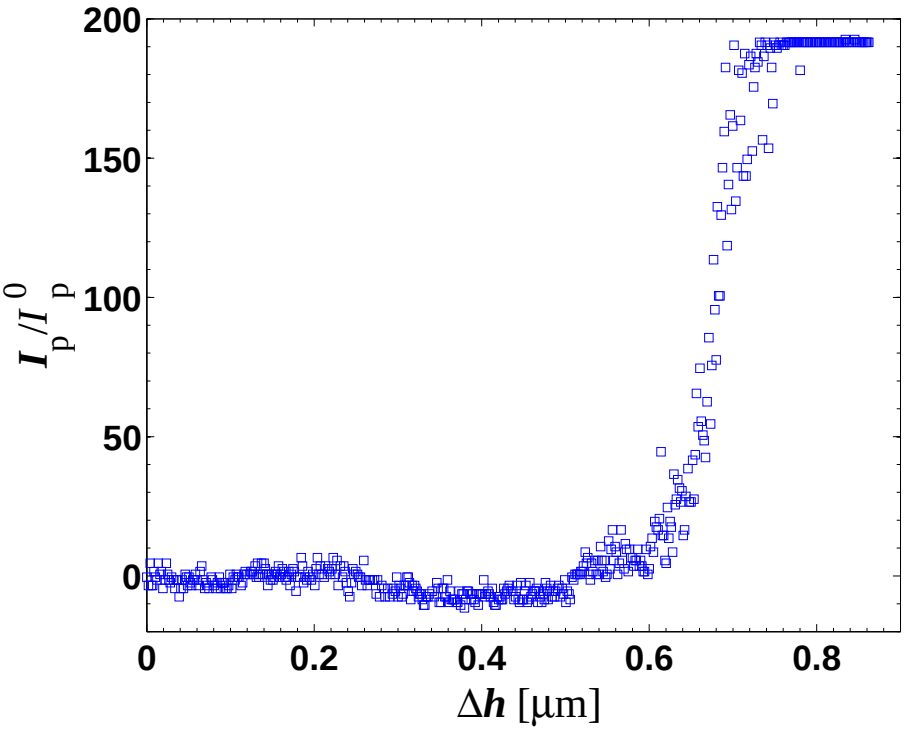

Figure 58: Raw image intensities for a particle illuminated by evanescent waves as a function of particle displacement Δh (recorded by the micro-stage) over a single experimental run.

towards the interface. Figure 59 shows a semi-log plot of I_p normalized by the maximum image intensity at the interface I_p^0 as a function of h for the same experimental run; a curve-fit of the data gives a characteristic $1/e$ length scale Z_1 of 93 nm for this single experiment. The mean characteristic length scale of the decay over ten such experiments was found to be 99 ± 14 nm, a value in good agreement with the penetration depth $z_p = 91$ nm calculated from Equation 5 based on the measured angle of incidence $\theta_i = 73.1°$, the refractive indices of water and fused silica and the illumination wavelength $\lambda = 488$ nm. Note that z_p differs here from that in the Poiseuille flow experiments because of changes in the optical path (and therefore θ_i) when a single fused silica slide is used in lieu of the microchannel. This result nonetheless verifies that Equation 29 can be used to determine z, the position of the particle center measured with respect to the wall from the particle image intensity

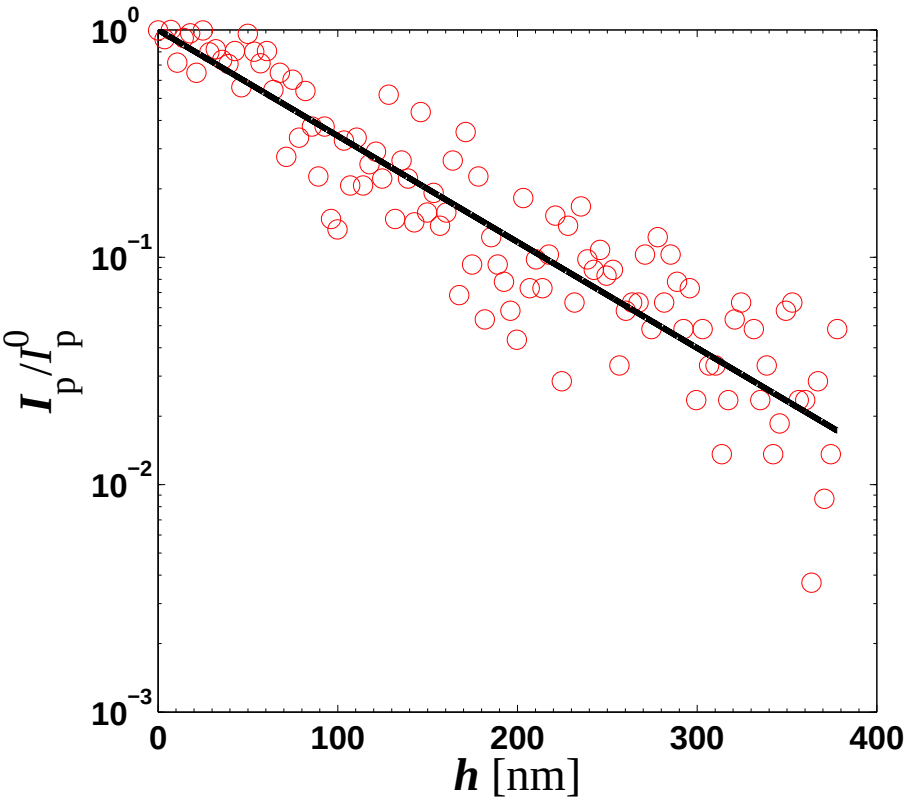

Figure 59: The normalized measured image intensity for a particle illuminated by evanescent waves (log scale) as a function of separation distance h from the wall for a single experiment. The solid line is a curve fit of these data, $I_\mathrm{p}/I_\mathrm{p}^0 = \exp(-h/Z_1)$, where $Z_1 = 93$ nm for this particular experimental run.

I_p, z_p and I_p^0.

6.2 Image Processing

6.2.1 Particle Image Compensation and Detection

The 600 image pairs recorded for each case, were first corrected for the nonlinear response of the CCD camera. The camera calibration data obtained at a camera gain $G_\mathrm{M} = 3400$ (Figure 45b in Section 5.2.2.3) were curve-fit to the ratio of a quadratic polynomial and a cubic polynomial:

$$P_\mathrm{n} = \frac{-21.89V_\mathrm{n}^2 + 23.20}{-3.64V_\mathrm{n}^3 + 1.67V_\mathrm{n}^2 - 27.91V_\mathrm{n} + 31.21} \tag{30}$$

which is plotted in Figure 60 (solid line). The actual power incident on the CCD P_n can be calculated from the grayscale value recorded in the images V_n using Equation 30. Individual particle images were then identified in each image (Appendix D), and particles with high e, corresponding to flocculated particles were removed as described in Section 6.1.2.1.

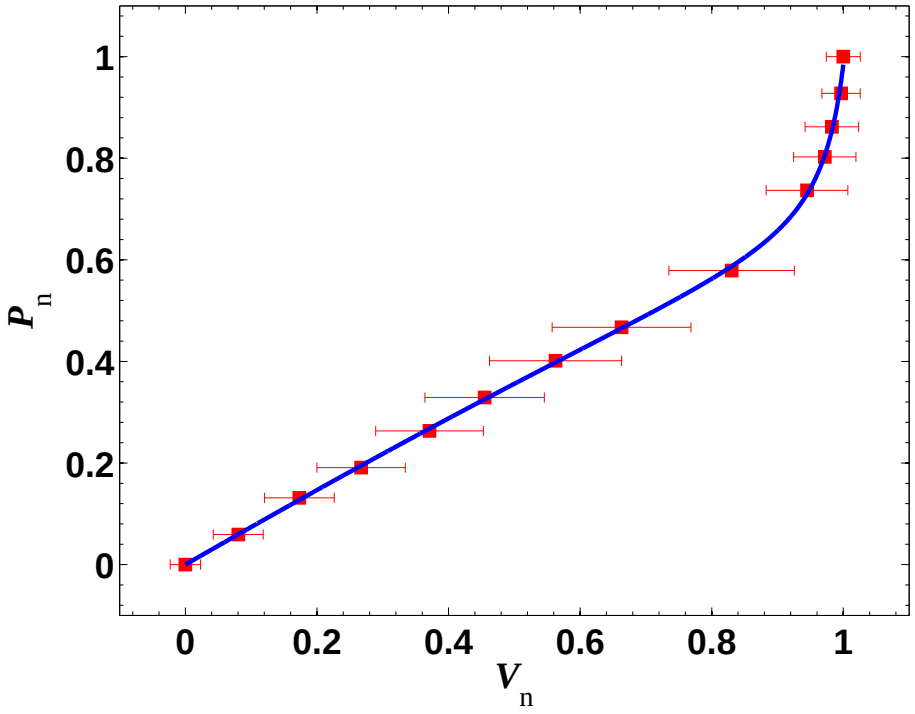

Figure 60: Camera calibration showing the normalized incident power P_n as a function of the normalized imaged grayscale value V_n (■) and a curve-fit to these data (solid line). The error bars represent 95% confidence intervals.

6.2.2 Particle Distribution and Binning

Inverting Equation 29 to obtain the particle position with respect to the wall from the measured particle intensity I_p requires determining the parameters z_p and I_p^0. While z_p can be calculated from Equation 5 based on the properties of the illumination setup, I_p^0, which corresponds to the image intensity of particles attached to the wall, must be measured for the tracers and experimental setup identical to those used in the actual experiments.

To determine I_{p}^0, $a = 50$ nm particles were attached onto the channel surface by electrostatic forces using a 10 mM $CaCl_2$ solution, and illuminated and imaged with the same setup described in the previous Chapter. The images were processed as described previously to determine I_{p} over about 7000 stationary particles. The resultant standard deviation in I_{p} was about 9%, probably due to variations in the amount of fluorophore in each particle, particle polydispersity and random camera noise. The constant I_{p}^0 was defined as the maximum value of I_{p} over these stationary particles; typically about 4% of the stationary particles had a maximum grayscale value of I_{p}^0. Equation 29 was then used to determine the distance between the lower particle edge and the wall $h = z_{\mathrm{p}}\ln(I_{\mathrm{p}}^0/I_{\mathrm{p}})$, over a sequence of 600 image pairs. The 95% confidence interval of the calculated h, which was estimated based on the uncertainties in I_{p}^0 and z_{p} (Appendix C), increases slightly from 20.4 nm at the wall ($h = 0$) to 22.9 at the upper boundary of the imaged volume. Given this uncertainty, we calculated the velocity averaged over sub-layers, each containing $O(10^3)$ particles occupying a range of z-positions. This ensures that each sub-layer has a large enough number of samples to accurately capture the flow statistics.

Figure 61 shows the particle number density c as a function of z for a $C = 10$ mM $Na_2B_4O_7$ solution based on a total of about 8×10^4 "valid" particle images. Note that z here is measured from particle center and therefore $z = h + a$. The results suggest that there are almost no particles within 100 nm ($2a$) of the wall, presumably due to the electrostatic repulsion between the fused silica surface (which should be negatively charged at this pH) and the carboxylate-modified polystyrene particles, which should also have a negative surface charge. The particle density reaches a maximum around $z = 150$ nm, then decays to a roughly uniform value of 5.5×10^{16} m^{-3} for $z > 200$ nm. These data clearly show that the tracer distribution near the wall is strongly non-uniform, and that this non-uniformity affects how the particles sample near-wall velocities, and hence the average z-location associated with the measured particle

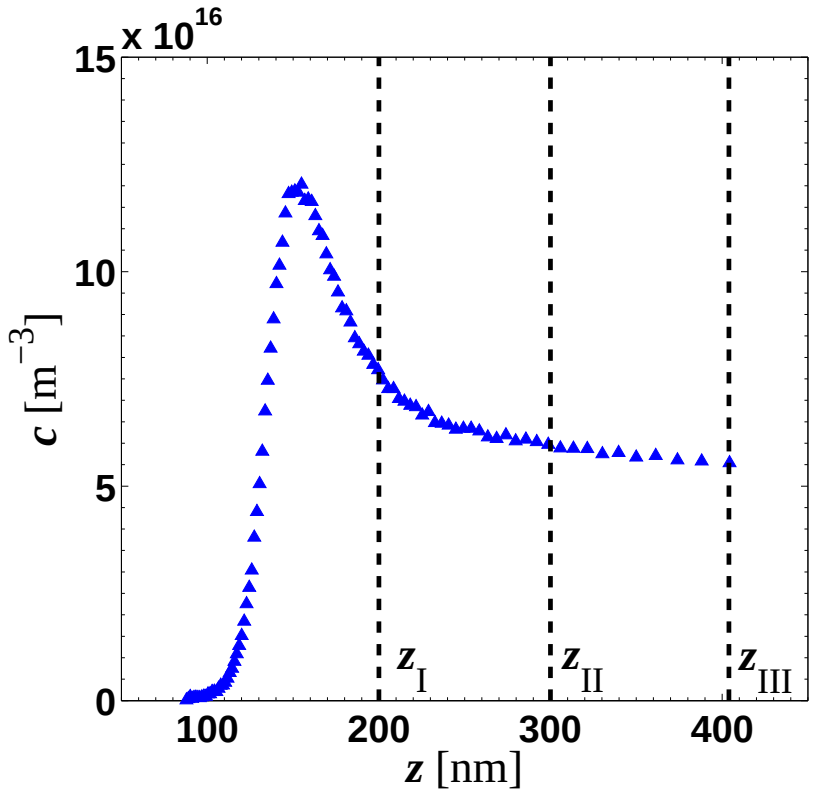

Figure 61: Particle number density c as a function of z the distance between the particle center and the wall for the 10 mM sodium tetraborate solution.

velocity.

These particle distribution data were then used to determine the boundaries of the sub-layers for subsequent MnPIV processing. Using the criterion that all layers should contain roughly the same number of particles, we tentatively divide the particle images, based upon their I_{p}, into three layers spanning the following z-positions:

I. $a = 50$ nm $\leq z < z_{\mathrm{I}}$, where $z_{\mathrm{I}} = 200$ nm;

II. $z_{\mathrm{I}} = 200$ nm $\leq z < z_{\mathrm{II}}$, where $z_{\mathrm{II}} = 300$ nm;

III. $z_{\mathrm{II}} = 300$ nm $\leq z \leq z_{\mathrm{III}}$, where $z_{\mathrm{III}} \approx 400$ nm.

The upper boundary of the region imaged by MnPIV, namely $z_{\mathrm{III}} \approx 400$ nm, was defined to be the z-location of the particle with the lowest image intensity. This upper limit was further verified by showing that a standard cross-correlation PIV

analysis of the image pairs after all the particles that were detected with the particle identification scheme used here were removed and replaced with background noise gave only stochastic displacements, suggesting that all "detectable" particles had been removed. Figure 62 shows an original (but inverted) nPIV image divided into three sub-images corresponding to the three layers specified above for the Poiseuille flow of 10 mM $Na_2B_4O_7$ at $G = 1720\ s^{-1}$. Note that each sub-image contains about one-third of the particles.

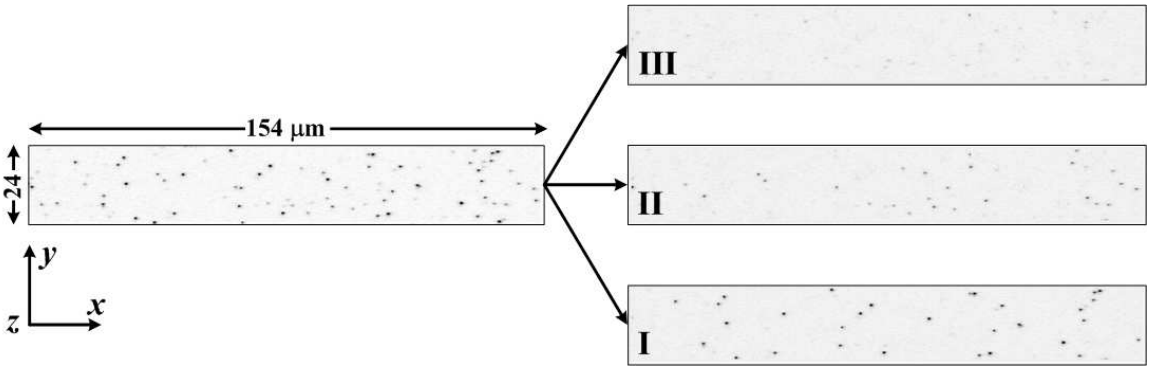

Figure 62: A typical nPIV image [left] of 100 nm particles and the same image divided into three sub-images, each containing about 1/3 of the particles [right]. The images have been inverted to improve contrast.

6.2.3 Expected Particle Velocity

Based on the discussion in Section 4.1, the non-uniform illumination characteristic of evanescent waves can bias the velocities processed using cross-correlation based method towards the value sampled by brighter particles. To minimize this effect, particle-tracking velocimetry (PTV) based on the approach of Baek and Lee [5] was used to determine individual velocity vectors. The velocity data of each layer were then temporally and spatially averaged over all 600 image pairs to obtain u_M, the average tracer velocity in that layer. In all cases, velocities of particles moving between layers over Δt were excluded from the average.

In a shear-dominated flow, there can be "slip" between the particle tracers and the fluid due to the rotation of the particle. Since MnPIV measures the tracer velocity, the

analysis of Goldman et al [56] was used to obtain the expected tracer velocity profile $u'(z)$ from the predicted fluid velocity profile $u(z)$ of Equation 24. This correction had no discernible effect on the data, however, because there are almost no particles within a particle diameter of the wall (*cf.* Figure 61). The mean expected tracer velocity for each layer $\overline{u}_{\rm p}$ described by $z_{\rm L} \leq z \leq z_{\rm u}$ can then be calculated as the weighted mean of $u'(z)$ using the actual tracer distribution $c(z)$ in Figure 61 as the weighting coefficients:

$$\overline{u}_{\rm p} = \frac{\int_{z_{\rm L}}^{z_{\rm U}} c(z)u'(z)dz}{\int_{z_{\rm L}}^{z_{\rm U}} c(z)dz} \tag{31}$$

We can then use the known velocity profile $u'(z)$ and $\overline{u}_{\rm p}$ to interpolate $\langle\overline{z}\rangle$, corresponding to the z-location where $u'(\langle\overline{z}\rangle) = u_{\rm p}$. Table 5 compares the geometric center $z_{\rm c}$ and $\langle\overline{z}\rangle$ for the three layers. In the layer adjacent to wall, $\langle\overline{z}\rangle$ is significantly greater than $z_{\rm c}$ due to the lack of particles at $z < 2a$; $\langle\overline{z}\rangle \approx z_{\rm c}$ in the other two layers with their nearly uniform particle distributions (*cf.* Figure 61).

Table 5: Comparison of $z_{\rm c}$ and $\langle\overline{z}\rangle$ for the three layers for C = 10 mM sodium tetraborate solution.

Layer	$\langle\bar{z}\rangle$ [nm]	$z_{\rm c}$ [nm]
I - [50 : 200 nm]	162	125
II - [200:300 nm]	249	250
III - [300:400 nm]	354	350

6.3 Results and Discussion

Figure 63 shows the velocity U as a function of z for the 10 mM $Na_2B_4O_7$ solution at three different shear rates G = 620 s^{-1} (▲), 1000 s^{-1} (■) and 1720 s^{-1} (●). The solid line represents the expected "linear" particle velocity profile $u'(z)$, which is essentially linear within 400 nm of the wall, obtained as discussed in Section 6.2.3. The expected shear rate G, was then calculated by linear regression of this velocity

profile for $z \leq$ 400 nm and the maximum uncertainty in G based on the measurement uncertainties in the pressure gradient, channel height and viscosity is estimated to be 3.2% at the minimum dp/dx (Appendix C). The shaded circle on the lower right of Figure 63 denotes the region occupied by a single 100 nm tracer touching the wall. The MnPIV results (points) are placed at $\langle \overline{z} \rangle$ and compared with the expected mean velocity of each layer $\overline{u}_{\mathrm{p}}$. Each of these data points is the average over five independent experimental runs; the error bars represent 95% confidence intervals. For each shear rate, the linear least-squares curve-fit (assuming that the no-slip condition holds at the wall, or $U(0) = 0$) is shown in the figure by the dashed line.

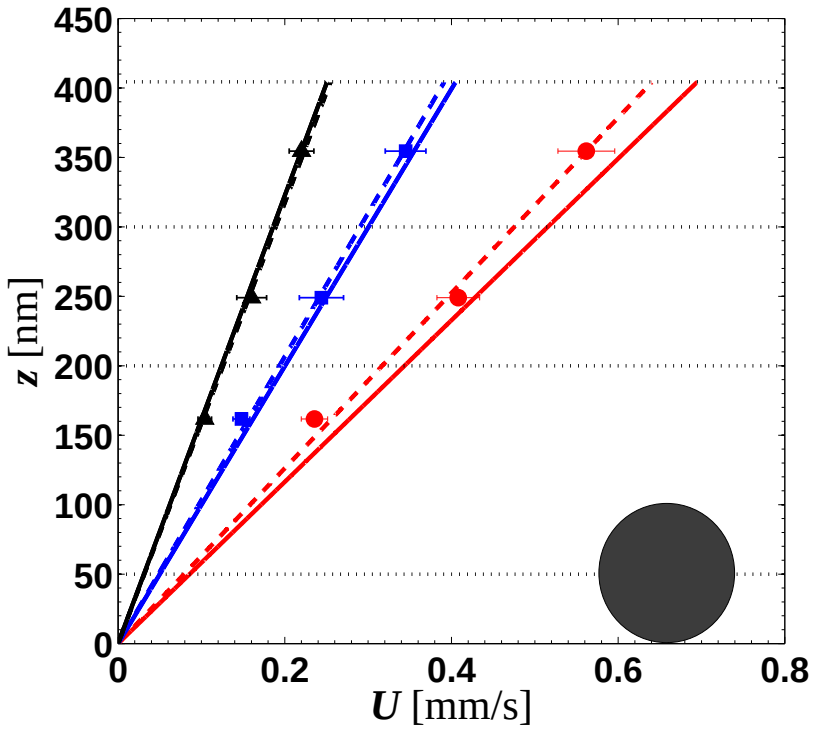

Figure 63: MnPIV velocity profiles for the average velocity U as a function of the wall-normal distance z measured with respect to the particle center in the three layers (points) compared with the expected velocity profile (solid line) for 10 mM $Na_2B_4O_7$ at G = 620 (▲), 1000 (■) and 1720 (●) s^{-1}. The dashed lines denote a linear curve-fits of the MnPIV points and origin. The error bars represent the 95% confidence interval.

The studies using synthetic images in Chapter 3 concluded that MnPIV tends to

overestimate the velocities in the layer next to wall (layer I) due to the asymmetric diffusion in this region (*i.e.*, the no-flux boundary condition imposed by the wall) and underestimates the velocities in the layer farthest away from wall (layer III) due to the non-uniform contribution to the cross-correlation function from particles with different intensities caused by evanescent-wave illumination. The layer I results of Figure 63 do not, however, show the expected overestimation. Brownian dynamics simulations using the Fokker-Planck equation showed that the overestimation in layer I, which is described by a dimensionless parameter $\Omega* = D_\infty \Delta t/(z_\mathrm{U} - z_\mathrm{L} + 0.8a)^2$ (proportional to the unconfined Brownian diffusion coefficient D_∞ and the time interval $\triangle t$ and inversely proportional to a quantity related to the layer thickness $(z_\mathrm{U} - z_\mathrm{L})$), increases with $\Omega*$ for $\Omega* > 0.25$ [156]. In this study, layer I comprises about one-third of the particles, and its thickness is therefore greater than the value used in Chapter 3. This thicker near-wall layer, along with a smaller Δt, gives $\Omega* = 0.13$, suggesting that Brownian diffusion-induced overestimation is negligible for these data. In layer III, the underestimation was greatly reduced by our use of particle tracking, *vs.* cross-correlation-based methods.

At each shear rate, the velocity gradient $\partial U/\partial z$ can then be estimated from the three MnPIV datapoints and the origin as the slope of the dashed lines in Figure 63. These slopes G_3 are compared in Table 6 with the expected velocity gradients G, which are the slopes of the solid lines. The average discrepancy (based on absolute values) was 4%. Given that only two points should be sufficient to estimate the slope of this "linear" velocity profile, and the data in the layer nearest the wall are likely to have the greatest errors, we also estimate the velocity gradient from only the layers II and III MnPIV results and the origin. These estimates for the velocity gradient, G_2, appear to be slightly closer to G. These results suggest that MnPIV can be used to obtain velocity gradients—and hence wall shear stress data—within about 400 nm of the wall.

Table 6: Comparison of expected velocity gradients G (slope of the solid line in Figure 63), G_3 from a curve-fit of the three MnPIV datapoints (slope of the dashed line in Figure 63) and G_2 estimated from the MnPIV datapoints in layers II and III for three different shear rates. All the curve-fits assume no slip at the wall.

G (s^{-1})	G_3 (s^{-1})	$\frac{\lvert G_3-G\rvert}{G}$(%)	G_2 (s^{-1})	$\frac{\lvert G_2-G\rvert}{G}$(%)
620	630	1.6	630	1.6
1000	970	3.0	980	2.0
1720	1590	7.6	1600	7.0

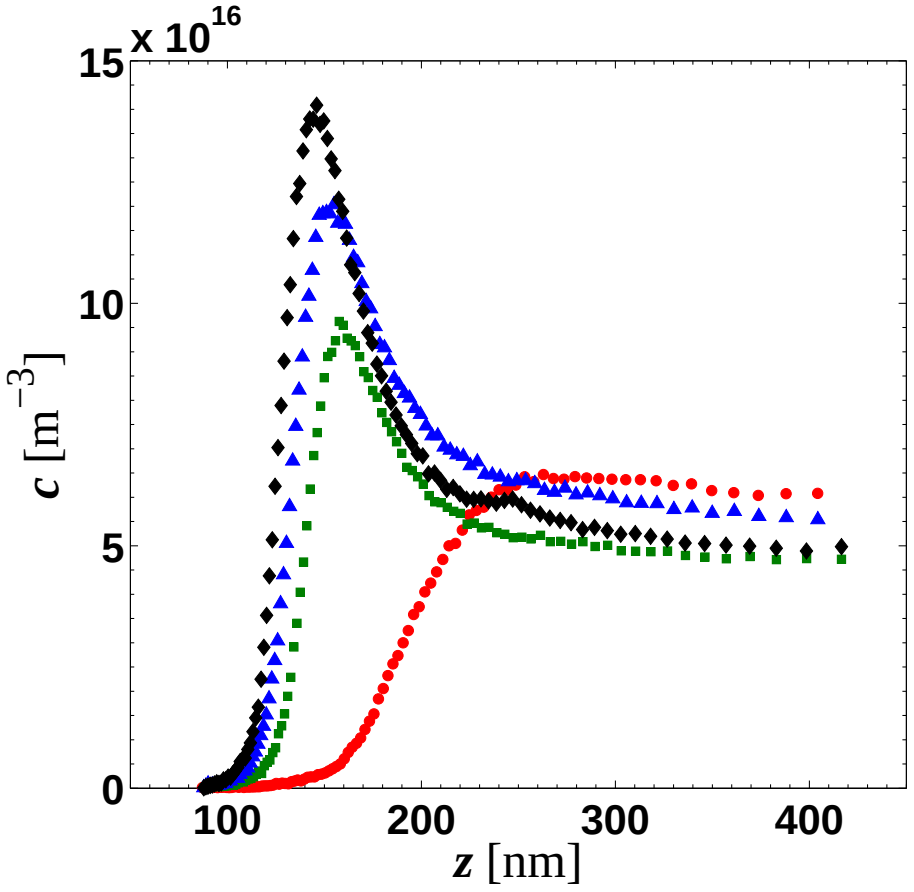

Figure 64: Particle number density as a function of z, the distance between the particle center and the wall, for the four working fluids studied here (● Nanopure water; ■, ▲, ♦ 1 mM, 10 mM and 20 mM $Na_2B_4O_7$ solutions, respectively).

Similar experiments were performed for water and two other $Na_2B_4O_7$ solutions at molar concentrations of 1 mM and 20 mM. Figure 64 shows the particle number

density c as a function of wall-normal distance z for all four working fluids (● Nanopure water; ■, ▲, ♦ 1 mM, 10 mM and 20 mM $Na_2B_4O_7$ solutions, respectively). In all cases, there are almost no particles at $z < 100$ nm, due mainly to electrostatic repulsion effects. The particle depletion region is much thicker for water, however, with almost no particles within 150 nm of the wall. Even low concentrations of $Na_2B_4O_7$ reduces the z-extent of this particle depletion region, presumably because the greater ionic strength of the sodium tetraborate solutions reduces the thickness of the electrical double layer (EDL) and the wall zeta-potentials of the particles and the fused silica wall are altered by the change in pH between Nanopure water (pH $\sim$ 5.5) and the $Na_2B_4O_7$ solutions (pH $\sim$ 9). Varying the molar concentration of the salt does not, however, have a major effect on the particle distribution, although the particles move closer to the wall as C increases, possibly due to the reduction in the thickness of the particle and wall EDLs (the Debye screening length is estimated to be 1.5, 2.1 and 6.8 nm for C = 20, 10 and 1 mM, respectively). This effect was also shown in the particle potential energy obtained from these particle distributions (Appendix F). Figure 65a shows the MnPIV velocities for the 1 mM $Na_2B_4O_7$ solution at G = 670 s^{-1} (▲), 1110 s^{-1} (■) and 1910 s^{-1} (●); Figure 65b shows MnPIV results for 20 mM $Na_2B_4O_7$ at similar shear rates G = 600 s^{-1} (▲), 1010 s^{-1} (■) and 1760 s^{-1} (●). Although not shown here, the deviations between the measured velocity gradients and the expected values are about 7% for all 1 mM $Na_2B_4O_7$ cases and range from 1% to 15% for the 20 mM $Na_2B_4O_7$ cases.

As shown in Figure 66, MnPIV results were also acquired for water, although different layer boundaries (z_I = 267 nm and z_{II} = 341 nm, *vs.* z_I = 200 nm and z_{II} = 300 nm for the $Na_2B_4O_7$ cases) were used to ensure that the particles were roughly evenly divided between the three layers. Again, the measured velocities (data points) and velocity gradients (dashed lines) are compared with the expected velocity profiles (solid lines).

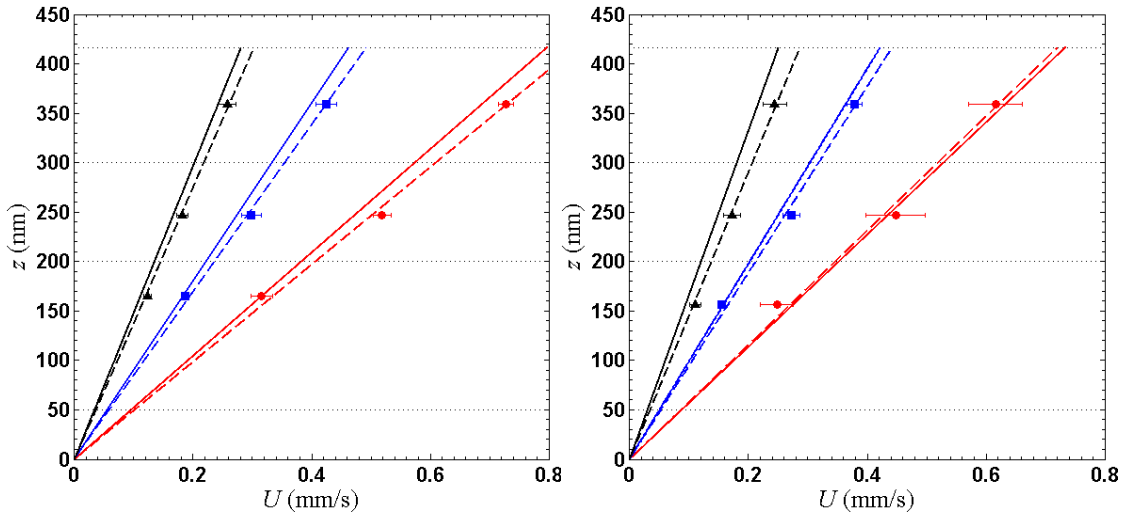

(a) 1 mM $Na_2B_4O_7$ solution (b) 20 mM $Na_2B_4O_7$ solution

Figure 65: MnPIV velocity profiles for the average velocity U as a function of the wall-normal distance z measured with respect to the particle center in the three layers (points) compared with the expected velocity profile (solid line) for (a) 1 mM $Na_2B_4O_7$ solution at $G = 670$ (▲), 1110 (■) and 1910 (●) $^{-1}$ and (b) 20 mM $Na_2B_4O_7$ at $G = 600$ (▲), 1010 (■) and 1760 (●) $^{-1}$. The dashed lines denote a linear-curve fit of the MnPIV points and origin. The error bars represent the 95% confidence interval.

Table 7: Comparison of velocity gradients G obtained from the predicted velocity profile by Equation 24 using the measured pressure gradient and fluid viscosity (slope of the solid line in Figure 66), G_3 from a curve-fit of the three MnPIV data points and origin (slope of the dashed line in Figure 66) and G_2 estimated from the MnPIV data points in layers II and III and origin for three different shear rates.

G (s^{-1})	G_3 (s^{-1})	$\frac{\lvert G_3-G\rvert}{G}$(%)	G_2 (s^{-1})	$\frac{\lvert G_2-G\rvert}{G}$(%)
680	680	0.0	660	2.9
1110	1130	1.8	1110	0.0
1910	1930	1.0	1880	1.6

The results in Figure 66 show although there is an overestimation in measured velocities in the layer next to wall, the velocity gradients obtained using the two velocity data points farther away from the wall G_2 and those estimated over all three data points G_3 showed similar agreement with the expected values as shown in Table 7; the MnPIV estimates of the velocity gradient are within 2% on average of the

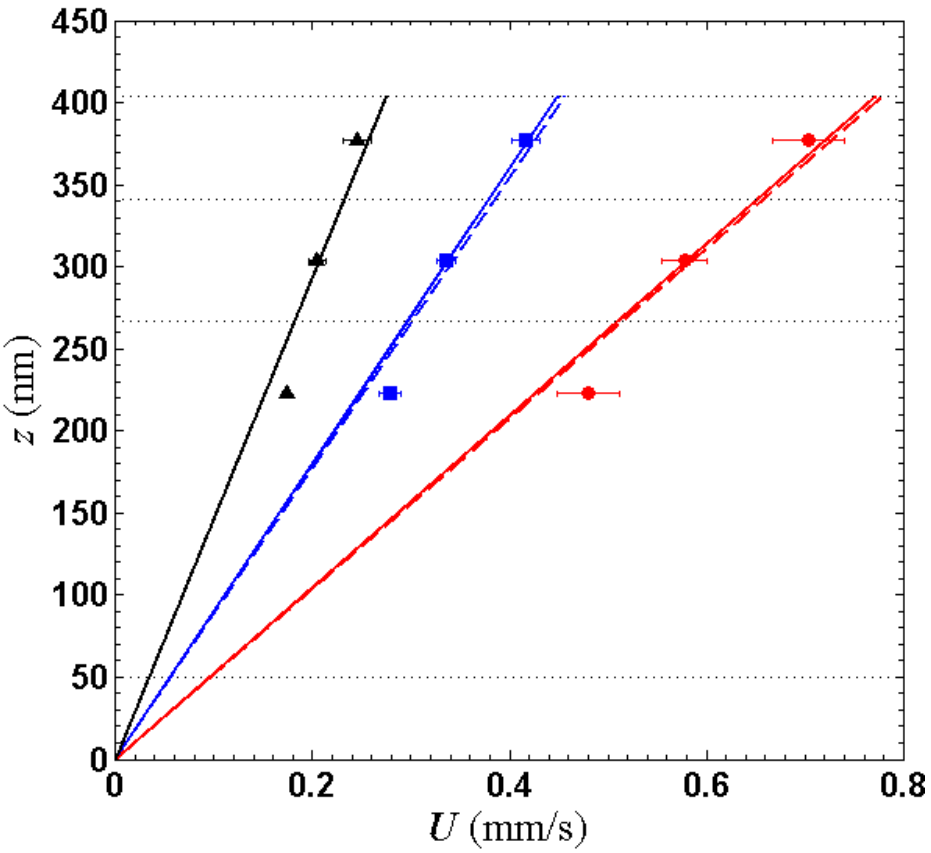

Figure 66: Similar to Figure 65, but for water at G = 680 (▲), 1110 (■) and 1910 (●) s^{-1} for water.

predicted values G. We are however not certain why this near-wall overestimation is observed for water and not for the sodium tetraborate cases; this discrepancy warrants further investigation. For the four working fluids, the shear rates calculated from the MnPIV results are, on average, within 5% of the values given by Equation 24.

6.4 Summary

The studies reported here using MnPIV for fully-developed and incompressible Poiseuille flow through 41 μm fused silica channels are the first experimental demonstration of MnPIV. Images of colloidal fluorescent polystyrene tracers illuminated by evanescent waves and convected by this flow were divided into three sub-layers within about 400 nm of the wall and obtained in-plane velocity components at three different distances from the wall. The first velocity datapoint next to wall is within 200 nm of the wall,

about a two-fold improvement in spatial resolution normal to the wall over current evanescent wave-based velocimetry techniques. Moreover, the results suggest that MnPIV, with appropriate calibrations and processing, can measure velocity gradients within the first 400 nm next to the wall with the three velocity datapoints obtained with the technique. This work also demonstrates that accurate data on the highly non-uniform particle distribution with respect to the wall, due for example to electrostatic effects and shear-induced particle-fluid "slip," is required to determine which flow velocities are actually sampled by the tracers.

It appears that velocity gradients obtained from the data points of the two sub-layers farther away from the wall may be as accurate, if not slightly more accurate, than those based on all three velocity data points in most of the cases. This implies that ignoring the brightest tracers, *i.e.*, those in the sub-layer nearest the wall, when using MnPIV to obtain velocity gradients would reduce processing without adversely affecting the accuracy of the results.

As shown in the synthetic image studies of Chapter 3, both the non-uniform illumination and asymmetric diffusion bias the measured velocities. In current study, the underestimation in velocity due to the non-uniform nature of the illumination in the layer farthest away from the wall was effectively eliminated using particle tracking instead of cross-correlation methods. In the layer nearest the wall, reducing the time interval between the two images within the image pair and increasing the layer thickness minimized the overestimation due to asymmetric diffusion.

CHAPTER VII

SLIPPAGE OF AQUEOUS SOLUTIONS OVER SOLID SURFACES WITH VARYING WETTABILITY

This thesis has already demonstrated that multilayer nano-particle image velocimetry (MnPIV) can be used to obtain in-plane velocity components at a few different wall-normal, or z-distances from the wall within the first $\sim$ 500 nm next to the wall. This chapter focuses on using MnPIV to measure near-wall velocity profiles and by extrapolating these velocity profiles, to obtain slip lengths for the flow of Newtonian liquids past solid surfaces of varying wettability. Section 7.1 details the experimental descriptions. Section 7.2 summarizes the results of these slip studies, followed by a brief discussion in Section 7.3.

7.1 Experimental Descriptions

Since the experimental setup used here is very similar to that described in Chapter 5, this Section emphasizes the minor modifications made to the earlier setup for the slip length experiments.

New microchannels were fabricated in fused silica using the photolithography and chemical wet-etching procedures detailed in Section 5.1.1. Instead of etching individual 50 mm $\times$ 50 mm $\times$ 1 mm fused silica substrates, eight channels were wet-etched at a time in a 100 mm $\times$ 100 mm $\times$ 2.2 mm fused silica wafer (Telic Company), precoated with layers of chrome (120 nm in thickness) and photoresist AZ 1518 (530 nm thick), using a dark-field photomask. The wafer was then diced into eight 50 mm $\times$ 25 mm substrates containing the etched channel "trenches"; each of these eight substrates was then individually bonded to 1 mm thick fused silica lids to form sealed

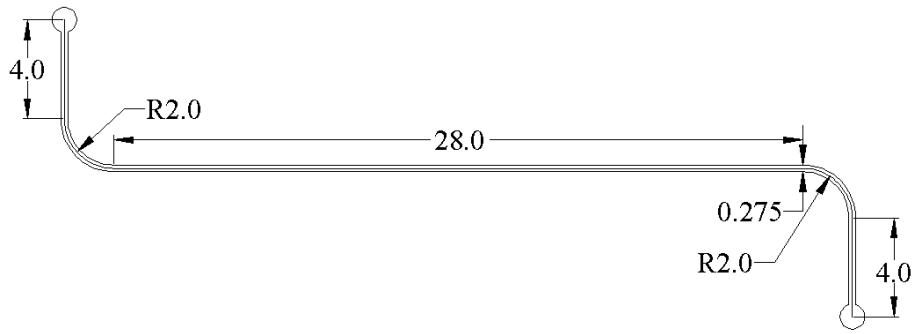

Figure 67: The AutoCAD drawing of the channel used to determine the channel length. All dimensions are given in mm.

channels. The resultant microchannels, which have slightly trapezoidal cross sections, are about 33 μm in depth and 530 μm in width. These dimensions were measured, before bonding, at the half-depth of the channel with a profilometer (model P-15, KLA-Tencor). The channel lengths were estimated from the AutoCAD drawing used to fabricate the photo mask to be 42.3 mm (Figure 67).

A bare, untreated fused silica surface is naturally hydrophilic. To make the silica surfaces hydrophobic, the channel walls were coated with a self-assembled monolayer (SAM) of octadecyltrichlorosilane (OTS) [190]. Before coating, the channels were cleaned by successive rinses in acetone, Nanopure water, a 1 M sodium hydroxide (NaOH) solution and Nanopure water. These steps should create a fresh silicon oxide layer on the channel walls with a high density of surface silanol groups. After being thoroughly dried, the cleaned channel is flushed with chloroform for 40 min, then a 10 mM solution of OTS in chloroform for 3 h and chloroform again for 1 h by driving the solutions through the channel using a syringe pump. The channel is then dried and baked in an oven at 150 °C for 1 h. This process creates an approximately 2 nm thick uniform and robust layer of silylating agent on the channel walls with hydrophobic chains facing outward (*i.e.*, towards the fluid). Given the practical difficulties in measuring the contact angle on the inner surfaces of the sealed channel, the contact angle of the coated surface was estimated from measurements on a fused silica

substrate (from the same batch of silica as that used as the channel lid) processed using same procedure as that used for the channel. The contact angle between water and the coated substrate was measured using a contact angle goniometer (model 200 Ramé-hart Instrument Co.) to be $100 \pm 4.1\,^{\circ}$.

Poiseuille flows were generated inside these microchannels with a hydrostatically created pressure gradient using the system discussed in Section 5.1.2. Near-wall velocity data were obtained at six different pressure gradients $\Delta P/L$ = 1.18, 1.06, 0.90, 0.74, 0.51 and 0.25 Bar/m, corresponding to height differences between the upstream and downstream free surfaces of 0.51, 0.46, 0.39, 0.32, 0.22 and 0.11 m, respectively. The flow Reynolds numbers for these flows based on the average velocity and hydraulic diameter of the channel $Re = 0.05 - 0.22$.

Monovalent aqueous solutions at two different salt molar concentrations C and pH were studied to determine if changing the ionic strength I_s and pH of the working fluids affected the slip length measurements. Aqueous solutions of ammonium bicarbonate (NH_4HCO_3) and ammonium acetate (CH_3COONH_4), both weak buffers because of the presence of the ammonium ion, at $C = 2$ mM and 10 mM were chosen because of their simple dissociate in water. Sodium tetraborate solutions, with their rather high pH values of ~ 9.1, were not used in these studies to avoid damaging the hydrophobic coating due to dissolution of fused silica in the solutions at these high pH values [75].

The properties of the four working fluids are given in Table 8. The NH_4HCO_3 solutions were prepared with Nanopure water and analytical grade NH_4HCO_3 (Acros Organics, Catalog No. 370930250) following the procedure detailed in Section 5.1.3. The CH_3COONH_4 solutions were simply diluted with Nanopure water to the desired concentrations from a 7.5 M stock solution (MP Biomedicals Inc., Catalog No. 198759). The solutions were then filtered, seeded with tracer particles, and sonicated as described in Section 5.1.3. Since previous studies have reported that dissolved gasses in the working fluid may nucleate at the wall and affect slip, the solutions were

degassed by placing them in a vacuum chamber at a pressure of -0.9 Bar for 30 min.

Table 8: Ionic strength and pH of the working fluids.

C [mM]	I_s [mM]	pH [-]
NH_4HCO_3		
2	2	7.55 at 19.7 °C
10	10	7.79 at 19.1 °C
CH_3COONH_4		
2	2	6.18 at 20.1 °C
10	10	6.61 at 19.6 °C

The evanescent-wave illumination system used in these experiments was similar to that of Section 5.2.1. The angle of incidence θ_i at the interface between the fused silica wall and the working fluid where TIR occurs to create the evanescent save was calculated using a slightly different procedure from that described in Section 5.2.1, however. After each experimental run, the two TIR spots on the bottom surface of the microchannel immediately adjacent to the spot that actually illuminates the flow (labeled in red in Figure 68 were visualized using a Rhodamine B solution and imaged through the built-in Bertrand lens of the microscope onto the CCD camera to measure the distance between the two spots; the distance was averaged over all the experimental cases $d_s = 5.45 \pm 0.17$ mm. Since the etched substrate and lid that form the channel have different thicknesses (2.2 mm and 1 mm, respectively), d_t is redefined as the thickness of the lid which, averaged over 5 different substrates, was determined to be 0.871 ± 0.03 mm. From these data, the angle of incidence $\theta_i = \tan^{-1}(d_s/2d_t) = 72.27° \pm 0.77°$. The resultant penetration depth of the evanescent wave illumination (calculated from Equation 5) $z_p = 95.6 \pm 4.8$ nm (Appendix C).

The fluorescence emission from the particles was imaged using the microscope optics and CCD camera discussed in Section 5.2.2. Figure 69, which compares the mean images averaged over all 600 image pairs for flow through the (a) bare and

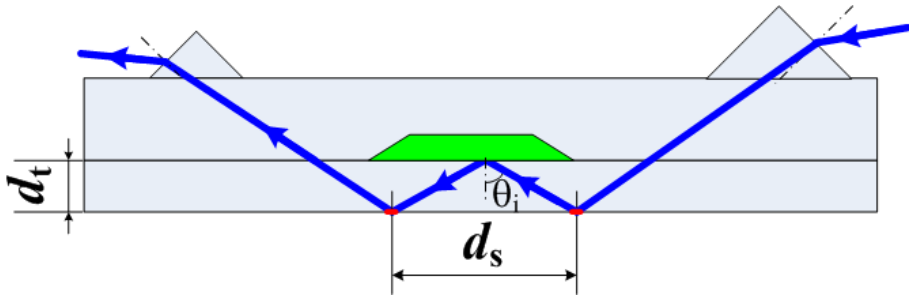

Figure 68: Sketch illustrating the procedure for calculating θ_i. Note that the parameters d_s and d_t have definitions that differ from those given in Section 5.2.1. The imaged TIR spots on the bottom surface of the microchannel are shown in red.

(b) coated channels, showed that a much larger number of tracers adhere to the hydrophobic surface, since it is expected that only particles that are stationary will appear in the mean image. Although the particle distribution along the z-direction and near-wall velocities for the flows through the bare channel were obtained from the images using the same processing methods as those used in the previous Chapter, the images for the flows inside the hydrophobically coated channel were processed with a slightly different procedure as described subsequently, to minimize the effects of the particles attached to the wall.

After compensating for the camera nonlinearity, the mean image calculated over the 600 image pairs was subtracted from each individual image. The potential particle centers were then determined from these "background-subtracted" images. The properties (*e.g.*, size, eccentricity and intensity) of the particle image located at each of these potential particle centers was then calculated from the image that was only processed to compensate for the camera nonlinearity.

7.2 Results and Discussions

The measured particle distributions within about 350 nm of the wall are plotted in Figure 70 for both the (a) bare and (b) coated channels. In all cases, there are almost no particles at $z < 100$ nm. The number density c reaches a maximum at around $z = 120$ nm, then decays to a roughly constant value for $z > 250$ nm. For

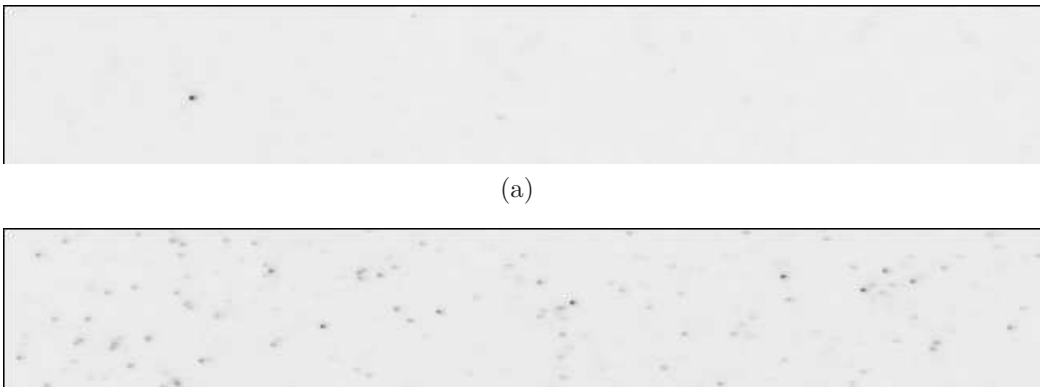

(a)

(b)

Figure 69: Mean experimental images taken inside the (a) bare and (b) coated channels averaged over the 600 image pairs obtained in a single experimental run. The images are inverted for clarity.

a given channel, the particle distribution appears to depend more strongly upon the ionic strength (*vs.* the pH) of the working fluid: the two curves at the higher molar concentration (10 mM NH_4HCO_3 and 10 mM CH_3COONH_4) are slightly to the left of the corresponding 2 mM cases. The inset in Figure 70a, which compares the curves for 10 mM NH_4HCO_3 flowing through the bare and coated channels, suggests that the particle distribution in the coated channel is slightly to the left of that in the bare channel, presumably because the hydrophobic coating reduces the magnitude of the negative charge on the channel wall. Independent streaming-potential measurements using 20mM phosphate buffer (pH = 6.8) show that the wall zeta potential averaged over the four channel walls of the coated channel is essentially zero, compared with -3.5 mV for the bare channel.

The particles were then divided into three layers, each containing about one-third of the particles: I) $50 < z \leq 150$ nm; II) $150 < z \leq 250$ nm; and III) $250 < z \leq 350$ nm. The mean velocity of each layer was then determined from data obtained over 5 independent runs using the processing procedure described in the previous Chapter. Figure 71 shows these velocities measured at six different (expected) shear rates $G =$ 491, 983, 1412, 1720, 2029 and 2255 s^{-1} for the Poiseuille flows of 10 mM NH_4HCO_3

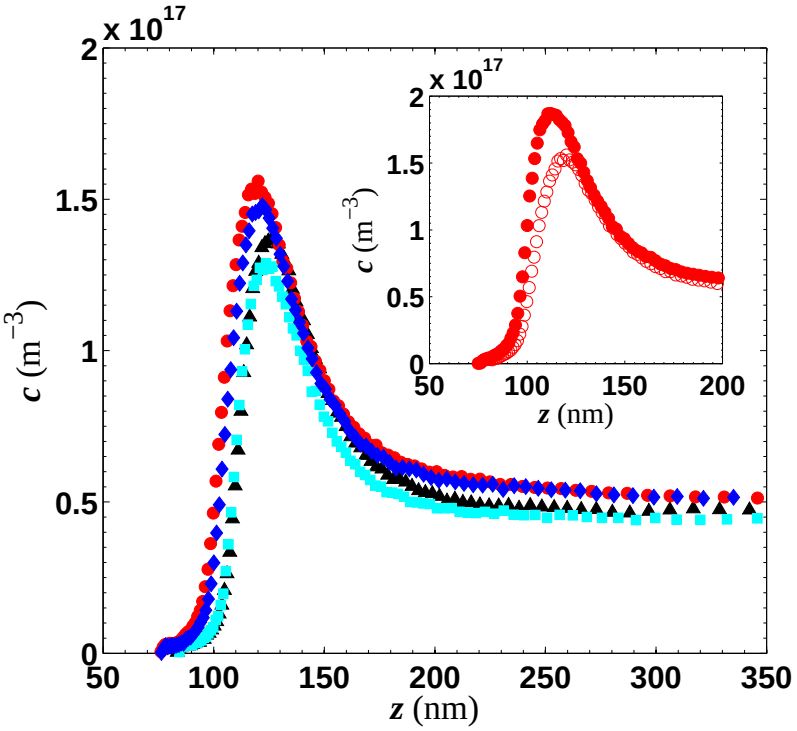

(a)

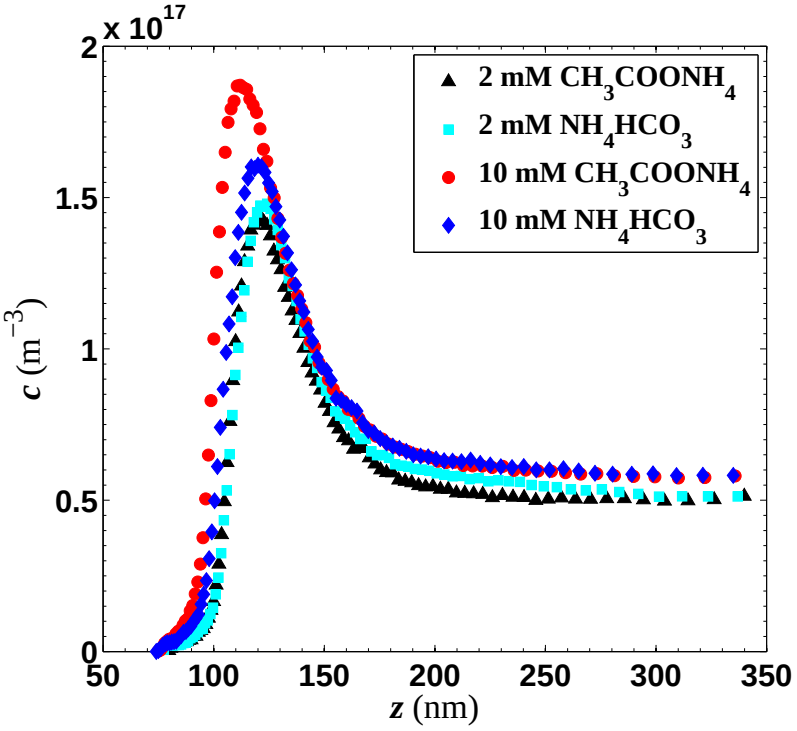

(b)

Figure 70: Measured particle number density as a function of z for (a) bare and (b) coated channels. The inset compares distributions for 10 mM NH_4HCO_3 solutions measured in the bare (open symbols) and coated (closed symbols) channels.

through the bare channel. For each case, the dashed line is a linear curve-fit of the three data points, while the solid line represents the expected linear velocity profile at the shear rate G predicted from the analytical solution for 2D Poiseuille flow using the measured pressure gradient, channel depth and viscosity of the working fluid. Unlike the previous Chapter, the linear curve-fits presented here are only over the three velocity data points (and do not include the origin, which would assume that the no-slip condition holds). Table 9, which compares the measured shear rate G_3 (*i.e.*, the slope of the dashed lines) with G, shows that the maximum discrepancy between G_3 and G is 9% for the case at the smallest shear rate $G = 491$ s^{-1}. The velocity results for the Poiseuille flows of the other working fluids through the bare and coated channels, shown in Appendix A, were qualitatively similar.

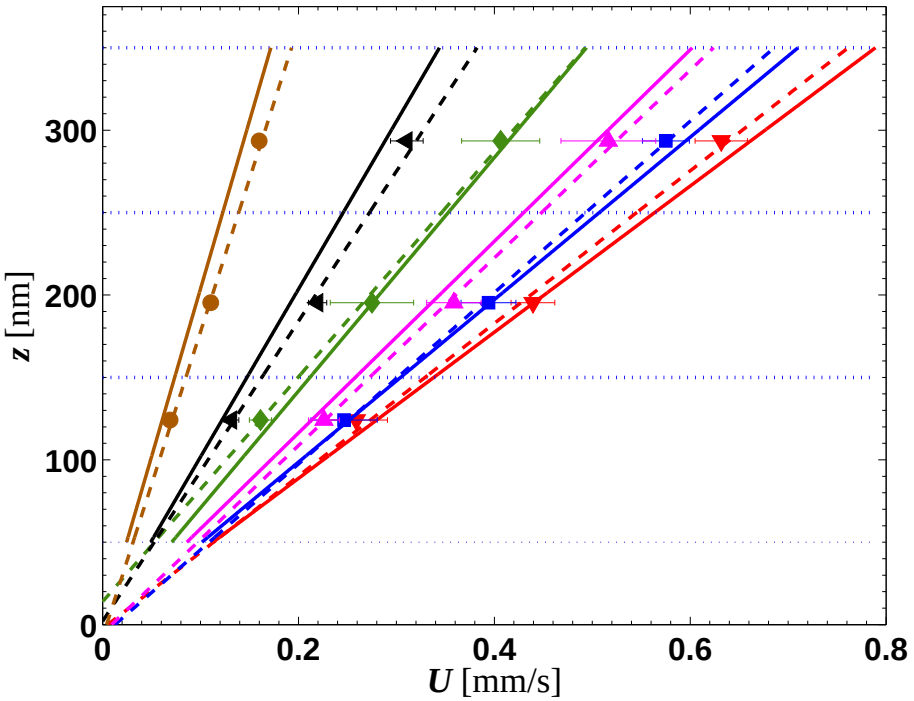

Figure 71: MnPIV velocity profiles for the average velocity U as a function of the wall-normal distance z measured with respect to the particle center in the three layers (points) compared with the expected velocity profile (solid line) for 10 mM NH_4HCO_3 at $G = 490$ (●), 983 (◀), 1412 (♦), 1720 (▲), 2029 (■) and 2255 (▼) s^{-1}. The dashed lines denote linear curve-fits of the MnPIV results. The error bars represent the 95% confidence intervals.

Table 9: Comparison of expected velocity gradients G (slope of the solid line in Figure 71) and G_3 from a curve-fit of the three MnPIV datapoints (slope of the dashed line in Figure 71) for the six different shear rates. The last column represents the slip lengths obtained for these cases.

G [s^{-1}]	G_3 [s^{-1}]	$\lvert G_3 - G\rvert/G$ [%]	b [nm]
2255	2160	4.2	2.4
2029	1923	5.2	6.6
1720	1756	2.1	5.2
1412	1466	3.9	-13.9
983	1099	11.8	-2.0
491	540	9.9	7.7

The slip length b for each case can then be obtained by extrapolating these linear curve-fits to the z-position where $U = 0$. The slip length results for the 10 mM NH_4HCO_3, bare channel case are given in the last column of Table 9. Note that negative values of b denote that U goes to zero above the wall (*i.e.*, at a z-location inside the flow). For each case, the 95% confidence interval in the measured slip length was estimated based on uncertainties in the measured velocities and therefore the uncertainties in the linear curve-fit parameters (Appendix C).

Figure 72 graphs the slip lengths determined from the MnPIV results for all the flows studied here through the (a) bare and (b) hydrophobically-coated channels as a function of the shear rate. The error bar in each sub-figure represents the 95% confidence interval, or twice the standard deviation, in the measured slip lengths averaged over all 24 cases. The average standard deviation in b was 27 nm and 31 nm in the hydrophilic and hydrophobic channels, respectively. Though some of the papers using tracer-based velocimetry techniques to measure slip length, do not report measurement uncertainties (and it is unclear whether these uncertainties are 95% confidence intervals or standard deviations), Joseph and Tabeling [83] reported an uncertainty of about 100 nm in their slip length estimate obtained from μPIV data.

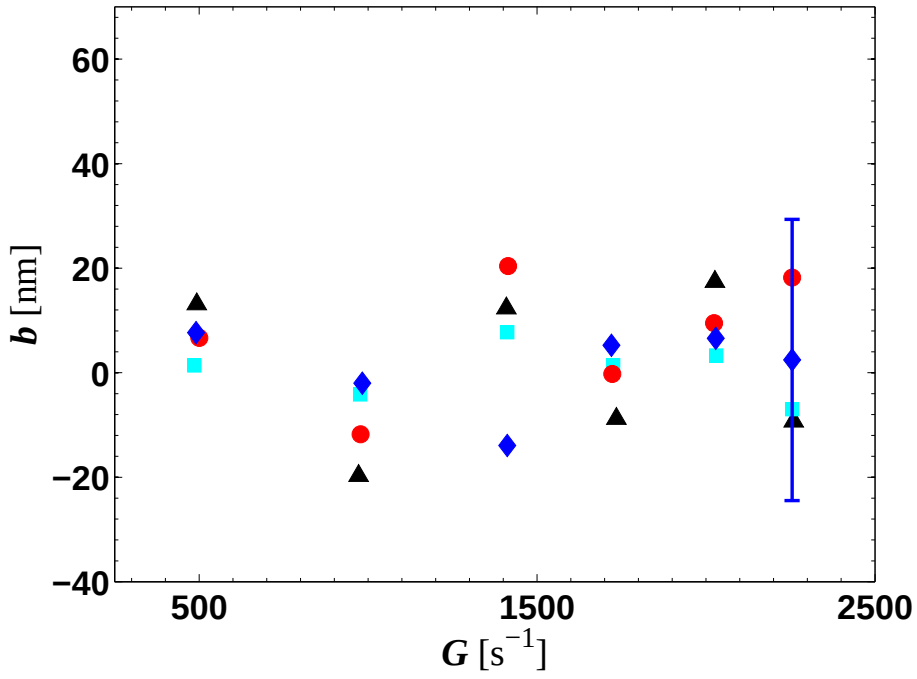

(a)

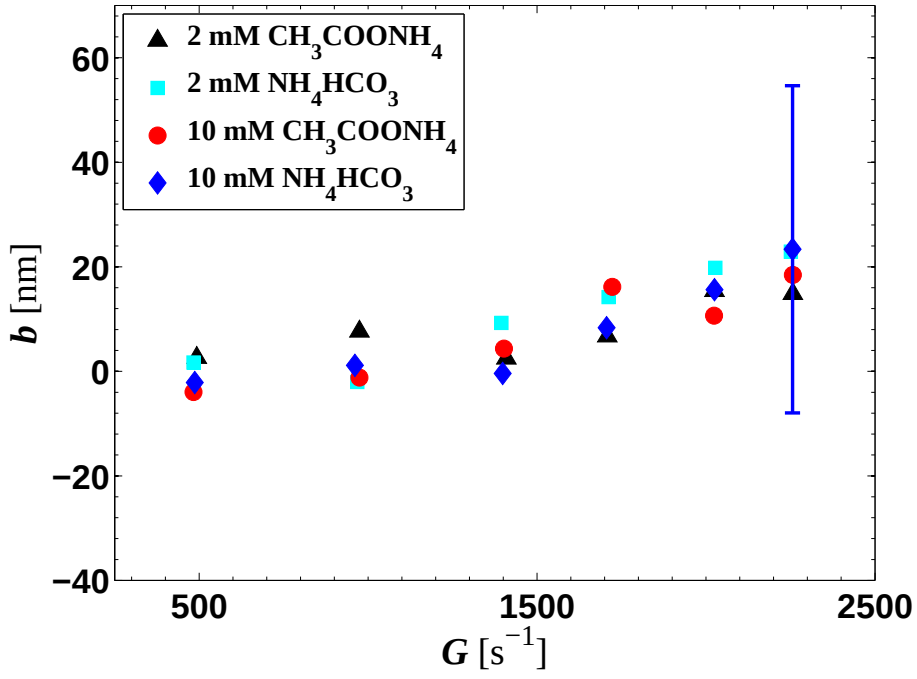

(b)

Figure 72: Graphs of slip lengths b obtained for the Poiseuille flow of aqueous 2 mM and 10 mM NH_4HCO_3 and CH_3COONH_4 solutions (*cf.* legend) through (a) bare and (b) hydrophobically-coated channels as functions of shear rate G. The error bars denote typical 95% confidence intervals for b determined based on the uncertainties in the linear curve-fits.

Schmatko et al. [164, 165] estimated the uncertainties of their slip length obtained using TIR-FRAP to be about 50 nm. Finally, Joly et al., who inferred their slip length from the measurements of hindered Brownian diffusion coefficients using FCS, reported an uncertainty of 5 nm in b. The experimental uncertainties reported here for MnPIV data are therefore less than those for either μPIV or TIR-FRAP.

Figure 72a shows that both positive and "negative" slip lengths, all with magnitudes of less than 20 nm, were found for the hydrophilic channels. These results suggest that the slip lengths are in all cases within the experimental uncertainty which is on average 27 nm for the hydrophilic surfaces.

For the results obtained in the hydrophobically-coated channel (Figure 72b), however, most of the slip lengths are positive and appear to increase with the shear rate. Studies using tracer-based velocimetry [72], volume flow rate based [29] and AFM-based force data [125] have also reported slip lengths that vary with G, albeit at much higher shear rates: 8000 s^{-1} for Neto et al. [125] and 10^5 s^{-1} for Choi et al. [29].

The maximum slip length in the hydrophobic channel based on a linear curve-fit of the MnPIV data is about 25 nm at the highest shear rate. This slip length value is consistent with several studies [95, 81, 29] that have also reported slip lengths less than 50 nm. Choi et al. [29] reported $b \leq 30$ nm from flow rate measurements for the Poiseuille flows of water through OTS-coated microchannels. Lasne et al. [95], who used an evanescent-wave based velocimetry technique, obtained $b = 45$ nm for water flowing over glass surfaces with OTS coating. Joly et al. [81] who inferred a slip length of 18 nm from their measurements of the near-wall Brownian diffusion coefficients for tracers suspended in water above an OTS-coated surface. Slip lengths much larger than these values have also been reported. Tretheway and Meinhart [186], who reported $b = O(1\ \mu\text{m})$ based on their μPIV data for the Poiseuille flow of water over an OTS-coated surface. Huang et al. [72] reported a slip length of about 100 nm for water over a hydrophobic surface using a technique and flow similar to that used

here.

The results imply that neither the ionic strength nor the pH of the working fluid have much effect upon slip length for the ranges of parameters studied here. This is in agreement with Huang et al. [71], who showed that the slip length was essentially constant over a ten-fold change in salt molar concentration for aqueous NaCl solutions. Given that the studies here only considered a five-fold change in ionic strength, however, b may well be affected by larger changes in I_s. Lumma et al. [110] reported in their FCS studies a 70% drop in the measured slip length over a wetting glass slide when the molar concentration of their NaCl solutions is increased by two orders of magnitude.

Finally, the accuracy of the slip lengths for the hydrophobic cases may be affected by the "stationary particles" that adhere to the OTS-covered fused silica surface. Few, if any, such stationary particles were observed on the hydrophilic walls, which should be more negatively charged than the hydrophobically-coated fused-silica surfaces.

Although the projected area of the stationary particles occupy only 0.01% the full image area, these particles could affect these results in several aspects. First, as discussed in the previous Section, images of these stationary particles can cause difficulties when post processing the experimental images. Though care was taken to photobleach these particles before recording the 600 image pairs for each experimental run, these relatively dim images may still cause errors in the results for the hydrophobic channels since accurate particle image intensities are required to obtain estimates of the particles' z-positions. Second, a wall partially covered with stationary particles is effectively a surface with uneven OTS coverage. Such "incomplete" coverage may significantly reduce b; Pit et al. [140] reported that their measured values of slip length decreased by a factor of four for "even a slightly incomplete" OTS coating. This effect, unfortunately, can not be quantified with the current experimental setup. Third, stationary particles may prevent mobile particles from approaching the solid

wall because of both the excluded volume effect and the inter-particle repulsive electrostatic forces (assuming that the particles adhered to the wall are still negatively charged). Finally, the disturbance to the evanescent-wave illumination due to elastic scattering of the wave by these stationary particles is found to be negligible since the intensity of the scattered light at any direction scales with $1/r^2$ (where r is the distance measured from the particle center) and the average inter-particle distance is estimated to be more than 50 particle radii based on the volume fraction of the particles in the bulk of the fluid.

7.3 Summary

In this chapter, slip lengths were measured using MnPIV for aqueous 2 mM and 10 mM ammonium bicarbonate and ammonium acetate solutions over both hydrophilic bare and hydrophobic OTS-coated fused silica surfaces. The particle distribution results along the direction normal to the wall indicate that the distribution varies with the ionic strength of the solution and shifts slightly towards the wall as the solution ionic strength increases. The OTS coating also appears to affect the near-wall particle distribution slightly, shifting the particles closer to the wall, presumably due to the coating reducing the magnitude of the negative surface charge.

The particle distributions were then used to divide the particles into three layers which contain roughly equal number of particles. The average velocity of each layer was then placed at the mean z-position of the layer that is sampled by the particles determined from the distribution curve. These velocity data points were then curve-fit to a linear function to obtain the velocity gradient and the slip length.

The velocity gradients G_3 were determined as the slope of linear curve-fits of the three velocity data points without assuming any boundary condition at the wall and were compared with the values G obtained based on the predicted near-wall velocity profile using Equation 24 and the measured pressure gradient, channel depth and

viscosity of the working fluid. For the data obtained at the six nominal driving pressure gradients over all the working fluid-channel combinations, the maximum discrepancy between G_3 and G is within 13% (Appendix A). The discrepancy is typically biggest for the lower driving pressure gradients.

Slip lengths b were also determined from linear curve-fits of the MnPIV data for both the bare and coated microchannels. The measured b in the bare channel shows no dependence on shear rate G and its magnitude for all cases is within the experimental uncertainty ($\sigma_b = 27$ nm). For the OTS-coated channel, however, the values for b have much less "scatter" than those for the hydrophilic case, and the slip lengths appear to increase with shear rate G, reaching a maximum of about 25 nm at the highest shear rate of the study $G = 2250$ s^{-1}. Even this maximum value is still less than the measurement uncertainty ($\sigma_b = 31$ nm) for the hydrophobically-coated surfaces. Finally, the results for both hydrophilic and hydrophobic channels suggest that the properties (*e.g.*, pH and ionic strength) of the working fluids have little, if any, effect on the measured b.

CHAPTER VIII

CONCLUSIONS AND RECOMMENDATIONS

The major objectives of this doctoral thesis are: 1) to develop and validate a tracer-based technique, using evanescent-wave illumination to measure the two tangential velocity components at different z-distances from and within about 500 nm of the wall; and 2) to use this technique to study liquid slippage over solid walls of varying wettability. The feasibility of the technique, multilayer nano-particle image velocimetry (MnPIV), was first evaluated using synthetic images of plane Couette flows. The errors in MnPIV data due to the non-uniform illumination and the asymmetric Brownian diffusion of the tracers in the near-wall region were quantified with Brownian dynamics simulations. After determining the correlation between the image intensity of the particle and its distance from the wall from separate calibrations, MnPIV was used to determine the particle distribution as a function of z in experimental studies of incompressible, steady and fully-developed Poiseuille flow in microchannels. The tracers were then divided into three distinct layers and the temporally and spatially averaged velocity of the three layers and the velocity gradients were determined. Finally, MnPIV was used to measure slip lengths for the Poiseuille flow in microchannels of aqueous ammonium bicarbonate and ammonium acetate solutions over naturally hydrophilic and hydrophobically-coated fused silica surfaces. This chapter presents the conclusions and contributions of this investigation and recommendations for future work.

8.1 Conclusions

8.1.1 Studies using Synthetic Images and Brownian Dynamics Simulation

The feasibility and accuracy of MnPIV were studied using synthetic images of plane Couette flow incorporating hindered Brownian diffusion, non-uniform illumination and image noise. The results demonstrate that the obtained MnPIV results over three sub-layers (50 nm $< z \leq$ 80 nm, 80 nm $< z \leq$ 135 nm, and 135 nm $< z \leq$ 350 nm, respectively) are within 6% of the values averaged over the "true" particle locations recorded when creating the images. These investigations also showed that both the hindered Brownian diffusion and the non-uniform illumination cause errors in the measured velocities.

The studies indicated that the exponentially decaying intensity of the evanescent-wave illumination leads to an underestimation of the velocity obtained with cross-correlation approaches; this underestimation increases with an increase in the range of particle image intensities within a single frame. Using particle-tracking (*vs.* cross-correlation) methods to determine velocities gave velocities that were within 4% of the expected value.

The in-plane Brownian diffusion of the tracers increases the uncertainty in the measured displacements; This uncertainty can be minimized by averaging either the correlation functions or, alternatively, the actual displacements. The Brownian diffusion of the particles along the direction normal to the image (*i.e.*, along the optical axis) moves the tracers randomly into and out of the region illuminated by evanescent wave, resulting in particle mismatch, which further increases the uncertainty in the velocities obtained with MnPIV. Simulations using synthetic images showed that this particle mismatch could be reduced by either increasing the size of the interrogation windows or by reducing the time interval within the image pair.

The asymmetric and hindered out-of-plane Brownian diffusion of the tracers in the near-wall region, which increases the probability that the particle moves away

from, *vs.* towards, the wall, can lead to overestimation of near-wall velocities. This effect was quantified by determining the probability distribution functions (PDFs) of z-positions sampled by an ensemble of matched particles over a given time interval using Brownian dynamics simulations. These PDFs can be used to determine this Brownian diffusion-induced overestimation for a linearly varying velocity profile as a function of three experimental parameters: the particle radius a, the thickness of the region of interest in the wall-normal direction Z and the time interval within one image pair Δt. The results show that the overestimation can be reduced by either reducing the diffusion (*e.g.* by using bigger tracers or a shorter time interval within the image pair Δt) or increasing the thickness of the ROI.

8.1.2 Experimental Measurements of Particle Distributions, Velocities and Velocity Gradients

Calibrations were carried out to determine how the image intensity of 500 nm diameter particles illuminated by evanescent waves varied with the particle's distance normal to and measured from the wall. For the calibrations where the separation distance is controlled by a micro-translation state, the results demonstrated that the particle image intensity decays exponentially with the distance between the particle and the wall with a characteristic length scale within 9% of z_p, the penetration depth of the evanescent-wave illumination. It is therefore possible to estimate the distance between the particle and wall $h = z_\mathrm{p} \ln(I_\mathrm{p}^0/I_\mathrm{p})$ from the particle image intensity I_p, the penetration depth of the evanescent wave z_p and the image intensity of particles fixed on the wall I_p^0. The uncertainty in the measured z-positions is estimated to be about 20 nm.

Multilayer nPIV was used to determine the particle distribution along the direction normal to the wall for $z \leq 400$ nm in experimental studies of incompressible, steady and fully-developed Poiseuille flows of water and aqueous solutions of sodium tetraborate (C = 1 mM, 10 mM and 20 mM) through microchannels. The results

showed that for water, there are almost no particles within three particle radii of the wall presumably due to the electrostatic repulsion between the fused silica surface and the carboxylate-modified polystyrene particles. The addition of even a small amount of salt (1 mM $Na_2B_4O_7$) reduced the z-extent of this particle depletion region to about one particle diameter, in part because the increase in ionic strength reduces the thickness of the electrical double layer (EDL) on both the particle and wall surfaces and the change in pH between Nanopure water (pH 5.5) and the $Na_2B_4O_7$ solutions (pH 9) alters the wall zeta-potentials of the particles and the fused silica. The results also show increasing the salt molar concentration (from 1 mM to 10 mM and 20 mM) has a minimal effect on the particle distribution, although the particles do move slightly closer to the wall as C increases, presumably due to the associated decrease in the EDL thickness. The non-uniform near-wall tracer distribution affects the average z-location and hence the near-wall velocities sampled by the matched particles.

These experimentally determined particle distributions were used to "bin" the particles into three distinct layers spanning different ranges of z for $z < 500$ nm. The temporally and spatially averaged velocity of each layer, determined by particle tracking, was placed at the average z-position sampled by the particles in that layer, based on the measured particle distribution. The velocity gradients obtained with MnPIV were within 6% on average of predictions based on the analytical solution for two-dimensional Poiseuille flow using the measured pressure gradient, the viscosity of the working fluid and the depth of the microchannel.

8.1.3 Slip Lengths Measured with MnPIV

MnPIV was used to measure the near-wall velocities in the Poiseuille flow of aqueous solutions of ammonium bicarbonate and ammonium acetate at molar salt concentrations of 2 mM and 10 mM through fused-silica microchannels with both bare and hydrophobically-coated walls. The measured particle distributions vary with the

properties of the working fluids (pH and ionic strength) and shift slightly towards the wall for the coated channels presumably because the hydrophobic coating reduces the magnitude of the wall zeta-potential (*i.e.*, makes the walls less negatively charged). Velocities obtained using MnPIV at three different distances from the wall were used to determine the slip lengths. The results for the bare channel show that the measured slip lengths, which fluctuate about zero, have magnitudes less than 20 nm, which is within the experimental uncertainty. For the OTS-coated channel, the measured slip lengths have much less variation, and appear to increase with shear rate, reaching a maximum of 25 nm, a value that is also less than the uncertainty in b. Given that the average uncertainty for the results obtained inside the bare and coated channels are 27 nm and 31 nm, respectively, we conclude from these MnPIV studies that the slip lengths for the hydrophilic and hydrophobic cases are less than 27 nm and 31 nm, respectively, for this range of shear rates (G = 490 to 2250 s^{-1}). The greatest error in these slip length data is likely to be the contamination of the coated fused silica surface due to a significant number of negatively charged tracers adhering to the nearly neutrally charged OTS-coated fused-silica surface.

8.2 Contributions

The main contribution of this thesis, which is to our knowledge the first experimental demonstration of this new near-wall velocimetry technique, include:

1. Development and validation of the multilayer nano-particle image velocimetry (MnPIV) technique for measuring velocity components tangential to the wall at multiple distances from and within 400 nm of the wall [101, 102].

2. Quantification of the errors in MnPIV due to the non-uniform nature of evanescent-wave illumination and the asymmetric and hindered Brownian diffusion of near-wall particles using Brownian dynamic simulations. These analyses are valid for

any near-wall tracer-based velocimetry techniques utilizing evanescent-wave illumination [157, 156].

3. Experimental measurements showing that the near-wall particle distribution is highly nonuniform, with almost no particles within about a particle diameter of the wall, for various aqueous solutions of different pH and ionic strengths, and the conclusion that not accounting for this non-uniform distribution can introduce significant errors in near-wall tracer-based velocity data [102].

4. The experimental application of MnPIV to measure near-wall velocity gradients, and hence wall shear stress, with an average error of 6% in Poiseuille flows through microchannels [102].

5. The experimental application of MnPIV to measure slip lengths for the Poiseuille flow of aqueous solutions of ammonium salts over both hydrophilic bare and hydrophobically coated fused-silica surfaces. The results suggest that if the slip lengths are nonzero for both of these surfaces, they are less than the uncertainty in these results, or 27 nm and 31 nm for the hydrophilic and hydrophobic channels, respectively.

8.3 Recommendations for Future Work

Although this study has established the feasibility and capabilities of MnPIV, the results presented in this thesis suggest a number of potential improvements in the technique for the continuing work:

1. The current model for predicting the overestimation in the measured velocity of MnPIV should be modified to account for other particle-wall interactions (*e.g.*, electrostatic forces). The effect of a nonzero exposure time should also be included in the model to make it a more realistic approximation of actual MnPIV experiments.

2. The use of objective-based (or prismless) total internal reflection microscopy should be considered. This configuration greatly reduces the optical pathlength of the laser beam through the microchannel because it utilizes the microscope objective to guide the illumination beam to the fluid-wall interface that generates the evanescent wave. This reduced pathlength will enable the use of microchannels fabricated in other materials of lower optical quality such as PDMS, greatly reducing the complexity and cost of channel fabrication.

3. Using smaller tracers should be considered to improve the spatial resolution of the technique. For example, quantum dots with hydraulic diameters around 10 nm are already being considered for near-wall velocity measurements [142].

4. Varying the surface charge of both the particles and the microchannel walls by, for example, absorbing surfactants onto the particle and microchannel surfaces [80], should also be considered to reduce the extent of the particle depletion layer and improve the near-wall spatial resolution of MnPIV. Changing the surface charge of the particles may also improve the accuracy of MnPIV studies of slip. As shown in Chapter 7, the OTS-coated fused-silica surfaces are nearly neutrally charged. This reduction in the magnitude of the wall zeta-potential significantly increases the number of negatively charged tracers that adhere to the surface, and this surface contamination may affect the accuracy of the slip length estimates obtained in these studies.

APPENDIX A

SLIPPAGE OF AQUEOUS SOLUTIONS OVER SOLID SURFACES WITH VARYING WETTABILITY: MORE RESULTS

This appendix presents the remainder of the experimental MnPIV results on velocities, velocity gradients and slip lengths for Poiseuille flows of 2 mM and 10 mM aqueous ammonium bicarbonate (NH_4HCO_3) and ammonium acetate (CH_3COONH_4) solutions through bare and hydrophobic OTS-coated fused silica microchannels. Figure 73 and Table 10 give results for the Poiseuille flows of 10 mM CH_3COONH_4 through the bare channel at nominal shear rate $G = 501$ (●), 978 (◀), 1414 (⧫), 1723 (▲), 2024 (■) and 2255 (▼) s^{-1}. The boundaries of the three layers in all cases are: I) $z = 50$ nm-150 nm; II) $z = 150$ nm-250 nm; and III) $z = 250$ nm-350 nm.

Table 10: Comparison of expected velocity gradients G (*i.e.*, the slope of the solid line in Figure 73) and the velocity gradients obtained from linear curve-fits of the three MnPIV datapoints G_3 (*i.e.*, the slope of the dashed line in Figure 73) for the Poiseuille flow of 10 mM CH_3COONH_4 through the bare channel at six different shear rates. The last column lists the slip lengths obtained also from the linear curve-fits of the MnPIV data for these cases.

G [s^{-1}]	G_3 [s^{-1}]	$\lvert G_3 - G\rvert/G$ [%]	b [nm]
2255	2065	8.4	18.2
2024	1956	3.4	9.5
1723	1653	4.1	-0.2
1414	1281	9.4	20.4
978	971	0.7	-11.8
501	463	7.5	6.7

Figure 74 and Table 11 present MnPIV results for the Poiseuille flow of 2 mM

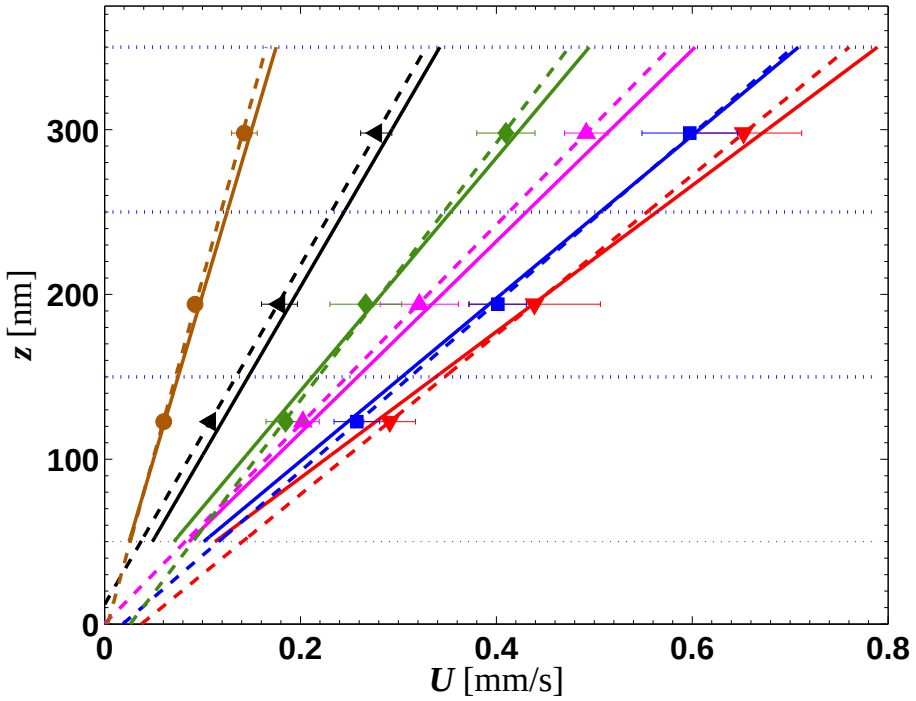

Figure 73: MnPIV velocity profiles of the average velocity U as a function of the wall-normal position of the particle center z in the three layers (points) for 10 mM CH_3COONH_4 at G = 501 (●), 978 (◀), 1414 (◆), 1723 (▲), 2024 (■) and 2255 (▼) s^{-1}. The dashed lines denote linear curve-fits of the MnPIV points, while the solid lines represent the velocity profile predicted by the analytical solution for 2D Poiseuille flow. The error bars represent the 95% confidence interval.

NH_4HCO_3, while Figure 75 and Table 12 show results for the flow of 2 mM CH_3COONH_4 both through the bare channel. Figure 76 and Table 13 show velocities and velocity gradients for 10 mM NH_4HCO_3 and Figure 77 and Table 14 show these data for 10 mM CH_3COONH_4, both inside the OTS-coated hydrophobic channel. Finally, the results for 2 mM NH_4HCO_3 and 2 mM CH_3COONH_4 inside the OTS-coated channel are given in Figure 78 and Table 15 and Figure 79 and Table 16, respectively.

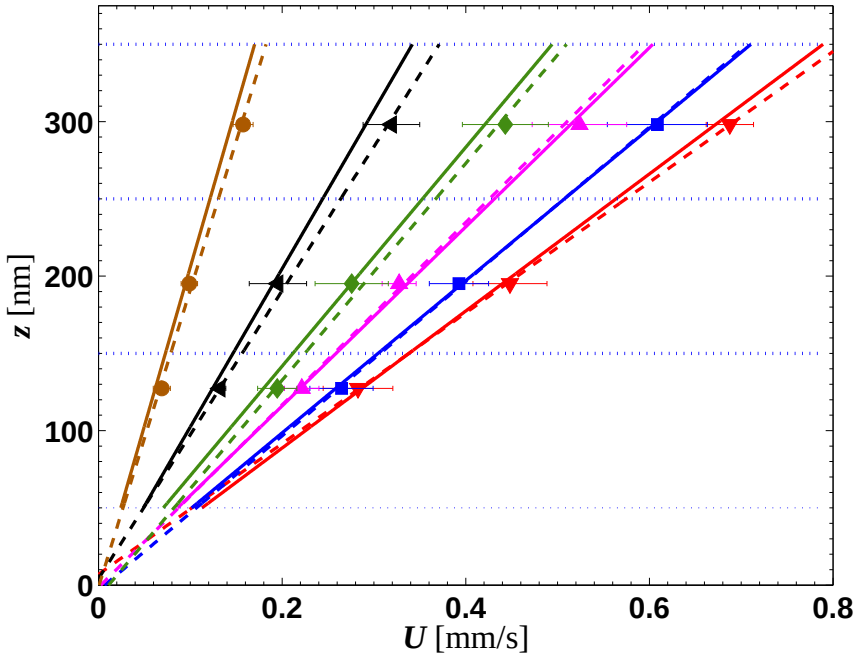

Figure 74: Similar to Figure 73, but for 2 mM NH_4HCO_3 in the bare channel at $G =$ 486 (●), 977 (◀), 1412 (◆), 1725 (▲), 2030 (■) and 2255 (▼) s^{-1}.

Table 11: Similar to Table 10, but for 2 mM NH_4HCO_3 in the bare channel

G [s^{-1}]	G_3 [s^{-1}]	$\lvert G_3 - G\rvert/G$ [%]	b [nm]
2255	2364	4.9	-7.0
2030	2002	1.4	3.3
1725	1693	1.8	1.5
1412	1425	1.0	7.7
977	1073	9.9	-4.1
486	520	6.9	1.4

Table 12: Similar to Table 10, but for 2 mM CH_3COONH_4 in the bare channel.

G [s^{-1}]	G_3 [s^{-1}]	$\lvert G_3 - G\rvert/G$ [%]	b [nm]
2260	2356	4.3	-9.3
2026	1849	8.7	17.4
1735	1799	3.7	-8.8
1409	1361	3.4	12.3
972	1107	13.9	-19.7
493	519	5.3	13.1

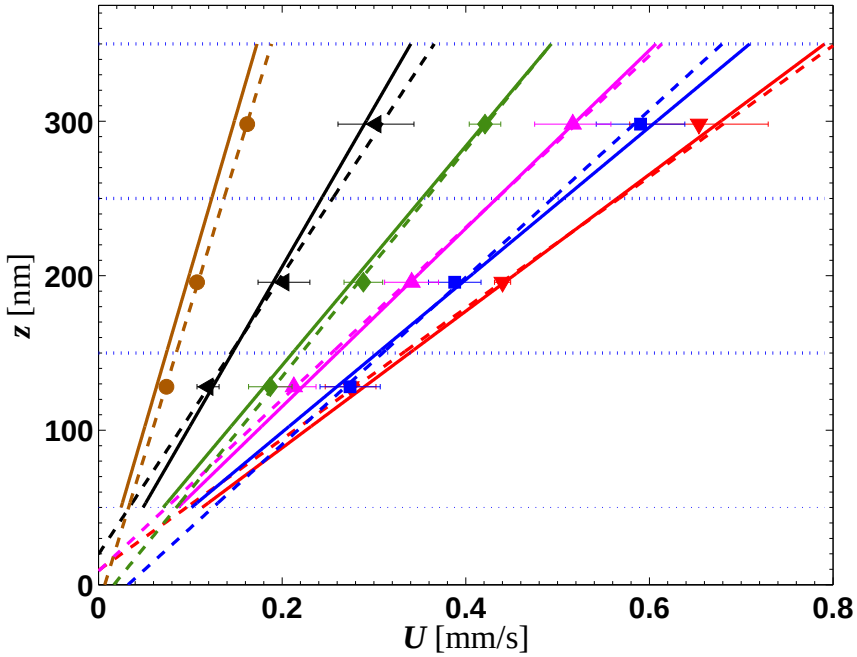

Figure 75: Similar to Figure 73, but for 2 mM CH_3COONH_4 in the bare channel at G = 493 (●), 972 (◀), 1409 (♦), 1735 (▲), 2026 (■) and 2260 (▼) s^{-1}. The dashed lines denote a linear curve-fits of the MnPIV points. The error bars represent the 95% confidence interval.

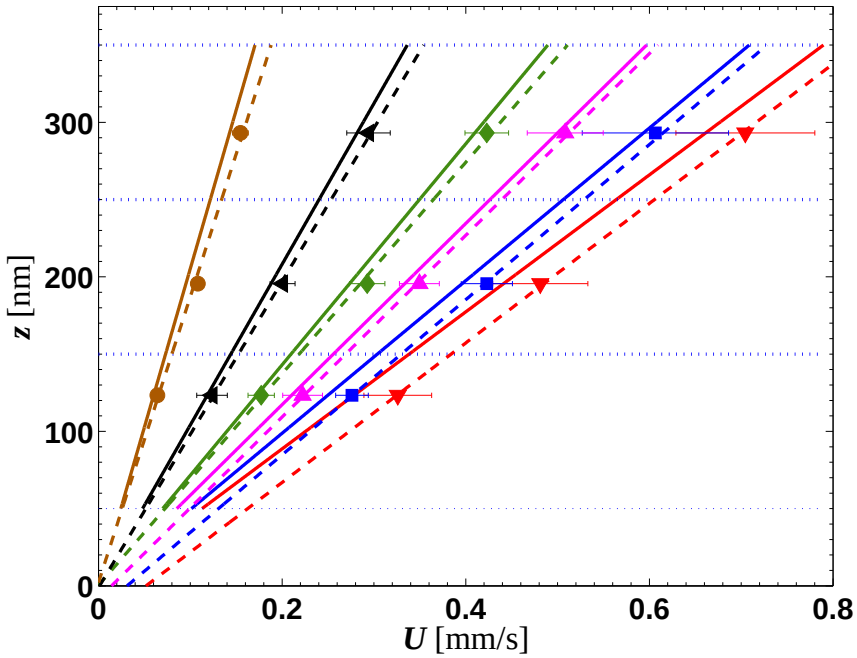

Figure 76: Similar to Figure 73, but for 10 mM NH_4HCO_3 in the coated channel at G = 487 (●), 961 (◀), 1398 (♦), 1706 (▲), 2025 (■) and 2256 (▼) s^{-1}. The dashed lines denote a linear curve-fits of the MnPIV points. The error bars represent the 95% confidence interval.

Table 13: Similar to Table 10, but for 10 mM NH_4HCO_3 in the coated channel.

G [s^{-1}]	G_3 [s^{-1}]	$\lvert G_3 - G\rvert/G$ [%]	b [nm]
2256	2215	1.8	23.4
2025	1992	1.6	15.6
1706	1701	0.3	8.4
1398	1461	4.5	-0.4
961	1009	5.0	1.1
487	541	11.0	-2.1

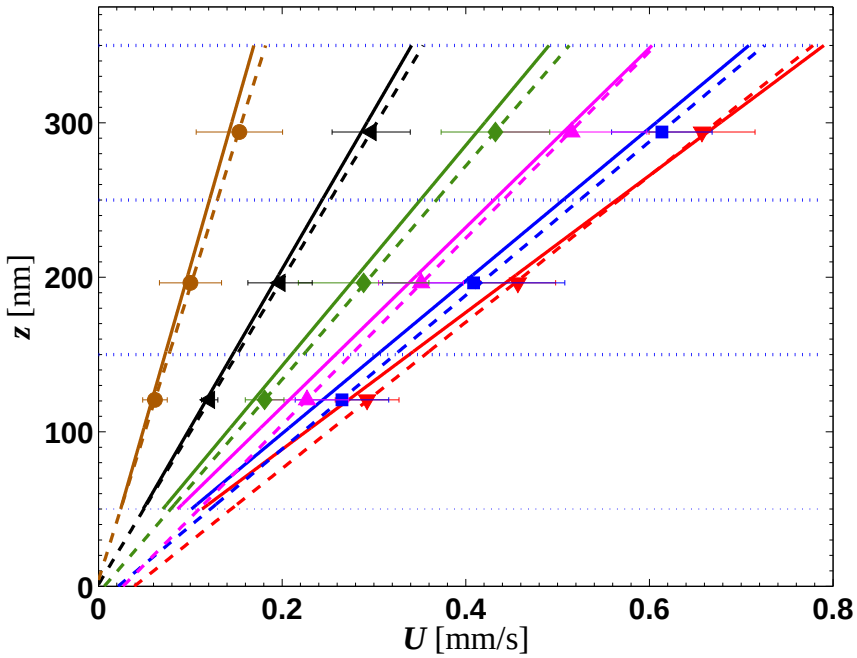

Figure 77: Similar to Figure 73, but for 10 mM CH_3COONH_4 in the coated channel at $G = 484$ (•), 974 (◀), 1402 (♦), 1723 (▲), 2024 (■) and 2257 (▼) s^{-1}. The dashed lines denote a linear curve-fits of the MnPIV points. The error bars represent the 95% confidence interval.

Table 14: Similar to Table 10, but for 10 mM CH_3COONH_4 in the coated channel.

G [s^{-1}]	G_3 [s^{-1}]	$\lvert G_3 - G\rvert/G$ [%]	b [nm]
2257	2112	6.4	18.5
2024	2011	0.6	10.7
1723	1657	3.8	16.2
1402	1447	3.2	4.4
974	1014	4.1	-1.2
484	526	8.8	-3.9

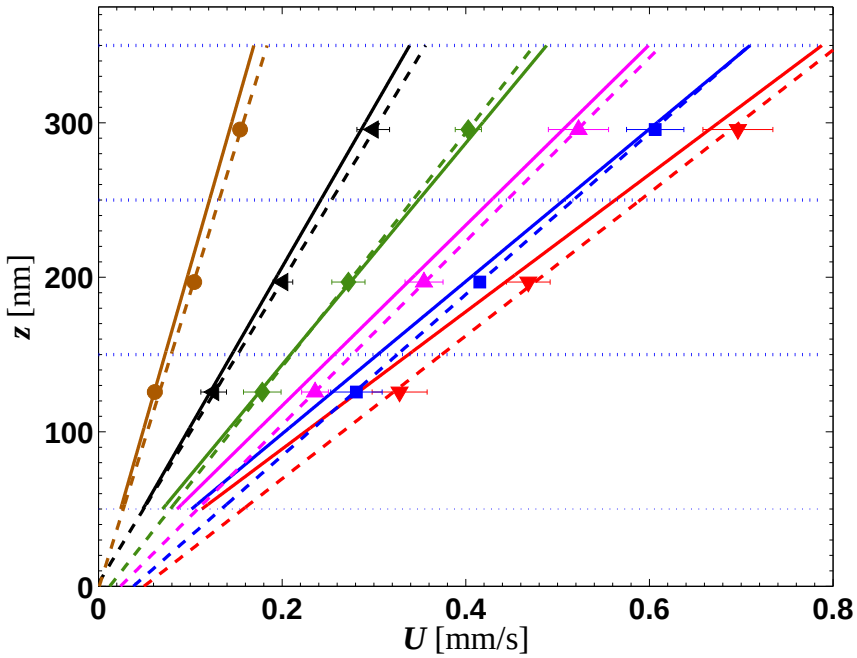

Figure 78: Similar to Figure 73, but for 2 mM NH_4HCO_3 in the coated channel at G = 484 (●), 968 (◀), 1395 (♦), 1712 (▲), 2028 (■) and 2251 (▼) s^{-1}. The dashed lines denote a linear curve-fits of the MnPIV points. The error bars represent the 95% confidence interval.

Table 15: Similar to Table 10, but for 2 mM NH_4HCO_3 in the coated channel.

G [s^{-1}]	G_3 [s^{-1}]	$\lvert G_3 - G\rvert/G$ [%]	b [nm]
2251	2162	3.9	22.9
2028	1917	5.5	19.8
1712	1684	1.6	14.2
1395	1321	5.3	9.3
968	1024	5.8	-2.0
484	522	8.0	1.7

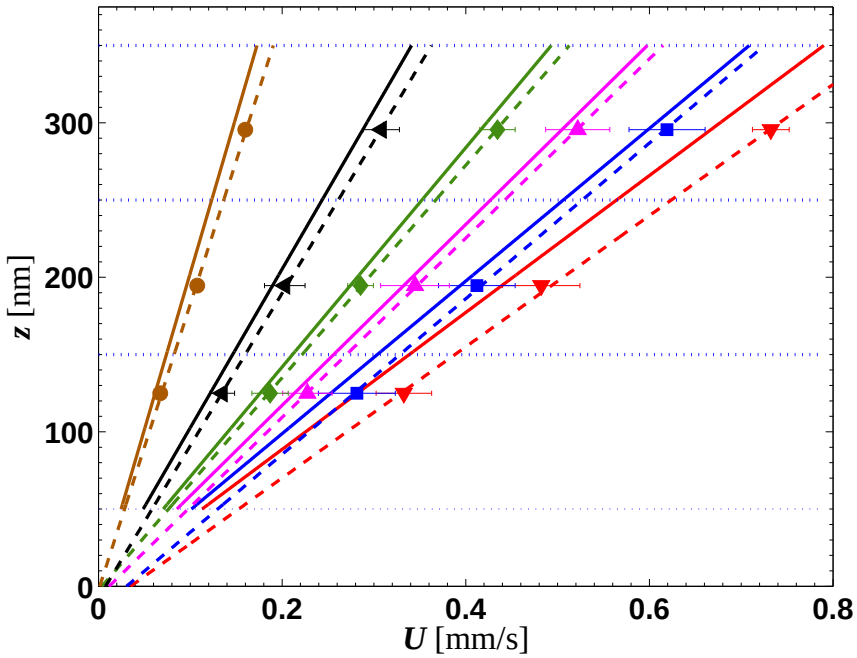

Figure 79: Similar to Figure 73, but for 2 mM CH_3COONH_4 in the coated channel at $G = 493$ (●), 974 (◀), 1409 (◆), 1708 (▲), 2025 (■) and 2257 (▼) s^{-1}. The dashed lines denote a linear curve-fits of the MnPIV points. The error bars represent the 95% confidence interval.

Table 16: Similar to Table 10, but for 2 mM CH_3COONH_4 in the coated channel.

G [s^{-1}]	G_3 [s^{-1}]	$\lvert G_3 - G\rvert / G$ [%]	b [nm]
2257	2210	2.1	25.1
2025	1985	2.0	15.4
1708	1724	0.9	6.7
1409	1455	3.2	2.5
974	1014	4.1	7.7
493	540	9.5	2.6

APPENDIX B

EVALUATION OF AN ALGORITHM FOR MEASURING "IN-PLANE" BROWNIAN DIFFUSION COEFFICIENT

The utility of a technique originally proposed for measuring the diffusion coefficients of non-colloidal spheres (on average $a = 45$ μm) in concentrated suspensions [18] was evaluated for estimating the Brownian diffusion coefficient of colloidal particles with a diameter $a \leq 0.25$ μm. An overview of the technique is first given in Section B.1, followed by descriptions of the tests of the technique with synthetic and experimental image in Sections B.2 and B.3, respectively.

B.1 Overview of the Method

Given its stochastic nature, Brownian diffusion is usually characterized by the diffusion coefficient, which can be obtained from the probability distribution function (PDF) of particle displacements over a given time interval Δt. Since a typical PIV image pair records the two-dimensional particle positions at two instants separated by a short interval Δt, such images can also be used to estimate the Brownian diffusion coefficient. Researchers have used several different methods to extract the Brownian diffusion coefficient from PIV (specifically, μPIV and nPIV) images. the method of Hohreiter et al. [67], who suggested that the diffusion coefficient could be determined from the width of the cross-correlation function of an image pair, is susceptible to errors due to background noise in the images, which can significantly broaden the correlation peak. Alternatively, a PDF of particle displacements can be built up by determining the displacements of inidividual particles using one-to-one particle matching [6, 70], similar to particle tracking velocimetry (PTV). Although

various particle matching algorithms have been proposed and tested in the literature, it becomes less accurate with increasing Δt because the probability that a particle will become "mismatched" due to its out-of-plane Brownian diffusion increases with Δt (*cf.* Section 4.2.2).

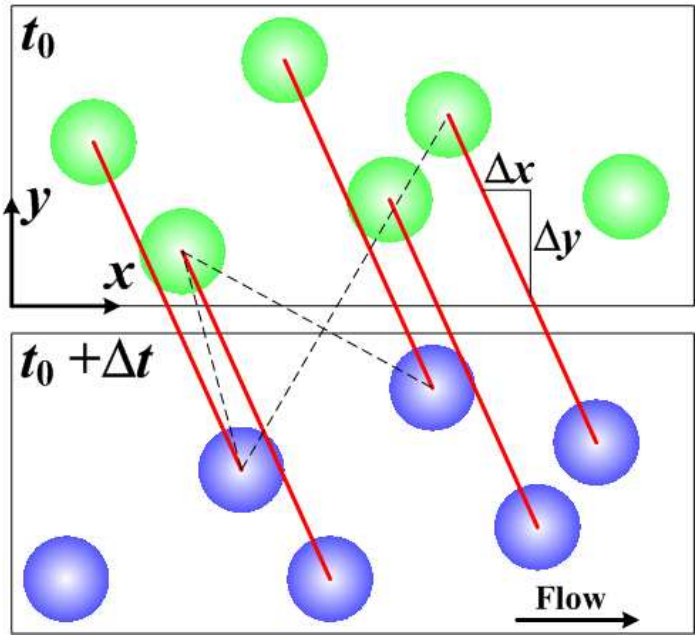

Figure 80: A group of particles imaged at times t_0 and $t_0 + \Delta t$.

Given the marked effects of Brownian diffusion in typical μPIV or nPIV images, a technique that does not require one-to-one particle matching was evaluated in these studies. Consider two images, or an image pair, of colloidal particles ($a \leq 0.25$ μm and $\rho = 1.05$ g/cm^3) suspended in water and convected by a uniform flow that are acquired at two times, namely t_0 and $t_0 + \Delta t$ (Figure 80). The particle centers are first located in the two images, where $(x_\mathrm{i}, y_\mathrm{i})$, $i = 1, 2, ..., N_1$ and $(X_\mathrm{j}, Y_\mathrm{j})$, $j = 1, 2, ..., N_2$ denote the positions of the particle centers in the first and second images, respectively. Then all the possible 2D particle displacement vectors between $(x_\mathrm{i}, y_\mathrm{i})$ and $(X_\mathrm{j}, Y_\mathrm{j})$ are calculated:

$$\Delta \mathbf{X}_{\mathrm{j,\,i}} = (\Delta x_{\mathrm{j,\,i}}, \Delta y_{\mathrm{j,\,i}}) = (X_\mathrm{j} - x_\mathrm{i}, Y_\mathrm{j} - y_\mathrm{i}). \tag{32}$$

A 2D histogram $H(\Delta x, \Delta y)$ of these vectors can then be constructed from the displacement vectors obtained from a number of image pairs.

For each particle shown in the first exposure at t_0, there is at most one particle image in the second exposure at $t_0 + \Delta t$ that is from the same particle or "matches" the particle image in the first exposure. The set of all possible displacement vectors $\Delta \mathbf{X}_{\mathrm{j,\,i}}$ therefore includes both displacement vectors from the particles in the first exposure to the positions of the same particle $\Delta \mathbf{X}_{\mathrm{true}}$ in the second exposure (red solid lines in Figure 80) and those to the positions of "mismatched" particles $\Delta \mathbf{X}_{\mathrm{false}}$ (black dashed lines in Figure 80). While the histogram of the vectors in the former category approximate the PDF of the particle displacements due to the diffusion and flow, the vectors in the latter category are merely noises. It is therefore required to isolate $\Delta \mathbf{X}_{\mathrm{true}}$ from $\Delta \mathbf{X}_{\mathrm{false}}$.

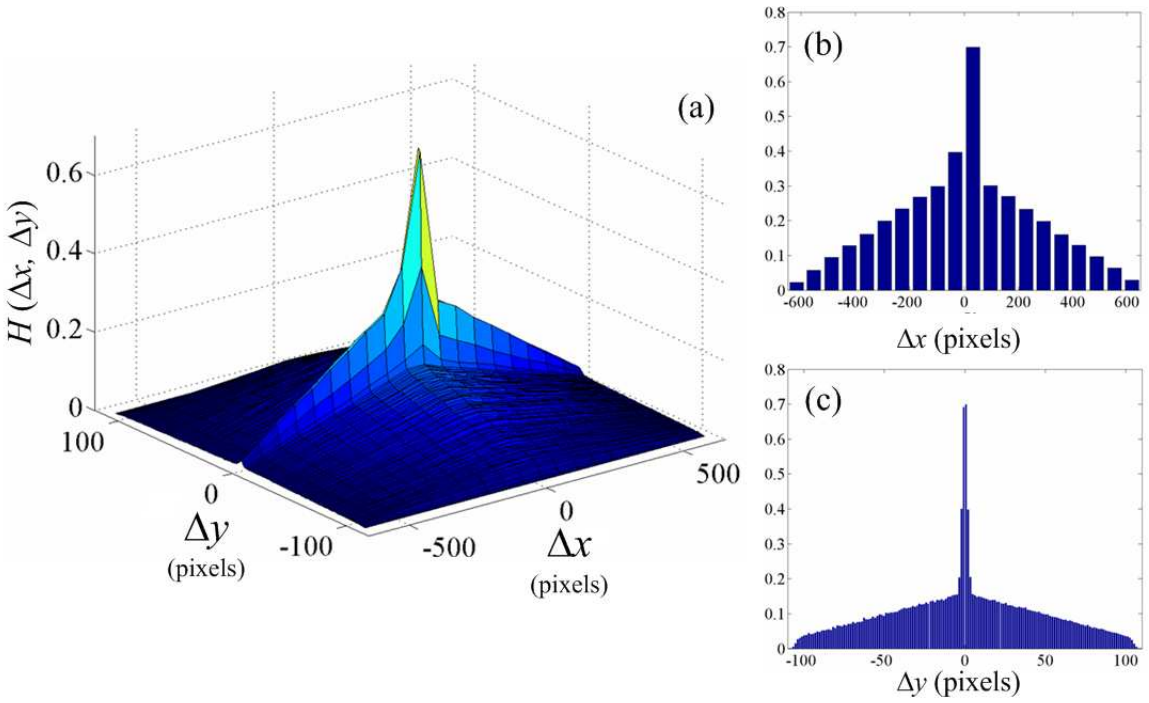

Figure 81: (a). Two-dimensional histogram $H(\Delta x, \Delta y)$ of the particle displacements obtained from the images. The cross sections of $H(\Delta x, \Delta y)$ at $\Delta y = 0$ and $\Delta x = 0$ shown in (b) and (c), respectively.

In the approach originally proposed by Breedveld et al. [18], the "true" particle

displacements $\Delta\mathbf{X}_{\text{true}}$ are separated from the "false" ones $\Delta\mathbf{X}_{\text{false}}$ based on their respective statistics. Figure 81a shows the 2D histogram $H(\Delta x, \Delta y)$, along with its cross-sections at $\Delta y = 0$ (Figure 81b) and $\Delta x = 0$ (Figure 81c). Since the flow is imaged so that the particles are convected by the flow from left to right, the peak associated with the true displacements should be shifted to positive values of $\Delta x \approx U\Delta t$, where U is the velocity. On the other hand, the false displacements should have a distribution that is symmetric about both the Δx and Δy axes. The histogram $H(\Delta x, \Delta y)$ for $\Delta x > 0$ should then contain both true and false displacements, while the histogram for $\Delta x < 0$ only false displacements. Based on this "symmetry argument," the true displacements can be isolated from the false ones simply by subtracting the histogram for $\Delta x < 0$ from that from $\Delta x > 0$:

$$H^{\text{true}}(\Delta x, \Delta y) = H(\Delta x, \Delta y) - H(-\Delta x, \Delta y), \text{ where } \Delta x > 0. \tag{33}$$

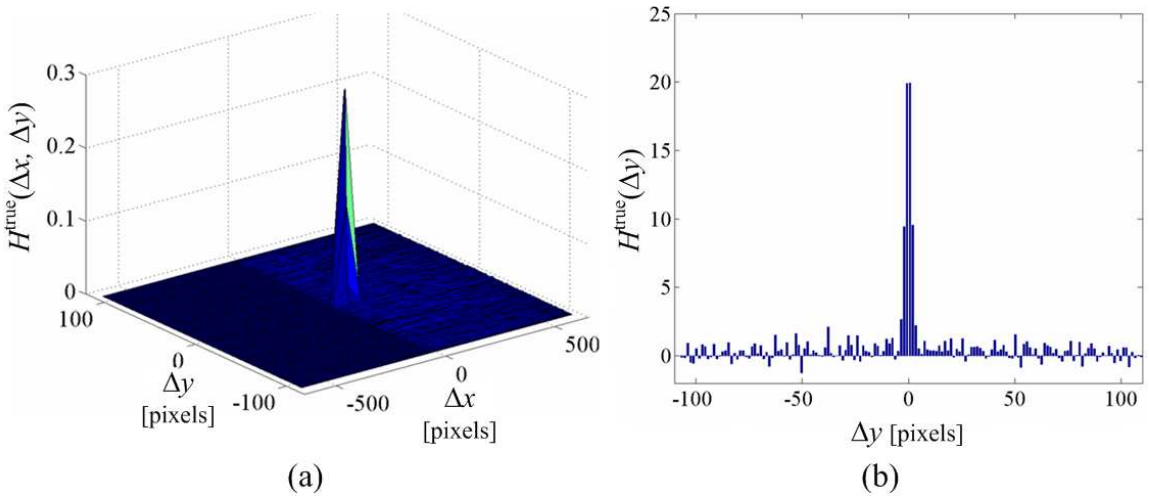

Figure 82: (a). The resultant histogram $H^{\text{true}}(\Delta x, \Delta y)$ after the operation in Equation 33. (b). The 1D displacement histogram $H^{\text{true}}(\Delta y)$ obtained by integrating $H^{\text{true}}(\Delta x, \Delta y)$ as shown in (a) along Δx.

Upon subtraction, the resultant 2D histogram $H^{\text{true}}(\Delta x, \Delta y)$ (Figure 82a) of the true displacement vectors is then reduced to a 1D histogram $H^{\text{true}}(\Delta y)$ by integrating along Δx (Figure 82b). This 1D histogram is then curve-fit to a Gaussian function:

$$H^{\text{true}}(\Delta y) = A \exp\left[-\frac{(\Delta y)^2}{2\sigma_y^2}\right] \tag{34}$$

where $\sigma_y^2 = 2D(\Delta t)$. The Brownian diffusion coefficient D can then be extracted from the curve-fit to the data obtained at a given time interval Δt (Figure 83). Alternatively, D can also be determined by obtaining values of σ_y^2 at different time intervals Δt and finding the slope of a linear curve-fit to a graph of σ_y^2 plotted as a function of Δt.

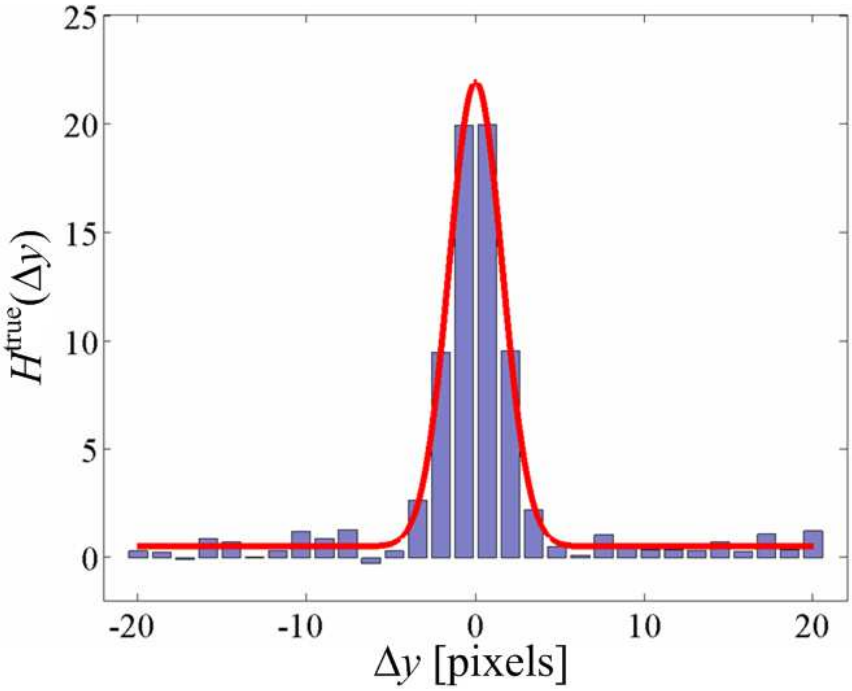

Figure 83: The hitogram $H^{\text{true}}(\Delta y)$ used to determine the Brownian diffusion coefficient. The data are fitted to a Gaussian function as solid line.

B.2 Test with Synthetic Images

Based on the above discussion, this technique requires a flow to shift the true particle displacements and separate them from the false displacements using the symmetry argument. It therefore follows that, there should be a minimum displacement due to the flow below which it may be practically impossible to extract $H^{\text{true}}(\Delta y)$ from the histogram, and hence estimate the diffusion coefficient. Also, the bin size in the

measurement dimension (here, y) b_s should be small enough to sample the peak in $H^{\text{true}}(\Delta y)$ with good spatial resolution. Finally, as discussed previously, particle mismatch due to out-of-plane Brownian diffusion causing particles to randomly "drop in" and "drop out" of imaging plane could also affect the accuracy of the diffusion coefficient measurement. The technique was therefore first tested on synthetic images with a known diffusion coefficient to determine the lower limits on the flow displacement magnitude and the number of bins and to study how particle mismatch affects the accuracy of the measured diffusion coefficients.

Since all measurements were performed far away from walls, synthetic images with uniform particle image intensities were created. For each image pair, about 200 particles that were randomly and uniformly distributed in the first exposure, are convected by a uniform flow and unconfined in-plane Brownian diffusion with a constant diffusion coefficient D_∞ (Equation 6) to their positions in the second exposure. Several tests were carried out with varying parameters, such as the particle radius a, the time interval within one image pair Δt and the flow velocity U.

The individual particle images were located using the method described in Appendix D; the particle positions were processed as discussed in the previous section for various bin sizes b_s. Figure 84 shows the measured diffusion coefficient D_m normalized by the expected value D_∞ as a function of b_s normalized by a lengthscale proportional to the rms displacement due to Brownian diffusion over the interval. The results demonstrate that for $b_s < 2\sqrt{D_\infty \Delta t}$, the measured diffusion coefficient is in good agreement with the expected value. As b_s increases beyond this value, however, the measured diffusion coefficient becomes significantly larger than the expected value because the number of data points is not sufficient to spatially resolve the peak, resulting in a poor curve-fit. In all cases, the particle displacements due to the uniform flow in these synthetic images were large enough to determine $H^{\text{true}}(\Delta x, \Delta y)$ using Equation 33.

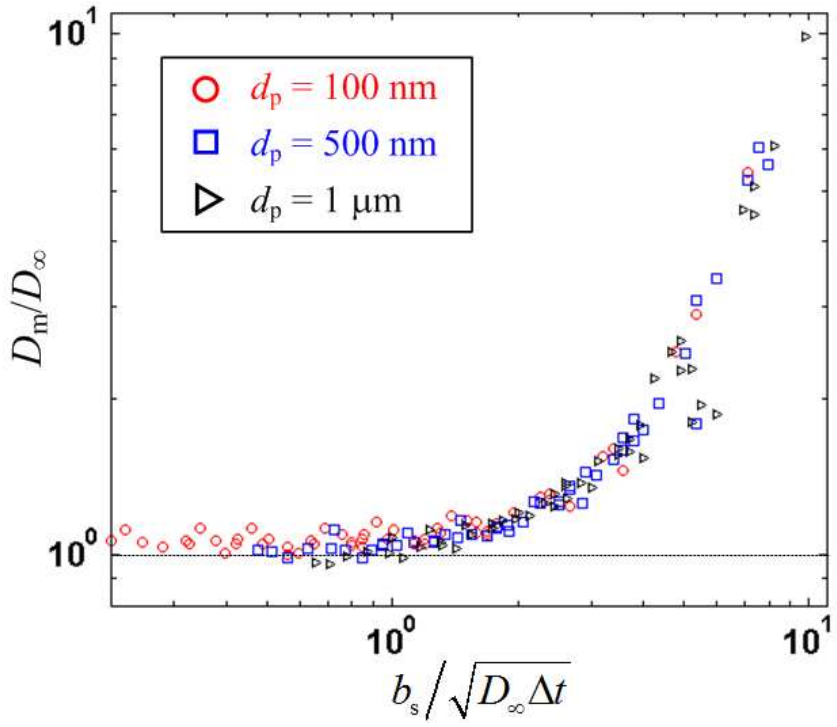

Figure 84: The measured Brownian diffusion coefficient D_{m} normalized by the expected value D_∞ as a function of normalized bin size that is used for the processing.

Synthetic images were also created for different flow velocities U and therefore different displacements over Δt to determine the minimum displacement in practice required to apply the "symmetry argument" to extract $H^{\mathrm{true}}(\Delta x, \Delta y)$ from $H(\Delta x, \Delta y)$. Based on the results of Figure 84, the data were processed with bin sizes $b_{\mathrm{s}} < \sqrt{D_\infty \Delta t}$. Figure 85 plots the normalized measured diffusion coefficients as a function of the displacement normalized by the diffusion length scale. The Figure shows that when displacement due to the flow $U\Delta t > \sqrt{D_\infty \Delta t}$, the measured and expected diffusion coefficients are in excellent agreement. For $U\Delta t < \sqrt{D_\infty \Delta t}$, however, there are significant discrepancies between D_{m} and D_∞.

Finally, the effect of particle mismatch was studied by creating "noisy" particle positions in the second exposure of the image pairs originally created to determine the maximum bin size. After detecting the particle positions in an image pair, a certain percentage F (varying between 10% and 80%) of the particle positions in the

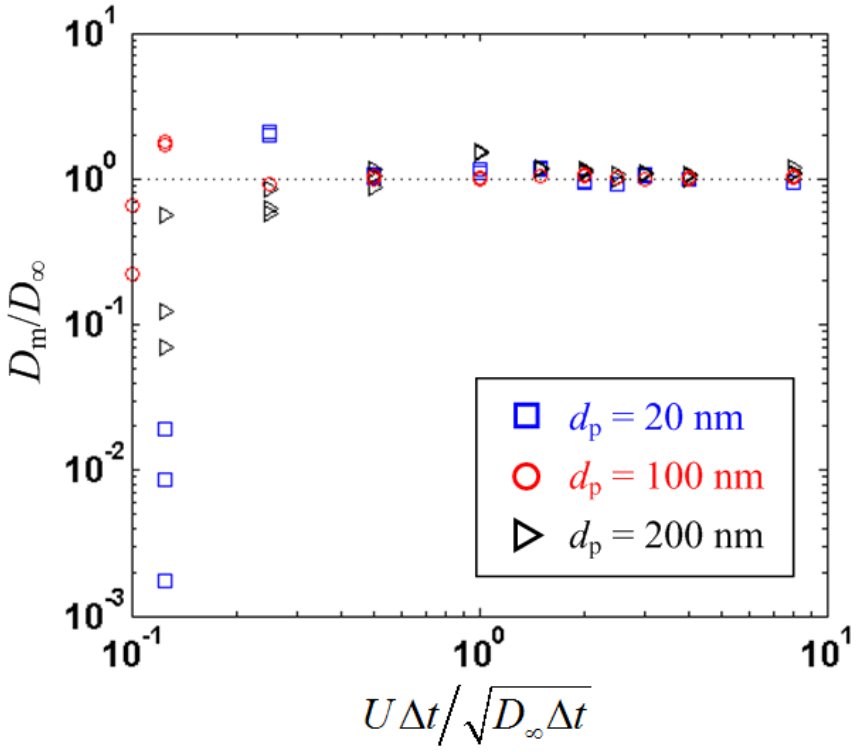

Figure 85: The normalized measured Brownian diffusion coefficient D_m/D_∞ as a function of normalized particle displacement due to the uniform flow $U\Delta t$.

second exposure were randomly chosen and replaced by random numbers to generate a known number of "wrong" displacement vectors. These new particle positions were then processed in the same fashion to extract the diffusion coefficient. Figure 86, which depicts the normalized measured diffusion coefficient as a function of F for two different particle sizes, shows that the measured diffusion coefficients are in excellent agreement with the expected value for F up to 50%, above which the discrepancy fluctuates wildly with F. Note that each data point here is averaged over results obtained for Δt values ranging from 0.14 ms to 9.8 ms.

B.3 Experimental Tests

The μPIV system shown in Figure 47 was used to image fluorescent particles of three different sizes, namely a = 105, 150 and 250 nm. The particles, suspended in water at volume fractions of $O(10^{-4} - 10^{-3})$, were convected by a Poiseuille flow

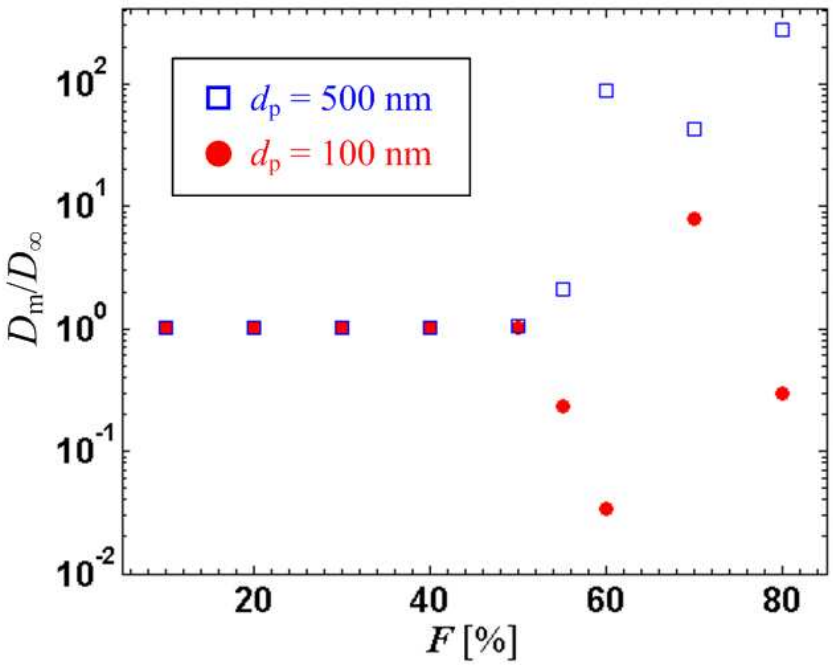

Figure 86: The normalized measured Brownian diffusion coefficient D_m/D_∞ as a function of fraction of mismatched particles F for two different particle sizes.

inside a microchannel with a nearly rectangular cross section (312 μm × 41 μm) at $\mathrm{Re} = O(10^{-2})$. To measure the bulk diffusion coefficient, the particles at the center of the channel were illuminated by light from a halogen lamp and imaged onto a CCD camera through a 63× 0.7 NA objective, a long-pass filter cube and a 0.5× camera adaptor. Given the relatively small depth of field defined by the objective of about 2 μm (*vs.* the channel depth of 41 μm), the flow inside the imaging volume can be assumed to be nearly uniform. For each particle size, sequences of 1500 images were obtained at framing rates between 60 Hz and 250 Hz. After recording each sequence, the illumination was shuttered and the temperature at the channel exit T was monitored with a thermocouple until it recovered to its "baseline" value (T varies typically less than 1 ° from this value) to minimize heating effects. This temperature was later used to calculate the viscosity of the working fluids (Section 5.3.1) which, together with T and a, is used in the Stokes-Einstein equation to predict the diffusion

coefficient D_∞. Figure 87 shows a typical image of 500 nm diameter particles taken at a frame rate of 128 Hz with an exposure time of 1 ms.

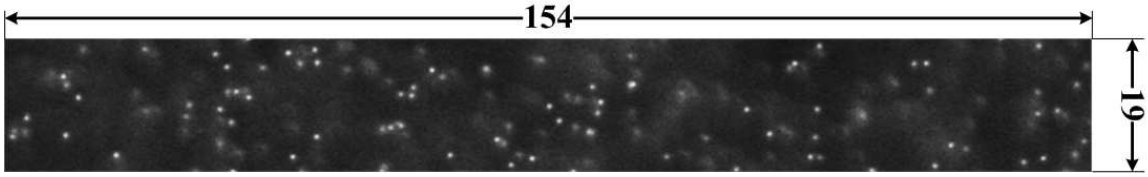

Figure 87: A sample image of 500 nm diameter particles taken at a frame rate of 128 Hz for the diffusion measurements. The dimensions are given in micrometers.

The width of the Gaussian curve σ_y^2 obtained for the three cases with different particle diameters is plotted against the time interval Δt in Figure 88. For a given particle size, σ_y^2 should vary linearly with Δt with a slope twice the diffusion coefficient. Table 17 compares the measured diffusion coefficient D_m with the expected values D_∞. Here, the uncertainties in D_∞ are determined based on the accuracy of the temperature measurement and uncertainties in the particle sizes while those in D_m represent 95% confidence interval (for more details about these calculations, *cf.* Appendix C). As indicated, the measured diffusion coefficients D_m agree reasonably well with expected values and the maximum discrepancy is 15%.

Table 17: Comparison between experimentally measured diffusion coefficients D_m and the values D_∞ predicted from the Stokes-Einstein equation based on measured fluid temperature.

a [nm]	D_∞ [m^2/s]	D_m [m^2/s]
105	2.0 ± 0.20	2.3 ± 0.1
150	1.6 ± 0.17	1.42 ± 0.08
250	1.1 ± 0.08	0.95 ± 0.04

B.4 Summary

In this chapter, a technique originally proposed for measuring diffusion coefficients of spheres in a high Peclet number concentrated suspensions has been extended to

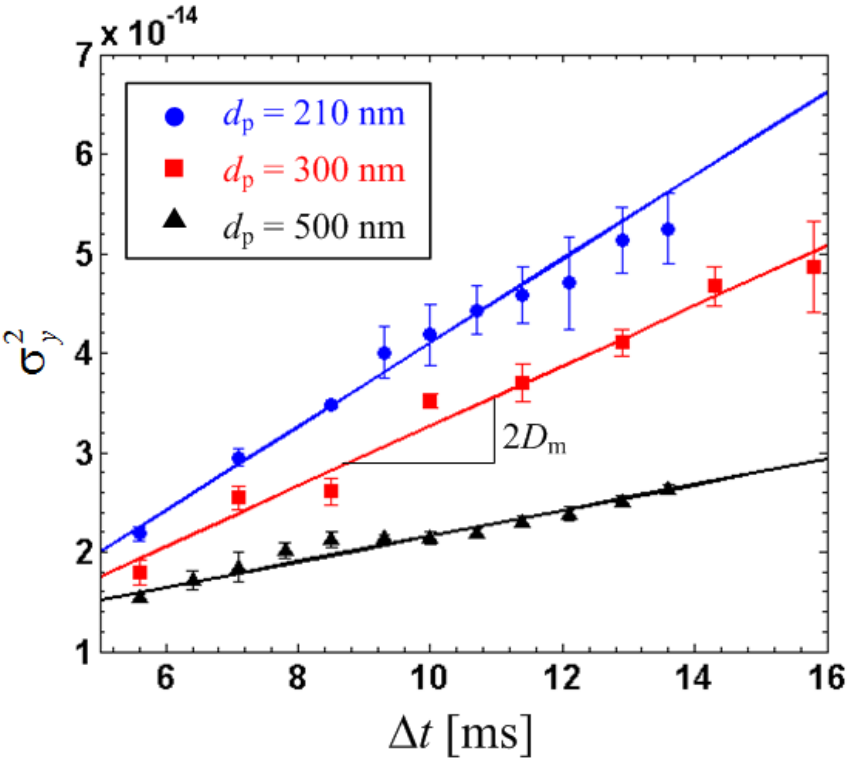

Figure 88: Experimentally determined values of σ_y^2 as functions of Δt for three particle sizes a = 105 nm (circles), 150 nm (squares), and 250 nm (triangles) denoted in different colors. The solid lines represent linear curve fits of the data and the slopes correspond to twice the diffusion coefficients.

measuring Brownian diffusion coefficients of colloidal particles using both synthetic and experimental images. Unlike previous approaches, this technique uses particle locations identified from the particle images (*vs.* cross-correlations of the particle images) and does not require one-to-one particle tracking. Instead, a histogram of all possible particle displacements is constructed and the true particle displacements are isolated from the false displacements by exploiting the differences in the statistics of the particle displacements in the presence of a unidirectional flow.

Simulations with synthetic images show that the particle displacement due to the flow should exceed $\sqrt{D\Delta t}$. Moreover, the bin size b_s used in the measurement direction (here, y) should be less than $\sqrt{D\Delta t}$ in order to sufficiently resolve the peak of the probability density function of the Brownian displacements. Interestingly,

significant particle mismatch up to 50% has minimal effects on the measured diffusion coefficient; particle mismatch above this level, however, greatly increases the errors in the estimated diffusion coefficient.

Finally, the method was tested on experimental images of particles with diameters of 500 nm or less in Poiseuille flows. The measured diffusion coefficients from these images are in all cases within 15% of the expected values.

APPENDIX C

UNCERTAINTY AND ERROR ANALYSIS

In this Appendix, the uncertainties in various experimental parameters are estimated based on the accuracy of the experimental measurements and their propagation following the approach suggested by Kline and McClintock [91]. Suppose that an experimental measurement, A, is a function of a number of independent variables $A = f(x_1, x_2, ..., x_n)$, and each of these variables has uncertainties $(\sigma_{x_1}, \sigma_{x_2}, ..., \sigma_{x_n})$. Then the uncertainty in the measurement, A, can be calculated from the weighted root-mean squared (rms) sum of the individual uncertainties:

$$\sigma_{\mathrm{A}} = \sqrt{\left(\frac{\partial f}{\partial x_1}\sigma_{x_1}\right)^2 + \left(\frac{\partial f}{\partial x_2}\sigma_{x_2}\right)^2 + ... + \left(\frac{\partial f}{\partial x_n}\sigma_{x_n}\right)^2} \tag{35}$$

C.1 Prediction of Near-Wall Shear Rate G

Equation 24 was used to calculate the Poiseuille flow velocity profile cross the channel depth, *i.e.*, along z. The uncertainty in the average shear rate over the first 400 nm of the wall was estimated to be that of the shear rate G at the wall ($z = 0$), which can be related to the uncertainties of the measured pressure difference ΔP, the channel length L, the viscosity of the working fluid μ (which is determined by the uncertainty in the temperature T) and the channel depth (z dimension) H.

$$G = \left.\frac{\partial u}{\partial z}\right|_{z=0} = \left.\frac{\Delta P}{2\mu L}(H - 2z)\right|_{z=0} = \frac{\Delta P H}{2\mu L} \tag{36}$$

The uncertainty in this shear rate is then:

$$\frac{\sigma_{\mathrm{G}}}{G} = \sqrt{\frac{\sigma_{\Delta P}^2}{\Delta P^2} + \frac{\sigma_H^2}{H^2} + \frac{\sigma_\mu^2}{\mu^2} + \frac{\sigma_L^2}{L^2}} \tag{37}$$

In this study, the pressure difference $\Delta P = \rho g(h_2 - h_1)$ is calculated from the measured heights h_1 and h_2 of the upstream and downstream free surfaces, respectively. The uncertainty in ΔP can therefore be estimated from the accuracy of the measurements of these free-surface heights:

$$\frac{\sigma_{\Delta P}}{\Delta P} = \frac{\sqrt{2}\sigma_{h_1}}{h_2 - h_1} \tag{38}$$

where $\sigma_{h_2} = \sigma_{h_1} = 0.55$ mm. For the experimental studies presented in this thesis, $0.1 \text{ m} \leq h_2 - h_1 \leq 0.5$ m. The uncertainty $\sigma_{\Delta P}/\Delta P$ is therefore below 1% in all cases.

The viscosity of the working fluid was taken to be that of water and calculated from the measured temperature T using Equation 25. The uncertainty in μ is therefore:

$$\frac{\sigma_\mu}{\mu} = \frac{507.881\sigma_T}{(149.39 - T)^2} \tag{39}$$

where the uncertainty in the temperature measurement σ_T is determined by the measurement accuracy of the thermocouple reading, which, according to the manufacturer, was taken to be 1% for the actual temperature reading plus 10 "counts" or 10 times the minimum temperature resolution of the meter of 0.1 °C. Since all experiments were carried out at a working fluid temperature of about 25°C, σ_T is estimated to be 1.3°C, leading to an uncertainty in viscosity of $\sigma_\mu/\mu = 3\%$.

The uncertainty in the channel depth σ_H was determined from repeated measurements of the etched channels before bonding. In each of the five channels, the depth was measured at three different positions along the channel length using a profilometer; σ_H was then taken to be twice the maximum standard deviation of the depth measurements obtained over the five channels , or 0.28 μm. The uncertainty σ_H/H is estimated to be 0.8%.

As discussed in Section 5.1.1, the channel length L is determined by summing the

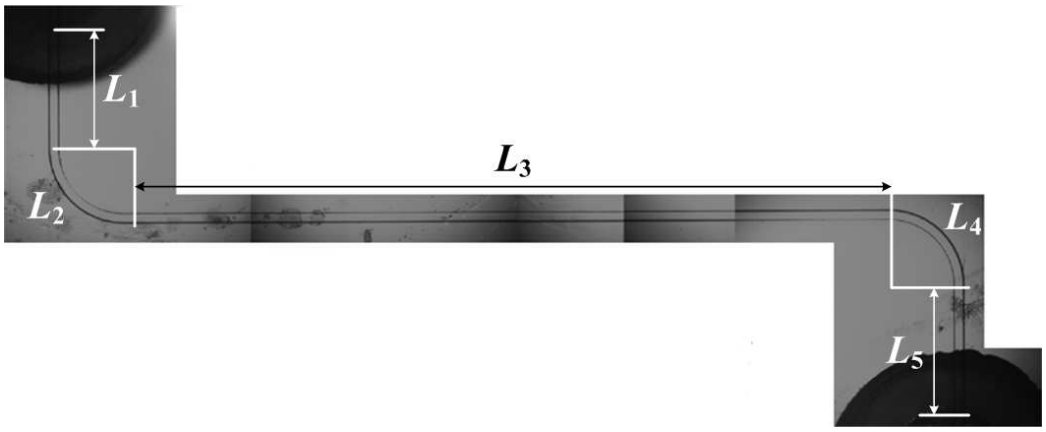

Figure 89: A composite image of the microchannel. The overall channel length was determined as summation of the lengths of the 5 segments.

lengths of 5 segments estimated from a composite image of the channel $L = \sum_{i=1}^{5} L_{\mathrm{i}}$ where L_{i} is the length of the i^{th} segment as labeled in Figure 89. The length of the straight segments (*i.e.*, L_1, L_3, L_5), was estimated from the difference in their endpoint coordinates, while the length of the curved segments which were assumed to be circular arcs, was calculated from the radius of the arc estimated from the endpoint coordinates. If the uncertainty in determining the position of the each endpoint σ_{loc} is taken to be 5 pixels, corresponding to the typical linewidth of various features in the image, the uncertainties in the lengths of straight line segments and arcs are $\sqrt{2}\sigma_{\mathrm{loc}}$ and $\pi\sqrt{2}\sigma_{\mathrm{loc}}/2$, respectively. The uncertainty in the overall channel length σ_{L} is then 19.9 pixels, or 0.27 mm. The ratio σ_{L}/L is therefore 0.8% based on an overall channel length of 35.4 mm.

Based on this discussion, the maximum uncertainty in the shear rate G is estimated from Equation 35 to be 3.2%. Note that this uncertainty is dominated by the uncertainty in measuring the temperature, and hense estimating the viscosity of the working fluid.

C.2 Particle-Wall Separation Distance

The separation distance between the particle's lower edge and the wall is determined as: $h = z_{\mathrm{p}} \ln(I_{\mathrm{p}}^0/I_{\mathrm{p}})$ where the intensity of the particles touching the wall I_{p}^0 is determined from experimental calibrations and the penetration depth z_{p} is calculated from the measured angle of incidence using Equation 5 as discussed in Section 2.2. The uncertainty in h can be obtained from the uncertainties in z_{p} and I_{p}^0, or σ_{z_p} and $\sigma_{I_p^0}$, respectively:

$$\sigma_{\mathrm{h}} = \sqrt{\left[\ln\left(\frac{I_{\mathrm{p}}^0}{I}\right)\sigma_{z_p}\right]^2 + \left(\frac{\sigma_{I_p^0}}{I_{\mathrm{p}}^0} z_{\mathrm{p}}\right)^2} \tag{40}$$

The uncertainty in the intensity of the particles touching the wall $\sigma_{I_p^0}/I_{\mathrm{p}}^0$ is estimated to be 18% based on the calibration data (Section 6.2.2). The results show that the uncertainty increases for particles farther away from the wall (*i.e.*, at larger z).

The penetration depth z_{p} is calculated using Equation 5 from the experimental parameters of the system and the measured angle of incidence θ_{i}. As shown in Figure 37, θ_{i} is determined in these MnPIV experiments from the thickness of the microchannel piece d_{t} and distance between two adjacent TIR spots d_{s} as follows: $\theta_{\mathrm{i}} = \tan^{-1}(2d_{\mathrm{s}}/d_{\mathrm{t}})$. The uncertainty in the angle of incidence σ_{θ_i} is related to the uncertainties in d_{t} and d_{s}, or σ_{d_t} and σ_{d_s}, respectively:

$$\sigma_{\theta_{\mathrm{i}}} = \frac{2d_{\mathrm{t}}}{d_{\mathrm{t}}^2 + 4d_{\mathrm{s}}^2}\sqrt{\sigma_{d_s}^2 + \left(\frac{d_{\mathrm{s}}}{d_{\mathrm{t}}}\sigma_{d_t}\right)^2} \tag{41}$$

In Chapter 6, the average values of d_{t} and d_{s} over multiple measurements were found to be 1.84 mm and 2.56 mm respectively. The uncertainties were taken to be twice the standard deviation of these measurements, giving $\sigma_{d_t} = 0.011$ mm and $\sigma_{d_s} = 0.046$ mm. The angle of incidence θ_{i} and its uncertainty σ_{θ_i} are then 70.2 ° and 0.3 °, respectively.

The channels used in Chapter 7, have a somewhat different configuration, and

d_t and d_s represent different quantities (Figure 68). The angle of incidence $\theta_\mathrm{i} = \tan^{-1}(d_\mathrm{s}/2d_\mathrm{t}) = 72.27\,^\circ$, and the uncertainty in this angle σ_{θ_i} is:

$$\sigma_{\theta_\mathrm{i}} = \frac{2d_\mathrm{t}}{4d_\mathrm{t}^2 + d_\mathrm{s}^2}\sqrt{\sigma_{d_s}^2 + \left(\frac{d_\mathrm{s}}{d_\mathrm{t}}\sigma_{d_t}\right)^2} \tag{42}$$

The uncertainty in this angle is then calculated to be 0.77°.

The uncertainty in the penetration depth σ_{z_p} is given by:

$$\frac{\sigma_{z_\mathrm{p}}}{z_\mathrm{p}} = \frac{n_1^2 \sin 2\theta_\mathrm{i}\sigma_{\theta_\mathrm{i}}}{2(n_1^2 \sin^2\theta_\mathrm{i} - n_2^2)} \tag{43}$$

where refractive indices $n_1 = 1.4630$ and $n_2 = 1.3333$ are taken to be the values for fused silica and water at $\lambda = 488$ nm, respectively. The penetration depth were calculated to be 113.1 ± 3.4 nm for the experiments in Chapter 6 and 95.6 ± 4.8 nm in Chapter 7.

Finally, these results can be used in Equation 40 to estimate the uncertainty in h, or the z-position of the particle measured between its lower edge and the wall. For the parameters used in Chapter 6, σ_h increases from 20.4 nm at the wall ($h = 0$) to 22.9 nm at the upper boundary of the imaging region ($h = 350$ nm). Similarly, σ_h increases from 17.2 nm at the wall to 23.2 nm at $h = 300$ nm for the experiments described in Chapter 7.

C.3 Slip Lengths Measured with MnPIV

In Chapter 7, the slip length was obtained from the curve-fit of the three velocity data points measured with MnPIV to a linear function $U = Az + B$. A least-squares based algorithm [144] that considers the uncertainties in the velocities σ_U, corresponding to the sizes of the error bars in Figure 71, was used to obtain the fitting parameters A and B, along with their uncertainties σ_A and σ_B. The slip length b was then simply determined as $b = B/A$ and its uncertainty σ_b can be estimated from σ_A and σ_B:

$$\frac{\sigma_b}{b} = \sqrt{\left(\frac{\sigma_A}{A}\right)^2 + \left(\frac{\sigma_B}{B}\right)^2} \tag{44}$$

The uncertainties in b calculated for the Poiseuille flows of 10 mM NH_4HCO_3 at the six nominal driving pressure gradients inside the bare channel were listed in the last column of Table 18.

Table 18: The uncertainty in the slip lengths σ_b determined using MnPIV for Poiseuille flows of 10 mM NH_4HCO_3 through the bare channel at six different driving pressure gradients.

$\Delta P/L$ [Bar/m]	b [nm]	σ_b [nm]
1.18	2.4	24.4
1.06	6.6	28.5
0.90	5.2	24.3
0.74	-13.9	23.5
0.51	-2.0	16.1
0.25	7.7	14.4

C.4 Diffusion Coefficient Calculated from Stokes-Einstein Equation

In Appendix B, the diffusion coefficient D_∞ is calculated from the Stokes-Einstein equation based on the measured temperature of the working fluid T, the fluid viscosity calculated from T and the particle size a. The uncertainty in D_∞ is therefore a function of the uncertainties in T, μ, and a:

$$\frac{\sigma_{D_\infty}}{D_\infty} = \sqrt{\left(\frac{\sigma_T}{T}\right)^2 + \left(\frac{\sigma_\mu}{\mu}\right)^2 + \left(\frac{\sigma_a}{a}\right)^2} \tag{45}$$

According to the manufacturer, σ_a/a are 9.6%, 10% and 6.4% for a = 105 nm, 150 nm and 250 nm particles, respectively. Using these values and uncertainties in T and μ given in the previous section, the uncertainties in the calculated diffusion coefficient

$\sigma_{D_\infty}/D_\infty$ are 10.1%, 10.4% and 7.1% for particles with diameters a = 105 nm, 150 nm and 250 nm, respectively.

C.5 Solution Concentration

As discussed in Section 5.1.3, all of the sodium tetraborate and ammonium bicarbonate solutions were prepared by first making a stock solution of concentration c_i by adding a mass m_i of salt to v_i = 25 mL Nanopure water. The uncertainty in the concentration of this stock solution can be calculated from the accuracy of the mass and volume measurements.

$$\frac{\sigma_{c_i}}{c_\mathrm{i}} = \sqrt{\left(\frac{\sigma_{m_i}}{m_\mathrm{i}}\right)^2 + \left(\frac{\sigma_{v_i}}{v_\mathrm{i}}\right)^2} \tag{46}$$

This stock solution is then diluted to make a volume v_f = 25 mL of the solution at its final concentration c_f by mixing a volume v_s of stock solution with Nanopure. The concentration of the actual working fluid c_f and its uncertainty σ_{c_f} can be obtained as:

$$c_\mathrm{f} = \frac{c_\mathrm{i} v_\mathrm{s}}{v_\mathrm{f}}, \quad \frac{\sigma_{c_f}}{c_\mathrm{f}} = \sqrt{\left(\frac{\sigma_{m_i}}{m_\mathrm{i}}\right)^2 + \left(\frac{\sigma_{v_i}}{v_\mathrm{i}}\right)^2 + \left(\frac{\sigma_{v_s}}{v_\mathrm{s}}\right)^2 + \left(\frac{\sigma_{v_f}}{v_\mathrm{f}}\right)^2} \tag{47}$$

The accuracy of the measurements were assumed to be one half (1/2) of the minimum resolution of the balance and graduated cylinder used to measure mass and volume, respectively: σ_{m_i} = 0.5 mg and $\sigma_{v_i} = \sigma_{v_f}$ = 0.1 mL respectively. Since the concentration of the stock solution is usually about 10 times that of the final solution ($c_\mathrm{i} \approx 10 c_\mathrm{f}$), $v_\mathrm{s} \approx$ 2.5 mL. Measuring this solution requires using the 1 mL pipette (with an accuracy of $\sigma_\mathrm{p} = \pm 0.005$ mL) three times, so the uncertainty in v_s is estimated to be $\sigma_{v_s} = \sqrt{3}\sigma_p$. For all of the solutions made with this procedure (*i.e.*, the 1, 10 and 20 mM sodium tetraborate and 2 and 10 mM ammonium bicarbonate solutions), the maximum uncertainty in the final concentration $\sigma_{c_f}/c_\mathrm{f}$ is 1.4% for the 1 mM sodium tetraborate solution.

Ammonium acetate solutions at 2 and 10 mM were prepared directly from a 7.5 mM stock solution by a two-step dilution procedure. A volume of 0.833 mL of the stock solution was first diluted to make 25 mL of a solution at an intermediate concentration of 250 mM; this solution was then further diluted to the desired concentration. The uncertainties in the final concentration, calculated following an approach similar to that as discussed above, are found to be 2.6% and 1.0% for the 2 and 10 mM solutions respectively.

APPENDIX D

PARTICLE DETECTION

As detailed in Chapter 3, when a cross-correlation based method is used to determine flow velocities from PIV images where the tracers have non-uniform image intensities, the resultant velocities are biased towards those sampled by the brightest images. To minimize this bias, a particle-tracking method was used to determine the tracer velocities by finding the displacement of the center of each tracer image over Δt, time delay within the image pair. This Appendix first describes the algorithms used to locate the center of the tracer image and to determine its properties such as the radius, intensity and eccentricity in Section D.1, followed by the tests of the algorithm using synthetic images in Section D.2.

D.1 Particle Detection Algorithm

The algorithm for locating each particle image, originally proposed for digital video microscopy applications by Crocker and Grier [39], was implemented in an in-house code (written in MATLAB v7.2). For an image over the entire field of view, the background at each pixel location is first removed by subtracting the grayscale value averaged over all pixels surrounding actual pixel location within a diameter of $d_{\mathrm{p,e}}$ (in pixels) specified by the user; this diameter is the estimated size of the actual particle image. The image is then convolved with a Gaussian mask to identify individual particle images, which should have a nearly Gaussian grayscale distribution. This resultant "filtered image" should therefore have sharply defined Gaussian functions located at the center of each particle image with a radial extent similar to that of the original particle image.

The local maxima in grayscale values over a pixel's immediate neighborhood are then identified in these filtered image. These maxima are then evaluated using two criteria as possible locations of particle centers. First, all maxima with grayscale values below a user-specified threshold V_{t} (based on the background noise level of the image) are eliminated since the particle images should be brighter than the background noise. Next, if two (or more) peaks are found to be separated by a distance less than the estimated image diameter $d_{\mathrm{p,e}}$, only the brighter or (the brightest) of these peaks is kept.

The remaining identified particle image centers are then processed as follows. First, the grayscale value-weighted centroid is calculated in the filtered image over an area surrounding the particle image center with a size slightly bigger than the estimated image diameter (usually $d_{\mathrm{p,e}} + 2$). Then the particle image intensity I_{p}, defined as the maximum grayscale value over this area is calculated from the original image. The particle image diameter $d_{\mathrm{p,i}}$ is taken to be twice the grayscale value-based "radius of gyration," which is calculated from the filtered images over the area surrounding the center of the particle image:

$$d_{\mathrm{p,i}} = 2\sqrt{\sum_i V_{\mathrm{i}} r_{\mathrm{i}}^2 \Big/ \sum_i V_{\mathrm{i}}} \tag{48}$$

Here, V_{i} is grayscale value of the i^{th} pixel in this area and r_{i} is its distance from the center of the particle image. The eccentricity of the particle image ϵ_{p}, which measures how much the image shape deviates from a circle (where, by definiation, $\epsilon_{\mathrm{p}} = 0$) or alternatively, the symmetry of the distribution of the image grayscale values about the image center, is given by:

$$\epsilon_{\mathrm{p}} = \frac{\sqrt{\left[\sum_{\mathrm{j}} V_{\mathrm{j}} \cos\theta_{\mathrm{j}}\right]^2 + \left[\sum_{\mathrm{j}} V_{\mathrm{j}} \sin\theta_{\mathrm{j}}\right]^2}}{\sum_{\mathrm{j}} V_{\mathrm{j}} - V_{\mathrm{center}}} \tag{49}$$

where θ_j is the angular position of the j^{th} pixel measured with respect to the particle center and the horizontal and V_{center} is the grayscale value at the particle center. Note that ϵ_p was calculated from the filtered images.

D.2 Performance Tests of the Algorithm

In this section, the robustness, reliability and accuracy of the particle-locating algorithm was evaluated with synthetic images. As discussed previously, this algorithm requires two input parameters, namely the estimated tracer image diameter $d_{p,e}$ and the lower limit on the particle image intensity V_t. Although $d_{p,e}$ should vary with the tracer image size in the actual images, the nonuniform nature of the illumination used in MnPIV implies that particle image diameters vary by as much as 2 pixels even within a single MnPIV image. The algorithm was therefore tested at various particle image sizes (d_{pi} = 5, 7 and 9 pixels) using the value of $d_{p,e}$ corresponding to the largest images. Since the background noise clearly affects the accuracy of the particle center locations determined by the algorithm, test were carried out for images at several different SNRs, where the SNR is defined to be the ratio of the image intensity to the mean of the background noise, which was modeled by a series of random numbers with a Gaussian distribution. Finally, particle images were placed at x- and y-positions with different fractional portions to evaluate the effects of pixel biasing [39] on this algorithm; pixel biasing usually increases the error in the estimates of particle center locations at certain fractional portions of locations if the input value for $d_{p,e}$ is too small compared with the actual size of the particle images.

Figure 90 shows two typical synthetic particle images distributed on a x-y grid with different particle image sizes and SNRs. These images were then processed using the algorithm discussed above with $d_{p,e} = 11$ pixels and a value of V_t estimated from the background noise of the image. The resultant particle positions were then compared with the true values used to generate the particle images to determine the

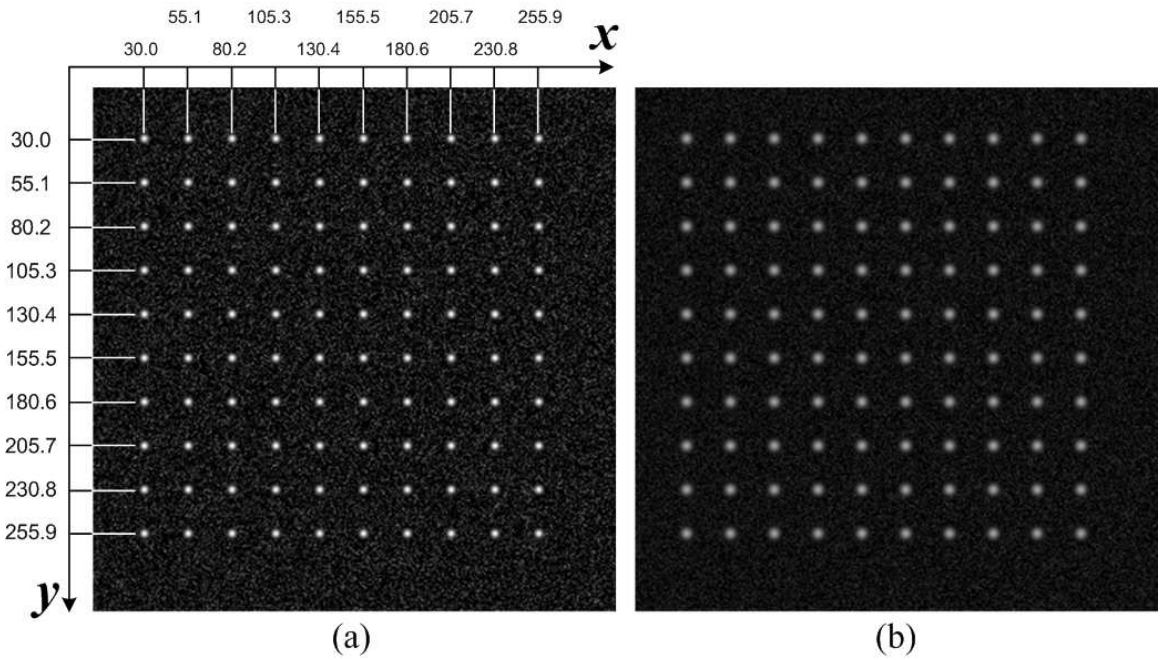

Figure 90: Synthetic images used to test the performance of the particle-detection algorithm: (a) $d_{\mathrm{pi}} = 5$ pixels and SNR = 8 and (b) $d_{\mathrm{pi}} = 9$ pixels and SNR=3. The numbers represent the x- and y-positions of the individual particle images in pixels.

absolute error in the estimated particle locations.

Figure 91 shows the absolute error as a function of the fractional portion of the particle position (in pixels) for particle images with $d_{\mathrm{pi}} = 5$ pixels and various SNRs ranging from 3 to 25. The results show that the overall error in the detected particle position is less than 0.1 pixel. As the SNR decreases, the errors increase, reaching a maximum of 0.08 pixels at SNR = 3. As discussed in the previous section, the grayscale value-weighted particle center position was determined in the filtered image with a much lower noise level, and therefore higher SNR, compared with the original data; this "pre-filtering" should improve the accuracy of the detected particle center positions.

Figure 92 shows similar plots for synthetic images with three different image diameters $d_{\mathrm{pi}} = 5$ (circles), 7 (squares) and 9 (triangles) pixels at SNR = 5 (open symbols) and 8 (closed symbols). For particle images at the same SNR (*e.g.* for SNR = 8), the accuracy improves as the image size increases, probably because the increased number

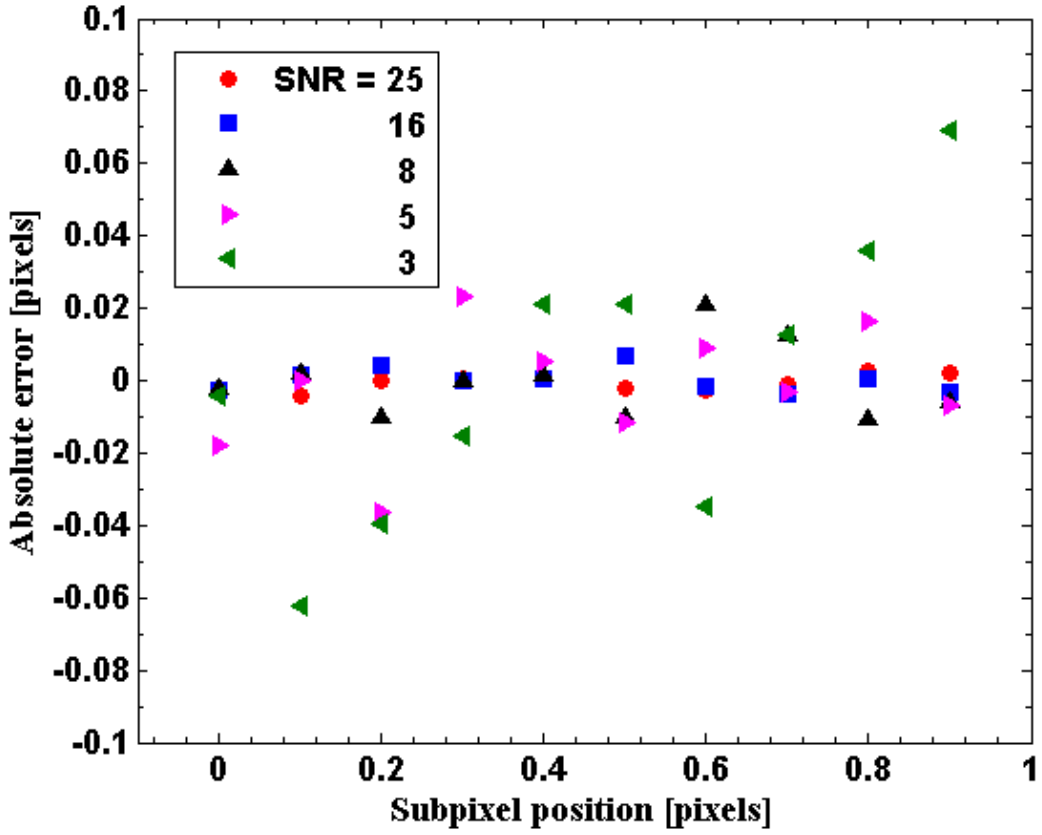

Figure 91: The absolute error in the detected particle center position as function of the fractional portion of the particle position for synthetic images with a particle image diameter $d_{\text{pi}} = 5$ pixels at 5 different SNRs (*cf.* legend).

of pixels enhances the spatial resolution of the image intensity profile. A comparison of open and closed symbols at a given d_{pi} also suggests that the image SNR has a bigger effect on the accuracy of the estimated location of the particle positions.

As discussed previously, the non-uniform illumination used in MnPIV, results in a wide range of particle image intensities and hence SNRs within a single MnPIV image. The results presented here imply that the absolute error in the particle positions for dimmer particle images, which have a lower SNR, are therefore likely to be greater than that for the brighter particle images with their higher SNR.

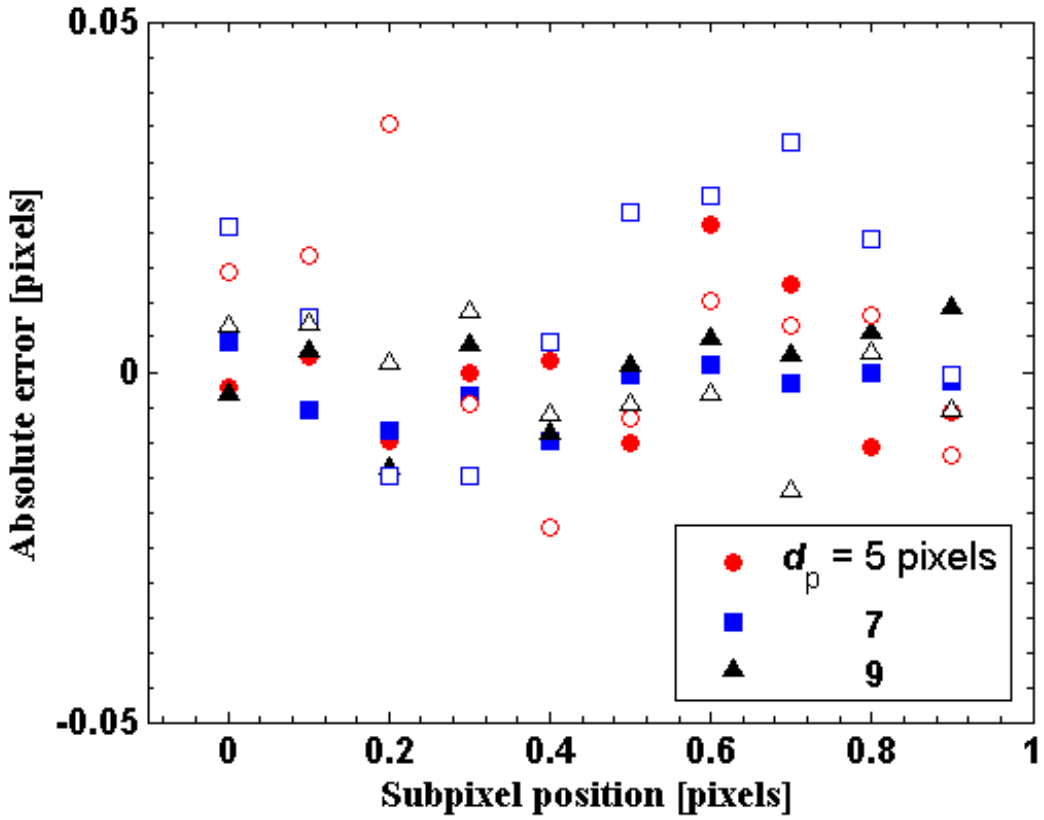

Figure 92: The absolute error in the detected particle center position as a function of the fractional portion of the particle position for three different particle image sizes (*cf.* legend) at SNR = 5 (open) and 8 (closed symbols).

APPENDIX E

MAJOR AND MINOR LOSSES OF THE FLOW-DRIVING SYSTEM

The pressure difference used to verify the MnPIV results is calculated from the measured height of the free surface inside the bottle under the assumption that the losses in the flow system are negligible. To verify this assumption, the major loss along the flow path (tubing components 2, 4 and 7 in Figure 35) and minor losses due to the various fittings between the bottle and channel inlet was quantified. These fittings include the round outlet of the bottle, a sudden contraction (component 3 in Figure 35), T-connectors (components 5 and 6 in Figure 35) and the sudden contraction at the channel inlet. The total head loss for the system Δh_{T} can then be estimated by:

$$\Delta h_{\mathrm{total}} = \frac{\Delta P_{\mathrm{tubing}}}{\rho g} + \frac{K_{\mathrm{L,bottle}}\overline{U}_2^2}{2g} + \frac{K_{\mathrm{L},3}\overline{U}_4^2}{2g} + \frac{K_{\mathrm{L},5,6}\overline{U}_4^2}{2g} + \frac{K_{\mathrm{L,inlet}}\overline{U}_{\mathrm{c}}^2}{2g} \qquad (50)$$

Here, $\Delta P_{\mathrm{tubing}}$ represents the overall pressure drop inside all of the segments of tubing along the flow path, K_{L} is the minor loss coefficient for a given component, $\overline{U}_{\mathrm{c}}$ is the average velocity inside the channel and $\overline{U}_2$, $\overline{U}_4$ and $\overline{U}_7$ denote the average velocities inside tubing segments 2, 4, and 7, respectively, as labeled in Figure 35.

In the current calculation, $\overline{U}_{\mathrm{c}}$ is taken to be that predicted by the analytical solution of 2D Poiseuille flow based on the measured pressure gradient, channel depth and water viscosity. The velocities inside the tubing segments were then calculated from U_{c} under the assumption of continuity; the velocity in segment 2, for example was:

$$\frac{\overline{U}_{\mathrm{c}}^2 \pi d_{\mathrm{h}}^2}{4} = \frac{\overline{U}_2^2 \pi d_2^2}{4} \tag{51}$$

where d_{h} is the hydraulic diameter of the channel.

To obtain a conservative estimate, the losses were calculated for the "worst case," *i.e.*, the highest driving pressure gradient, corresponding to the maximum loss. The experimental parameters used in this calculation are shown in Table 19. The magnitudes of each term in Equation 50 is listed in Table 20, which shows that the maximum head loss, specifically, the major head loss, is $O(1\ \mu\mathrm{m})$. The head loss in the flow system therefore have a negligible effect on the measured pressure difference compared with the height differences between the upstream and downstream free surfaces, which are five order of magnitude greater, or $O(0.1\ \mathrm{m})$.

Table 19: Experimental parameters used to calculate the major and minor losses of the system. The loss coefficients are from the handbook by Avallone and Baumeister [4].

Parameter	Description	Value
d_{h}	Channel hydraulic diameter	75.4 μm
$\overline{U}_{\mathrm{c}}$	Mean velocity in channel	3.05×10^{-3} m/s
L_2	Tubing length (No. 2)	420 mm
d_2	Tubing diameter (No. 2)	9.5 mm
$\overline{U}_2$	Mean velocity in tubing No. 2	1.89×10^{-7} m/s
$L_{4,7}$	Tubing length (No. 4, 7)	1.85 m
$d_{4,7}$	Tubing diameter (No. 4, 7)	3.2 mm
$\overline{U}_4$, $\overline{U}_7$	Mean velocity in tubing No. 4, 7	1.70×10^{-6} m/s
$K_{\mathrm{L,bottle}}$	Round outlet of bottle	0.05
$K_{\mathrm{L},3}$	Sudden contraction (No. 3)	0.42
$K_{\mathrm{L},5,6}$	Inline flow at T-connecters (No. 5, 6)	0.2 each
$K_{\mathrm{L,inlet}}$	Sudden contraction at channel inlet	0.5

Table 20: The magnitudes of all of the head loss terms in Equation 50.

Term	Δh (m)
$\frac{\Delta P_{\text{tubing}}}{\rho g}$	1.3×10^{-6}
$\frac{K_{\text{L,bottle}}\overline{U}_2^2}{2g}$	9.1×10^{-17}
$\frac{K_{\text{L},3}\overline{U}_4^2}{2g}$	6.2×10^{-14}
$\frac{K_{\text{L},5,6}\overline{U}_4^2}{2g}$	6.0×10^{-14}
$\frac{K_{\text{L,inlet}}\overline{U}_{\text{c}}^2}{2g}$	2.4×10^{-7}

APPENDIX F

PARTICLE-WALL INTERACTION POTENTIAL DETERMINED FROM MEASURED PARTICLE DISTRIBUTIONS

The probability of finding a particle at a certain particle-wall separation distance $p(z)$ can be obtained from the measured particle number density distributions $c(z)$, as shown in Figure 64. This probability is directly related to the particle's potential energy $\phi(z)$ via the Boltzmann distribution [145]:

$$p(z) = A \exp\left\{\frac{\phi(z)}{kT}\right\} \tag{52}$$

where A is a normalization constant that ensures $\int p(z)dz = 1$. The potential $\phi(z)$ can therefore be estimated by solving Equation 52 using the $p(z)$ obtained from the measured $c(z)$. The constant A can be eliminated by normalizing $p(z)$ with its value at a reference z-position $p(z_{\mathrm{m}})$:

$$\frac{\phi(z) - \phi(z_{\mathrm{m}})}{kT} = \ln\left\{\frac{p(z)}{p(z_{\mathrm{m}})}\right\} \tag{53}$$

Note that the z-position z_{m} corresponds to the particle-wall separation distance where the probability of finding a particle is maximum. This approach has been used in total internal reflection microscopy (TIRM) to measure the colloidal interaction between a single particle of $O(1\ \mu\mathrm{m})$ diameter and a flat plate in an aqueous environment [145, 53, 198, 167].

The resultant potential curves can be compared with theoretical models. For a sphere suspended in a conducting medium (*e.g.*, an electrolyte solution) near a

dielectric wall, the net interaction potential energy $\phi(z)$ consists of the van der Waals, electrical double-layer and gravitational potential energies, or ϕ_{VDW}, ϕ_{EDL}, and ϕ_{G}, respectively using linear superposition:

$$\phi(z) = \phi_{\mathrm{VDW}} + \phi_{\mathrm{EDL}} + \phi_{\mathrm{G}} \tag{54}$$

Given the relatively thick particle depletion layer near wall observed in the measured particle distributions and the short-ranged nature of van der Waals forces, which are typically significant only over separation distances below 10 nm [61], the effects of van der Waals forces should be negligible in these studies.

The potential energy associated with the interaction between the electric double layers on the particle and wall surfaces can be approximated, for the case where the Debye length κ^{-1} is much less than the particle radius a and the particle-wall separation distance, by the Derjaguin approximations [145]:

$$\phi_{\mathrm{EDL}}(h) \propto \exp(-\kappa h) \tag{55}$$

Here, h is the distance between the particle's lower edge and wall. The Debye length κ^{-1} for the monovalent sodium tetraborate solutions used here is:

$$\kappa^{-1} = \sqrt{\frac{\epsilon_{\mathrm{p}} kT}{4CN_{\mathrm{A}}e_{\mathrm{c}}^2}} \tag{56}$$

where $N_{\mathrm{A}} = 6.02 \times 10^{23}$ is Avogadro's number, C is the molar concentration of the sodium tetraborate solutions, ϵ_{p} is the dielectric permittivity of water and e_{c} is the magnitude of charge on an electron 1.602×10^{-19} C. The Debye length is therefore 6.8 nm, 2.1 nm and 1.5 nm for sodium tetraborate solutions with C = 1, 10 and 20 mM, respectively.

The gravitational potential energy is essentially the product of the net force due to the weight of the particle and the buoyancy force acting on the particle and its altitude h:

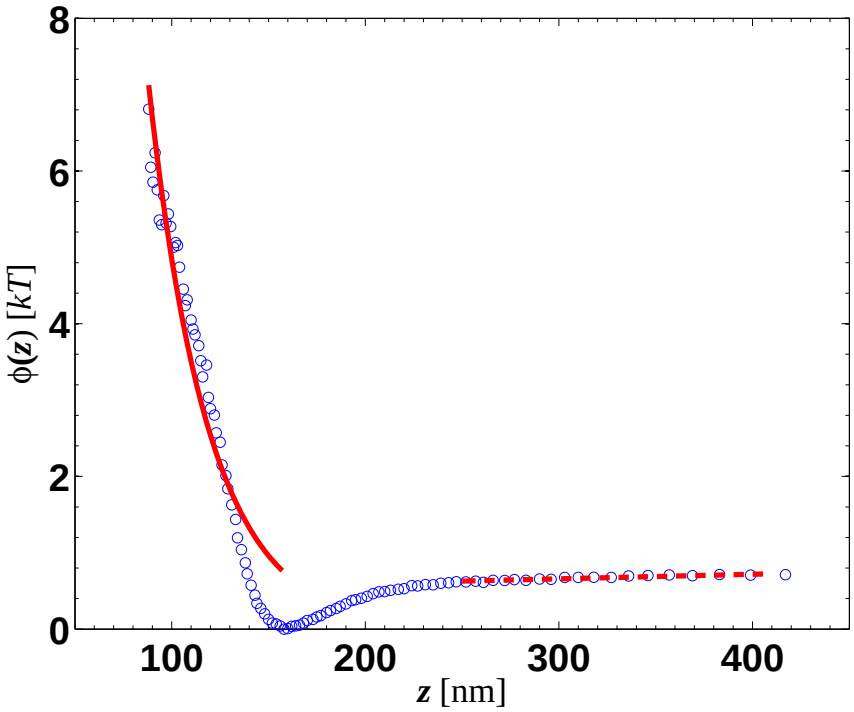

Figure 93: Interaction potential energy $\phi(z)$ obtained from the measured particle distribution for 20 mM sodium tetraborate solution (Figure 64). The solid and dashed lines represent curve-fits of the data at $z < 140$ nm and $z > 250$ nm, respectively, with exponential and linear functions of z, respectively.

$$\phi_{\rm G} = \frac{4}{3}\pi a^3(\rho_{\rm p} - \rho_{\rm f})gh \tag{57}$$

Here, $\rho_{\rm p} = 1.05$ g/cm^3 and $\rho_{\rm f} = 1.0$ g/cm^3 are the particle and fluid densities, respectively. Since $\phi_{\rm EDL}(z)$ has an exponential decay in z, while $\phi_{\rm G}(z)$ increases linearly with z, electrostatic interactions are dominant at small particle-wall separation distances, while the longer-ranged gravitational interactions become important at larger z.

Figure 93 presents the potential $\phi(z)$ obtained from the particle distribution for the $C = 20$ mM sodium tetraborate solution. As shown, the potential reaches a minimum at $z \approx 140$ nm, then increases linearly for $z > 250$ nm. The data for $z < 140$ nm, where short-ranged electrostatic interactions are dominant, were curve-fit to an exponential function to obtain estimates of the Debye length. The length

scales for the exponential decay are found to be 31 nm, 26 nm and 21 nm for $C = 1$, 10 and 20 mM, respectively. Although these results suggest that the length scales for these electrostatic interactions increase with decreasing electrolyte concentration (*i.e.*, ionic strength), they are nevertheless much larger than the Debye lengths predicted for these solutions using Equation 56.

The discrepancy between the length scales estimated from the potential curves and those predicted by Equation 56 could be due to a number of factors. First, unlike the other studies that we are aware of in colloid science which obtain potential curves by studying a particle in equilibrium (*i.e.*, in the absence of flow), the particles in current study are subject to shear flows, which implies that the distributions of particle positions obtained with MnPIV may reflect additional forces acting on the particle. Unfortunately, obtaining particle distributions for particles suspended in a quiescent fluid is difficult using the current experimental setup because of the photobleaching of the fluorescent tracers used in MnPIV. Moreover, these studies also differ from almost all other colloid science studies in that the particle z-positions are obtained for an ensemble of particles at the same time, *vs.* for a single particle sampled at different times. The results presented here therefore represent the particle-wall interaction averaged over all the particles and wall surface positions in the ensemble, much like the so-called ensemble TIRM technique [198]. Variations in both the particle and wall properties (*e.g.* size, roughness, surface charge) may affect these results. A few studies have also suggested that this overestimation of the Debye length is due to the properties of the polystyrene sphere surface or extra particle-wall interactions that are neglected in the model [176, 8, 167]. Suresh and Walz [176], who modeled the electrostatic interaction potential energy for a rough sphere over a smooth plate, showed that the electrostatic interactions were felt by the particle over a bigger range of separation distances as the surface roughness of the particle increased. Behrens et al. [8] measured decay lengths that were larger than the theoretical predictions in KCl

solutions at salt concentrations exceeding 0.1 mM and attributed this discrepancy to additional interactions between the polymer strands protruding from the PS particles into the solution. Sharp and Dickinson [167], who studied interactions between a yeast cell and a glass surface, also reported measurements of decay lengths greater than theoretical predictions, and hypothesized that these larger decay lengths were related to additional repulsive (*e.g.*, steric) forces that is neglected in the model. While quantifying these factors is beyond the scope of this thesis, this result suggests that detailed characterization of the surface properties of the particles and the wall could further improve the capabilities of MnPIV.

REFERENCES

[1] Adrian, R. J., "Twenty years of particle image velocimetry," *Exp Fluids*, vol. 39, no. 2, pp. 159–169, 2005.

[2] Albrecht, H., Borys, M., Damaschke, N., and Tropea, C., *Laser-Doppler and Phase-Doppler Measurement Techniques*. Springer-Verlag, Berlin, 2002.

[3] Attard, P., "Nanobubbles and the hydrophobic attraction," *Adv Colloid Interfac*, vol. 104, pp. 75–91, 2003.

[4] Avallone, E. and Baumeister, T., *Marks' Standard Handbook for Mechanical Engineers*. McGraw-Hill., 10th ed., 1996.

[5] Baek, S. J. and Lee, S. J., "A new two-frame particle tracking algorithm using match probability," *Exp Fluids*, vol. 22, no. 1, pp. 23–32, 1996.

[6] Banerjee, A. and Kihm, K. D., "Experimental verification of near-wall hindered diffusion for the Brownian motion of nanoparticles using evanescent wave microscopy," *Phys Rev E*, vol. 72, no. 4, p. 042101, 2005.

[7] Barrat, J. L. and Bocquet, L., "Large slip effect at a nonwetting fluid-solid interface," *Phys Rev Lett*, vol. 82, no. 23, pp. 4671–4674, 1999.

[8] Behrens, S. H., Plewa, J., and Grier, D. G., "Measuring a colloidal particle's interaction with a flat surface under nonequilibrium conditions - total internal reflection microscopy with absolute position information," *Eur Phys J E*, vol. 10, no. 2, pp. 115–121, 2003.

[9] Bevan, M. A. and Prieve, D. C., "Hindered diffusion of colloidal particles very near to a wall: revisited," *J Chem Phys*, vol. 113, no. 3, pp. 1228–1236, 2000.

[10] Blake, T. D., "Slip between a liquid and a solid - tolstoi,d.m. (1952) theory reconsidered," *Colloid Surface*, vol. 47, pp. 135–145, 1990.

[11] Bocquet, L. and Barrat, J. L., "Flow boundary conditions from nano- to micro-scales," *Soft Matter*, vol. 3, no. 6, pp. 685–693, 2007.

[12] Bonaccurso, E., Butt, H. J., and Craig, V. S. J., "Surface roughness and hydrodynamic boundary slip of a newtonian fluid in a completely wetting system," *Phys Rev Lett*, vol. 90, no. 14, p. 4, 2003.

[13] Bonaccurso, E., Kappl, M., and Butt, H. J., "Hydrodynamic force measurements: Boundary slip of water on hydrophilic surfaces and electrokinetic effects," *Phys Rev Lett*, vol. 88, no. 7, p. 076103, 2002.

[14] Bourdon, C. J., Olsen, M. G., and Gorby, A. D., "The depth of correlation in micro-PIV for high numerical aperture and immersion objectives," *J Fluid Eng-T ASME*, vol. 128, no. 4, pp. 883–886, 2006.

[15] Bourdon, C., Olsen, M., and Gorby, A., "Validation of an analytical solution for depth of correlation in microscopic particle image velocimetry," *Meas Sci Technol*, vol. 15, no. 2, pp. 318–27, 2004.

[16] Bown, M. R., MacInnes, J. M., Allen, R. W. K., and Zimmerman, W. B. J., "Three-dimensional, three-component velocity measurements using stereoscopic micro-PIV and PTV," *Meas Sci Technol*, vol. 17, no. 8, pp. 2175–2185, 2006.

[17] Brandner, J. J., Bohn, L., Henning, T., Schygulla, U., and Schuberth, K., "Microsructure heat exchanger applications in laboratory and industry," *Heat Transfer Eng*, vol. 28, no. 8-9, pp. 761–771, 2007.

[18] Breedveld, V., Van den Ende, D., Tripathi, A., and Acrivos, A., "The measurement of the shear-induced particle and fluid tracer diffusivities in concentrated suspensions by a novel method.," *J Fluid Mech*, vol. 375, pp. 297–318, 1998.

[19] Brenner, H., "The slow motion of a sphere through a viscous fluid towards a plane surface.," *Chem Eng Sci*, vol. 16, pp. 242–251, 1961.

[20] Breuer, K., *Microscale diagnostic techniques*. New York: Springer, Berlin Heidelberg, 2005.

[21] Burke, M. W., *Image Acquisition*. London: Chapman & Hall, 1996.

[22] Celata, G. P., Cumo, M., McPhail, S., and Zummo, G., "Characterization of fluid dynamic behaviour and channel wall effects in microtube," *Int J Heat Fluid Fl*, vol. 27, no. 1, pp. 135–143, 2006.

[23] Cenedese, A. and Paglialunga, A., "A new technique for the determination of the third velocity component with PIV," *Exp Fluids*, vol. 8, pp. 228–230, 1989.

[24] Chandrasekhar, S., "Stochastic problems in physics and astronomy.," *Rev Mod Phys*, vol. 15, no. 1, pp. 1–89, 1943.

[25] Cheng, J. T. and Giordano, N., "Fluid flow through nanometer-scale channels.," *Phys Rev E*, vol. 65, p. 031206, 2002.

[26] Chew, H., McNulty, P. J., and Kerker, M., "Model for Raman and fluorescent scattering by molecules embedded in small particles," *Phys Rev A*, vol. 13, no. 1, pp. 396–404, 1976.

[27] Chew, H., Wang, D. S., and Kerker, M., "Elastic-scattering of evanescent electromagnetic-waves," *Appl Optics*, vol. 18, no. 15, pp. 2679–2687, 1979.

[28] Cho, J. H. J., Law, B. M., and Rieutord, F., "Dipole-dependent slip of newtonian liquids at smooth solid hydrophobic surfaces," *Phys Rev Lett*, vol. 92, no. 16, p. 166102, 2004.

[29] Choi, C. H., Westin, K. J. A., and Breuer, K. S., "Apparent slip flows in hydrophilic and hydrophobic microchannels," *Phys Fluids*, vol. 15, no. 10, pp. 2897–2902, 2003.

[30] Choi, C. K., Margraves, C. H., and Kihm, K. D., "Examination of near-wall hindered brownian diffusion of nanoparticles: Experimental comparison to theories by brenner (1961) and goldman et al. (1967)," *Phys Fluids*, vol. 19, no. 10, p. 103305, 2007.

[31] Christenson, H. K. and Claesson, P. M., "Direct measurements of the force between hydrophobic surfaces in water," *Adv Colloid Interfac*, vol. 91, no. 3, pp. 391–436, 2001.

[32] Churaev, N. V., Ralston, J., Sergeeva, I. P., and Sobolev, V. D., "Electrokinetic properties of methylated quartz capillaries," *Adv Colloid Interfac*, vol. 96, no. 1-3, pp. 265–278, 2002.

[33] Clark, A. T., Lal, M., and Watson, G. M., "Dynamics of colloidal particles in the vicinity of an interacting surface.," *Faraday Discuss Chem Soc*, vol. 83, pp. 179–191, 1987.

[34] Cottin-Bizonne, C., Barrat, J. L., Bocquet, L., and Charlaix, E., "Low-friction flows of liquid at nanopatterned interfaces," *Nat Mater*, vol. 2, no. 4, pp. 237–240, 2003.

[35] Cottin-Bizonne, C., Cross, B., Steinberger, A., and Charlaix, E., "Boundary slip on smooth hydrophobic surfaces: Intrinsic effects and possible artifacts," *Phys Rev Lett*, vol. 94, no. 5, p. 056102, 2005.

[36] Cottin-Bizonne, C., Steinberger, A., Cross, B., Raccurt, O., and Charlaix, E., "Nanohydrodynamics: The intrinsic flow boundary condition on smooth surfaces," *Langmuir*, vol. 24, no. 4, pp. 1165–1172, 2008.

[37] Craig, V. S. J., Neto, C., and Williams, D. R. M., "Shear-dependent boundary slip in an aqueous newtonian liquid," *Phys Rev Lett*, vol. 8705, no. 5, p. 054504, 2001.

[38] Crevillen, A. G., Hervas, M., Lopez, M. A., Gonzalez, M. C., and Escarpa, A., "Real sample analysis on microfluidic devices," *Talanta*, vol. 74, no. 3, pp. 342–357, 2007.

[39] Crocker, J. C. and Grier, D. G., "Methods of digital video microscopy for colloidal studies," *J Colloid Interf Sci*, vol. 179, no. 1, pp. 298–310, 1996.

[40] Cross, B., Steinberger, A., Cottin-Bizonne, C., Rieu, J. P., and Charlaix, E., "Boundary flow of water on supported phospholipid films," *Europhys Lett*, vol. 73, no. 3, pp. 390–395, 2006.

[41] Cuche, E., Marquet, P., and Depeursinge, C., "Simultaneous amplitude-contrast and quantitative phase-contrast microscopy by numerical reconstruction of Fresnel off-axis holograms," *Appl Optics*, vol. 38, no. 34, pp. 6994–7001, 1999.

[42] Czarske, J., Buttner, L., Razik, T., and Muller, H., "Boundary layer velocity measurements by a laser Doppler profile sensor with micrometre spatial resolution," *Meas Sci Technol*, vol. 13, no. 12, pp. 1979–1989, 2002.

[43] Czarske, J., "Laser Doppler velocimetry profile sensor using a chromatic coding," *Meas Sci Technol*, vol. 12, pp. 52–57, 2001.

[44] Datta, S., Conlisk, A. T., Li, H. F., and Yoda, M., "Effect of divalent ions on electroosmotic flow in microchannels," *Mech Res Commun*. DOI 10.1016/j.mechrescom.2008.07.006.

[45] Dinkelacker, F., Schäfer, M., Ketterle, W., Wolfrum, J., Stolz, W., and Köhler, J., "Determination of the third velocity component with PTA using an intensity graded light sheet," *Exp Fluids*, vol. 13, pp. 357–359, 1992.

[46] Doshi, D. A., Watkins, E. B., Israelachvili, J. N., and Majewski, J., "Reduced water density at hydrophobic surfaces: Effect of dissolved gases," *P Natl Acad Sci USA*, vol. 102, no. 27, pp. 9458–9462, 2005.

[47] Dubois, F., Joannes, L., and Legros, J. C., "Improved three-dimensional imaging with a digital holography microscope with a source of partial spatial coherence," *Appl Optics*, vol. 38, no. 34, pp. 7085–7094, 1999.

[48] Durst, F., Melling, A., and Whitelaw, J. H., *Principles and Practice of Laser-Doppler Anemometry*. London: Academic Press, 1981.

[49] Einav, S. and Berman, H. J., "Fringe mode transmittance laser Doppler microscope anemometer - its adaptation for measurement in the microcirculation," *J Biomed Eng*, vol. 10, no. 5, pp. 393–399, 1988.

[50] Einstein, A., "Über die von der molekularkinetischen theorie der wärme geforderte bewegung von in ruhenden flssigkeiten suspendierten teilchen.," *Ann Phys*, vol. 17, no. 3, pp. 549–560, 1905.

[51] Ermak, D. L. and McCammon, J. A., "Brownian dynamics with hydrodynamic interactions," *J Chem Phys*, vol. 69, no. 4, pp. 1352–1360, 1978.

[52] Faxén, H., "Der widerstand gegen die bewegung einer starren kugel in einer zähen flüssigkeit, die zwischen zwei parallelen ebenen wänden eingeschlossen ist.," *Ann Phys*, vol. 4, no. 68, pp. 89–119, 1922.

[53] Flicker, S. G. and Bike, S. G., "Measuring double-layer repulsion using total internal-reflection microscopy," *Langmuir*, vol. 9, no. 1, pp. 257–262, 1993.

[54] Galea, T. M. and Attard, P., "Molecular dynamics study of the effect of atomic roughness on the slip length at the fluid-solid boundary during shear flow," *Langmuir*, vol. 20, no. 8, pp. 3477–3482, 2004.

[55] Gingell, D., Heavens, O. S., and Mellor, J. S., "General electromagnetic theory of total internal-reflection fluorescence - the quantitative basis for mapping cell substratum topography," *J Cell Sci*, vol. 87, pp. 677–693, 1987.

[56] Goldman, A. J., Cox, R. G., and Brenner, H., "Slow viscous motion of a sphere parallel to a plane wall – I Motion through a quiescent fluid," *Chem Eng Sci*, vol. 22, pp. 637–651, 1967.

[57] Goldstein, S., *Modern Developments in Fluid Dynamics*. Oxford: Clarendon Press, 1938.

[58] Gosch, M., Blom, H., Holm, J., Heino, T., and Rigler, R., "Hydrodynamic flow profiling in microchannel structures by single molecule fluorescence correlation spectroscopy," *Anal Chem*, vol. 72, no. 14, pp. 3260–3265, 2000.

[59] Guasto, J. S. and Breuer, K. S., "Simultaneous, ensemble-averaged measurement of near-wall temperature and velocity in steady micro-flows using single quantum dot tracking," *Exp Fluids*, vol. 45, no. 1, pp. 157–166, 2008.

[60] Hagsäter, S., Westergaard, C., Bruus, H., and Kutter, J., "A compact viewing configuration for stereoscopic micro-PIV utilizing mm-sized mirrors," *Exp Fluids*. DOI 10.1007/s00348-008-0523-3.

[61] Hamaker, H. C., "The london - van der waals attraction between spherical particles," *Physica*, vol. 4, pp. 1058–1072, 1937.

[62] Heavens, O. S. and Gingell, D., "Film thickness measurement by frustrated total reflection fluorescence," *Opt Laser Technol*, vol. 23, no. 3, pp. 175–179, 1991.

[63] Henry, C. L., Neto, C., Evans, D. R., Biggs, S., and Craig, V. S. J., "The effect of surfactant adsorption on liquid boundary slippage," *Physica A*, vol. 339, no. 1-2, pp. 60–65, 2004.

[64] Herpfer, D. C. and Jeng, S. M., "Planar measurement of three-component velocity by streaked-particle-imaging velocimetry," *Appl Optics*, vol. 34, no. 13, pp. 2301–2304, 1995.

[65] Hill, D. F., Sharp, K. V., and Adrian, R. J., "Stereoscopic particle image velocimetry measurements of the flow around a rushton turbine," *Exp Fluids*, vol. 29, no. 5, pp. 478–485, 2000.

[66] Hinsch, K. D., "Holographic particle image velocimetry," *Meas Sci Technol*, vol. 13, no. 7, pp. R61–R72, 2002.

[67] Hohreiter, V., Wereley, S. T., Olsen, M. G., and Chung, J. N., "Cross-correlation analysis for temperature measurement.," *Meas Sci Technol*, vol. 13, pp. 1072–1078, 2002.

[68] Honig, C. D. F. and Ducker, W. A., "No-slip hydrodynamic boundary condition for hydrophilic particles," *Phys Rev Lett*, vol. 98, no. 2, p. 028305, 2007.

[69] Hu, H., Saga, T., Kobayashi, T., and Taniguchi, N., "A study on a lobed jet mixing flow by using stereoscopic particle image velocimetry technique," *Phys Fluids*, vol. 13, no. 11, pp. 3425–3441, 2001.

[70] Huang, P. and Breuer, K. S., "Direct measurement of anisotropic near-wall hindered diffusion using total internal reflection velocimetry," *Phys Rev E*, vol. 76, no. 4, 2007.

[71] Huang, P. and Breuer, K. S., "Direct measurement of slip length in electrolyte solutions," *Phys Fluids*, vol. 19, no. 2, p. 028104, 2007.

[72] Huang, P., Guasto, J. S., and Breuer, K. S., "Direct measurement of slip velocities using three-dimensional total internal reflection velocimetry," *J Fluid Mech*, vol. 566, pp. 447–464, 2006.

[73] Hyvaluoma, J. and Harting, J., "Slip flow over structured surfaces with entrapped microbubbles," *Phys Rev Lett*, vol. 100, no. 24, p. 246001, 2008.

[74] Ikeda, Y., Yamada, N., and Nakajima, T., "Multi-intensity-layer particle-image velocimetry for spray measurement," *Meas Sci Technol*, vol. 11, pp. 617–626, 2000.

[75] Iler, R. K., *The Chemistry of Silica: Solubility, Polymerization, Colloid and Surface Properties and Biochemistry of Silica*. New York: Jon Wiley & Sons, 1979.

[76] Israelachvili, J. N. and Adams, G. E., "Measurement of forces between 2 mica surfaces in aqueous-electrolyte solutions in range 0-100 nm," *J Chem Soc Faraday T*, vol. 74, p. 975, 1978.

[77] Jacobson, S. C., Moore, A. W., and Ramsey, J. M., "Fused quartz substrates for microchip electrophoresis," *Anal Chem*, vol. 67, no. 13, pp. 2059–2063, 1995.

[78] Jehle, M. and Jarhne, B., "A novel method for three-dimensional three-component analysis of flows close to free water surfaces," *Exp Fluids*, vol. 44, no. 3, pp. 469–480, 2008.

[79] Jin, S., Huang, P., Park, J., Yoo, J. Y., and Breuer, K. S., "Near-surface velocimetry using evanescent wave illumination," *Exp Fluids*, vol. 37, no. 6, pp. 825–833, 2004.

[80] Jódar-Reyes, A. B., Ortega-Vinuesa, J. L., and Martín-Rodríguez, A., "Electrokinetic behavior and colloidal stability of polystyrene latex coated with ionic surfactants," *Journal Of Colloid And Interface Science*, vol. 297, pp. 170–181, 2006.

[81] Joly, L., Ybert, C., and Bocquet, L., "Probing the nanohydrodynamics at liquid-solid interfaces using thermal motion," *Phys Rev Lett*, vol. 96, no. 4, p. 046101, 2006.

[82] Joseph, P., Cottin-Bizonne, C., Benoit, J. M., Ybert, C., Journet, C., Tabeling, P., and Bocquet, L., "Slippage of water past superhydrophobic carbon nanotube forests in microchannels," *Phys Rev Lett*, vol. 97, no. 15, 2006.

[83] Joseph, P. and Tabeling, P., "Direct measurement of the apparent slip length," *Phys Rev E*, vol. 71, p. 035303, 2005.

[84] Kaminsky, R., Kallweit, S., Weber, H. J., Claessens, T., Jozwik, K., and Verdonck, P., "Flow visualization through two types of aortic prosthetic heart valves using stereoscopic high-speed particle image velocimetry," *Artif Organs*, vol. 31, no. 12, pp. 869–879, 2007.

[85] Kampmeyer, P. M., "The temperature dependence of viscosity for water and mercury," *J Appl Phys*, vol. 23, no. 1, pp. 99–102, 1952.

[86] Kanda, K., Ogata, S., Jingu, K., and Yang, M., "Measurement of particle distribution in microchannel flow using a 3D-TIRFM technique," *J Visual-Japan*, vol. 10, no. 2, pp. 207–215, 2007.

[87] Kihm, K. D., Banerjee, A., Choi, C. K., and Takagi, T., "Near-wall hindered Brownian diffusion of nanoparticles examined by three-dimensional ratiometric total internal reflection fluorescence microscopy (3-D R-TIRFM)," *Exp Fluids*, vol. 37, pp. 811–824, 2004.

[88] Kim, S. and Lee, S., "Measurement of dean flow in a curved micro-tube using micro digital holographic particle tracking velocimetry," *Exp Fluids*. DOI 10.1007/s00348-008-0555-8.

[89] Kinoshita, H., Kaneda, S., Fujii, T., and Oshima, M., "Three-dimensional measurement and visualization of internal flow of a moving droplet using confocal micro-PIV," *Lab Chip*, vol. 7, no. 3, pp. 338–346, 2007.

[90] Klank, H., Goranovic, G., Kutter, J. P., Gjelstrup, H., Michelsen, J., and Westergaard, C. H., "PIV measurements in a microfluidic 3D-sheathing structure with three-dimensional flow behaviour," *J Micromech Microeng*, vol. 12, no. 6, pp. 862–869, 2002.

[91] Kline, S. J. and McClintock, F. A., "Describing uncertainties in single-sample experiments.," *Mech Eng*, vol. 75, no. 1, pp. 3–9, 1953.

[92] Koochesfahani, M., *Experiments on turbulent mixing and chemical reactions in a liquid mixing layer.* PhD thesis, California Institute of Technology, Pasadena, CA, USA, 1984.

[93] Koochesfahani, M. M. and Nocera, D. G., "Molecular tagging velocimetry," in *Handbook of Experimental Fluid Mechanics* (Foss, J., Tropea, C., and Yarin, A., eds.), Springer-Verlag, 2007.

[94] Koplik, J., Banavar, J., and Willemsen, J., "Molecular dynamics of fluid flow at solid surfaces," *Phys Fluids A*, vol. 5, no. 1, p. 781, 1999.

[95] Lasne, D., Maali, A., Amarouchene, Y., Cognet, L., Lounis, B., and Kellay, H., "Velocity profiles of water flowing past solid glass surfaces using fluorescent nanoparticles and molecules as velocity probes," *Phys Rev Lett*, vol. 100, no. 21, p. 4, 2008.

[96] Lauga, E. and Brenner, M. P., "Dynamic mechanisms for apparent slip on hydrophobic surfaces," *Phys Rev E*, vol. 70, no. 2, p. 026311, 2004.

[97] Lauga, E., Brenner, M. P., and Stone, H. A., "Microfluidics: the no-slip boundary condition.," in *Handbook of Experimental Fluid Dynamics* (Tropea, C., Foss, J., and Yarin, A., eds.), NewYork: Springer-Verlag, 2005.

[98] Lauga, E. and Stone, H. A., "Effective slip in pressure-driven stokes flow," *J Fluid Mech*, vol. 489, pp. 55–77, 2003.

[99] Lee, E. H., Benner, R. E., Fenn, J. B., and Chang, R. K., "Angular-distribution of fluorescence from liquids and monodispersed spheres by evanescent wave excitation," *Appl Optics*, vol. 18, no. 6, pp. 862–868, 1979.

[100] Li, E., Tieu, K., and Mackenzie, M., "Interference patterns of two focused gaussian beams in an LDA measuring volume," *Opt Laser Eng*, vol. 27, no. 4, pp. 395–407, 1997.

[101] Li, H. F., Sadr, R., and Yoda, M., "Multilayer nano-particle image velocimetry," *Exp Fluids*, vol. 41, no. 2, pp. 185–194, 2006.

[102] Li, H. F. and Yoda, M., "Multilayer nano-particle image velocimetry (mnpiv) in microscale Poiseuille flows," *Meas Sci Technol*, vol. 19, no. 7, p. 075402, 2008.

[103] Li, H. F., Yoda, M., Gnanaprakasam, P., and Conlisk, A. T., "Effect of divalent electrolytes on electroosmotic flow (EOF)," *The American Physical Society 58th annual meeting of the Division of Fluid Dynamics, Seattle, Washington, USA*, 2005.

[104] Lima, R., Wada, S., Tsubota, K., and Yamaguchi, T., "Confocal micro-piv measurements of three-dimensional profiles of cell suspension flow in a square microchannel," *Meas Sci Technol*, vol. 17, no. 4, pp. 797–808, 2006.

[105] Lin, B., Yu, J., and Rice, S. A., "Direct measurements of constrained Brownian motion of an isolated sphere between two walls.," *Phys Rev E*, vol. 62, no. 3, pp. 3909–3919, 2000.

[106] Lin, D. J., Angarita-Jaimes, N. C., Chen, S. Y., Greenaway, A. H., Towers, C. E., and Towers, D. P., "Three-dimensional particle imaging by defocusing method with an annular aperture," *Opt Lett*, vol. 33, no. 9, pp. 905–907, 2008.

[107] Lindken, R., Westerweel, J., and Wieneke, B., "Stereoscopic micro particle image velocimetry," *Exp Fluids*, vol. 41, no. 2, pp. 161–171, 2006.

[108] Liu, B. J., Yu, X. J., Liu, H. X., Jiang, H. K., Yuan, H. J., and Xu, Y. T., "Application of SPIV in turbomachinery," *Exp Fluids*, vol. 40, no. 4, pp. 621–642, 2006.

[109] Lum, K., Chandler, D., and Weeks, J. D., "Hydrophobicity at small and large length scales," *J Phys Chem B*, vol. 103, no. 22, pp. 4570–4577, 1999.

[110] Lumma, D., Best, A., Gansen, A., Feuillebois, F., Radler, J. O., and Vinogradova, O. I., "Flow profile near a wall measured by double-focus fluorescence cross-correlation," *Phys Rev E*, vol. 67, no. 5, p. 056313, 2003.

[111] Maali, A., Cohen-Bouhacina, T., and Kellay, H., "Measurement of the slip length of water flow on graphite surface," *Applied Physics Letters*, vol. 92, no. 5, p. 053101, 2008.

[112] Maccarini, M., "Water at solid surfaces: A review of selected theoretical aspects and experiments on the subject," *Biointerphases*, vol. 2, no. 3, pp. MR1–MR15, 2007.

[113] Majumder, M., Chopra, N., Andrews, R., and Hinds, B. J., "Nanoscale hydrodynamics - enhanced flow in carbon nanotubes," *Nature*, vol. 438, no. 7064, p. 44, 2005.

[114] Margraves, C. H., Choi, C. K., and Kihm, K. D., "Measurements of the minimum elevation of nano-particles by 3D nanoscale tracking using ratiometric evanescent wave imaging," *Exp Fluids*, vol. 41, no. 2, pp. 173–183, 2006.

[115] Martini, A., Hsu, H. Y., Patankar, N. A., and Lichter, S., "Slip at high shear rates," *Phys Rev Lett*, vol. 100, no. 20, p. 206001, 2008.

[116] Maynes, D. and Webb, A. R., "Velocity profile characterization in sub-millimeter diameter tubes using molecular tagging velocimetry," *Exp Fluids*, vol. 32, pp. 3–15, 2002.

[117] McKee, C. T., Clark, S. C., Walz, J. Y., and Ducker, W. A., "Relationship between scattered intensity and separation for particles in an evanescent field," *Langmuir*, vol. 21, no. 13, pp. 5783–5789, 2005.

[118] Meinhart, C. D. and Wereley, S. T., "The theory of diffraction-limited resolution in microparticle image velocimetry," *Meas Sci Technol*, vol. 14, no. 7, pp. 1047–1053, 2003.

[119] Meinhart, C. D., Wereley, S. T., and Santiago, J. G., "A PIV algorithm for estimating time-averaged velocity fields," *J Fluid Eng-T ASME*, vol. 122, no. 2, pp. 285–289, 2000.

[120] Meng, H., Pan, G., Pu, Y., and Woodward, S. H., "Holographic particle image velocimetry: from film to digital recording," *Meas Sci Technol*, vol. 15, no. 4, pp. 673–685, 2004.

[121] Meyer, K. E., Ozcan, O., and Westergaard, C. H., "Flow mapping of a jet in crossflow with stereoscopic PIV," *J Visual-Japan*, vol. 5, no. 3, pp. 225–231, 2002.

[122] Migler, K. B., Hervet, H., and Leger, L., "Slip transition of a polymer melt under shear-stress," *Phys Rev Lett*, vol. 70, no. 3, pp. 287–290, 1993.

[123] Mishina, H., Asakura, T., and Nagai, S., "Laser Doppler microscope," *Optics Communications*, vol. 11, no. 1, pp. 99–102, 1974.

[124] Moreno, D., Santoyo, F., Guerrero, J., and Funes-Gallanzi, M., "Particle positioning from charge-coupled device images by the generalized Lorenz-Mie theory and comparison with experiment," *Appl Optics*, vol. 39, no. 8, pp. 5117–5124, 2000.

[125] Neto, C., Craig, V. S. J., and Williams, D. R. M., "Evidence of shear-dependent boundary slip in newtonian liquids," *Eur Phys J E*, vol. 12, pp. S71–S74, 2003.

[126] Neto, C., Evans, D. R., Bonaccurso, E., Butt, H. J., and Craig, V. S. J., "Boundary slip in newtonian liquids: a review of experimental studies," *Rep Prog Phys*, vol. 68, no. 12, pp. 2859–2897, 2005.

[127] Oetama, R. J. and Walz, J. Y., "A new approach for analyzing particle motion near an interface using total internal reflection microscopy," *J Colloid Interf Sci*, vol. 284, no. 1, pp. 323–331, 2005.

[128] Olsen, M. G. and Adrian, R. J., "Out-of-focus effects on particle image visibility and correlation in microscopic particle image velocimetry," *Exp Fluids*, vol. [Suppl.], pp. 166–174, 2000.

[129] Olsen, M. G. and Adrian, R. J., "Brownian motion and correlation in particle image velocimetry," *Opt Laser Technol*, vol. 32, pp. 621–627, 2000.

[130] O'Neill, M. E., "A slow motion of viscous liquid caused by a slowly moving solid sphere," *Mathematika*, vol. 11, pp. 67–74, 1964.

[131] Ovryn, B., "Three-dimensional forward scattering particle image velocimetry applied to a microscopic field-of-view," *Exp Fluids*, vol. [Suppl.], pp. 175–184, 2000.

[132] Pagac, E. S., Tilton, R. D., and Prieve, D. C., "Hindered mobility of a rigid sphere near a wall," *Chem Eng Commun*, vol. 150, pp. 105–122, 1996.

[133] Palchetti, I. and Mascini, M., "Electroanalytical biosensors and their potential for food pathogen and toxin detection," *Anal Bioanal Chem*, vol. 391, no. 2, pp. 455–471, 2008.

[134] Panton, R. L., *Incompressible flow*. John Wiley and Sons, New York, 1995.

[135] Park, J. S., Choi, C. K., and Kihm, K. D., "Optically sliced micro-PIV using confocal laser scanning microscopy (CLSM)," *Exp Fluids*, vol. 37, no. 1, pp. 105–119, 2004.

[136] Paul, P. H., Garguilo, M. G., and Rakestraw, D. J., "Imaging of pressure- and electrokinetically driven flows through open capillaries," *Anal Chem*, vol. 70, pp. 2459–2467, 1998.

[137] Penner, S. S. and Jerskey, T., "Use of lasers for local measurement of velocity components, species densities, and temperatures," *Annu Rev Fluid Mech*, vol. 5, no. 1, pp. 9–30, 1973.

[138] Pereira, F., Lu, J., Castano-Graff, E., and Gharib, M., "Microscale 3D flow mapping with μDDPIV," *Exp Fluids*, vol. 42, no. 4, pp. 589–599, 2007.

[139] Pit, R., Hervet, H., and Leger, L., "Friction and slip of a simple liquid at a solid surface," *Tribol Lett*, vol. 7, no. 2-3, pp. 147–152, 1999.

[140] Pit, R., Hervet, H., and Leger, L., "Direct experimental evidence of slip in Hexadecane: solid interfaces," *Phys Rev Lett*, vol. 85, no. 5, pp. 980–983, 2000.

[141] Pouya, S., Koochesfahani, M. M., Greytak, A. B., Bawendi, M. G., and Nocera, D. G., "Experimental evidence of diffusion-induced bias in near-wall velocimetry using quantum dot measurements," *Exp Fluids*, vol. 44, no. 6, pp. 1035–1038, 2008.

[142] Pouya, S., Koochesfahani1, M., Snee, P., Bawendi, M., and Nocera, D., "Single quantum dot (QD) imaging of fluid flow near surfaces," *Exp Fluids*, vol. 39, no. 4, pp. 784–786, 2005.

[143] Prasad, A. K., "Stereoscopic particle image velocimetry," *Exp Fluids*, vol. 29, no. 2, pp. 103–116, 2000.

[144] Press, W. H., Teukolsky, S. A., Vetterling, W. T., and Flannery, B. P., *Numerical Recipes in C: the art of scientific computing*. New York: Cambridge University Press, 2nd ed., 1992.

[145] Prieve, D. C., "Measurement of colloidal forces with TIRM," *Adv Colloid Interfac*, vol. 82, no. 1-3, pp. 93–125, 1999.

[146] Prieve, D. C. and Walz, J. Y., "Scattering of an evanescent surface-wave by a microscopic dielectric sphere," *Appl Optics*, vol. 32, no. 9, pp. 1629–1641, 1993.

[147] Priezjev, N., "Effect of surface roughness on rate-dependent slip in simple fluids," *Journal of Chemical Physics*, vol. 127, p. 144708, 2007.

[148] Priezjev, N., "Rate-dependent slip boundary conditions for simple fluids," *Phys Rev E*, vol. 75, p. 051605, 2007.

[149] Priezjev, N. V., "Effect of surface roughness on rate-dependent slip in simple fluids," *Journal Of Chemical Physics*, vol. 127, no. 14, p. 144708, 2007.

[150] Priezjev, N. V. and Troian, S. M., "Influence of periodic wall roughness on the slip behaviour at liquid/solid interfaces: molecular-scale simulations versus continuum predictions," *J Fluid Mech*, vol. 554, pp. 25–46, 2006.

[151] Psaltis, D., Quake, S. R., and Yang, C., "Developing optofluidic technology through the fusion of microfluidics and optics," *Nature*, vol. 442, no. 27, pp. 381–386, 2006.

[152] Pumera, M., "Trends in analysis of explosives by microchip electrophoresis and conventional CE," *Electrophoresis*, vol. 29, no. 1, pp. 269–273, 2008.

[153] Raffel, M., Willert, C., Wereley, S., and Kompenhans, J., *Particle image velocimetry a practical guide*. Berlin: Springer-Verlag, 2007.

[154] Roetmann, K., Schmunk, W., Garbe, C. S., and Beushausen, V., "Micro-flow analysis by molecular tagging velocimetry and planar raman-scattering," *Exp Fluids*, vol. 44, no. 3, pp. 419–430, 2008.

[155] Royer, H., "Holography and particle image velocimetry," *Meas Sci Technol*, vol. 8, no. 12, pp. 1562–1572, 1997.

[156] Sadr, R., Hohenegger, C., Li, H. F., Mucha, P. J., and Yoda, M., "Diffusion-induced bias in near-wall velocimetry," *J Fluid Mech*, vol. 577, pp. 443–456, 2007.

[157] Sadr, R., Li, H. F., and Yoda, M., "Impact of hindered Brownian diffusion on the accuracy of particle-image velocimetry using evanescent-wave illumination," *Exp Fluids*, vol. 38, no. 1, pp. 90–98, 2005.

[158] Sadr, R., Yoda, M., Gnanaprakasam, P., and Conlisk, A. T., "Velocity measurements inside the diffuse electric double layer in electroosmotic flow.," *Applied Physics Letters*, vol. 89, no. 4, p. 044103, 2006.

[159] Sadr, R., Yoda, M., Zheng, Z., and Conlisk, A. T., "An experimental study of electro-osmotic flow in rectangular microchannels," *J Fluid Mech*, vol. 506, pp. 357–367, 2004.

[160] Santiago, J. G., Wereley, S. T., Meinhart, C. D., Beebe, D. J., and Adrian, R. J., "A particle image velocimetry system for microfluidics," *Exp Fluids*, vol. 25, no. 4, pp. 316–319, 1998.

[161] Sarkar, A., Robertson, R. B., and Fernandez, J. M., "Simultaneous atomic force microscope and fluorescence measurements of protein unfolding using a calibrated evanescent wave," *P Natl Acad Sci USA*, vol. 101, no. 35, pp. 12882–12886, 2004.

[162] Satake, S.-i., Kunugi, T., Sato, K., Ito, T., Kanamori, H., and Taniguchi, J., "Measurements of 3D flow in a micro-pipe via micro digital holographic particle tracking velocimetry," *Meas Sci Technol*, no. 7, p. 1647, 2006.

[163] Sbragaglia, M., Benzi, R., Biferale, L., Succi, S., and Toschi, F., "Surface roughness-hydrophobicity coupling in microchannel and nanochannel flows," *Phys Rev Lett*, vol. 97, no. 20, p. 204503, 2006.

[164] Schmatko, T., Hervet, H., and Leger, L., "Friction and slip at simple fluid-solid interfaces: The roles of the molecular shape and the solid-liquid interaction," *Phys Rev Lett*, vol. 94, no. 24, p. 244501, 2005.

[165] Schmatko, T., Hervet, H., and Leger, L., "Effect of nanometric-scale roughness on slip at the wall of simple fluids," *Langmuir*, vol. 22, no. 16, pp. 6843–6850, 2006.

[166] Schumacher, A. and van der Ven, T. G. M., "Borownian motion of charged colloidal particles surrounded by electric double layers," *Faraday Discuss Chem Soc*, vol. 83, pp. 75–85, 1987.

[167] Sharp, J. M. and Dickinson, R. B., "Direct evaluation of dlvo theory for predicting long-range forces between a yeast cell and a surface," *Langmuir*, vol. 21, no. 18, pp. 8198–8203, 2005.

[168] Sinton, D., "Microscale flow visualization.," *Microfluid Nanofluid*, vol. 1, pp. 2–21, 2004.

[169] Sinton, D., Xuan, X., and Li, D., "Thermally induced velocity gradients in electroosmotic microchannel flows: the cooling influence of optical infrastructure," *Exp Fluids*, vol. 37, pp. 872–882, 2004.

[170] Sosa, P. P., Moreno, D., Guerrero, J. A., and Funes-Gallanzi, M., "Low-magnification particle positioning for 3D velocimetry applications," *Opt Laser Technol*, vol. 34, pp. 59–68, 2002.

[171] Speidel, M., Jonas, A., and Florin, E. L., "Three-dimensional tracking of fluorescent nanoparticles with subnanometer precision by use of off-focus imaging," *Opt Lett*, vol. 28, no. 2, pp. 69–71, 2003.

[172] Steinberg, A. M., Driscoll, J. F., and Ceccio, S. L., "Measurements of turbulent premixed flame dynamics using cinema stereoscopic PIV," *Exp Fluids*, vol. 44, no. 6, pp. 985–999, 2008.

[173] Steinberger, A., Cottin-Bizonne, C., Kleimann, P., and Charlaix, E., "High friction on a bubble mattress," *Nat Mater*, vol. 6, no. 9, pp. 665–668, 2007.

[174] Stolz, W. and Köhler, J., "In-plane determination of 3D-velocity using particle tracking anemometry (PTA)," *Exp Fluids*, vol. 17, pp. 105–109, 1994.

[175] Sun, G. X., Bonaccurso, E., Franz, V., and Butt, H. J., "Confined liquid: Simultaneous observation of a molecularly layered structure and hydrodynamic slip," *Journal Of Chemical Physics*, vol. 117, no. 22, pp. 10311–10314, 2002.

[176] Suresh, L. and Walz, J. Y., "Direct measurement of the effect of surface roughness on the colloidal forces between a particle and flat plate," *Journal Of Colloid And Interface Science*, vol. 196, no. 2, pp. 177–190, 1997.

[177] Tan, H. Y., Loke, W. K., Tan, Y. T., and Nguyen, N. T., "A Lab-on-a-Chip for detection of nerve agent sarin in blood," *Lab Chip*, vol. 8, no. 6, pp. 885–891, 2008.

[178] Tanahashi, M., Murakami, S., Choi, G. M., Fukuchi, Y., and Miyauchi, T., "Simultaneous CH-OHPLIF and stereoscopic PIV measurements of turbulent premixed flames," *P Combust Inst*, vol. 30, pp. 1665–1672, 2005.

[179] Tatum, J. A., Finnis, M. V., Lawson, N. J., and Harrison, G. A., "3D particle image velocimetry of the flow field around a sphere sedimenting near a wall part 2. effects of distance from the wall," *J Non-Newton Fluid*, vol. 127, no. 2-3, pp. 95–106, 2005.

[180] Thompson, B. R., Maynes, D., and Webb, B. W., "Charaterization of the hydrodynamically developing flow in a microtube using MTV," *J Fluid Eng-T ASME*, vol. 127, pp. 1003–1012, 2005.

[181] Thompson, N. L., Burghardt, T. P., and Axelrod, D., "Measuring surface dynamics of biomolecules by total interal-reflection fluorescence with photobleaching recovery or correlation spectroscopy," *Biophys J*, vol. 33, pp. 435–454, 1981.

[182] Thompson, P. A. and Troian, S. M., "A general boundary condition for liquid flow at solid surfaces," *Nature*, vol. 389, no. 6649, pp. 360–362, 1997.

[183] Tien, W. H., Kartes, P., Yamasaki, T., and Dabiri, D., "A color-coded backlighted defocusing digital particle image velocimetry system," *Exp Fluids*, vol. 44, no. 6, pp. 1015–1026, 2008.

[184] Tieu, A. K., Mackenzie, M. R., and Li, E. B., "Measurements in microscopic flow with a solid-state LDA," *Exp Fluids*, vol. 19, no. 4, pp. 293–294, 1995.

[185] Tolstoi, D., "Molecular theory for slippage of liquids over solid surfaces," *Dokl Acad Nauk SSSR*, vol. 85, pp. 1089–1092, 1952.

[186] Tretheway, D. C. and Meinhart, C. D., "Apparent fluid slip at hydrophobic microchannel walls," *Phys Fluids*, vol. 14, no. 3, pp. L9–L12, 2002.

[187] Tretheway, D. C. and Meinhart, C. D., "A generating mechanism for apparent fluid slip in hydrophobic microchannels," *Phys Fluids*, vol. 16, no. 5, pp. 1509–1515, 2004.

[188] Tropea, C., "Laser-Doppler anemometry - recent developments and future challenges," *Meas Sci Technol*, vol. 6, no. 6, pp. 605–619, 1995.

[189] Tyrrell, J. W. G. and Attard, P., "Viscoelastic study using an atomic force microscope modified to operate as a nanorheometer," *Langmuir*, vol. 19, no. 13, pp. 5254–5260, 2003.

[190] Ulman, A., "Formation and structure of self-assembled monolayers.," *Chem Rev*, vol. 96, pp. 1533–1554, 1996.

[191] Vinogradova, O. I., "Slippage of water over hydrophobic surfaces," *Int J Miner Process*, vol. 56, no. 1-4, pp. 31–60, 1999.

[192] Vinogradova, O. I. and Yakubov, G. E., "Surface roughness and hydrodynamic boundary conditions," *Phys Rev E*, vol. 73, no. 4, p. 4, 2006.

[193] Voronov, R. S., Papavassiliou, D. V., and Lee, L. L., "Slip length and contact angle over hydrophobic surfaces," *Chem Phys Lett*, vol. 441, no. 4-6, pp. 273–276, 2007.

[194] Westerweel, J., "Fundamentals of digital particle image velocimetry," *Meas Sci Technol*, vol. 8, no. 12, pp. 1379–1392, 1997.

[195] Westerweel, J., "Theoretical analysis of the measurement precision in particle image velocimetry," *Exp Fluids*, vol. 29, pp. S3–S12, 2000.

[196] Willert, C. E. and Gharib, M., "Three-dimensional particle imaging with a single camera," *Exp Fluids*, vol. 12, no. 6, pp. 353–358, 1992.

[197] Willmott, G. R. and Tallon, J. L., "Measurement of newtonian fluid slip using a torsional ultrasonic oscillator," *Phys Rev E*, vol. 76, no. 6, p. 066306, 2007.

[198] Wu, H. J. and Bevan, M. A., "Direct measurement of single and ensemble average particle-surface potential energy profiles," *Langmuir*, vol. 21, no. 4, pp. 1244–1254, 2005.

[199] Yamada, J., "Evanescent wave Doppler velocimetry for a wall's near field," *Applied Physics Letters*, vol. 75, no. 12, pp. 1805–1806, 1999.

[200] Yang, C. T. and Chuang, H. S., "Measurement of a microchamber flow by using a hybrid multiplexing holographic velocimetry," *Exp Fluids*, vol. 39, no. 2, pp. 385–396, 2005.

[201] Yang, J. W., Duan, J. M., Fornasiero, D., and Ralston, J., "Very small bubble formation at the solid-water interface," *Journal of Physical Chemistry B*, vol. 107, no. 25, pp. 6139–6147, 2003.

[202] Yoon, J. H. and Lee, S. J., "Investigation of the near-field structure of an elliptic jet using stereoscopic particle image velocimetry," *Meas Sci Technol*, vol. 14, no. 12, pp. 2034–2046, 2003.

[203] Yoon, S. Y. and Kim, K. C., "3D particle position and 3D velocity field measurement in a microvolume via the defocusing concept," *Meas Sci Technol*, vol. 17, no. 11, pp. 2897–2905, 2006.

[204] Zama, Y., Kawahashi, M., and Hirahara, H., "Simultaneous measurement of droplet size and three-components of velocity in spray," *Opt Rev*, vol. 11, no. 6, pp. 358–364, 2004.

[205] Zettner, C. M. and Yoda, M., "Particle velocity field measurements in a near-wall flow using evanescent wave illumination," *Exp Fluids*, vol. 34, no. 1, pp. 115–121, 2003.

[206] Zhu, L. D., Tretheway, D., Petzold, L., and Meinhart, C., "Simulation of fluid slip at 3D hydrophobic microchannel walls by the lattice boltzmann method," *Journal Of Computational Physics*, vol. 202, no. 1, pp. 181–195, 2005.

[207] Zhu, Y. and Granick, S., "Rate-dependent slip of newtonian liquid at smooth surfaces.," *Phys Rev Lett*, vol. 87, p. 096105, 2001.

[208] Zhu, Y. X. and Granick, S., "Limits of the hydrodynamic no-slip boundary condition," *Phys Rev Lett*, vol. 88, no. 10, p. 106102, 2002.